Analysis and Design of Piezocomposite Ultrasonic Transducers using Finite Element Technique and Surface Displacement Profiles

Paul Reynolds

Submitted in November 1998

for the degree of Doctor of Philosophy

Ultrasonics Research Group

Department of Electronic and Electrical Engineering

The University of Strathclyde

204 George Street, Glasgow G1 1XW

Scotland, United Kingdom

Table of Contents

Acknowledgements

I would like to thank my supervisor, Professor Gordon Hayward of the Ultrasonics Research Group at Strathclyde University, for his guidance, support, and encouragement during the writing of this thesis, and also for the opportunities that have presented themselves from working in this group.

In addition, I would like to thank the following people for the assistance they have given:

- Mr. T. McCunnie for his manufacturing skill and expertise, and the long hours he spent manufacturing transducers and matching layers for me.
- Dr. A. Cochran for his assistance and comments on my work, which while not always welcome at the time, often proved to be worth having been said.
- Mr. G. Benny for his extensive work on the laser scanning system.
- Mr. J. Hyslop, for at least attempting to provide some competition in finite element modelling, hogging computer resources, and proving particularly good fodder for practical jokes.
- And to all other members of the Ultrasonics Group including Dr. A. Gachagan, Dr. R. Farlow, Mr. W. Galbraith, Mr. S. Kelly and Mr. R. Banks for their assistance throughout this work.
- Mr. J. Wilson for maintaining the network and preventing me from losing my sanity, by reassuring me that, yes, they really are that stupid.

Finally, I would like to thank my mother, Anne, and my sisters, Elaine and Louise, for all their support during the writing of this thesis.

Abstract

Ultrasonic transducers have found extensive applications in the fields of non-destructive testing, biomedicine, and SONAR. Piezocomposite ultrasonic transducers can offer significant advantages over their pure ceramic counterparts, but at the expense of increased manufacturing complexity and the introduction of additional resonant modes that may reduce transducer efficiency if the device is not carefully designed. Extensive work has been carried out over the last twenty years to characterise the behaviour of piezocomposite devices, resulting in many design guidelines, some of which are only applicable in a limited range of device structures. This Thesis presents a new theory of the generation of inter-pillar modes that is based upon the generation of *Lamb waves* in the piezocomposite plate.

Through the use of finite element analysis and a scanning laser interferometer, the resonant mode displacement shapes of piezocomposite transducers are studied and analysed. Excellent correlation between modelled and experimental results is observed, and leads to the conclusion that Lamb waves, rather than Bragg scattering, are responsible for the generation of the high frequency inter-pillar modes. To facilitate these analyses, a comprehensive finite element modelling procedure that includes all piezocomposite microstructure effects as well as matching, backing and fluid loading effects was developed. Additionally, it was demonstrated that for low drive voltages, the acousto-optic effect has minimal effect on the through-water laser scanning of piezocomposite transducers.

Finally, the analysis tools developed for the examination of piezocomposites were used to improve the design of an existing flexible ultrasonic transducer used for non-destructive testing. This resulted in a thinner, higher frequency, pulse-echo device capable of producing similar results to the original, while considerably reducing the complexity of the transducer.

List of Symbols Commonly Used

Symbol	Description	Units
g_{ij}	Piezoelectric Voltage Constant	VmN^{-1}
d_{ij}	Piezoelectric Strain Constant	mV^{-1} or CN^{-1}
k_t	Thickness Mode Coupling Coefficient	
k_{33}	Laterally Unclamped Coupling Coefficient	
Z	Acoustic Impedance	MRayl
ε_r	Permittivity Relative to ε_0	Fm^{-1}
ε_0	Permittivity of Free Space	Fm^{-1}
T	Mechanical Stress	Nm^{-2}
S	Mechanical Strain	
v_x	Velocity	ms^{-1}
ρ	Density	Kgm^{-3}
υ	Poisson's ratio	
t	Time	S
f_x	Frequency	Hz
f_n	Electrical Resonance	Hz
f_m	Mechanical Resonance	Hz
ω	Angular Frequency	$Rads.s^{-1}$
R	Reflection Coefficient	
τ	Transmission Coefficient	
L or l	Distance	m
λ_x	Wavelength	m
θ_x	Angle	Rads
[M]	Mass Matrix	
[C]	Damping Matrix	
[K]	Stiffness Matrix	
F	Force	N

u	Displacement	m
ϕ	Electrical Potential	V
σ	Charge Density	Cm^{-3}
D	Flux Density	Cm^{-2}
E	Electric Field	Vm^{-1}
W	Work	Joules
Y	Youngs Modulus	Nm^{-2}
P_x	Pressure	Pa
I	Current	Amps
n	Refractive Index	
Q	Charge	C
Q_{xxx}	Dilation Quality	
α	Mass Damping	
β	Stiffness Damping	
ξ	Ratio of Damping to Critical Damping	
d_0	Pillar Separation (Saw Pitch)	m

Chapter 1

Introduction

1.1 Introduction

Ultrasonic techniques have found extensive applications in the fields of SONAR, biomedicine and non-destructive testing. Conventional ultrasonic transducers utilise piezoceramic as the active material to generate ultrasound, with frequency of operation determined by piezoceramic material properties and device thickness. There has been extensive work in developing piezoceramics with a range of material properties to allow the selection of ceramic to suit each application. For example, Modified Lead Titanate has extremely low piezoelectric coupling between lateral and thickness modes, Lead Metaniobate has high damping for broadband applications, while Lead Zirconate Titanate materials have relatively high electromechanical coupling coefficients and dielectric constants. Even with this wide selection of ceramics from which to choose, a number of problems exist in the use of piezoceramics. Due to the continuous nature of the ceramic transducers, width and radial modes are generated in the transducer in the directions normal to the thickness mode, and can adversely affect transducer performance. In addition, the high acoustic impedance of the ceramics introduce a large impedance mismatch at the boundary between ceramic and some load media, such as air, water, or body tissue.

To overcome these problems, a new type of device comprising the active piezoceramic and a passive polymer, called piezocomposites, was developed. By addition of a polymer component, lateral modes would be highly damped, the coupling coefficient of the devices would be increased, and the effective acoustic impedance would be lowered, improving the overall performance of the device. A variety of device microstructures are possible in piezocomposite devices – a collection of piezoceramic pillars surrounded by polymer (1-3 piezocomposites), alternating

ceramic and polymer bars (2-2 piezocomposites), or small piezoceramic particles randomly distributed within the polymer (0-3 piezocomposites), are three common examples. Unfortunately, the addition of a second material in the most efficient 1-3 configuration introduced an element of periodicity into the transducer structure, creating lateral resonant modes between constituent phases. Design rules were quickly developed to ensure that these modes did not impinge upon the thickness mode, and modelling techniques were developed that worked well, providing these lateral resonances were sufficiently removed from the desired thickness mode.

As increasing demands were placed on ultrasonic technology, composite transducers began to reach the finite construction limits placed on them by equipment and design rules. As these devices have become increasingly complex, the limits of unidimensional modelling techniques have become clear, and an alternative method of modelling was required. It is proposed that a finite element modelling technique is an ideal approach for modelling piezocomposite transducers, as it accounts for all resonances, both thickness and lateral, as well as the effect of ancillary components such as backing blocks and matching layers. In addition, analysis can be carried out in both the time and frequency domains, lending itself to determination of impedance profiles against frequency, and transient behaviour of devices.

This thesis presents an attempt to analyse the resonant behaviour of piezocomposite devices, with a view to improving the performance of such transducers. To this end, a variety of tools, such as a finite element modelling system and a laser vibrometer scanning rig, have been developed. Ultimately, these systems and the knowledge

obtained from composite analysis are used to improve the design of a flexible ultrasonic array for non destructive testing.

It is the intention of the author that this work should expand the knowledge of the behaviour of piezocomposite devices, and to develop a comprehensive modelling system for analysis of such devices. This modelling system is intended to be both adaptable and reliable, such that it can confidently be used in the improvement of existing ultrasonic transducer designs, and the rapid development of new technologies.

1.2 Thesis Content

The study of piezocomposites begins in Chapter 2, with an extensive literature review listing the background and history of piezocomposites in ultrasound, their construction, and the development of design rules. A number of important design criteria and figures of merit that will be referred to throughout this thesis are outlined here.

Chapter 3 explains the development and history of finite element analysis, and the reasons behind the choice of this modelling technique for piezocomposites. Basic finite element techniques and notation are detailed, and the application of finite element theory to piezoelectricity is analysed. Advantages and disadvantages of the technique are discussed, and again figures of merit used later in the thesis are listed. New modelling techniques developed in the writing of this thesis are presented here.

The development of a laser vibrometer scanning system and its application to piezocomposites is the subject of Chapter 4. Basic interferometer theory is presented, and the assembly of the components of the laser scanning system detailed. Limitations of laser scanning are noted, with particular reference to the scanning of transducers through water. Techniques for the minimisation of experimental error have been developed, along with the development of theory and experimental results to indicate that the acousto-optic effect has no bearing on results taken at the power levels used in this thesis.

Chapter 5 is an extensive study of the resonant behaviour of piezocomposite devices, and the ability of finite element techniques to predict their response. The relevance of existing design rules is examined, with particular attention paid to the generation of inter-pillar resonances. Inadequacies of current theories are highlighted and a new theory of propagation of inter-pillar resonances by Lamb waves presented. Methods of predicting inter-pillar resonant frequencies are examined, and mode shapes at the first two inter-pillar resonances demonstrated.

The expertise developed during the writing of this thesis is used in the improvement of the design of a flexible device for non-destructive testing, and is presented in Chapter 6. Finite element techniques are used in the selection of material properties and array component sizes. All aspects of transducer design are studied, including array design and construction techniques. Ultimately, a simplified and improved design is manufactured, and experimental imaging results presented.

A summary of the findings of this thesis, and suggestions for further work conclude the thesis in Chapter 7.

1.3 Contributions to the Field of Ultrasound

The following lists the major achievements of this thesis and their contribution to the field of ultrasound.

- Development of a finite element modelling procedure, capable of modelling both 2-2 and 1-3 connectivity piezocomposite transducers, with matching and backing materials, and fluid loading. Multiple techniques for the improvement of modelling efficiency and effectiveness are presented, such as the use of 2.5 D modelling to obtain impedance profiles.
- Development of a laser scanning system capable of scanning objects with sub-nanometer resolution at micrometer step sizes, both in air and in water. Techniques for assuring the accuracy of such scans through water have been developed, and a theory demonstrating the insignificant effect of acousto-optic behaviour in water at low power levels is presented.
- The various resonant modes that arise within 1-3 composite transducers are shown and explained through surface displacement profiles and finite element analysis. Comparison of such results with existing design rules has been presented, with inadequacies of current Bragg scattering theory highlighted. A theory of inter-pillar resonance propagation by Lamb waves is presented.
- Maximum pillar aspect ratios for 2-2 composites to behave in a unimodal manner are presented, for PZT-5H transducers with both hardset and softset fillers.

- It has been shown that for a piezocomposite to operate in air at the same thickness mode frequency both with and without a matching layer, the matching layer must be a half wavelength thick at the thickness mode frequency. Additionally, it appears that the resonant mode generated by the full composite/matching layer structure generates displacements of magnitudes significantly greater than at the composite thickness mode frequency.
- An improved flexible ultrasonic array has been developed, with greatly reduced thickness, fewer layers, and a higher operating frequency than previous flexible arrays. Experimental imaging results demonstrate the ability of this device to image multiple flaw configurations on curved test subjects. Techniques for the improvement of the manufacture of the devices are also developed and presented.

1.4 Publications Arising from the Writing of this Thesis

Journal Publications

- Reynolds P, Hayward G, 'Design and Construction of a New Generation of Flexible Ultrasonic Transducer Arrays', Insight, 1998, Vol. 40, No. 2, pp101-106
- Gachagan A, Hayward G, McNab A, Reynolds P, Pierce SG, Philp WR, Culshaw B, 'Generation and Reception of Ultrasonic Guided Waves in Composite Plates using Conformable Piezoelectric Transmitters and Optical Fibre Detectors', Accepted for Publication, IEEE Transactions on Ultrasonics Ferroelectrics and Frequency Control, January 1999.

- A. Cochran, P. Reynolds, G. Hayward, 'Progress in Stacked Piezocomposite Ultrasonic Transducers for Low Frequency Applications', Ultrasonics, No.36, 1998, pp 969 - 977

Papers Submitted for Publication

- Reynolds, P., Hyslop, J., Hayward, G., 'Generation of Inter-pillar Resonances in Piezocomposites by Lamb Waves – A Study using Finite Element Analysis', Submitted to the IEEE Transactions on Ultrasonics, Ferroelectrics and Frequency Control, Submitted June 1999.
- Reynolds, P., Hyslop, J., Hayward, G., 'A Study of Piezocomposite Inter-pillar Resonant Behaviour using a Scanning Laser Vibrometer', Submitted to the IEEE Transactions on Ultrasonics, Ferroelectrics and Frequency Control, Submitted June 1999.

Conference Proceedings

- Gachagan A, Reynolds P, Hayward G, Monkhouse R, Cawley P, 'Piezoelectric Materials for Application in Low Profile Interdigital Transducer Designs', IEEE Symposium on Ultrasonics, Ferroelectrics and Frequency Control, Toronto, October 1997, pp 1025 – 1028.
- Reynolds P, Hyslop J, Hayward G, 'The Influence of Constructional Parameters on the Practical Performance of 1-3 Piezocomposite Transducers', IEEE Symposium on Ultrasonics, Ferroelectrics and Frequency Control, San Antonio, November 1996, pp 853 – 856.
- Gachagan A, Reynolds P, Hayward G, McNab A, 'Construction and Evaluation of a New Generation of Flexible Ultrasonic Transducers', IEEE Symposium on

Ultrasonics, Ferroelectrics and Frequency Control, San Antonio, November 1996, pp 967 – 970.

Chapter 2

Piezocomposite Construction and Operation

2.1 Background to Piezocomposite Design

The field of piezocomposite study can be identified as the understanding of new materials constructed from two or more constituent phases, at least one of which is piezoelectrically active. By appropriate selection of materials, device microstructure, and relative quantities of each phase, the performance of piezocomposites can be altered significantly, affording the careful designer great scope in the tailoring of each piezocomposite device to a particular application. Of course, a designer can only take into account such effects as are currently available in the field of knowledge, and a principal aim of this thesis is to expand this body of knowledge to allow design of more efficient and versatile transducers. In order to improve upon an existing body of knowledge, it is important to understand the current 'state of the art' in the field, and the work upon which that was built. The purpose of this chapter, therefore, is to examine the background literature in the field of piezocomposites, the constituent material properties, and the influence of ancillary components such as backing blocks and matching layers on transducer behaviour.

Piezocomposites were first examined in the early 1970's when researchers such as Pauer [1] were attempting to create a flexible piezoelectric device. The potential advantages of such devices over ceramic transducers were clear, and by the early 1980's extensive work had been carried out regarding many aspects of composite design. Early work by Newnham [2] indicated that the class of composites named 1-3 connectivity piezocomposites were the most efficient, and consequently most subsequent work was carried out in relation to these composites. At this time the 'dice and fill' technique for composite construction was reported by Savakus [3], thus ensuring that square ceramic pillars in composites became the standard.

From 1983 to 1985 there was a plethora of excellent papers analysing the performance of 1-3 composites. Reports by Smith and Shaulov [4,5,6], working for Phillips Laboratories, extensively analysed the properties and performance of piezoelectric composite transducers. Auld and Wang [7-11] also produced detailed papers on the performance of these devices with particular reference to resonant modes, as did Gururaja who published an extremely detailed analysis of resonant modes and biomedical applications in PZT devices in a two part paper [12,13]. While there have been many papers published since then, most of the current 'state of the art' still relies heavily on this early work. Later papers of note include work done by Hayward [14-19] and Hossack [20-22], Oakley [23,24], and Certon et al [25]. All these papers will be referred to in more detail in subsequent sections of this chapter. Indeed, an excellent review was presented by Smith at the 1992 SPIE International Symposium [26], and is recommended to anyone interested in a comprehensive review of 1-3 piezocomposites.

An obvious corollary of this work on the behaviour of composite materials was the creation of an accurate, detailed model of the devices. Early models used the electrical circuit analogy to describe behaviour, such as in Mason's Model [27]. Whilst this three-port approximation of a transducer was extremely simple and easy to use, a 'non-real' component, a negative capacitance, was required for the model to function adequately. The Krimholtz, Leedom, and Matthaei model (KLM model) [28] attempted to improve upon the Mason model with another three-port electrical analogy. While being a slightly simpler model, a 'non-real' component was still required, this time a frequency dependent reactance. Work by Hayward [29] introduced the novel concept of a feedback model, splitting the transducer into small,

intuitively understandable components, combining to give an accurate unidimensional model without the requirement for unreal components.

While providing an accurate model for a wide range of transducers, all these models suffered from assumptions that limited their effectiveness. These included restrictions such as no motion or electric field other than in the thickness direction, that the device width is significantly greater than the height to remove the effect of width modes, and that the device can be treated as a single homogenous material. Consequently, while providing accurate information on the thickness mode behaviour of the device, these models failed to take into account the physical construction of the device, or the effect of mode coupling.

A possible solution to this problem lay in the use of Finite Element Analysis (FEA). Such modelling techniques take full account of device construction, and the finite element equations for the behaviour of piezoelectric materials had been presented in 1969 by Allik and Hughes [30]. FEA was used in 1976 by Kagawa and Yamabuchi [31] to model a piezoceramic circular rod, and then a composite structure in 1979 [32]. Extensive work in the FEA of piezocomposite devices was not carried out until the late 1980's, possibly due to a combination of the satisfactory nature of uni-dimensional models, and the cost of computing power in that era. In 1986 Ostergaard and Pawlak [33] of Swanson Analysis Systems developed a three dimensional piezoelectric finite element for ANSYS [54], a popular commercial finite element package, increasing the potential for piezoelectric FEA. By 1990, Hayward and Hossack had utilised the ANSYS package to quantify the effect of lateral mode coupling within piezocomposites [20] and the effect of pillar shape. In the same year,

Lerch [34] used his own FE code developed for Siemens to gain deeper insights into the mechanisms of acoustic wave propagation in piezoelectric media. The versatility of ANSYS was also improved this year, as a new boundary element method of acoustic energy absorption was developed by Rajakumar [35]. Subsequent years provided further work by Lerch [36,39], Wojcik et al [37,38] of Weidlinger Associates who had developed a time domain based piezoelectric analysis code called PZFlex, and Hladky-Hennion [40] with the ATILA FE code. Extensive studies of the effect of 1-3 composite geometry was published by Bennett and Hayward [41,42], while also including the effects of ancillary components such as backing blocks and matching layers.

While it is impossible within a single thesis to detail all the findings of papers mentioned previously, certain key information is required should the reader wish to fully understand the behaviour of piezocomposites, and is now presented, with reference to particular authors if necessary.

2.1.1 Piezoelectric Materials

The active phase in piezocomposite transducers is typically a piezoelectric (or ferroelectric) material. The piezoelectric effect was first discovered by the Curies in 1880, in the naturally occurring material quartz.

The piezoelectric effect is quite simply this – should the piezoelectric material undergo mechanical deformation (strain) then electrical charge will be generated at the material surface. Conversely, should an electrical field be applied across the material, then it will mechanically deform. The governing equations for the electrical

and mechanical behaviour of piezoelectric materials are well understood [30], and are presented in more detail in subsequent chapters.

Within the structure of naturally occurring piezoelectric crystals such as quartz, the centre of positive charge does not coincide with the centre of negative charge. Should an electric field be applied to the material, non-identical atoms will displace by different quantities. In *ferroelectric* (man-made) materials, these internal dielectric moments are randomly aligned and consequently there is no overall polarisation of the material. Should, however, the ferroelectric material be heated to a certain temperature (the Curie temperature) while a constant electric field is applied across the material, the domains will tend to align with the field, and will remain so upon cooling of the material. The material can the then be said to be piezoelectric, having undergone this *poling* process.

It is clear that the poling effect will ensure that a piezoelectric material will be *anisotropic* – that is, the material will not have the same properties in all axes. It is therefore important to establish a form of notation to clearly distinguish which direction is referred to in any statements regarding a piezoelectric material. Such a method is presented in Figure 2.01, where the 3 direction is in the direction of poling (the z or *thickness*) direction, and the 1 and 2 directions represent the axes perpendicular to the 3 axis (x and y, or *width* directions). A piezoelectric material is typically electroded along the planes perpendicular to the upper and lower ends of the 3 axis. The directions 4, 5, and 6 refer to rotations about the 1, 2, and 3 axes respectively. These axes numbers are often used in subscripts of material constants, in

the form $\mathbf{x}_{ij}$ where **x** is the constant value, *i* represents the resultant response, and *j* represents the applied stimulus.

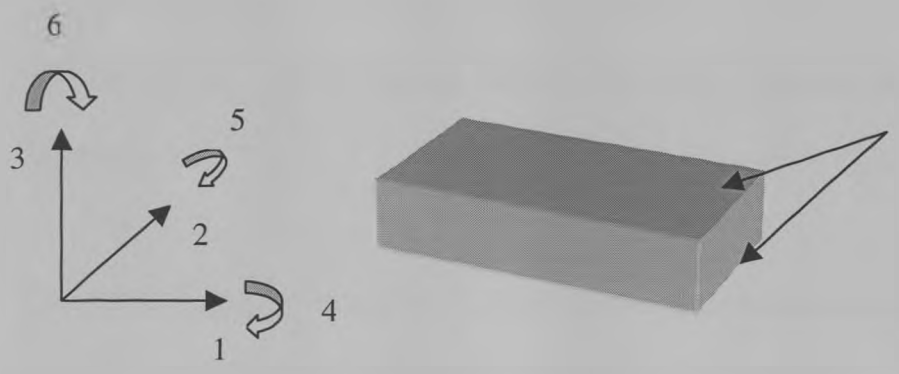

Figure 2.01 Convention for Axis Numbering

Two constants can be referred to which define the piezoelectric behaviour of a material. The first is the *Piezoelectric Voltage Constant*, the symbol for which is $\mathbf{g}_{ij}$. This refers to the electric field generated across the material by an applied unit stress (vmN^{-1}), under open circuit conditions. This is a measure of the direct piezoelectric effect and is typically used in reference to reception characteristics. The second is the *Piezoelectric Strain Constant,* $\mathbf{d}_{ij,}$ and is the more commonly used of the two constants (in this thesis), as it is a measure of the inverse piezoelectric effect and the material transmission characteristics. Under open circuit conditions, the constant is given by the strain produced by a unit electric field, and has the units mv^{-1} or CN^{-1}.

A third dimensionless constant will also be referred to, the electromechanical coupling coefficient $\mathbf{k}_{ij}$ which represents the quantity of electrical energy converted to mechanical energy over a single cycle. The most commonly used form of this constant is $\mathbf{k}_t$, the thickness coupling coefficient, and this will be examined in more depth in subsequent chapters. Also of interest is $\mathbf{k}_{33}$, the coupling coefficient for a laterally unclamped thickness mode (such as in a tall thin pillar).

2.1.2 Modern Piezoelectric Materials

Piezoelectric materials utilised today are significantly more advanced than the quartz crystal examined by the Curies. Wide ranges of materials now exist that are piezoelectrically active, amongst which the most common are the ferroelectric ceramics.

Piezoceramics have a number of characteristics that make them highly suitable for a wide range of ultrasonic transducer applications. These include

- High specific acoustic impedance (**Z**, 20 to 35 MRayl), which has a direct bearing upon the transmission and reflection of energy at material boundaries. Thus piezoceramics couple well into metals such as copper and steel (acoustic impedances of 42 and 45 MRayl respectively), but poorly into low impedance media such as water and air (1.5 MRayl and 434 Rayl impedances respectively)
- High electromechanical coupling coefficients, ranging from 0.5 to 0.7, maximising transducer efficiency
- High permittivity (ε_r ranging from 140 to 1750), to reduce transducer input impedance and allow good electrical matching
- A wide range of lateral coupling coefficients, with the value of $\mathbf{d}_{31}$ ranging from $-10*10^{-12}$ CN^{-1} to $-274*10^{-12}$ CN^{-1} for common ceramics.

There is no one ceramic that is ideal for use in all transducer applications – a designer must choose the ceramic material carefully for each individual circumstance. Some of the most commonly used ceramics are now listed in more detail.

The lead zirconate titanate family (PZT) of materials is one of the more widely used groups of ceramics, each differing by the variation of zirconium/titanium ratio and the addition of impurities. All the PZT ceramics have extremely high electromechanical coupling factors, as high as 0.7, allowing construction of extremely efficient devices. PZT-4 has extremely low losses whilst maintaining large mechanical displacements, and is often referred to as Navy Type I. The PZT-5 family has greater thickness mechanical displacement properties, at the expense of increased lateral coupling and increased losses. PZT-5H (Navy Type VI) has a relative permittivity almost twice as large as that of PZT-5A (Navy Type II), and therefore tends to match better to electrical circuitry, as well as a slightly higher electromechanical coupling coefficient. PZT-5H, however, still does not enjoy the same manufacturing consistency as PZT-5A.

Modified Lead Titanate (MPT) and Lead Metaniobate (PMN) both have low piezoelectric strain constants, but have the advantage of extremely low lateral coupling coefficients, greatly reducing cross coupling in transducers utilising these materials. Both also have low relative permittivities. PMN has a very high Curie temperature and mechanical damping, making it more appropriate for high temperature and wideband applications.

Another type of piezoelectric material is the piezopolymer group, such as polyvinylidene fluoride (PVDF). This material is produced in thin (25 to 110μm), flexible sheets with a very low specific acoustic impedance (4 MRayl), allowing higher transmission coefficients to materials such as water and air. Unfortunately it

has a low electromechanical coupling coefficient (0.2) and a very low relative permittivity (ε_r approximately 12), making it a poor transmitter of ultrasound.

There is continuous improvement in the characteristics of piezoceramic materials, with one of the most promising being relaxor-based piezoelectric single crystals [43]. These materials offer coupling coefficients (k_{33}) of 90%, dielectric constants approaching 5000, and piezoelectric strain constants (d_{33}) greater than 2000 pCN^{-1}. While offering great promise for the future, problems with manufacturing consistency and temperature dependence prevent these materials becoming used commonly. Consequently, all composites manufactured for the present work utilise standard ceramic materials.

Piezocomposites were developed in a desire to create a material that had most of the advantages of piezoceramics (high electromechanical coupling coefficient, high permittivity) with the advantages of piezopolymers (lower acoustic impedance, low lateral coupling). Details of some common configurations are now presented.

2.2 Connectivity of Piezocomposites

Piezocomposites utilised in ultrasonic applications are typically constructed from two constituent phases – the active piezoelectric ceramic, and the passive (usually polymer) phase. Polymeric materials have a number of characteristics that make them a useful component of piezocomposites. These include

- Low specific acoustic impedance (2 to 4 MRayl), to allow better matching to low acoustic impedance media
- High mechanical losses, to reduce the effect of lateral resonances
- Low relative permittivity (ε_r approximately 4).

By combining the ceramic and polymer into one composite material, many of the material properties can be altered. By variation of the volume of the ceramic within the overall composite volume (often called the Volume Fraction, VF), specific acoustic impedance can be made lower than that of pure ceramic, thus allowing greater transmission of acoustic energy to low impedance media. Although the relative permittivity will be reduced from that of pure ceramic, it will still be significantly higher than that of a piezopolymer. Depending upon the microstructure of the device, the thickness mode electromechanical coupling coefficient can exceed that of the original ceramic and often approaches the value of $\mathbf{k}_{33}$. Lateral resonances are also reduced due to the mechanically lossy polymer, while bandwidth is increased Thus, we have a device that should have high electromechanical coupling efficiency, high relative permittivity, and a specific acoustic impedance that can be altered according to the application.

Whilst it appears that the construction of a piezocomposite transducer would bring many benefits, there is still the matter of the physical layout of the ceramic within the polymer phase (or microstructure) to decide. This is often referred to as the *connectivity* of the composite, and for a ceramic polymer device is typically referred to as a *X-Y connectivity composite.* Here, *X* refers to the connectivity of the ceramic, and *Y* to the connectivity of the polymer. To determine the connectivity of a

composite, each constituent material is looked at separately. If within a material, a straight line can be drawn from one side of a transducer to the other, parallel to a particular axis, and entirely within that particular material, then the material is said to be connected in that axis. This procedure is repeated for all three axes, in all constituent phases, until the connectivity is determined. Figures 2.02 (a) and (b) show two of the most common types of piezocomposite connectivity. Figure 2.02 (a) shows a 2-2 connectivity piezocomposite, which consists of bars of ceramic alternating in one width direction with bars of polymer, while Figure 2.02 (b) shows a 1-3 connectivity composite that consists of pillars of ceramic surrounded by a polymer matrix. Although there are many other possible connectivity options available for the transducer designer, the 2-2 and 1-3 types will be the ones examined in detail for this thesis, as a comprehensive study of all connectivity types is outwith the scope of the work.

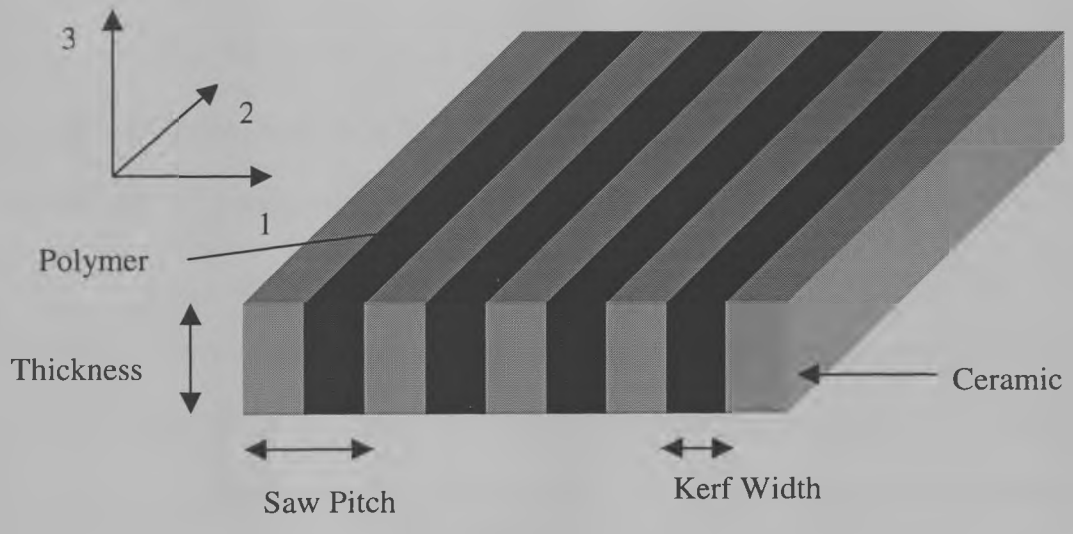

Figure 2.02 (a) 2-2 Connectivity Piezocomposite

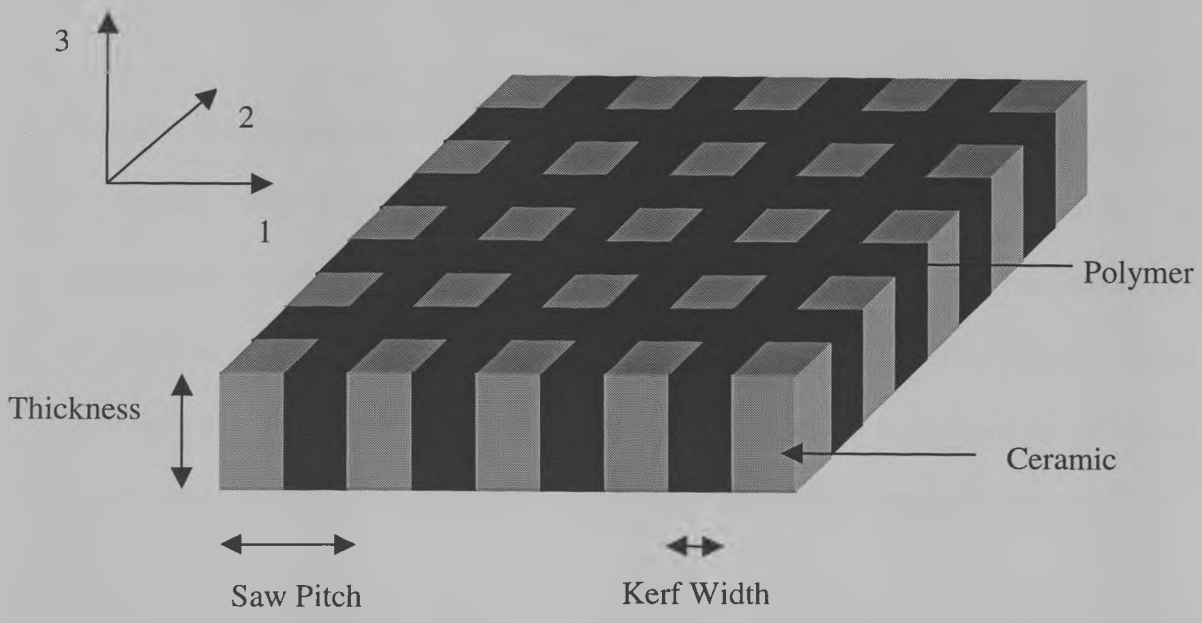

Figure 2.02 (b) 1-3 Connectivity Piezocomposite

It is common for the words connectivity and piezo to be dropped when referring to this type of device, and so a 1-3 connectivity piezocomposite will commonly be referred to as a 1-3 composite.

The two types of transducers mentioned previously lend themselves well to the 'Dice and Fill' construction technique detailed by Savakus [3]. Figure 2.03 details the procedure of machining a solid ceramic block into a 1-3 composite device. Initially the ceramic block is placed in a mechanical saw and cut at regular spacing intervals to a specific depth. The block is then rotated 90 degrees and the procedure repeated until the block consists of pillars of ceramic surrounded by air. After removing the block from the saw, the gaps are filled by the chosen passive filler, and left until the filler has set. The block is then returned to the saw, and sliced in a plane perpendicular to

the thickness axis, with the thickness of the slice determining the frequency of operation of the device. Obviously, the 2-2 connectivity composites are constructed in an identical fashion, without the need for the second set of saw cuts.

Another possible manufacture technique is the use of *injection moulding*, as detailed by Bowen [44]. Injection moulding allows considerably greater scope in the manufacture of composites than with the Savakus technique, allowing fine control of all physical structure characteristics such as pillar shape and pillar spacing. This technique lends itself well to mass production, but involves significant initial set-up costs. All composites manufactured for this thesis utilised the 'dice and fill' method.

At this point it is important to define the term Aspect Ratio (AR), which in a 1-3 composite is the ratio of the ceramic pillar width to ceramic pillar height. This term will be used extensively in the remainder of this thesis, as it is extremely important to the overall behaviour of a piezocomposite device.

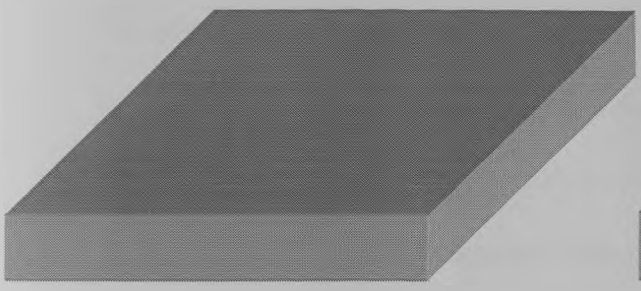

Step 1 – Solid Ceramic Block

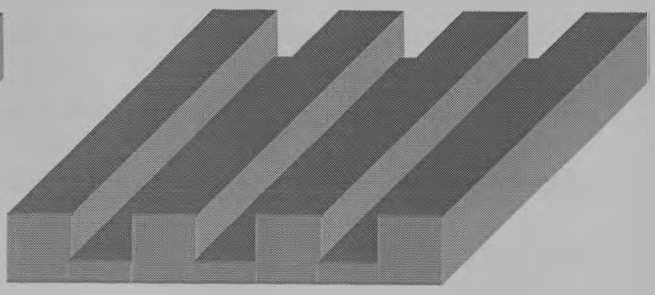

Step 2 – Block Cut with Saw

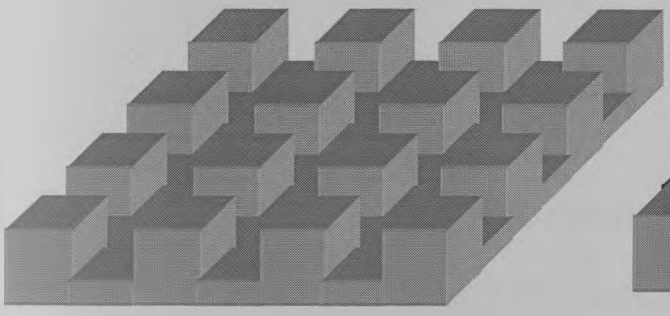

Step 3 – Block Cut again at 90°

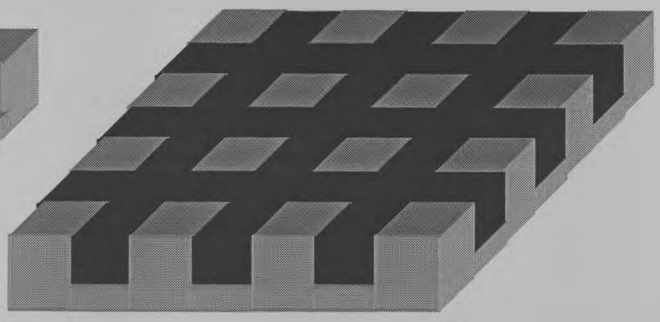

Step 4 – Passive Filler added to Cut Block

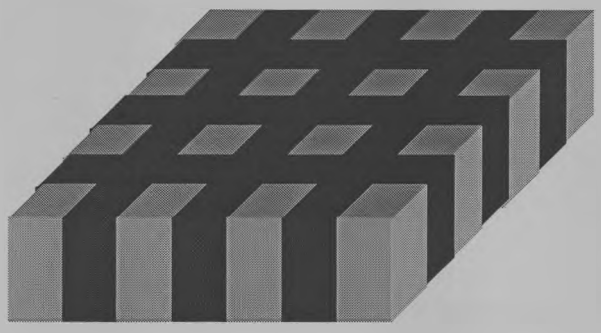

Step 5 – Stock Removed and Block Cut to Desired Thickness

Figure 2.03 'Dice and Fill' Method of Piezocomposite Construction

2.3 Energy Transmission and Reflection by Ultrasonic Transducers

As mentioned previously, the specific acoustic impedance of the materials involved in an ultrasonic system have a significant bearing upon the performance of the transducer. It is important, therefore, for a designer to understand exactly how the specific acoustic impedance will alter system behaviour. This will be accomplished by examination of wave propagation theory, which is extensively detailed by Kino [45], and is limited to the case for a monochromatic normally incident plane wave.

To begin, we must define the nature of specific acoustic impedance (Z) as

$$Z = -\frac{T}{v} \qquad \textbf{Eqn. 2.01}$$

where

T is the stress induced by the mechanical wave

v is the velocity of the mechanical wave.

Equation 2.01 can be re-written as

$$Z_C = -\frac{T_F}{v_F} = (\rho\, c)^{\frac{1}{2}} = V\rho \qquad \textbf{Eqn. 2.02}$$

where

Z_C is the characteristic impedance of the material

T_F is the forward travelling stress in the material

v_F is the forward travelling wave velocity

ρ is the mass density of the material

c is the elastic constant of the material

V is the particle velocity in the material.

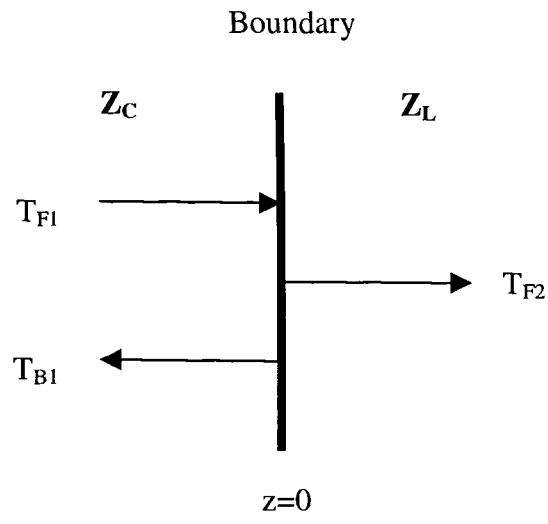

Figure 2.04 Reflected Waves at a Material Boundary

We now consider a wave reflected at a material boundary, as shown in Figure 2.04. For there to be equilibrium at this boundary, it is clear that both stress and velocity must be continuous at the interface. We can write the stress and velocity at the left side of the boundary (z=0) as

$$\hat{T}_1 = \left(T_{F1}e^{-jz\beta_1} + T_{B1}e^{jz\beta_1}\right)e^{j\omega t}$$

$$\hat{v}_1 = \left(v_{F1}e^{-jz\beta_1} + v_{B1}e^{jz\beta_1}\right)e^{j\omega t}$$

Eqn. 2.03 (a) & (b)

where

z and t are positions in space and time

β is the propagation constant, $\beta=\omega(\rho/c)^{1/2}$, or wavenumber

ω is the angular frequency of interest

T_{F1} and T_{B1} are the amplitudes of the forward and backward travelling waves

^ represents a quantity varying with distance, z.

The $e^{j\omega t}$ term will now be dropped and the equations evaluated at a specific point in time. At this point, the reflection coefficient, R, can also be defined as

$$R = \frac{T_{B1}}{T_{F1}} \qquad \textbf{Eqn. 2.04}$$

In a similar way to above, the equations for stress and velocity at the right hand side of the interface can be written as

$$\hat{T}_2 = T_{F2} e^{-jz\beta_2}$$

$$\hat{v}_2 = -\frac{T_{F2}}{Z_2} e^{-jz\beta_2} \qquad \textbf{Eqn. 2.05 (a) \& (b)}$$

where all symbols represent the parameters as stated above, and the subscript 2 referring to the transmitted parameter in the second material.

By equilibrium, stresses and velocities on either side of the interface must be equal, so by equating Eqns. 2.03 (a)&(b) and 2.05 (a)&(b), then substituting with Eqn. 2.04, we find that

$$R = \frac{Z_2 - Z_1}{Z_2 + Z_1} \qquad \textbf{Eqn. 2.06}$$

And knowing that the transmission coefficient, τ, is equal to $1+R$, gives the transmission coefficient in terms of acoustic impedances as

$$\tau = \frac{2Z_2}{Z_2 + Z_1} \qquad \textbf{Eqn. 2.07}$$

It is clear from the last two equations that should there be a large mismatch in acoustic impedance between the transducer and the load media, most of the acoustic energy will be reflected at the boundaries of the two media. Additionally, Equations 2.06 or 2.07 resulting in a negative value indicates that the wave has undergone a phase inversion (that is, its phase has been altered by 180°)

2.3.1 Ideal Matching Layers

In order to overcome this problem and increase the efficiency of the transducer, a *matching layer*, of acoustic impedance Z_M, thickness l, and propagation constant β_M, can be inserted between the active layer and the load media. It is evident that if z=0 is moved to the boundary of the matching layer and the load, as shown in Figure 2.05,

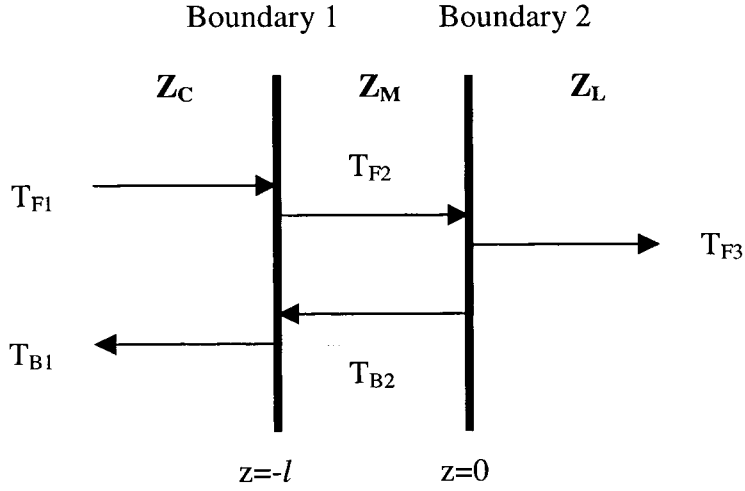

Figure 2.05 Boundary Reflections with a Matching Layer

then the input impedance seen by the active layer is given by

$$Z_{IN} = -\frac{T_{(-l)}}{v_{(-l)}} \qquad \textbf{Eqn. 2.08}$$

and by substituting in a similar method that resulted in Equation 2.06, we see that

$$Z_{IN} = Z_M \left(\frac{e^{jl\beta_M} + R_M e^{-jl\beta_M}}{e^{jl\beta_M} - R_M e^{-jl\beta_M}} \right) \qquad \textbf{Eqn. 2.09}$$

where R_M is the reflection coefficient between the matching layer and the load. By expansion of the exponential terms, and full substitution for R_M gives

$$Z_{IN} = Z_M \left(\frac{Z_L \cos(\beta_M l) + jZ_M \sin(\beta_M l)}{Z_M \cos(\beta_M l) + jZ_L \sin(\beta_M l)} \right) \qquad \textbf{Eqn. 2.10}$$

For efficient energy transfer across the matching layer, the value of Z_{IN} must be real, as imaginary components indicate energy loss, and there are two conditions under which this can occur. The first is attained by setting the sin ($\beta_M l$) terms to zero, but this results in the solution $Z_{IN}=Z_L$, implying that the matching layer has no effect, and so this solution is ignored. Should the components cos ($\beta_M l$) be set to zero, however, we arrive with the solution

$$Z_{IN} = \frac{Z_M^{\,2}}{Z_L} \qquad \textbf{Eqn. 2.11}$$

This obviously gives greater scope in varying the load impedance seen by the active layer. Ideally, the load seen will be equal to that of the active layer (Z_C), which, substituting in Equation 2.11, gives the ideal matching layer impedance of

$$Z_M = \sqrt{Z_C Z_L} \qquad \textbf{Eqn. 2.12}$$

As well as the impedance of the layer, the matching layer thickness is also critical in ensuring that cos ($\beta_M l$) be set to zero. In order for this to be the case,

$$(\beta_M l) = \frac{n\pi}{2} \quad \forall \quad n = 1,3,5,.... \qquad \textbf{Eqn. 2.13}$$

implying that

$$l = \frac{\lambda}{4}, \frac{3\lambda}{4}, \frac{5\lambda}{4}, ...$$

thickness l should therefore be a quarter wavelength thick, based upon the speed of sound in the matching layer material.

Thus it is clear that should the matching layer be of a quarter wavelength thickness, and its acoustic impedance be equal to the geometric mean of the active and load media impedances, then perfect transmission for one frequency can be achieved. This ideal situation, however, is extremely difficult to achieve, as it is not always possible to select a material with exactly the correct impedance. To overcome this problem, multiple matching layers may be used.

Work has been carried out by Jackson [46], which showed that for multiple matching layers (total N), optimum impedance of the n^{th} layer should be

$$Z_n = \left(Z_C^{N+1-n} Z_T^n\right)^{\frac{1}{N+1}} \qquad \textbf{Eqn. 2.14}$$

Obviously, as the number of matching layers increases, manufacturing difficulty also increases, often offsetting any benefits that could be gained from utilising multiple layers.

The addition of a matching layer also introduces additional resonances, affecting the maximum bandwidth achievable by the transducer, and is well documented by both Kossof [47] and DeSilets [48]. Additionally, the overall thickness of the transducer has been increased, thus increasing the transit time for waves to travel from the front face of the device to the absorbing backing block, increasing time to ring down and reducing bandwidth. While this will often be of negligible consequence to the performance of the transducer, in some cases it may have a significant effect, and the effect of the matching layer is examined in more detail in following chapters.

2.4 Backing Block Design

Consideration must also be given to the rear face of the active material. Whilst a matching layer is designed to maximise the energy output from the front face of the transducer, a backing block is designed to maximise the energy *loss* at the rear face. This is accomplished by closely matching the acoustic impedance of the backing block to that of the transducer, with perfect absorption occurring (theoretically) when the two impedances are equal. Typical methods of constructing a backing block involve loading a hard setting polymer with powdered metal of high acoustic impedance such as tungsten, which has an acoustic impedance of 100 MRayl. As energy absorbed at the rear face of the transducer increases, signal ring down time decreases, thus increasing the bandwidth of the device. Unfortunately, this increase in bandwidth occurs at the expense of decreased sensitivity, and so the chosen impedance of the backing block will have to be a compromise between maximising bandwidth while still maintaining an acceptable sensitivity.

2.5 Resonances in Piezocomposite Devices

A variety of different resonances can exist within the structure of a piezocomposite device due to its periodic nature. Each has its own particular frequency and mode shape, and each contributes to the overall behaviour of the device. In order to understand how such resonances affect device behaviour, we must consider each in turn.

2.5.1 Thickness Mode Resonance

The *thickness* mode in an ultrasonic transducer is usually the dominant mode of any present, and is caused by the vibration of the piezoceramic in the 3 axis. It occurs due to the finite thickness of the device, and its wavelength is equal to twice the thickness of the transducer. The frequency of this mode, therefore, is dependent upon the transducer thickness and the velocity of sound in the thickness direction. For a given transducer thickness a_T the frequency of the thickness mode can be shown to be

$$2a_T = n\lambda_T \quad \forall \quad n = 1,3,5,\ldots$$

$$a_T = \frac{n\lambda_T}{2} \qquad \textbf{Eqn. 2.15 (a), (b), \& (c)}$$

$$f_T = \frac{nv_T}{2a_T}$$

where

λ_T is the wavelength in the thickness direction

v_T is the particle velocity in the thickness direction

f_T is the frequency of the thickness mode.

It should be noted that this equation assumes that the device has higher acoustic impedance than the surrounding media. Consequently only the odd harmonics of this mode can be sustained, thus limiting the value of n to 1,3,5,....

Any resonant mode is characterised by two distinct points on an electrical impedance profile – the *electrical resonant frequency* (f_n), and the *mechanical resonant frequency* (f_m), and both are clearly labelled on the typical transducer electrical impedance graph shown in Figure 2.06. The electrical resonance is associated with the point of lowest impedance magnitude on an impedance plot, and the frequency at which the impedance phase crosses from -90° to +90°. It is generally the frequency at which surface displacement of the transducer is at its greatest, and the optimum frequency for transmission purposes. The mechanical resonant frequency is determined by an impedance maxima occurring at a frequency slightly higher than the electrical resonance, and it is at this resonance that impedance phase shifts from +90° to -90°.

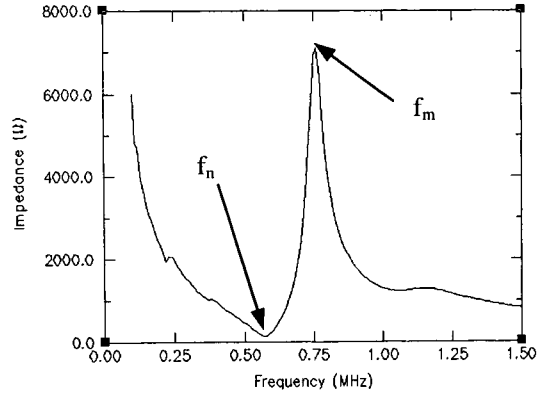

Figure 2.06 (a) Transducer Electrical Impedance Magnitude against Frequency

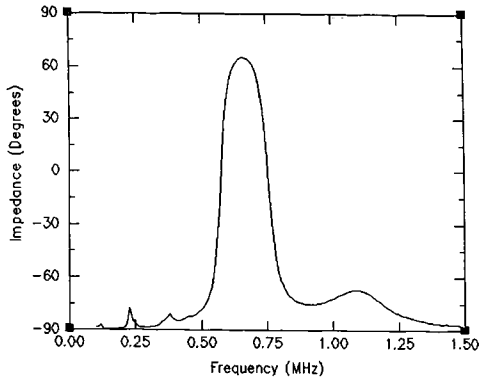

Figure 2.06 (b) Transducer Electrical Impedance Phase against Frequency

Many types of modelling only consider thickness mode resonances for simplification purposes, and in many cases this assumption is valid. There are cases, however, when other (non-thickness mode) resonances are present and can significantly affect the transducer behaviour.

2.5.2 Width Mode Resonances

The second mode type is the *width* mode. This is similar to the thickness mode, but occurs due to the finite width of the transducer, and hence a width mode travels perpendicular to a thickness mode, along axes 1 and 2. The frequency of this mode is dependent upon both the width of the transducer and the speed of sound in the width direction. This may result in more than one width mode should the transducer not be identical in the 1 and 2 axes. For example, a square 1-3 connectivity composite will have two identical width modes in the 1 and 2 axes, but a 2-2 connectivity composite will have two different modes. The polymer matrix present in piezocomposites tends to have high damping and so the energy contained within these modes is significantly dissipated, illustrating another advantage of piezocomposite design over monolithic

ceramics. As the width and thickness of a typical ultrasonic transducer can differ by over an order of magnitude, the thickness and width modes will usually be well separated in the frequency spectrum, as can be seen in Figure 2.06. The effect of these modes must still be taken into account during the design of any transducer, particularly in cases of low frequency, high volume fraction and small aperture transducers.

2.5.3 Microstructure Resonances

Both the thickness and the width modes of any transducer are related to the overall scale of the transducer, termed the device *macrostucture*. The remaining two mode types, however, relate to the internal construction of any device, and depend upon the device *microstructure*.

2.5.3.1 Inter-pillar Resonances

The first of these modes is typically called the inter-pillar mode, or inter-plate mode should it occur in a 2-2 composite. These modes arise due to standing wave patterns within a periodic composite lattice. As the ceramic vibrates in the 3 axis (the thickness direction), there is a certain amount of displacement in the 1 and 2 axes, depending on Poisson's ratio for the material. This lateral motion gives rise to shear waves that in turn may give rise to standing wave patterns that may couple strongly into the composite structure. Brillouin scattering theory is typically used to describe this behaviour, and extensive work has been carried out in this area by Auld and Wang [7-11], and Gururaja et al [12].

In order to allow approximation of the composite structure to the Brillouin lattice shown in Figure 2.07, certain criteria must be met. It should be noted that the theory presented here is directly applicable to 1-3 composites (and not 2-2 composites), as it is the more general of the two.

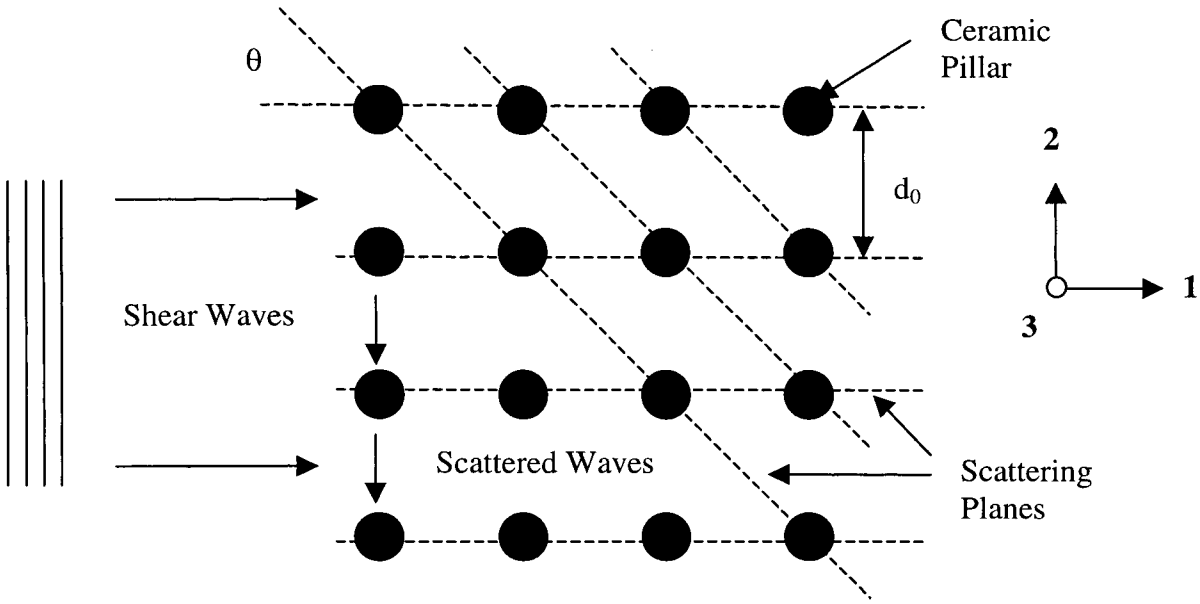

Figure 2.07 Brillouin Scattering Lattice

- Pillar height must be greater than pillar spacing
- Pillar width must be significantly less than pillar spacing
- Polymer losses must be sufficiently low to allow transverse waves to be sustained
- Composite pillar spacing must be similar to the transverse wavelength at the operating frequency. Should the wavelength be too large (as with fine pillar spacing) then there is no standing wave formation and constructive interference cannot take place. In these cases the composite displaces in a piston like manner in the thickness direction. Estimates by Gururaja state

that the transverse wavelength must be greater than three times the periodicity to prevent inter-pillar resonances forming.

As the wavelength is reduced below this ratio limit (typically due to increasing pillar aspect ratio), coupling between the ceramic and polymer can become very strong, and may result in polymer and ceramic vibrating anti-phase in relation to one another.

Consideration must also be given to high frequency behaviour, as wavelengths can be very small and polymer shear losses very high. Under such circumstances, shear coupling may be very weak and ceramic and polymer will tend to vibrate independently.

Should the above criteria be met, then the composite structure can be represented by a Brillouin lattice, which originates from X-ray diffraction in crystal lattices. In such lattices, the actual size of each unit cell is ignored, and is instead represented by a single point in the two-dimensional lattice, as shown in Figure 2.07. Each node within this Figure represents a ceramic pillar within the polymer matrix.

Constructive interference will occur most strongly when the path difference of any scattered wave is an integral number of wavelengths. This is called Bragg scattering and is represented by the equation

$$2d_0 \sin\theta = n\lambda \quad \forall \quad n = 1,2,3,... \qquad \textbf{Eqn. 2.16}$$

where

d_0 is the distance between scattering planes

θ is the angle between the scattering plane and the incident wave

λ is the wavelength of the incident wave.

It is evident that there are certain planes, angles, and wavelengths for which constructive scattering will occur. For a 1-3 composite, the shear waves will travel in the lateral directions, and hence there are three possible diffraction planes – horizontal, vertical, and diagonal. It should be noted that the horizontal and vertical cases are identical, and will therefore be referred to as the horizontal/vertical case.

2.5.3.1.1 The Horizontal/Vertical Case

Under these circumstances, the inter-plane spacing is $\mathbf{d}_0$, where d_0 is the pillar separation, and the angle of incidence is 90°. This will result in Equation 2.16 being expressed as

$$2d_0 \sin 90° = n\lambda_S$$

$$d_0 = \frac{n\lambda_S}{2} \qquad \textbf{Eqn. 2.17 (a), (b) \& (c)}$$

$$f_{HV} = \frac{nv_S}{2d_0}$$

where

λ_S is the incident wave wavelength

v_S is the incident wave velocity

f_{HV} is the frequency of the horizontal or vertical mode.

2.5.3.1.2 The Diagonal Case

In the case of diagonal coupling, the incident angle will be 45° and the plane spacing will be $d_0/\sqrt{2}$. This results in Equation 2.16 appearing as

$$2\left(\frac{d_0}{\sqrt{2}}\right)\sin 45° = n\lambda_S$$

$$d_0 = n\lambda_S \qquad \textbf{Eqn. 2.18 (a), (b) \& (c)}$$

$$f_D = \frac{nv_S}{d_0}$$

where

f_D is the frequency of the diagonal mode.

As the standing waves in Eqn. 2.17(b) and 2.18(b) are established from the same shear wave, the equations must be compatible. This ensures that the only modes coupling strongly into the lattice will be those satisfying the equation

$$\lambda_S = \frac{d_0}{n} \quad \forall \quad n = 1,2,3,.... \qquad \textbf{Eqn. 2.19}$$

2.5.3.1.3 Shear Waves Propagating at 45° to Transducer Edges

There is also an additional case where the shear waves may be propagating at 45° to the 1 and 2 axes. In this case the path length will be $\sqrt{2}(d_0)$, and the scattering angle will be 90°. Equation 2.16 can now be written as

$$2\sqrt{2}d_0 \sin 90° = n\lambda_S$$

$$d_0 = \frac{n\lambda_S}{2\sqrt{2}} \qquad \textbf{Eqn. 2.20 (a), (b) \& (c)}$$

$$f_{D2} = \frac{nv_S}{2\sqrt{2}d_0}$$

for coupling into the diagonal paths, where f_{D2} is the frequency of the 45° shear mode. These will also couple into the 1 and 2 axes, with a plane spacing of d_0 and an angle of 45°, giving rise to a mode at frequency f_{HV2}.

$$2d_0 \sin 45° = n\lambda_S$$

$$d_0 = \frac{n\lambda_S}{\sqrt{2}} \qquad \textbf{Eqn. 2.21 (a), (b) \& (c)}$$

$$f_{HV2} = \frac{nv_S}{\sqrt{2}d_0}$$

For equations 2.20(b) and 2.21(b) to be compatible, the shear wavelengths that will couple strongly into the lattice will be those with the wavelength

$$\lambda_S = \frac{\sqrt{2}d_0}{n} \quad \forall \quad n = 1,2,3,.... \qquad \textbf{Eqn. 2.22}$$

2.5.4 Sustainability of Inter-pillar Modes

Although it has just been shown that there are four possible mechanisms for inter-pillar modes within a piezocomposite, certain criteria have not been taken into account, which will further limit the range of modes possible. In a typical piezocomposite, the electrodes are uniformly applied to the upper and lower surfaces in a monolithic fashion. Such an electrode arrangement ensures that the ceramic pillars will displace in phase with one another. By examining certain mode shapes predicted by Equation 2.17(b), it is clear from Figure 2.08(a) that not all these modes are possible in a real world situation. Adjacent ceramic pillars must vibrate in phase to create a sustainable mode, requiring that the only strongly coupling modes in the 1 and 2 axes will be those whose nodes vibrate in phase.

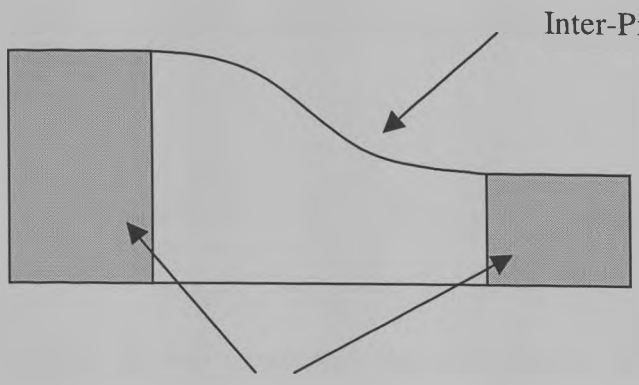

Figure 2.08 (a) Unsustainable Mode

The effect of this constraint means that the first mode generated due to the effects described in Equation 2.17(b), for the value n=2, is shown in Figure 2.08(b). This will cause the polymer between pillars to vibrate in phase with the ceramic, but the polymer on the diagonal will move in anti-phase to the ceramic.

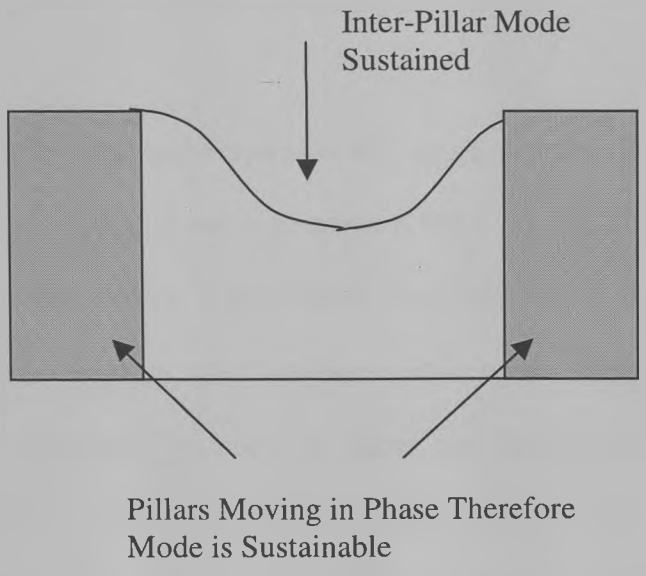

Figure 2.08 (b) Sustainable Inter-pillar Mode

We can therefore conclude that the first three strongly coupled lateral modes are those with the frequencies

$$f_{L1} = \frac{v_S}{d_0} \qquad f_{L2} = \frac{\sqrt{2}v_S}{d_0} \qquad f_{L3} = \frac{2v_S}{d_0} \qquad \textbf{Eqn. 2.23 (a), (b) \& (c)}$$

Obviously, as the mode number increases, the complexity of the mode and its interaction with the structure will increase, but this will be mitigated by the increased polymer damping at the higher frequencies.

In order to ensure that lateral resonances have little effect on transducer performance, several researchers have suggested design rules to separate them from the thickness mode. Oakley [23] suggested that polymer width must be less than a quarter of a shear wavelength, while Smith [49] recommends that the first lateral mode frequency should be greater than two times the thickness mode, and Gururaja [12] that the transverse wavelength be at least three times the periodicity.

Additional work by Bennett and Hayward [42], confirmed the conclusions of Smith and Oakley, and recommended that a Maximum Pillar Aspect Ratio (MPAR) be set for 1-3 composite transducers. The MPAR describes, for a transducer of given thickness and volume fraction, the maximum pillar width to height ratio that can provide sufficient separation between thickness and lateral modes for acceptable transducer behaviour. Further conclusions of this work indicate that transducers utilising soft setting polymers with high damping are less likely to be seriously affected by inter-pillar resonances than those incorporating hard set polymers.

2.5.5 Methods of Eliminating Inter-pillar Resonances

While it is possible to design composites where the lateral resonances do not interfere with the thickness mode, there are a number of methods of altering manufacture to attempt to minimise the problem.

Although the 'dice and fill' method of manufacture will always have pillars with straight edges, it is possible to remove all parallel faces by cutting pillars as triangles as opposed to squares. Additionally, if injection moulding methods are available, circular pillars with no flat faces can be produced. Work has been carried out in this area by Hayward and Hossack [20] and concluded that circular pillars had no significant difference in resonant modes from those of square pillars due to radial modes. Triangular pillars, provided no sides facing were parallel, were shown to offer an increased range of aspect ratios which would provide acceptable transducer behaviour, effectively increasing the MPAR of the device.

Further options investigated included tapered ceramic pillars, and irregular pillar spacing. Tapering the pillars would result in a diversity of inter-pillar spacing, and consequently there should be no single strongly coupled lateral mode. This was shown to be the case [22] and again the MPAR of a device would be increased, although the study did not continue past an AR of 0.6. By variation of inter-pillar spacing, Hossack and Auld [51] showed that spurious lateral resonances could be reduced significantly, thus removing the need for finely diced composites in some cases. This technique, however, increases the manufacturing complexity of a composite and so is not considered in this work.

Most recently, work by Certon et al [25], compared the Bloch waves theory used by Auld and Wang [50] to a 'membrane model' of solving the propagation equations by a finite difference method. Both these methods are superior to the Bragg scattering comparison, as they take into account the geometry of the ceramic pillars, as opposed to reducing them to single point nodes. While this removes the limitations of AR for which the models can be applied to composites, both these methods are considerably more complex than the Bragg scattering model. Solutions to the two newer methods are likely to require a computer based solution, and as such are now competing with other analyses packages such as ANSYS and PZFlex. These latter codes are written to enable analysis of the mechanical behaviour of objects, and in both cases elements specifically exist for piezoelectric problems. Additionally, these finite element codes allow for ancillary components such as bondlines and matching layers to be taken into account, and include their effect on resonant behaviour. Under these circumstances, it is likely to be a more efficient approach to utilise the more versatile commercial codes for transducer analysis, whilst using the Bragg scattering model as a simple, intuitive guide to transducer analysis.

2.5.6 Intra-pillar Resonances

The second resonance to be influenced by the microstructure of the composite is the intra-pillar resonance. In this case, the resonance is created by standing waves set up within a ceramic pillar due to the waves reflected at the ceramic/polymer boundary. In general, the high velocity of sound in ceramic, coupled with the low AR requirements set by the inter-pillar modes, ensure that any intra-pillar modes are of a very high frequency, and consequently have little impact on device performance. In certain cases, however, these modes may become important, particularly should the AR

become greater than 1. For this reason it is important to quantify the likely frequencies at which intra-pillar modes will likely occur. In a similar method to that used for inter-pillar modes, it can be shown that the behaviour of a standing wave set up between the parallel faces of a square pillar is

$$2d_1 = n\lambda_C \quad \forall \quad n = 1,3,5,...$$

$$d_1 = \frac{n\lambda_C}{2} \qquad \textbf{Eqn. 2.24 (a), (b) \& (c)}$$

$$f_C = \frac{nv_C}{2d_1}$$

where

f_C is the frequency of the intra-pillar mode

v_C is the velocity of sound in the ceramic

λ_C is the wavelength of sound in the ceramic

d_1 is the pillar width.

It should be noted that according to Equation 2.06, the reflection coefficient between a ceramic of 25 MRayl and a polymer of 2.5 MRayl would be –0.81. This negative sign indicates that a phase inversion has occurred with the reflected wave, and as in the thickness mode, only odd harmonics will be sustained.

2.6 Conclusions

It is clear that piezocomposite devices offer significant advantages over piezoceramics and piezopolymers, and will become increasingly important in the fields of

biomedicine, non-destructive testing, and SONAR. The complex microstructure of these devices has required that most modelling procedures analyse the composite as a homogenous medium, and will therefore fail to incorporate the effects of any resonance other than the thickness mode. While this will be adequate for many transducers, as the demands upon piezocomposite devices increase there will be a greater need for the understanding and prediction of composite resonant behaviour, and the effects of all ancillary components on such. Indeed, with careful design, it may be possible to utilise these modes to create more versatile devices. While there are many methods available for calculating the frequencies of these modes, the most versatile and promising approach is the use of Finite Element Analysis. FEA ensures that the geometry of the composite, the individual material parameters, and all ancillary components are taken into account, thus surpassing the modelling capabilities of previous uni-dimensional models. This method of analysis is computationally very expensive, but in today's world of low cost memory and disk drives, and high powered processors, FEA is potentially an accurate, efficient, and cost effective analysis tool for piezocomposite devices.

Chapter 3

Finite Element Analysis

3.1 Overview of Finite Element Analysis

It is apparent that in order to accurately model a piezocomposite, the method used must incorporate the effects of microstructure, macrostructure, and ancillary components. One such method is Finite Element Analysis (FEA), a complex but efficient method of numerical solution, ideally suited to computer implementation. In order to use this tool, it is necessary to understand the governing equations and solution options in the method. A brief history of FEA has been included to place the current work in the proper context.

FEA is a numerical procedure to solve a collection of differential equations, usually applied to an engineering problem. It is difficult to find a single individual to credit with its invention, and after its discovery it remained a mathematical curiosity for many years before an application was found. In the early 1950's, a number of factors combined to give FEA the 'push' it needed to become a practical engineering tool. Firstly, following the Second World War and the beginning of the Cold War, the aerospace industry had not only a requirement for analytical tools for solving complex engineering problems, but the resources to fund such work and purchase the necessary equipment. Secondly, and more importantly, digital computers had reached the stage of development where they could be used to solve mathematical problems that would otherwise be too large. Given the difficulty of programming complex geometrical structures into these early computers, matrix notation became the standard input method. Soon after its initial use in the aerospace industry, it was shown that FEA was a variation of the Rayleigh-Ritz method of minimising the potential energy of a system [52], and later that the finite element equations could be derived by using a weighted residual approach such as Galerkin's method [53] and could therefore be

applied to any system, and so FEA began to spread into the fields of civil and mechanical engineering. The vast increase in computing power since the invention of the computer has allowed larger problems to be solved, opening the method to more areas of scientific and engineering endeavour – one such field is ultrasonics.

A large number of finite element codes exist today ranging from specialist codes for particular applications to general codes for use in almost any discipline. The code used for this thesis has been the ANSYS package [54], with version 5.4 current at time of writing, and is a general code widely used in a number of industries. Despite being a general code, ANSYS contains piezoelectric, fluid, and structural elements, which may be used in the simulation of ultrasonic transducers, although with certain restrictions that will be mentioned later. The licence used during a substantial part of the writing of this thesis limited the total number of nodes and elements each to 32,000. Whilst this number may seem large, models of multi-layered devices such as a composite transducer with backing, matching, and fluid loading can rapidly reach this limit, particularly when modelled in three dimensions. This restriction was completely removed towards the end of the work presented, when the licence was upgraded from the university version 5.3 to a full multiphysics version 5.4.

3.2 Basic Concepts of Finite Element Analysis for Ultrasound

The basic idea behind FEA is quite simple – if any structure is divided into a sufficient number of small (finite) elements, approximations to shape and stress can be readily made and only the magnitude remains to be found. The equations governing the behaviour of each element ensure that displacements are continuous

across element boundaries, and that all boundary conditions are satisfied. Figure 3.01 shows how a curve can be approximated by a collection of trapezoids, with accuracy increasing as the shape is divided into more and more elements.

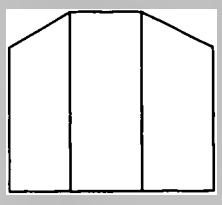

Small Number of Elements –
Poor Approximation

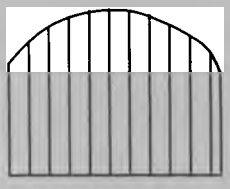

Large Number of Elements –
Acceptable Approximation

Figure 3.01 Approximation of a Curve by Trapezoids

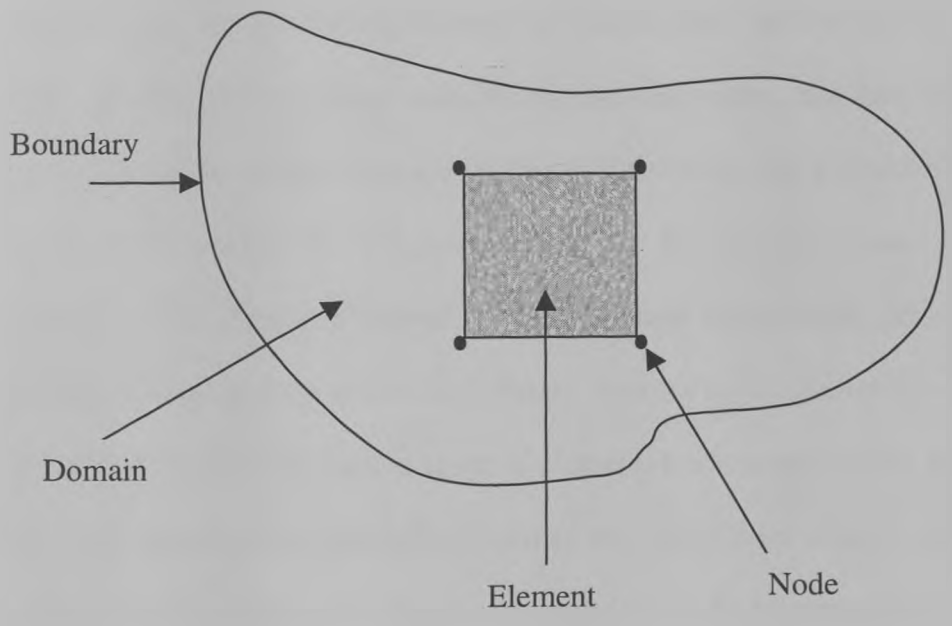

Figure 3.02 Basic Concepts in FEA

The first requirement of the user when initiating a FEA is to select the assumptions (effectively limitations) that will be made in the model. For an example, taken to the extreme case, the model of a piezocomposite without assumptions would require the computer to model not only the composite, but the surrounding air, room and beyond. Whilst this may seem ridiculous, the user must decide which information is pertinent to the model. In the above case, such a composite sitting in air would not require the air to be included (as will be shown later), but the same device sitting in a water bath would require such fluid to be modelled. The user must therefore decide the outside limits of his model, known as the *domain*, and this is illustrated in Figure 3.02.

Within this domain are a number of discrete points known as *nodes,* which form the framework for the model. These nodes are then connected together into a series of finite *elements*, each element having its own set of governing equations and material properties, with the appropriate element type having been selected by the user. As the number of elements increases, solution accuracy increases, and this division of the modelled volumes is known as *meshing*. Each of the nodes has a number of degrees of freedom (DOF) which are ultimately decided by the type of element that they are contained within. Typical examples of DOF include temperature, pressure, voltage, and displacement in each of the axes. Nodes always exist at the vertices of elements, and can also exist within certain types of element. For example, if the typical 8-node solid brick element (one node at each corner of a cube) is insufficient for a particular model, a 20-node solid brick element type could be used with one node at each corner, plus one node along each edge, as shown in Figure 3.03. The 20 node elements are typically used when the structure is required to tolerate irregular shapes. Obviously, the greater the number of nodes, the greater the expense of computation, and so the

user must try to use the simplest element type that will give sufficiently accurate results. Finally, at the edge of the domain are the boundaries that simulate the effect of the 'rest of the world'. In the example, the composite held rigidly in a solid metal casing might require the side edges of the device restricted from moving in the lateral directions. These restrictions on the behaviour of the model are known as *boundary conditions.*

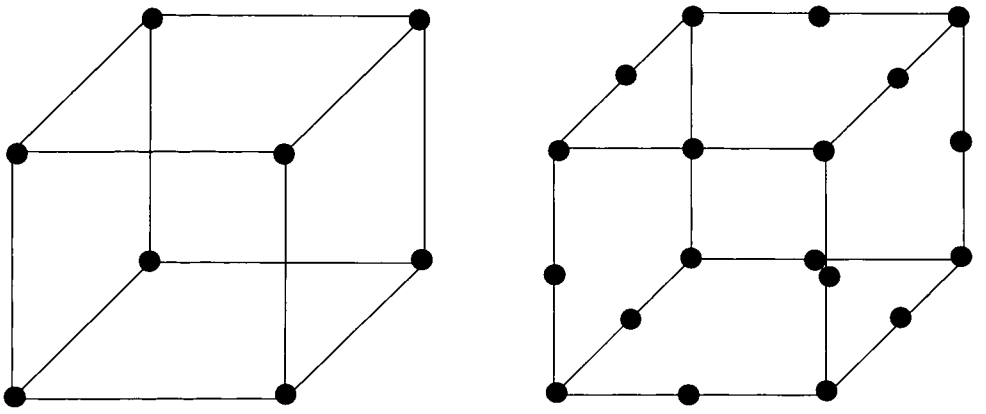

8–node Solid Element 20–node Solid Element

Figure 3.03 8 and 20 Node Elements

The 'art' of finite element modelling is to make the correct assumptions which will allow solution in a reasonable amount of time, whilst maintaining accuracy. For example, sometimes the restriction of lateral motion may suffice to model a transducer, whilst in other cases the holder and the holder/composite bond must be included. The FEA user must decide when this is necessary.

3.2.1 Structuring of Finite Element Analysis

Finite Element procedures can be split into three sections. The first is *pre-processing,* when the model is generated using the appropriate elements, boundary conditions and

loads, and the desired solution type is selected – it is the input stage of the analysis. The *solution* solves the matrix that has been generated during pre-processing in an efficient manner. The user has no control during this stage in the analysis. The final stage is known as *post-processing* which involves analysis and presentation of results to the user. The structuring of FEA can therefore be illustrated in Figure 3.04.

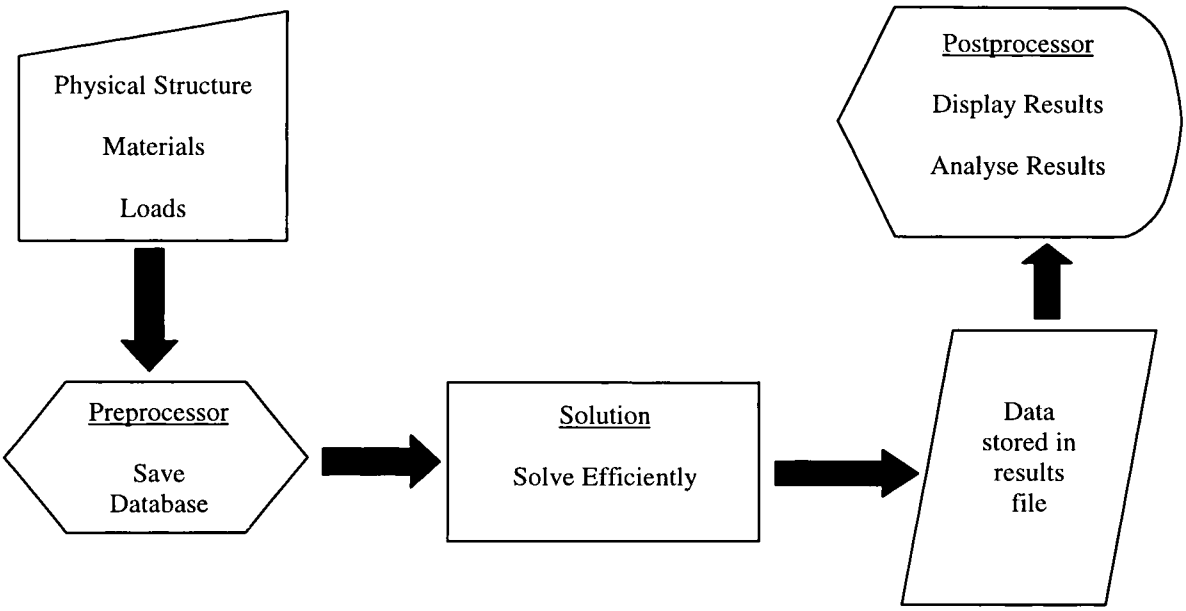

Figure 3.04 Structure of FEA

3.2.2 Types of Finite Element Analysis

When FEA is performed, the user must specify the type of analysis, dependent upon the output desired from the model. The most common types of analysis are *static*, *modal, harmonic,* and *transient*, and within each of these there can be sub-types. These types are specific forms of the general equation

$$[\mathbf{M}]\{\ddot{\mathbf{u}}\}+[\mathbf{C}]\{\dot{\mathbf{u}}\}+[\mathbf{K}]\{\mathbf{u}\}=\{\mathbf{F}\} \qquad \textbf{Eqn. 3.01}$$

where

[**M**] is the mass matrix

[**C**] is the damping matrix

[**K**] is the stiffness matrix

{**u**} is the displacement vector

{**F**} is the force vector.

Each point above a vector indicates differentiation with respect to time. Each type is dealt with in the subsections that follow.

In most cases of a finite element model, a node is connected only to its immediate neighbours, and so certain techniques for simplifying the solution of sparse matrices can be applied. The ANSYS code attempts re-ordering of the nodes to reduce the wavefront, which is defined as the number of non-zero DOF in any row or column. The smaller the wavefront, the smaller the computation time for any given problem.

3.2.2.1 Static Analysis

Static analysis is used to calculate the steady state behaviour of a system when a constant load is applied. As the dynamic frequency of operation is extremely small, time derivatives of the degrees of freedom approach zero and can be removed from Equation 3.01 to give

$$[\mathbf{K}]\{\mathbf{u}\}=\{\mathbf{F}\} \qquad \textbf{Eqn. 3.02}$$

The standard method of solving an equation of this form is called triangular decomposition, and is performed as follows.

$$[\mathbf{K}]=[\mathbf{L}][\mathbf{U}]$$

$$[\mathbf{Y}]=[\mathbf{L}]^{-1}\{\mathbf{F}\} \qquad \textbf{Eqn. 3.03 (a), (b) \& (c)}$$

$$[\mathbf{U}]\{\mathbf{u}\}=[\mathbf{Y}]$$

where

[**L**] is the lower triangular matrix of [**K**]

[**U**] is the upper triangular matrix of [**K**]

The value of {**u**} in Equation 3.03c can then be solved by back substitution. As the stiffness matrix is symmetrical, there is no need to calculate [**L**] explicitly as it is merely [**U**] transposed. This procedure is known as Gaussian elimination. Another similar method is Cholesky factorisation. It relies on the stiffness matrix being symmetrical and positive definite, and factorises the matrix into the form

$$[\mathbf{K}]=[\mathbf{L}][\mathbf{L}]^{\mathrm{T}} \qquad \textbf{Eqn. 3.04}$$

In this case, solutions are found by both forward and backward substitution, both of which are quite quick to perform, as the matrices are triangular.

Whilst these two methods seem very similar, there are significant differences in the way in which the matrices are assembled. The Gaussian elimination method is used in conjunction with a frontal solution process, in which element assembly and equation triangularisation are combined, ensuring that a full set of assembled equations is never formed. Instead, the equations are factorised during assembly of [**K**], meaning that the triangularised matrix is built up at the same time as [**K**], thus effectively being formed directly. The Cholesky method forms [**K**] as one complete step, and then factorises as the second step. Both methods have a similar degree of accuracy and computational

expense. All the types of matrix manipulation mentioned in this thesis are described in more detail elsewhere [55].

3.2.2.2 Modal Analysis

Modal analysis can be used to extract the natural frequencies and mode shapes (the shape of structural deformation) of linear elastic structures. Three assumptions exist within modal analysis

- There is no damping: **[C]**=0
- **[M]** and **[K]** matrices are constant
- No loads, such as forces or pressures, are applied

Given that the above conditions are satisfactory, and that a modal analysis is carried out, the following theory shows how the natural frequencies and mode shapes are calculated.

The equation for free, undamped vibration is

$$[\mathbf{M}]\{\ddot{\mathbf{u}}\}+[\mathbf{K}]\{\mathbf{u}\}=\mathbf{0} \qquad \textbf{Eqn. 3.05}$$

and for a linear structure, displacements are harmonic and are of the form

$$\mathbf{u}=\mathbf{u}_0\cos\omega t \qquad \textbf{Eqn. 3.06}$$

where

$\mathbf{u_0}$ is the maximum displacement of the structure

ω is the angular frequency of vibration

t is the time, taken from initial motion at **t**=0

Differentiating and substituting Equation 3.06 in Equation 3.05 it is found that

$$\left([\mathbf{K}]-\omega^2[\mathbf{M}]\right)\{\mathbf{u}_0\}=\mathbf{0} \qquad \textbf{Eqn. 3.07}$$

Neglecting non-trivial solutions (i.e. $\{\mathbf{u}.\}\neq\mathbf{0}$), it may be concluded that

$$\left|[\mathbf{K}]-\omega^2[\mathbf{M}]\right|=\mathbf{0} \qquad \textbf{Eqn. 3.08}$$

In other words, the determinant of the matrix operations must equal zero. If the matrices are of order *n* then the equation is an *n* order polynomial with *n* roots, ω_1^2, ω_2^2, ...ω_n^2. These roots are called the *eigenvalues* of the equation. When substituted into Equation 3.05, the vectors $\mathbf{u_1}$, $\mathbf{u_2}$, ...$\mathbf{u_n}$ can be determined, and are known as *eigenvectors*. The eigenvalues are the squares of the natural frequencies of the structure, and the eigenvectors are the corresponding mode shapes.

One method of solving the matrix is by the Jacobian method of orthogonal transformation. This transformation is performed by repeatedly calculating

$$[\mathbf{A}_i]=[\mathbf{Y}_i]^T[\mathbf{A}_{i-1}][\mathbf{Y}_i] \qquad \textbf{Eqn. 3.09}$$

where $[\mathbf{A_0}]=[\mathbf{K}]^{-1}[\mathbf{M}]$ and [**Y**] is a self orthogonal matrix (i.e. $[\mathbf{Y}]^T=[\mathbf{Y}]^{-1}$). This method will eventually reduce the matrix to a diagonal matrix (as all off-diagonal terms will effectively be zero), where the diagonals are the eigenvalues of the system. The terms of [**Y**] are chosen to ensure that successive off-diagonal terms in [**A**] are forced to zero. As each term is altered to zero, the previous term is made non-zero,

thus requiring that a number of 'passes' be made in order to ensure that the off-diagonal terms are sufficiently close to zero. One method of expediting this procedure is to perform the operations on the largest off-diagonal term during each pass.

After performing a modal analysis, the user can find the natural vibration frequencies of a structure, and also the mode shapes. It is important to note that the displacements determined are only relative to one another, and do not correspond to an actual magnitude.

3.2.2.3 Harmonic Analysis

Harmonic analysis is used when a sinusoidal load of known amplitude and frequency is applied to a structure. The solution indicates the steady state response of the structure as a function of frequency. At this stage the equations for a purely mechanical analysis will be defined, with a full piezoelectric analysis left until section 3.3.1. The equation of motion governing the harmonic behaviour of a structure is given by

$$[\mathbf{M}]\{\ddot{\mathbf{u}}\}+[\mathbf{C}]\{\dot{\mathbf{u}}\}+[\mathbf{K}]\{\mathbf{u}\}=\mathbf{F}_0 e^{i(\omega t+\theta)} \qquad \textbf{Eqn. 3.10}$$

where

$\mathbf{F_0}$ is the maximum forcing amplitude

i denotes a complex operator

θ denotes a phase angle, in radians.

The forcing function can be expanded as follows:

$$\begin{aligned}\mathbf{F}_0 e^{i(\omega t+\theta)} &= \mathbf{F}_0 e^{i\theta} e^{i\omega t} \\ &= \mathbf{F}_0(\cos\theta + i\sin\theta)e^{i\omega t} \\ &= (\mathbf{F}_1 + i\mathbf{F}_2)e^{i\omega t}\end{aligned} \qquad \textbf{Eqn. 3.11}$$

where

$\mathbf{F_1}$ is the real component of the forcing function

$\mathbf{F_2}$ is the imaginary component of the forcing function.

In any harmonic analysis all components of Equation 3.11 will be known. In a similar method to the forcing function, the displacement vector, **u**, can be written as

$$\mathbf{u} = \mathbf{u}_0 e^{i(\omega t+\theta)} = (\mathbf{u}_1 + i\mathbf{u}_2)e^{i\omega t} \qquad \textbf{Eqn. 3.12}$$

Here, $\mathbf{u_1}$ is the real component of the displacement vector, and $\mathbf{u_2}$ is the imaginary component of the displacement vector. Although the forcing frequency is known, the two quantities of amplitude ($\mathbf{u_0}$) and phase (θ) are unknown. By differentiating and substituting Equations 3.11 and 3.12 into Equation 3.10, it is found that

$$(-\omega^2[\mathbf{M}] + i\omega[\mathbf{C}] + [\mathbf{K}])(\mathbf{u}_1 + i\mathbf{u}_2) = (\mathbf{F}_1 + i\mathbf{F}_2) \qquad \textbf{Eqn. 3.13}$$

This equation can now be solved to provide the appropriate displacements and their relative phases. It is important to note that in almost all cases the solution will be complex. Piezoelectric harmonic analyses are typically used to determine an impedance/frequency plot, and magnitudes for mode shapes.

3.2.2.4 Transient Analysis

The final type of analysis to be discussed is used to obtain *transient* solutions. This calculates the dynamic response of a structure that is subjected to a time dependent load, in much the same way that a harmonic analysis solves for a frequency dependent load. The governing equation for a transient analysis is given by

$$[\mathbf{M}]\{\ddot{\mathbf{u}}\}+[\mathbf{C}]\{\dot{\mathbf{u}}\}+[\mathbf{K}]\{\mathbf{u}\}=\mathbf{F}_0(\mathbf{t}) \qquad \textbf{Eqn. 3.14}$$

A direct integration scheme is used to calculate the response of the system at any given time point, and is an implicit, unconditionally stable method based on the Newmark [56] method. It is *implicit* as the output is based on both present and previous displacements, accelerations and velocities (i.e. the initial condition of the system *must* be known in order for an analysis to be possible). The term 'unconditionally stable' indicates that the solution of a (linear) system will never diverge regardless of the time step size. The equation of motion 3.14, at any time *t*, can be reduced to the integration equation

$$\begin{aligned}(\mathbf{a}_0[\mathbf{M}]+\mathbf{a}_1[\mathbf{C}]+[\mathbf{K}])\{\mathbf{u}_t\}=\{\mathbf{F}_t\}+[\mathbf{M}](\mathbf{a}_0\{\mathbf{u}_{t-\Delta t}\}+\mathbf{a}_2\{\dot{\mathbf{u}}_{t-\Delta t}\}+\mathbf{a}_3\{\ddot{\mathbf{u}}_{t-\Delta t}\})\\ +[\mathbf{C}]\,(\mathbf{a}_1\{\mathbf{u}_{t-\Delta t}\}+\mathbf{a}_4\{\dot{\mathbf{u}}_{t-\Delta t}\}+\mathbf{a}_5\{\ddot{\mathbf{u}}_{t-\Delta t}\})\end{aligned} \qquad \textbf{Eqn. 3.15}$$

where

$\mathbf{a}_x$ are integration constants, which are functions of γ

γ is a user-input damping variable.

If non-linearities exist, then Equation 3.15 can be solved iteratively, with the number of iterations defined by the user. Should the problem be linear, then the **[K], [M],** and **[C]** matrices can be 'reduced' using Guyan reduction for faster solution times.

Displacements at time t=0 are set either to zero, or a static analysis is performed and those displacements used. Accelerations at t=0 are always taken as zero, and velocities are either set to zero initially, or a second static analysis is performed at time t_1 and the rate of change of the displacement between t_0 and t_1 used.

A transient analysis requires that the integration time step (ITS) be defined i.e. the time between each solution point. As the ITS decreases, solution accuracy increases, but there is corresponding increase in computation time. A typical value to choose for good accuracy is about 20 to 60 points per cycle at the highest frequency of interest. Additionally, if wave propagation effects are to be analysed, element size must be sufficiently small for the wave shape to be accurately resolved.

3.3 Element Types

Once the user has decided what type of analysis is required, the element configuration must be chosen. Each type of element has its own set of governing equations to determine its behaviour, and its own unique properties. In the ANSYS package there are over 100 element types, and so the user must carefully select the elements to suit the modelled problem.

3.3.1 Piezoelectric Elements

The ANSYS package has three elements applicable to piezoelectric problems - SOLID5, an 8-node multi-field solid brick element with degrees of freedom for displacement in three axes (UX, UY, UZ) and also voltage. PLANE13 is a 4-node multi-field planar element with degrees of freedom in two axes, and voltage, and

SOLID98 is the tetrahedral version of SOLID5. The initial work in deriving the governing equations was carried out by Allik and Hughes [57], and applied to the ANSYS package by Ostergaard and Paulak [58].

The equations presented below are derived from the laws of conservation of momentum and conservation of charge within a closed system, and the principal of virtual work density [56].

Virtual work density is defined as

$$\delta \mathbf{W} = \{\delta \mathbf{u}\}^T \{\mathbf{F}\} - \delta\phi\sigma \qquad \textbf{Eqn. 3.16}$$

where

δ denotes a virtual quantity

ϕ represents electrical potential

σ denotes the charge density

The superscript **T** denotes a transposed matrix.

Conservation of momentum is given in the form of Hooke's law

$$\{\mathbf{T}\} = [\mathbf{c}]\{\mathbf{S}\} \qquad \textbf{Eqn. 3.17}$$

where

$\{\mathbf{T}\}$ is the stress tensor

$[\mathbf{c}]$ is the material stiffness matrix under a constant electric field

$\{\mathbf{S}\}$ is the strain tensor

Stress is defined as

$$\mathbf{T} = \frac{\text{Force Applied to Element (N)}}{\text{Cross - sectional Area of Element (m}^2\text{)}} \qquad \textbf{Eqn. 3.18}$$

And strain is defined as

$$\mathbf{S} = \frac{\text{Change in Length of Element (m)}}{\text{Original Length of Element (m)}} = [\mathbf{B}_u]\{\mathbf{u}_i\} \qquad \textbf{Eqn. 3.19}$$

where $[\mathbf{B}_u]$ is the mechanical displacement shape function

$$[\mathbf{B}_u] = \begin{bmatrix} \delta/\delta x & 0 & 0 \\ 0 & \delta/\delta y & 0 \\ 0 & 0 & \delta/\delta z \\ \delta/\delta y & \delta/\delta x & 0 \\ 0 & \delta/\delta z & \delta/\delta y \\ \delta/\delta z & 0 & \delta/\delta x \end{bmatrix} [\mathbf{N}_u]^T \qquad \textbf{Eqn. 3.20}$$

$[\mathbf{N}_u]$ is the displacement *shape function* matrix.

Conservation of charge can be similarly described by

$$\{\mathbf{D}\} = [\varepsilon][\mathbf{E}] \qquad \textbf{Eqn. 3.21}$$

where

$\{\mathbf{D}\}$ is the electrical flux density vector

$[\varepsilon]$ is the dielectric tensor at constant mechanical strain

$\{\mathbf{E}\}$ is the electric field vector

Electric field strength is defined as

$$\mathbf{E} = \frac{\text{Potential Difference Across Element (V)}}{\text{Distance Across Element (m)}} = -[\mathbf{B}_\phi]\{\phi_i\} \qquad \textbf{Eqn. 3.22}$$

where $[\mathbf{B}_\phi]$ is the **grad** function, often shown as ∇, and can be represented as

$$[\mathbf{B}_\phi] = \nabla = \begin{bmatrix} \delta/\delta x \\ \delta/\delta y \\ \delta/\delta z \end{bmatrix} \{\mathbf{N}_\phi\}^T \qquad \textbf{Eqn. 3.23}$$

$\{\mathbf{N}_\phi\}$ is an electrical shape function vector. Finally, charge density is defined as

$$\sigma = \frac{\text{Coulombs of Charge across Element (C)}}{\text{Cross} - \text{sectional Area of Element (m}^2\text{)}} \qquad \textbf{Eqn. 3.24}$$

From Equations 3.16, 3.17, and 3.21, it can be shown that

$$\{\mathbf{T}\} = [\mathbf{c}]\{\mathbf{S}\} - [\mathbf{e}]\{\mathbf{E}\} \qquad \textbf{Eqn. 3.25}$$

and

$$\{\mathbf{D}\} = [\mathbf{e}]^T\{\mathbf{S}\} + [\varepsilon]\{\mathbf{E}\} \qquad \textbf{Eqn. 3.26}$$

By applying the principle of variational work to Equations 3.01, 3.25, and 3.26 we obtain the relationships for the $\mathbf{i}^{th}$ element of any model

$$[\mathbf{M}]\{\ddot{\mathbf{u}}\} + [\mathbf{K}_{uu}]\{\mathbf{u}\} + [\mathbf{K}_{u\phi}]\{\phi_i\} = \{\mathbf{F}\}$$
$$[\mathbf{K}_{\phi u}]\{\mathbf{u}_i\} + [\mathbf{K}_{\phi\phi}]\{\phi_i\} = \{\mathbf{Q}_i\} \qquad \textbf{Eqn. 3.27 (a) \& (b)}$$

where

$$[K_{uu}] = \int\int\int_{v} [B_u]^T [c][B_u] dV$$

$$[K_{u\phi}] = \int\int\int_{v} [B_u]^T [e][B_\phi] dV$$

$$[K_{\phi u}] = \int\int\int_{v} [B_\phi]^T [e]^T [B_u] dV$$

$$[K_{\phi\phi}] = -\int\int\int_{v} [B_\phi]^T [\varepsilon]^T [B_\phi] dV$$

These four matrices are referred to as the stiffness matrix, the piezoelectric stiffness matrix, the transposed piezoelectric stiffness matrix, and the dielectric stiffness matrix respectively.

Equations 3.27 (a) and (b) can be combined to represent the system as a whole, as shown in Equation 3.28

$$\begin{bmatrix} [M] & 0 \\ 0 & 0 \end{bmatrix} \{\ddot{u}\} + \begin{bmatrix} [C] & 0 \\ 0 & 0 \end{bmatrix} \{\dot{u}\} + \begin{bmatrix} [K_{uu}] & [K_{u\phi}] \\ [K_{\phi u}] & [K_{\phi\phi}] \end{bmatrix} \begin{bmatrix} \{u\} \\ \{\phi\} \end{bmatrix} = \begin{bmatrix} \{F\} \\ \{Q\} \end{bmatrix} \qquad \textbf{Eqn. 3.28}$$

To solve this equation, the user must know the density and volume of the materials, damping coefficients, stiffness values (either explicitly as a stiffness or compliance matrix, or implicitly from Young's modulus, shear modulus, and Poisson's ratio), a piezoelectric matrix, and a permittivity matrix. Some boundary conditions, such as forces, charge, displacements and voltages must also be supplied.

It should be noted that in all cases, the piezoelectric elements are symmetrical, allowing matrix simplification techniques to be used and consequently reducing computation times.

As well as being used for piezoelectric elements, the SOLID5 and PLANE13 elements were sometimes used to simulate the polymer utilised in piezocomposites. Whilst incurring a greater computational load than simple mechanical elements, use of these elements allowed the viewing of voltage effects throughout the transducer, without limiting electrical fields to piezoceramic sections only. Material characteristics for polymers that utilised this element were defined in exactly the same manner as for a piezoelectric element, with the piezoelectric matrix set to an infinitesimally small value.

3.3.2 Isotropic Solid Elements

The ANSYS elements SOLID45, SOLID95, and PLANE42 are chosen when an isotropic solid material, such as a polymer, must be modelled. SOLID45 is an 8-node brick element each node having the three displacement DOF, and SOLID95 is its 20-node equivalent. PLANE42 is the 2-D equivalent of SOLID45, and consequently has only 4 nodes, each with two displacement degrees of freedom. These elements were typically chosen to model backing blocks, matching layers and bondlines.

The compliance matrix [s] for an isotropic material under constant electrical field is given by

$$[s]=\begin{bmatrix} s_{11} & s_{12} & s_{12} & 0 & 0 & 0 \\ s_{12} & s_{11} & s_{12} & 0 & 0 & 0 \\ s_{12} & s_{12} & s_{11} & 0 & 0 & 0 \\ 0 & 0 & 0 & s_{44} & 0 & 0 \\ 0 & 0 & 0 & 0 & s_{44} & 0 \\ 0 & 0 & 0 & 0 & 0 & s_{44} \end{bmatrix} \qquad \textbf{Eqn. 3.29}$$

where

$$s_{11} = \frac{1}{Y} \qquad s_{12} = -\frac{\upsilon}{Y} \qquad s_{44} = 2(s_{11} - s_{12}) \quad \textbf{Eqn. 3.30 (a), (b) \& (c)}$$

and υ is Poisson's ratio.

The stiffness matrix [c] can then be calculated as $[c]=[s]^{-1}$, and from these, the longitudinal (v_l) and shear wave (v_s) velocities may be calculated as

$$v_L = \sqrt{\frac{c_{11}}{\rho}} \qquad v_S = \sqrt{\frac{c_{44}}{\rho}} \qquad \textbf{Eqn. 3.31 (a) \& (b)}$$

From Equations 3.30a - 3.31b, it is clear that by obtaining the shear and longitudinal wave velocities, and the density of a material, the complete matrix for an isotropic material can be established.

3.3.3 Acoustic Fluid Elements

An ultrasonic transducer will typically transmit into a medium (usually air, water or a metal) and this will often need to be simulated to obtain a true picture of transducer behaviour. While metals can be simulated by the solid elements, air and water have to be modelled by a fluid element, provided by FLUID30 (an 8-node, 3-D brick element) and FLUID29 (a 4-node, 2-D element). These elements have up to 4 DOF, one for each displacement axis and one for pressure. Input values used by these elements are the speed of sound in the fluid (**v**), fluid density (ρ), the acoustic energy transmission coefficient at fluid boundaries (**mu**), and any damping coefficients. From Kinsler and Frey [62]

$$\frac{1}{v^2}\frac{\delta^2 P}{\delta t} = \nabla^2 P \qquad \textbf{Eqn. 3.32}$$

where **P** is the fluid pressure, and assumptions are made that pressure and density changes are small compared to their starting values, there is no mean fluid flow, and the fluid is inviscid. By looking at the one-dimensional case of Equation 3.32, we see that

$$\frac{\delta^2 P}{t^2} = v^2 \frac{\delta^2 P}{x^2} \qquad \textbf{Eqn. 3.33}$$

and also that

$$P(x,t) = f(x - vt) + g(x + vt) \qquad \textbf{Eqn. 3.34}$$

where **f** is the function for a forward travelling wave, and **g** is the function for a backward travelling wave. For a wave varying harmonically with an angular frequency of ω this can be written as

$$P(x,t) = A_R e^{j\frac{\omega}{v}(x-vt)} + A_L e^{j\frac{\omega}{t}(x+vt)} \qquad \textbf{Eqn. 3.35}$$

Should these waves be reflected from solid boundaries located at a fixed distance, travelling and reflected waves will interfere to produce a standing wave that is stationary in space but varies harmonically in time. By substituting the values of the boundaries of the domain for **x**, the standing pressure wave equation can be obtained where $P^1(x)$ represents the spatial variation of the pressure. Obviously, as multiple reflecting boundaries and additional dimensions are introduced, these equations become increasingly complex.

$$P(x,t) = P^1(x)e^{j\omega t} \qquad \text{Eqn. 3.36}$$

It has been shown by Zeinkiewicz [9] that the matrix equations for a fluid element are

$$[M_f]\{\ddot{P}\} + [K_f]\{P\} = [F_f] \qquad \text{Eqn. 3.37}$$

Where the subscript **f** indicates that the matrix refers to the fluid. If the subscript **s** is taken to refer to the solid elements, and **[R]** to refer to the acoustic coupling matrix, then the final form of the general governing equation becomes

$$\begin{bmatrix} [M_S] & 0 \\ \rho_f [R]^T & [M_f] \end{bmatrix} \begin{Bmatrix} \ddot{u} \\ \ddot{P} \end{Bmatrix} + \begin{bmatrix} [C_S] & 0 \\ 0 & [C_f] \end{bmatrix} \begin{Bmatrix} \dot{u} \\ \dot{P} \end{Bmatrix} + \begin{bmatrix} [K_S] & -[R] \\ 0 & [K_f] \end{bmatrix} \begin{Bmatrix} u \\ P \end{Bmatrix} = \begin{Bmatrix} F_S \\ F_f \end{Bmatrix} \qquad \text{Eqn. 3.38}$$

When dealing with acoustic standing waves, two types of analysis may be performed, modal and harmonic. Guidelines for the mesh size of elements [54,61] indicate that the largest mesh size for modal analysis should be $\lambda/6$, and for harmonic analyses $\lambda/15$, where λ is the wavelength in the fluid at the highest frequency of interest.

3.3.3.1 Fluid Element Problems

All fluid elements that contact a solid boundary must have displacement as well as pressure DOF. This has the unfortunate effect of rendering the matrices unsymmetrical, and consequently analyses options are limited, and computation times will increase. To reduce the computation time, only those elements physically in contact with the displacing structure interface have the displacement degrees of freedom. All other fluid elements have these DOF removed, and are thus left with pressure only, reducing the computational load. This method is illustrated in Figure 3.05.

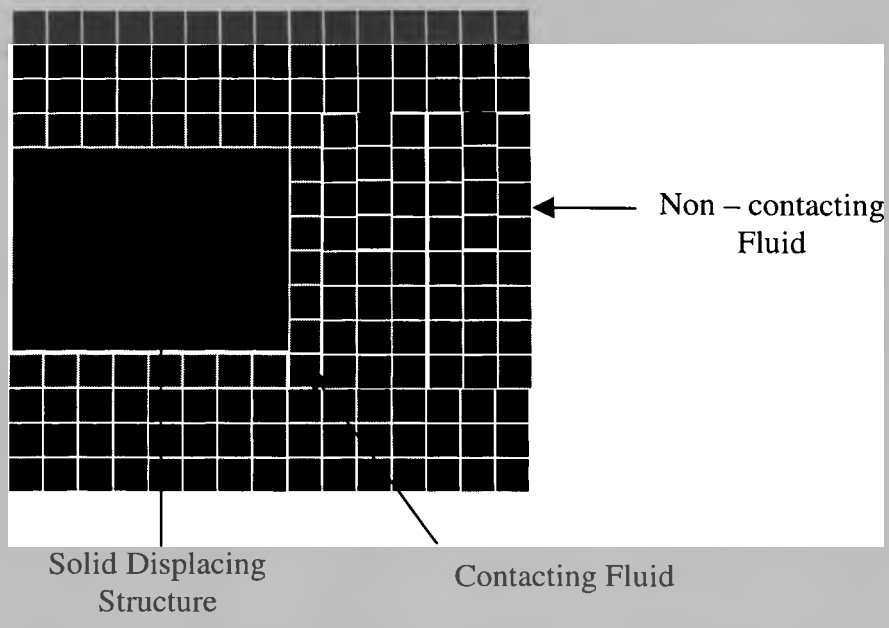

Figure 3.05 Contacting and Non-contacting Fluid Elements

In practice, the fluid surrounding an immersed ultrasonic transducer will be many times the size of the transducer itself. To attempt to model the complete fluid domain in the analysis will result either in extremely long computation times, or an inability to perform the modelling due to size restrictions. A solution recommended by Bennett [13] is to model the fluid as a column with the pressure degree of freedom set to zero at the outer boundaries, and a completely absorbing boundary also to simulate an acoustic field decaying to zero at infinity. While reasonably effective, the ideal solution for this problem is a *boundary element* (BE), which models the medium purely as a completely absorbing acoustic boundary. Such elements existed in ANSYS v5.3, as FLUID130 (three dimensional) and FLUID129 (two dimensional), but only in undocumented (and therefore still experimental) format. Additionally, the equations governing these elements restrict them to spherical geometries. This

problem is detailed by Rajakumar et al [59], and indicates that a FE-BE solution is faster to solve than a FE-FE method, as well as being more accurate. In release 5.4, however, these elements became fully documented and available and the method used during the majority of the work validated by ANSYS, Inc.

3.3.3.2 Modelling of Air as a Fluid

When a fluid is modelled in relation to an ultrasonic transducer, account should be taken of its specific acoustic impedance (**Z**) and the effect this will have on transducer performance. It is clear, however, that in the case of air, an exception can be made. If we compare the acoustic impedances of piezoceramic (20-35 MRayl), water (1.5 MRayl), and air (434 Rayl), we see that the impedance of air is several orders of magnitude smaller than that of water or piezoceramic. The air can consequently be considered a 'soft' boundary (defined as zero stress at the boundary, as opposed to zero strain at the boundary for a completely 'hard' boundary). If the air is modelled as 'void', then there will be negligible difference in the results, with a significantly decreased computation time. As mentioned previously, Bennett modelled a fluid load as a column of liquid with a zero pressure outer boundary, but stated that there were severe restrictions upon its accuracy, depending upon the application. In order to improve the accuracy, a new way of simulating the fluid was developed. Figure 3.06 shows how in 2-D the transducer is completely enclosed within a sphere of fluid elements.

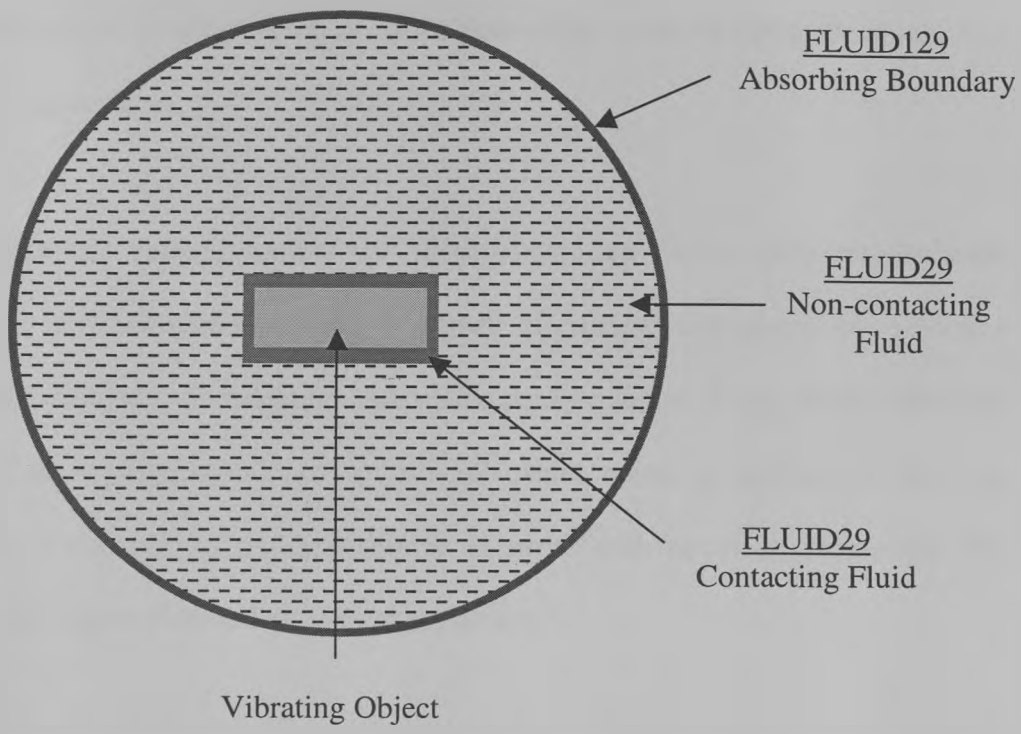

Figure 3.06 FEA 2-D Transducer with Circle of Fluid

This method can also be applied to 3-D problems, and has two benefits. Firstly, the fluid now loads all sides of the transducer, and secondly the spherical geometry allows use of the FLUID130 and FLUID129 boundary elements. Thus a far more accurate (though somewhat larger) model has been developed.

3.3.4 Circuit Elements

Sometimes, it is necessary to simulate the effects of any circuitry associated with a transducer. This is achieved in ANSYS by the use of the CIRCU124 elements that can be used to represent resistors, inductors, capacitors and voltage or current sources (both dependent and independent).

Resistors were typically implemented to model electrical connections between physically remote locations, such as in the connection between electrode shims in a multi-stack transducer.

The independent voltage source was most often used during transient analyses. Specifying *real constants* allowed a signal of almost any shape by selecting amplitude, frequency, start delay, phase delay, decay rate and signal shape (sinusoid, saw-tooth, or rectangular). Bursts of several cycles could be applied in the time domain by connection of multiple sources in series with identical frequencies, but variable amplitudes, time delays, and phase delays.

3.4 Boundary Conditions

The external DOF constraints placed on a model to simulate the conditions outside the model domain are known as boundary conditions. For an ultrasonic transducer, these take the form of voltage constraints to simulate the electrodes, displacement constraints to simulate rigid boundaries, and pressure constraints to simulate fluid boundaries.

In certain modelling problems, large sections of nodes will be 'linked' in some form, constraining particular DOF on those nodes to be identical regardless of any other factors. Such a case exists in the electrodes of ultrasonic transducers in the form of equipotential areas. By using *node coupling* to connect areas, only one node requires to have an applied voltage to correctly model the electrode. This simplifies both processing and subsequent analyses as the rank of the resultant matrix is lower.

3.4.1 Symmetrical Boundaries

In many cases of FEA, a model has one or more axes of symmetry - that is, identical conditions exist on either side of the boundary, and the boundary itself is in equilibrium ensuring no movement perpendicular to it. This is called a *symmetrical boundary*, which can be used to simplify any model with an axis of symmetry as shown in Figure 3.07. A full height model of an ultrasonic transducer is called a *one-quarter symmetry* model, while a half-height model is known as *one-eighth symmetry* model. It is clear that the addition of backing blocks, matching layers, and front-face fluid loading will render a model unsymmetrical in the thickness direction and restrict the user to one-quarter symmetry.

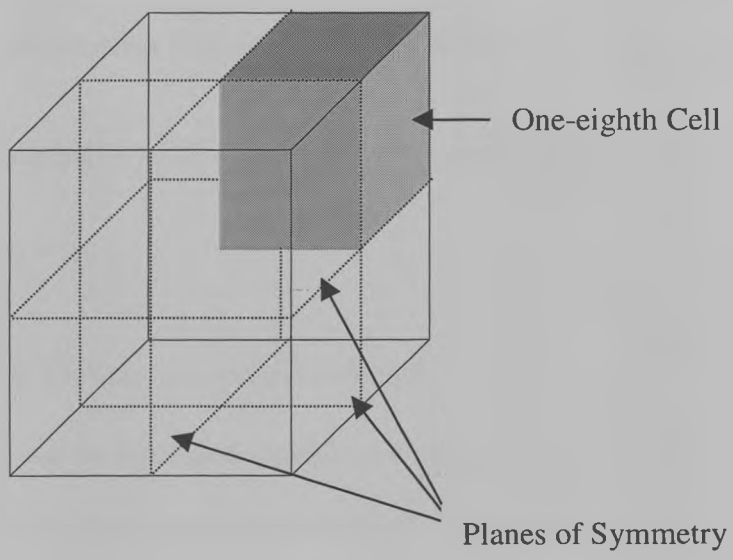

Figure 3.07 One-eighth Symmetry in Finite Element Models

By placing symmetrical boundaries on all edges parallel to the thickness direction, it is possible to simulate the effect of surrounding pillars on the behaviour of each unit cell [60] – that is, to model the transducer as an infinite plane. While this has many advantages over a unit cell modelled on its own, it fails to accommodate true conditions at the boundaries of transducers and their finite size, and hence fails to

consider the effects of width modes and transducer housing arrangements. Additionally, arrangements such as multi-element arrays and sub-diced matching layers would prove difficult to model. Consequently, where device macrostructure was of concern, the procedure of modelling single unit cells surrounded by symmetrical boundaries [60] was abandoned in preference of modelling the transducer in its entirety. This technique was found to be highly accurate in the modelling of composite transducers, although there was a large increase in computation time required for each model.

3.5 Damping Models in ANSYS

Previously, only the simplest version of the damping matrix [**C**] has been considered. The complete expression for [**C**], as available in ANSYS v5.4, is given by

$$[\mathbf{C}]=\alpha[\mathbf{M}]+\beta[\mathbf{K}]+\sum_{j=1}^{NMAT}\beta_j[\mathbf{K}_j]+\beta_C[\mathbf{K}]+\sum_{k=1}^{NEL}[\mathbf{C}_K] \qquad \textbf{Eqn. 3.39}$$

where

α is the mass damping coefficient

β_x are the structural stiffness damping coefficients

$[\mathbf{C_K}]$ is the individual element damping matrix

NMAT and NEL are the numbers of materials and elements respectively.

The values α and β are known as the Rayleigh damping coefficients, and are usually expressed as the ratio of actual damping to critical damping by ξ. Critical damping (c_{CRIT}) is defined as the damping required to ensure the fastest return to the equilibrium position.

$$\xi = \frac{\alpha}{2\omega} + \frac{\beta\omega}{2}$$

$$c_{CRIT} = 2\sqrt{KM}$$

Eqn. 3.40 (a) & (b)

where ω is the frequency of interest, K is the stiffness and M is the mass. It is apparent that α damping is inversely proportional to frequency, and hence damping will be greater at the lower frequencies. By examining Figure 3.09, it is apparent that over a certain range of frequencies the sum of the two damping ratios is almost constant. Only one value each of α and β can be specified for any model, and if used, the most dominant value must be chosen.

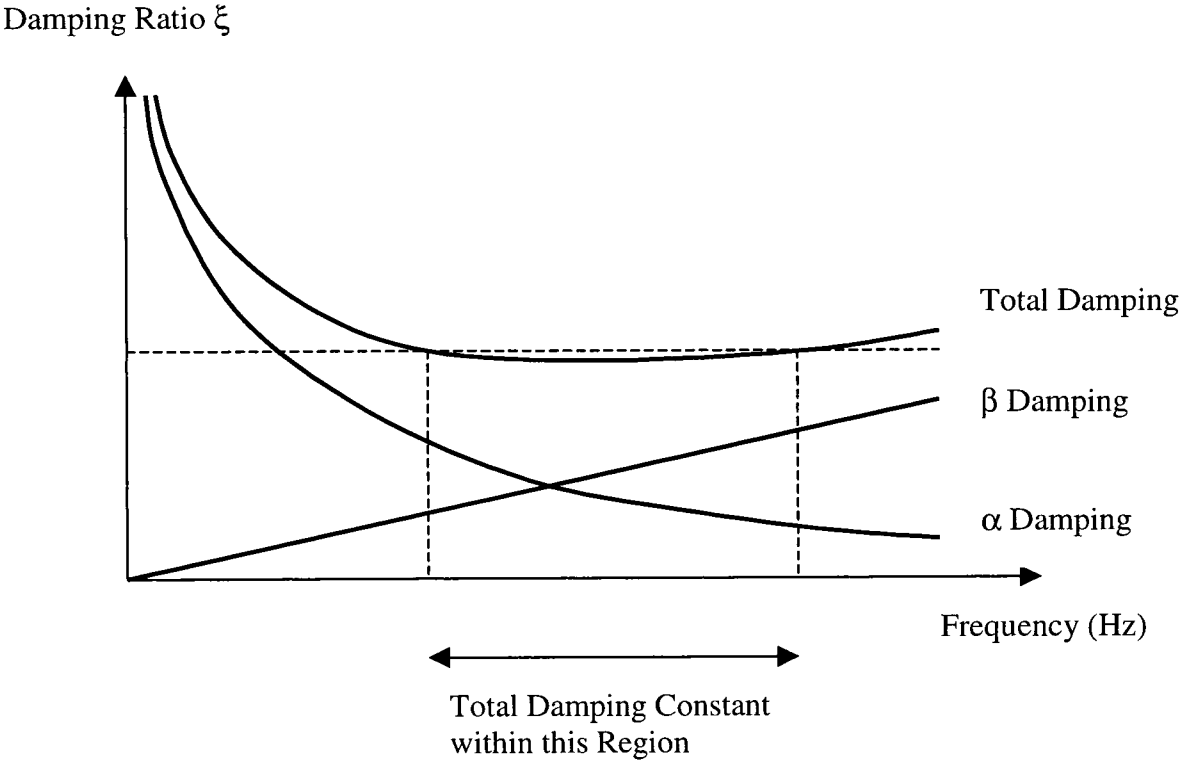

Figure 3.09 Frequency Dependent Damping in ANSYS

Three different forms of β can be specified in ANSYS. As well as the constant stiffness matrix multiplier mentioned previously, there is also β_j, the material dependent stiffness multiplier, and β_c, the frequency-dependent stiffness multiplier.

β_j is specified for each individual material, and only acts upon that portion of the stiffness matrix that applies to that material. β_c is defined in terms of a constant damping ratio ξ, where,

$$\beta_C = \frac{\xi}{\pi f} \qquad \textbf{Eqn. 3.41}$$

The value of this constant damping ratio should be chosen for the most dominant frequency. For example, in the modelling of a transmitting composite, the damping at the electrical resonant frequency should be chosen

The value of the discrete element damping $[\mathbf{C_k}]$ is defined by a completely separate element, MATRIX27. Due to the importance of micro-structure related resonant modes dependent upon losses in the ceramic and polymer, the dominant damping for ultrasonic transducers is β_j, the individual material damping constant. Unfortunately, only a single material damping constant could be applied to each material, which caused difficulties in materials with significantly different longitudinal and shear damping components. In such cases, a compromise value to best fit the problem was chosen. In addition, practical use of 'entire model' damping coefficients, such as α, proved too crude a tool to be used effectively, and was consequently abandoned.

It is clear that damping models within ANSYS are not ideal, and are likely to cause some difficulties in the modelling of piezocomposites.

3.6 Two Dimensional and Three Dimensional Analyses

Many of the models presented in this thesis are two-dimensional as opposed to a full three-dimensional analysis. By selecting a two-dimensional approach, the number of nodes and elements can be vastly reduced and with a lesser number of DOF at each node, computation times are significantly reduced, often from hours or days to minutes.

While two-dimensional analyses offer great advantages, the FEA user must take care to ensure that the assumptions made in a two-dimensional analysis do not introduce unacceptable limitations to the model. For example, a two-dimensional analysis of a 2-2 composite or solid ceramic transducer would often be acceptable due to uniformity in the 'unmodelled' axis, but a 1-3 composite (which in two dimensions looks identical to a 2-2 composite) may be inaccurately modelled should inter- or intra-pillar resonances be a significant factor in their behaviour. Additionally, a slice through a 1-3 composite results in a 'false' volume fraction, higher than in reality. Thus electrical impedances and resonant frequencies, and fluid load matching will all be incorrect.

To overcome these problems, a '2.5-D' solution was developed. The 1-3 composite is modelled as normal in one axis, and is then modelled as half a cell width (half saw-pitch) in the other axis. Symmetrical boundaries are then placed along edges normal

to the second axis. This results in a model that is effectively infinite in one axis, and has the correct size in the other. While still not as accurate as a full three-dimensional solution since whole-model modes from one axis not taken into account, volume fraction is accurately modelled, and solution times are significantly lower than for a full three-dimensional analysis.

3.7 Information Gained from FEA

Two main types of information are extracted during post-processing of an ultrasonic transducer model – electrical impedance/frequency characteristics and surface displacement profile (SDP) illustrating the mode shapes and magnitudes at any plane in the model. An example of an SDP is shown as Figure 3.10. Here, the X and Y axes represent the position along the side of a composite transducer, and the greyscale at each point indicating the magnitude of displacement in the thickness direction at that point. Black represents zero displacement through to white as the maximum displacement in a linear fashion.

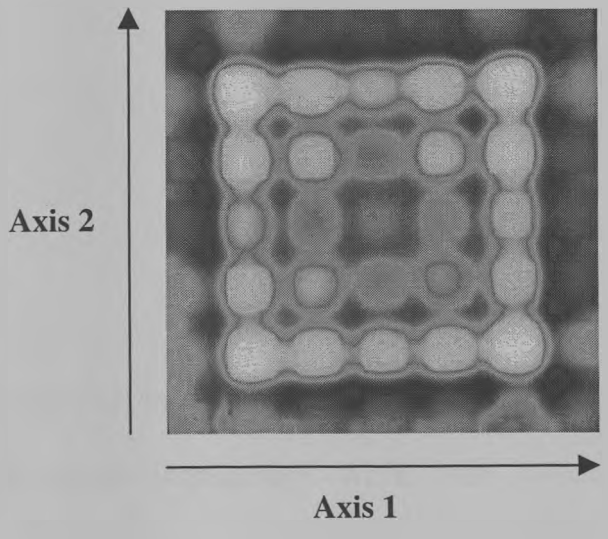

Figure 3.10 SDP of 1-3 Composite Transducer

The electrical impedance characteristics of a transducer are an important measure of the performance for a number of reasons. Firstly, the simulated result can be easily compared to the experimental plot from an actual transducer by an impedance analyser, such as the HP 4194A impedance/gain-phase analyser. Secondly, the input impedance also reveals the location of all resonant and anti-resonant modes, including thickness, inter- and intra- pillar, and width modes. It is often clear from the impedance plot exactly how 'unimodal' the transducer is, and if the desired mode is coupled to other resonances, the efficiency of the transducer is often drastically reduced. One measure of the efficiency of a transducer is the *electromechanical coupling coefficient* **k**, that is the quantity of electrical energy converted to acoustic energy, and vice-versa. This is defined as [87]

$$\mathbf{k}^2 = \frac{\mathbf{E}_M^2}{\mathbf{E}_D \mathbf{E}_{ST}} \qquad \textbf{Eqn. 3.42}$$

where

$$\mathbf{E}_D = \frac{1}{2}\left([\phi]^T [\mathbf{K}_{\phi\phi}][\phi]\right)$$

$$\mathbf{E}_M = \frac{1}{2}\left([\mathbf{u}]^T [\mathbf{K}_{u\phi}][\phi] + [\phi]^T [\mathbf{K}_{u\phi}][\mathbf{u}]\right)$$

$$\mathbf{E}_{ST} = \frac{1}{2}\left([\mathbf{u}]^T [\mathbf{K}_{uu}][\mathbf{u}]\right)$$

These three energies are known as the dielectric energy, the electromechanical energy, and the elastic energy respectively. While these values were available from an ANSYS FE solution, attempts to calculate exactly the coupling coefficients were not successful, as coupling coefficients of greater than 100% were always predicted. This

was reported to ANSYS technical support who confirmed that the methodology was correct and that fault lay with the ANSYS code. No solution to this problem had been received at the time of thesis submission.

Equation 3.42 is more commonly approximated as Equation 3.43, where $\mathbf{f_n}$ and $\mathbf{f_m}$ are the electrical and mechanical resonant frequencies.

$$k_t^2 = \frac{\pi}{2}\frac{f_n}{f_m}\cot\left(\frac{\pi f_n}{2f_m}\right) \qquad \textbf{Eqn. 3.43}$$

Unlike 3.42, this value of k_t is only strictly valid for a unimodal, loss-free composite operating in air. These values for the resonances may be obtained either from the results of a modal analysis, or from the impedance plot generated by a harmonic analysis.

As currents are not calculated explicitly during a harmonic analysis in ANSYS, they must be generated from the resultant charge. Equation 3.44 (a) is well known, and so from simple integration, we can express the value for I in the frequency domain as Equation 3.45:

$$\mathbf{dI} = \frac{\mathbf{dQ}}{\mathbf{dt}} \qquad \mathbf{I}(\omega) = j\omega\mathbf{Q}(\omega) \qquad \textbf{Eqn. 3.44 (a) \& (b)}$$

where both I and Q are complex numbers, j is the square root of -1, and ω is the angular frequency of interest. As the input voltage is $1\angle 0^{\circ}$, then the electrical impedance can be defined as

$$\mathbf{Z}_{IMP}(\omega) = \frac{\mathbf{1\angle 0}}{j\omega\mathbf{Q}(\omega)} \qquad \textbf{Eqn. 3.45}$$

By performing a 'sweep' across a large frequency range, the electrical input impedance for a transducer can be calculated.

Another form of transducer assessment is performed by examining SDP at a single frequency. The SDP is the magnitude and phase of displacement (typically in the thickness direction) in a plane of the transducer, often the front of the composite itself or the matching layer. By examining the behaviour (Figure 3.10), the user can gain a very useful insight into actual transducer performance that is not always evident from electrical impedance profiles, with effects such as mode coupling more easily seen. Additionally, by comparison with experimental SDP's, the accuracy of the simulation process can be established and improved. It is also possible to utilise the SDP to determine the pressure beam profile from the transducer. By comparison of any theoretical beam profiles with those obtained experimentally, progress can be made towards a reliable simulation package that can accurately predict pressure beam profiles (the real world ultrasonic transducer output) from transducer parameters before construction begins, thus ensuring a more efficient design process.

It is possible to compress much of the information contained within the SDP by the use of three figures of merit – Amplitude Dilation Quality (Q_{AMP}), Phase Dilation Quality (Q_{PHI}) and Average Displacement. Dilation Qualities express in a single number how uniform the measured aspect is across the transducer surface. These can be expressed as

$$\mathbf{Q}_{XXX} = \frac{\sum_{1}^{n} \mathbf{U}}{\mathbf{U}_{MAX}\,\mathbf{n}} \qquad \textbf{Eqn. 3.46}$$

where Q_{XXX} is the appropriate dilation quality, U is the magnitude or phase vector at each point, U_{MAX} is the maximum magnitude or phase at any point, and n is the total number of points in the surface.

Dilation Qualities cannot give as much information as a full surface displacement profile, but are a useful guide to the behaviour of a transducer. For example, for Q_{AMP} to be 1 both polymer and ceramic must displace by the same quantity, but as the discrepancy between the displacement in the two constituent phases increases, the value decreases towards zero. Should all points on the transducer surface be moving in phase, then Q_{PHI} will be equal to 1, but should half the surface be 180° out of phase with the remainder, then the value will be zero.

Average displacement across the transducer surface is included as a figure of merit, as it is possible for a transducer with high dilation qualities at a particular frequency to have extremely low average displacement, thus limiting the transducer output regardless of how uniform the surface motion is. By plotting a graph of the three figures of merit against frequency, it is possible for a designer to easily see if a transducer will operate efficiently. Figures 3.11 (a) and (b) demonstrate the transducer electrical impedance magnitude, and the three figures of merit against frequency, respectively. It is clear that at low frequencies (0 to 200 kHz), while dilation qualities are high, out-of-plane displacement is small and will result in little contribution to transducer output. The width mode at 220 kHz clearly reduces the uniformity of surface motion of the transducer, and although out-of-plane displacement increases to almost 40% of the maximum, transducer output will be far from ideal. Indeed,

between 220 kHz and just below the thickness mode electrical resonance at 500 kHz, the dilation qualities vary considerably, with no extended 'stable' frequency range.

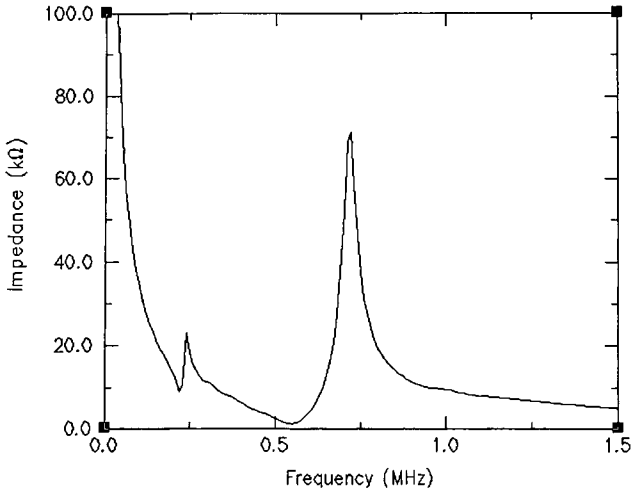

Figure 3.11 (a) Electrical Impedance Magnitude

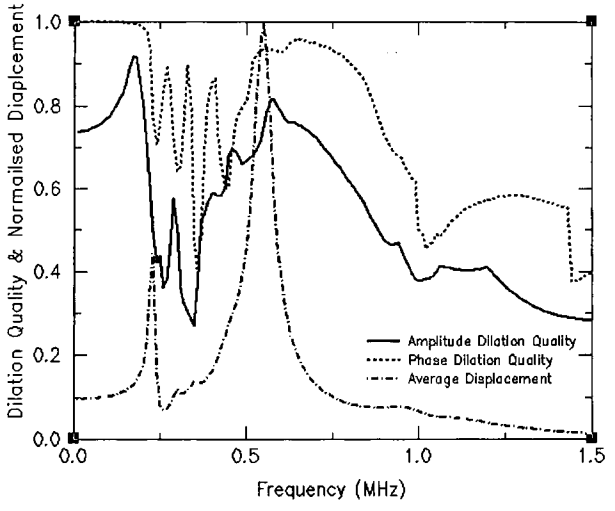

Figure 3.11 (b) Figure of Merit Graph

From just below electrical resonant frequency, to just above the thickness mode mechanical resonant frequency (750 kHz), dilation qualities are high and 'stable', and average displacement is much higher than at any other set of frequencies. It is clear that the transducer will operate most efficiently at these frequencies. Above these frequencies, the dilation qualities gradually reduce, and sometimes experience rapid variations as inter-pillar modes (1 MHz) interfere with the out-of-plane displacement.

This variation of surface dilation quality at the thickness mode due to width modes, despite significant separation from such lateral modes, is not an intuitive conclusion. It will, however, be demonstrated to be of concern during the design of a piezo-platelet transducer in chapter 6 of this work.

3.8 Conclusions

This chapter has served to describe the basic concepts of FEA, and the direct application of the procedure to the modelling of piezocomposite transducers. The basic governing equations and solution options have been detailed, and the methodology of model construction outlined. Finally, the data output formats have been described with particular reference to the impedance and surface displacement characteristics.

While it is of great interest to model the SDP, a method of correlation with experiment would serve to confirm model accuracy. Such a facility is available at the University of Strathclyde Ultrasonics Group – a scanning laser vibrometer.

Chapter 4

Development of a Laser Vibrometer Scanning System

4.1 Scanning Laser Interferometers

To measure accurately the surface behaviour of a piezocomposite transducer, a scanning system capable of resolving sub-nanometer displacement with micrometer spatial resolution is needed. A laser based system is ideal for this purpose as it is meets all these criteria, as well as being a non-contacting measurement system. Many methods of using lasers with ultrasound have been detailed, for example, by Monchalin[63], but the most common type of laser scanning systems are *interferometric,* relying on the interference between a reference laser beam and one which has been reflected from the object being scanned. This allows displacement measurement on a scale much smaller than the wavelength of the laser light by utilising the relationship between interferometer output and optical path length difference between the signal and reference beams. By measuring the phase difference between the two beams, overall displacement of the test surface can be measured with sub-nanometer resolution.

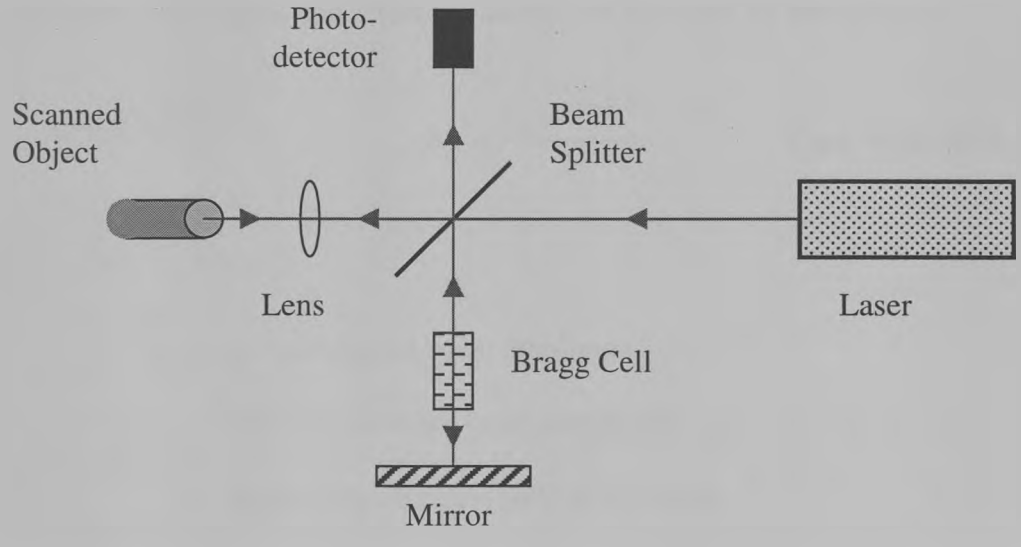

Figure 4.01 Schematic Diagram of a Laser Interferometer

A simplified layout of an interferometer is shown in Figure 4.01. Laser interferometry can be split into two possible methods called *homodyne* and *heterodyne*.

4.2.1 Homodyne Interferometers

An interferometer can be defined as homodyne when there is no frequency shifting of either laser beam (i.e. no Bragg cell). In this case, light amplitude emitted by the laser can be written as

$$A_L = \sqrt{I_L} e^{i\omega t} \qquad \textbf{Eqn. 4.01}$$

where

A_L represents the light amplitude

I_L represents the light intensity

ω is the light frequency.

The amplitude of the signal and reference beams can therefore be described as

$$A_S = \frac{A_E e^{i(\omega t - \theta_1)}}{2} \qquad A_R = \frac{A_E e^{i(\omega t - \theta_2)}}{2} \qquad \textbf{Eqn. 4.02 (a) \& (b)}$$

where

A_S is the signal beam amplitude

A_R is the reference beam amplitude

θ_x represents a phase shift in the beam.

Each beam will be phase shifted by an amount proportional to the optical distance travelled, which can be found using

$$\theta_x = \frac{2\pi L}{\lambda} \qquad \textbf{Eqn. 4.03}$$

where

θ_x represents the phase shift

L is the optical distance travelled

λ is the wavelength of the laser light.

The total amplitude at the detector can therefore be written as

$$A_{TOT} = A_S + A_R \qquad \textbf{Eqn. 4.04}$$

All photodetectors respond to the *intensity* of light, which is obtained by multiplying the amplitude by its complex conjugate.

$$I = A.A^* \qquad \textbf{Eqn. 4.05}$$

where

I is the light intensity

A is the light amplitude

A^* is the light amplitude complex conjugate.

Therefore at the photodetector

$$I = \frac{\left(A^2[1+\cos(\theta_R - \theta_S)]\right)}{2} \qquad \textbf{Eqn. 4.06}$$

If the path length of the reference beam does not change, and the laser is stationary, the phase change is based solely upon the displacement of the scanned object, and will vary according to the relationship

$$\theta_x = \frac{4\pi d}{\lambda} \qquad \textbf{Eqn. 4.07}$$

where

d is the displacement of the scanned object.

Unfortunately, this system is very sensitive to ambient vibrations which can cause motion of the reference mirror, and therefore invalidate results.

If the scanned object moves with a velocity v, then its position at a given time is given by

$$d(t) = vt \qquad \textbf{Eqn. 4.08}$$

where

$d(t)$ is the displacement at a given time

v is the velocity

t is the time.

The phase difference thus becomes time dependent

$$\Delta\theta = \frac{2\pi\, 2vt}{2\lambda} = \omega_D t \qquad \textbf{Eqn. 4.09}$$

Where ω_D is the Doppler frequency. From Equations 4.06 and 4.09 it can be seen that the light intensity at the detectors will be

$$I_S = \frac{A^2[1-\cos(\omega_D t)]}{2} \qquad I_R = \frac{A^2[1+\cos(\omega_D t)]}{2} \qquad \textbf{Eqn. 4.10 (a) \& (b)}$$

It is evident that a simple homodyne interferometer will provide surface displacement magnitude accurately, but will not give phase information. The lack of phase information from a homodyne interferometer is solved by placing a "Bragg cell" frequency modulator into the reference path to cause a frequency shift. This causes modulation of the output signal, which will increase or decrease from its steady state value depending on direction of motion. If such a device is added to an interferometer, it is said to be of the heterodyne type.

4.2.2 Heterodyne Interferometers

The Bragg cell itself is an acousto-optic cell that is driven at the frequency by which the laser beam is to be shifted. The light intensities at the photodetectors then become

$$I_S = \frac{A^2\left[1-\cos\left(\left(f_B+\frac{2v}{\lambda}\right)t\right)\right]}{2}$$

Eqn. 4.11 (a) & (b)

$$I_R = \frac{A^2\left[1+\cos\left(\left(f_B+\frac{2v}{\lambda}\right)t\right)\right]}{2}$$

where f_B is the frequency shift of the Bragg cell. Target motion now results in a direction dependent deviation from f_B allowing phase to be discriminated.

The detection circuitry that is attached to the interferometer can be arranged such that the output is proportional to either surface velocity or surface displacement. Frequency demodulation gives output as a function of velocity, while phase demodulation gives the output as a function of displacement. A schematic diagram (Figure 4.02) outlines the circuit necessary to ensure that the output signal is proportional to velocity. This frequency tracking technique uses feedback to ensure that the frequency discriminator is kept centred on f_B. The bandwidth of such a system is often restricted by the tuning characteristics of the voltage controlled oscillator, and is consequently limited to frequencies of a few megahertz. Additionally, as the frequency discriminator is centred on a high frequency, the system is practically immune to low frequency 'noise' such as ambient vibrations. Figure 4.03 is a block diagram of the circuitry required to implement a frequency tracker to give output proportional to displacement.

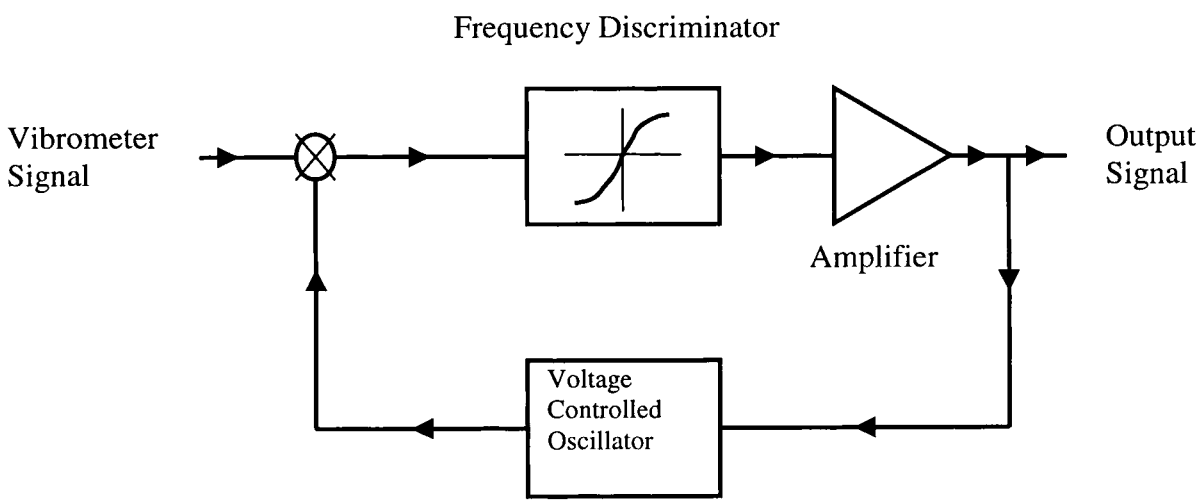

Figure 4.02 Frequency Tracker for Output Proportional to Velocity

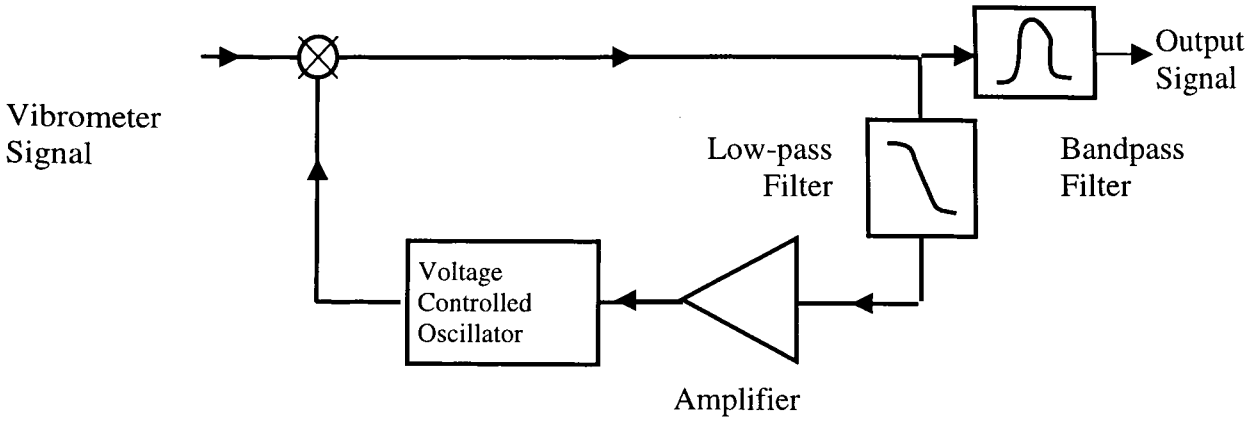

Figure 4.03 Frequency Tracker for Output Proportional to Displacement

Frequency modulators have a poor signal-to-noise ratio, and thus limit the bandwidth of velocity measurements. If phase demodulation is used, evaluation is limited to $\pm\pi/4$ and so displacement will be limited to ±75 nm for a laser of wavelength 633 nm, but with a much higher bandwidth.

4.3 Specification of Scanning Laser Interferometer

It is clear that the heterodyne type interferometer is a more versatile and reliable arrangement for a scanning system, and is consequently the type that was chosen for the system used in this work. The laser source chosen was a Polytec OFV302 Helium-Neon Class II laser (λ=633 nm) with a Polytec OFV2700 Vibrometer Controller incorporating an OVD30 Displacement Decoder. The laser has an average spot size of 20-25 μm when focused, giving more than adequate resolution when it is considered that typically the smallest scales encountered in the piezocomposites of interest are on the order of 100 μm. The decoder is capable of resolving to a resolution of 2.5 Angstroms under ideal conditions, up to a worst case scenario of 2 nm resolution with 2% of transmitted light returned. Frequency range extends from 25 kHz to 20 MHz, which allows for removal of low frequency noise which may otherwise interfere with results. The decoder has a limit of ±75 nm maximum displacement and has an output of

50 nm per volt [64], which is passed to a Sonotek Data Acquisition card in an Personal Computer (P.C.), which digitises the data with a sampling frequency of up to 100 MHz.

Position control was accomplished by two Physik Instrumente (P.I.) 300 mm micropositioning axes, capable of a resolution of 1 μm when connected to a P.I. C-560 Stepping Motor Controller, and a 1 m long z-axis with 24 μm resolution when connected to the same controller. Data input and controller instruction is performed using LabWindows software on the P.C. which is connected to the C-560 with an RS-232 serial link.

The ultrasonic transducers to be scanned were fixed to the micropositioner such that motion in the X and Y axes controlled the position of the laser spot on the front face. The laser was attached to the Z axis to allow fine distance control for focussing purposes.

Data is stored in column format, and details the X and Y position, magnitude of maximum displacement, and phase of displacement relative to the trigger pulse (equivalent to 0° on the sine wave). Other data such as overall scan size, frequency, excitation voltage and total averaging was also stored on the file.

As many surface scans require the transducer to be water loaded, a special water tank was constructed, with a high quality glass window to allow laser light to pass. De-ionised water was used at all times.

Transducers were typically scanned at a single frequency with continuous wave or burst mode excitation. Although transient behaviour could also be recorded, this is outside the scope of this thesis.

4.4 Data Presentation

Data presentation was performed using the commercially available software package PVWave from Visual Numerics, and could display the data in a number of formats. For presentation purposes, the isometric view shown in Figure 4.04 (a) is an eye-catching and colourful method of data display and contains all scaling data on the axes. This is, however, appropriate only for scans with relatively small quantities of data, as when the density of sample points increases this display method can become confusing, as can be seen in Figure 4.04 (b). It was decided, therefore, to utilise an image or 'plan' view of the data, and additionally to change the colour representation to a greyscale method.

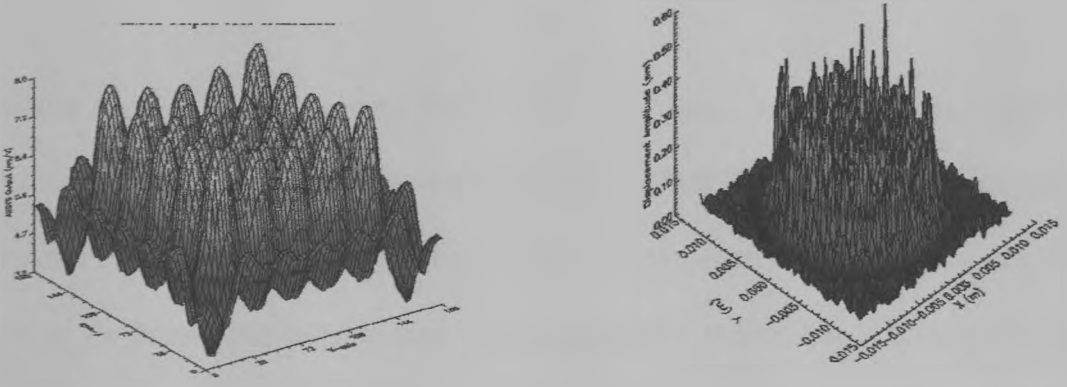

Figure 4.04 (a) & (b) 3-D View of Data in Colour

Whilst necessitating additional scales, this method gives a much clearer and consistent form of data output, as can be seen in Figures 4.05 (a) and (b), which presents identical data to that in 4.04 (a) and (b). Additionally, this method ensures data

integrity should such results ever be photocopied. It was decided that black on the greyscale would represent zero displacement through to white representing maximum displacement, in a linear fashion.

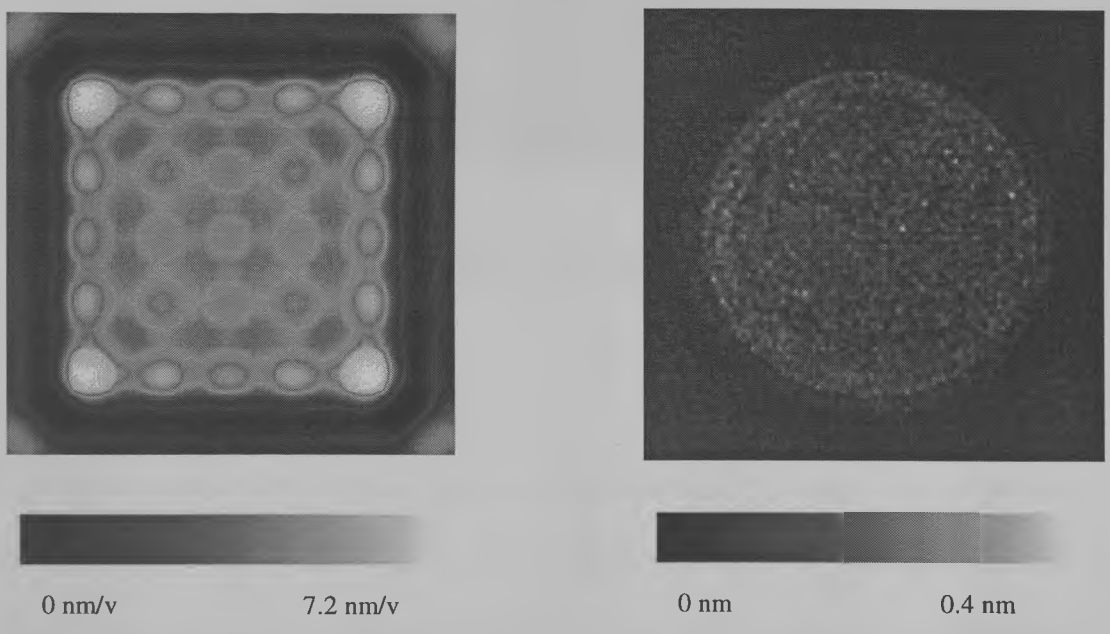

Figure 4.05 (a) & (b) Plan View of Data in Greyscale

A similar method was chosen to display the phase data, with maximum negative phase represented by black, and maximum positive phase by white on the greyscale. As $-\pi$ and $+\pi$ are effectively the same phase, there can often be a confusing display effect, as the phase may only change by a fraction of a radian, but is displayed as a large 'jump' from black to white, as shown in Figure 4.06. Whilst initially confusing, it is evident that there is no error present here and any attempts to remove this effect will only result in altered (and therefore inaccurate) data, and consequently phase data is to be presented in this format.

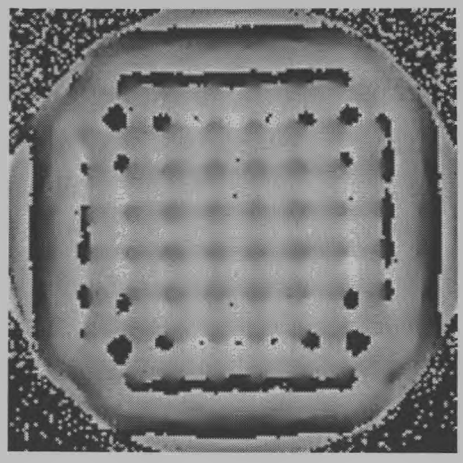

Figure 4.06 Image of Phase Plot with ±π Changeover

4.5 Reflectivity of Scanned Surfaces

As mentioned earlier, the reflectivity of a surface can alter the sensitivity of the laser vibrometer by almost as much as an order of magnitude, and is therefore critical to the efficient operation of the equipment. In addition, particles or 'steps' on the surface can cause scattering of light, affecting measurement accuracy at those locations.

All piezocomposite transducers manufactured for this work were lapped to a high degree of accuracy to ensure that upper and lower electrode surfaces are parallel and flat. Electrodes were deposited on the surfaces using a thin film evaporator, to deposit typically 10 nm of chromium then 200 nm of gold. This form of deposition ensures good adhesion and good electrode conductivity, as well as a highly reflective surface for accurate laser scanning.

Problems can arise if a mechanical matching layer is attached to the piezocomposite, as most polymers used for the layer are semi-transparent and there will consequently be no reflective surface. Although it would be possible to sputter a gold surface onto

the matching layer, this is an expensive technique and not economical for a temporary covering. An ideal solution to the problem is to apply additives to the polymer so that it becomes opaque, while material properties are unaffected. It was found, however, that the simplest and most consistent method involved the painting of the matching layer with silver paint.

4.6 Scanning of Surfaces through Water

While the surface displacement behaviour of a piezocomposite transducer in air is extremely useful for comparison with a finite element model, it is only when realistically loaded by placement in a water tank that a piezocomposite begins to behave as it would in many 'real world' applications. This, however, requires the laser beam to propagate through at least two materials of different optical properties. Even more critical is the fact that under a pressure load (such as that generated by an ultrasonic transducer) the refractive index of water can change, introducing the potential for significant errors. The light beam can be altered in terms of its amplitude, its direction, or its phase. Here, these are considered in turn.

4.6.1 Intensity Variation

It is known that the Polytec vibrometer will operate under conditions of as little as 2% reflectivity, and consequently intensity is the least important of the three considerations. It cannot be ignored, however, as the percentage of light returned affects the smallest detectable displacement. The reflectance, R, of light passing through two materials of refractive index n_1 and n_2 at normal incidence is [65]

$$R = \left(\frac{(n_1 - n_2)}{(n_1 + n_2)} \right)^2 \qquad \textbf{Eqn. 4.12}$$

where

n_1 is the refractive index of the first material

n_2 is the refractive index of the second material.

The refractive index of a material is defined as

$$n = \frac{v_v}{v_m} \qquad \textbf{Eqn. 4.13}$$

where

v_v is the velocity of light in a vacuum

v_m is the velocity of light in the material

Given that the refractive index of air is 1.00, glass is 1.52, and water is 1.33, 95.7% of the light will be transmitted at the air-glass boundary, and 99.55% of the energy will be transmitted at the glass-water boundary. The overall transmission coefficient for a light beam travelling from air through glass to water, and then returning to the photocell is 90.5%. Although only 10% of the energy in the laser beam will be lost, it is still important that the surface of the scanned transducer be highly reflective. It is clear that even under near-ideal conditions, the resolution of the scanner will not be as accurate as the theoretical limit of 0.25 nm, something that must be taken into consideration when deciding if a transducer is suitable for scanning.

The majority of the energy which is lost, occurs at the air/glass boundary and is reflected back to the laser vibrometer system. It was originally thought that as this

light will be unfocussed at this distance it will not interfere with the output signal, as the signal beam has significantly more energy than the air/glass reflected beam. As just over 4% of the light is reflected at the air-glass boundary, and the limit of detection of the system is 2%, some difficulties may arise. A possible solution to this is to place the water tank at a slight angle to the normal, such that any light reflected from the glass will 'miss' the optical detectors. In this case, as the refractive indices of water and air are different, the light beam leaving the glass is not parallel to the beam entering, causing some of the return signal to be lost. This can be accounted for by applying Snell's Law (Equation 4.14).

$$n_1 \sin\theta_1 = n_2 \sin\theta_2 \qquad \textbf{Eqn. 4.14}$$

where

θ_1 is the angle of incidence at the air/glass boundary

θ_2 is the angle of incidence at the glass/water boundary

n_1 is the refractive index of air

n_2 is the refractive index of water.

It is important to consider what angle of rotation is sufficient to ensure that the air/glass reflected beam misses the optical detectors. Using

$$u_d = \theta L \qquad \textbf{Eqn. 4.15}$$

where

u_d is the overall beam displacement on return to source

θ is the angle of rotation (in radians) of the tank

L is the optical path length.

Given that the total optical path length is approximately 20 cm, and that the total lateral displacement must be at least 2 cm, it can be seen that a minimum angle of almost 6° is required. From Equation 4.15, the angle of incidence in the water will be 4.5°, which is the angle through which the transducer requires rotation in order to ensure that the light beam is perpendicular to the surface of the transducer. A simple rotational holder can be constructed to accurately measure the angle of rotation. The overall arrangement is shown in plan view in Figure 4.07.

It is therefore possible to scan an object in a water tank, through an optical glass window, with sufficient light returned for an accurate scan. What has still not been considered is how the pressure field created by the displacing transducer will affect the direction or phase of the light beam.

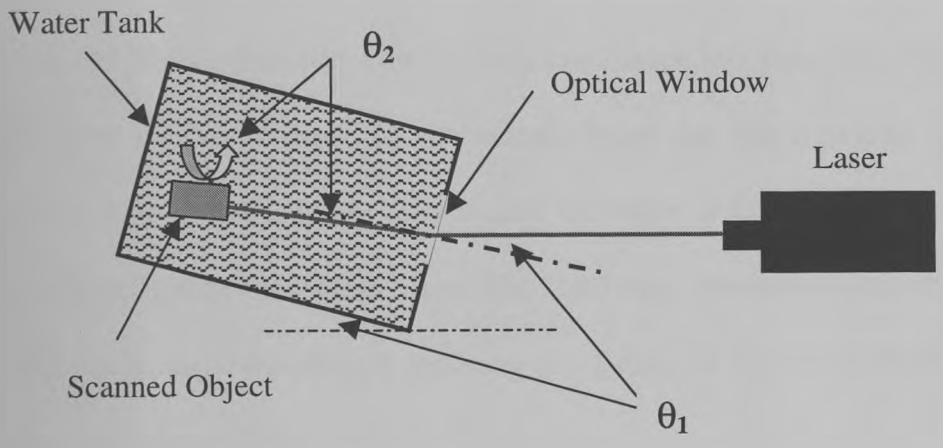

Figure 4.07 Diagram of Water Tank Rotation

4.6.2 Direction Variation of Light due to Acoustic Pressure Field

It is possible that the pressure field created by the ultrasonic transducer in water will affect the trajectory of the light beam, thus altering the experimental results. Kino [45]

defines two methods of determining the overall beam deflection. Firstly the *Raman-Nath* criteria must be satisfied. Here

$$Q_{RN} = \frac{k_a^2 z}{k_o} \qquad \textbf{Eqn. 4.16}$$

where

Q_{RN} representing the Raman-Nath parameter

k_a is the acoustic wavenumber ($2\pi/\lambda_a$)

λ_a is the acoustic wavelength

λ_o is the optical wavelength

k_o is the optical wavenumber ($2\pi/\lambda_o$)

z is the acoustic beam length.

The value of the Raman-Nath parameter determines how the light will interact with the acoustic beam. Should the value be extremely low (much less than $\pi/2$), Raman-Nath diffraction will occur. In this case, the acoustic beam acts like a grating on the light and creates several diffracted beams. Should the value of Q_{RN} be significantly greater than $\pi/2$ deflection may occur more like the *Bragg scattering* described in Chapter 2, with the acoustic wavelength replacing the spacing of the lattice structure.

For a 633 nm wavelength light beam passing through a 5 MHz ultrasonic transducer beam (wavelength 0.3 mm) in water tank of length 25 cm, the value of Q is approximately 3.5π. Should a device of much lower frequency be used (such as 50 kHz), then the value of Q is approximately $3.5 \times 10^{-4}\ \pi$. Lower frequencies, however,

will experience Raman-Nath diffraction, where a number of waves are diffracted with a set angle between each. These are both illustrated in Figure 4.08.

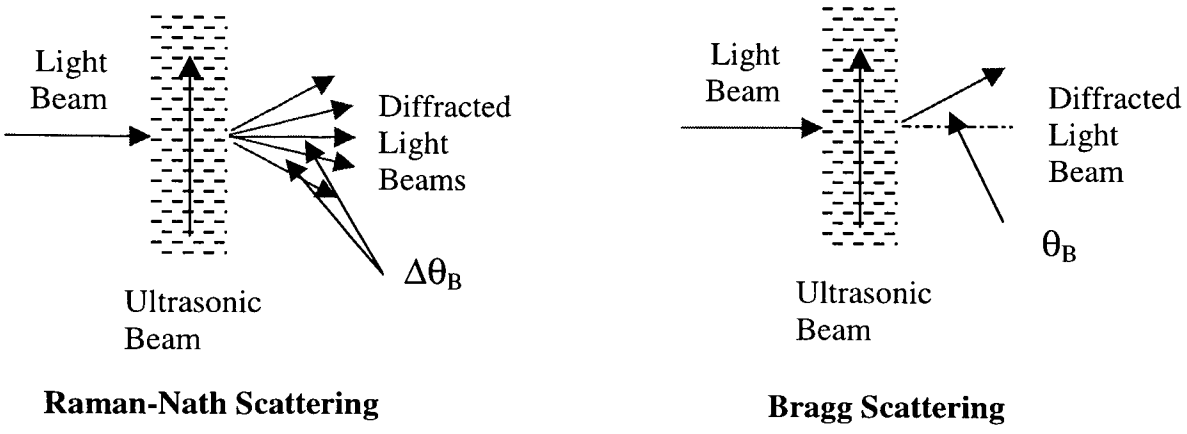

Figure 4.08 Types of Optical Scattering by Acoustic Waves

Both types of scattering will cause deflection at an angle of θ_B, defined by

$$\sin\theta_B = \left(\frac{\lambda_o}{2\lambda_a}\right) \qquad \textbf{Eqn. 4.17}$$

This results in a deflection angle of 0.06° for the 5 MHz transducer, and translates to a total deflection of 262 μm over a distance of 25 cm. Larger than the spot size of the laser (25 μm), this deflection is sufficient to cause significant errors in the vibrometer scan. The 50 kHz transducer will have an angle of separation between diffracted beams of 0.0006°, resulting in a maximum deflection of 2.6 μm. This is, however, a 'worst case scenario' where the light beam enters at right angles to the direction of the ultrasonic field propagation. As the angle at which the light beam enters the ultrasonic beam varies from the normal to the ultrasonic beam to the parallel, the maximum lateral deflection will reduce. Fortunately, when we consider the angle of incidence of the light beam on the ultrasonic field, it is apparent that in this particular case there

should be no deflection of the beam as it travels parallel to the field, regardless of the frequency of the ultrasonic wave.

Thus it is clear that the directional variation is not of the form that is likely to significantly alter the result of a laser vibrometer scan. This lack of variation in light beam direction is in fact a critical assumption in many fields of acousto-optics and holography, as detailed by Sliwinski in his review of acousto-optics and their applications [66].

4.6.3 Variation of Optical Phase

Variation of signal beam phase is likely to be the most critical of the three factors in any laser scan through water. Because of the small optical wavelength, tiny perturbations in the optical path length can cause large changes in the vibrometer output. The primary cause of optical path length change is an alteration in refractive index caused by a pressure field in the fluid.

The effect of variable refractive index upon a laser scan through water has been investigated by a number of authors. Bacon, in his 1988 paper [67], attempted to account for the variation by use of an effective refractive index, which was derived as follows:

$$q = 2\int_{u(t)}^{l} n\, dz - 2n_o l \qquad \textbf{Eqn. 4.18}$$

where

q is the optical path length change due to pressure

n is the altered refractive index of water

n_o is the original refractive index of water

l is the distance from the transducer to the optical window

$u(t)$ is the displacement of the scanned object

z is the laser beam axis.

The first part of Eqn. 4.18 represents the distance travelled by the optical beam when the refractive index has been altered, while the second part ($2n_0l$) represents the optical distance travelled when the refractive index of the water has not been altered by pressure.

The value of n can be written fully as

$$n = n_o + n_1\ p(z,t) \qquad \textbf{Eqn. 4.19}$$

where $p(z,t)$ is the instantaneous pressure at any point z and

$$n_1 = p\left(\frac{\partial n}{\partial p}\right) = \rho\, v_w{}^2\left(\frac{\partial n}{\partial p}\right) \qquad \textbf{Eqn. 4.20}$$

where

n_1 is the change in refractive index due to pressure

ρ is the density of water

v_w is the velocity of sound in water

When Equation 4.19 is inserted into Equation 4.18, and expanding only to the first order, the displacement in time can be given as

$$q(t) = -2n_o u(t) + 2\left(\frac{n_1}{\rho v_w^{\,2}}\right)\int_0^l p(z,t)dz \qquad \textbf{Eqn. 4.21}$$

and can be simplified for plane waves to

$$q(t) = -2n^* u(t) \qquad \textbf{Eqn. 4.22}$$

where

$$n^* = n_0 - n_1 \qquad \textbf{Eqn. 4.23}$$

This value of n^* is an effective refractive index that can be used to obtain the true phase shift, by combination with Equation 4.03

$$\Delta\theta = \frac{4\pi n^* u}{\lambda_o} \qquad \textbf{Eqn. 4.24}$$

The same conclusion was reached by Royer et al. [68]. In both cases, the effective refractive index of the water is a constant value, regardless of pressure variation within the fluid, which is not the intuitive conclusion.

In his 1993 paper [69], Bacon attempted a more detailed analysis of the problem, whilst removing the plane wave assumption made in his previous paper. He concludes by presenting a method of determining actual source velocity or displacement from that measured by the vibrometer, which takes the form

$$v_Z = F_T^{-1}\left\{\frac{F_T(q(t))}{-2.\left[n^* - n_1\left(\frac{\alpha_x^2+\alpha_y^2}{1-\alpha_x^2-\alpha_y^2}\right)\right]}\right\} \qquad \textbf{Eqn. 4.25}$$

where

v_Z is the true velocity in the z direction

F_T indicates a two dimensional Fourier transform

F_T^{-1} indicates an inverse two dimensional Fourier transform

α_x are the directional cosines of the plane wave

This is obviously a more complex method of calculating the true surface behaviour, even with the many approximations that were made during its derivation. This solution, however, again fails to take into account the variation of the pressure field on the value of n^*, despite the author concluding that the magnitude of the acousto-optic effect is dependent upon pressure wave amplitude. In an attempt to correct this, a new method of calculating the effective refractive index will now be presented.

4.6.3.1 Variation of Effective Refractive Index with Input Power

Variation of the refractive index of water under pressure is called the *photoelastic* or *piezo-optic* effect. Strain due to a pressure field causes an alteration in the atomic lattice spacing, thereby causing an alteration in dielectric constant proportional to pressure amplitude.

It is stated by Kino [5] that this can be represented by the equation

$$\frac{\Delta\varepsilon}{\varepsilon} = -\frac{\varepsilon}{\varepsilon_0}\psi S_0 \cos(\omega_a t - k_a x) \qquad \textbf{Eqn. 4.26}$$

where

ε is the dielectric constant of the material

ψ is piezo-optic coefficient of the material

S_0 is the peak strain in material ($\Delta l/l$)

The piezo-optic coefficient is available from a number of sources, such as Dixon [70]. Equation 4.26 describes how the change in permittivity varies sinusoidally, as one would expect in an ultrasonic pressure field.

Kino also states two further important relationships, namely

$$\frac{2\Delta n}{n_o} = \frac{\Delta\varepsilon}{\varepsilon} \qquad n_o^2 = \frac{\varepsilon}{\varepsilon_o} \qquad \textbf{Eqn. 4.27 (a) \& (b)}$$

Combining Equations 4.26, 4.27 (a), and 4.27 (b), an expression for the maximum variation in refractive index in terms of strain can be obtained.

$$\Delta n = \frac{n_o^3 \psi S_0}{2} \qquad \textbf{Eqn. 4.28}$$

The power in an the acoustic beam must now be defined. The total work done in a wave is the equivalent of the force applied multiplied by the displacement in the force direction. The velocity of a particle can be written as

$$v_p = \frac{du_p}{dt} \qquad \textbf{Eqn. 4.29}$$

where

v_p is the particle velocity

u_p is the particle displacement

Therefore over a small displacement

$$du_p = v_p\, dt \qquad \textbf{Eqn. 4.30}$$

The force can be defined as

$$F = \rho\, v_W\, A v_p \qquad \textbf{Eqn. 4.31}$$

where

F is the applied force

ρ is the medium density

v_W is the fluid wave velocity

A is the cross sectional area through which the wave travels.

It should be noted that the function v_p varies in both time and position. The work done (W) in a specific time interval is therefore

$$W = F du_p = \rho\, v_W\, A v_p^{\,2}\, dt \qquad \textbf{Eqn. 4.32}$$

And the total energy in any cycle will be given by integrating the real part of work over 2π.

$$E_T = \rho v_W A v_0 \int_0^{2\pi} \cos^2(\omega t - kx) dt \qquad \textbf{Eqn. 4.33}$$

where

E_T is the total energy

v_0 is the maximum peak particle velocity in any cycle

k is the wavenumber.

By substitution and integration, this can be simplified to

$$E_T = \frac{\rho \lambda A v_0^2}{2} \qquad \textbf{Eqn. 4.34}$$

The total power (P) in a acoustic beam cycle can therefore be calculated, by dividing by the cycle period or multiplying by frequency.

$$P = \frac{\rho v_W A v_0^2}{2} \qquad \textbf{Eqn. 4.35}$$

It is also known that the pressure in a wave is equivalent to the elastic modulus times the strain:

$$P_R = YS_0 = v_W^2 \rho S_0 \qquad \textbf{Eqn. 4.36}$$

where

P_R is the particle pressure

Y is the elastic modulus

S_0 is the peak strain.

Further, the particle velocity, acoustic impedance, Z, and particle pressure are related by

$$v_0 = \frac{P_R}{Z} \qquad \textbf{Eqn. 4.37}$$

As acoustic impedance is the product of wave velocity and medium density, we can therefore derive that

$$v_0 = v_W S_0 \qquad \textbf{Eqn. 4.38}$$

It is therefore possible to derive an equation for acoustic beam power in terms of strain by combining Equations 4.35 and 4.38, in the form

$$P = \frac{1}{2} A \rho v_w^3 S_0^{\,2} \qquad \textbf{Eqn. 4.39}$$

It then follows that

$$S_0 = \sqrt{\left(\frac{2P}{A \rho v_w^3} \right)} \qquad \textbf{Eqn. 4.40}$$

Combining Equations 4.28 and 4.40 we obtain the relationship

$$\Delta n = \frac{n_o^3 \psi}{2} \sqrt{\left(\frac{2P}{A \rho v_w^3} \right)} \qquad \textbf{Eqn. 4.41}$$

It is therefore possible to calculate the maximum change in refractive index based upon several known or easily obtainable parameters.

The ultrasonic transducers scanned for this thesis were typically 15 mm across, with an impedance of 10 Ω at electrical resonance frequency, driven at 10 V peak-to-peak. For water, the ambient refractive index is 1.33, the piezo-optic coefficient is 0.31, density is 1000 kgm^{-3} and the velocity of sound is 1500 ms^{-1}. This will result in a maximum value of refractive index change of 4.2×10^{-5}. Obviously, as the power input to the transducer is increased, the change in refractive index may become significant. Indeed, the variation stated here is too large, as the power used in Equation 4.29 was electrical input power, as opposed to mechanical output power, which will see a typical reduction of 50% for most piezocomposites. At the level of change predicted here, a composite will produce a 1% change in refractive index at 200v, a 4% change at 400v, and a 16% change at 800v.

Experimental responses were required to validate this theory. The most effective way of determining its veracity would be to scan a composite transducer several times, each time varying the input voltage in a range from 1 volt to several hundred volts, and comparing the output responses. Unfortunately, the typical displacement of a composite transducer is in the nanometer per volt range, and consequently the ±75 nm limit of the vibrometer was rapidly surpassed. While the replacement of the displacement decoder card with a velocity decoder would allow such an experiment to proceed, the replacement of the card was a considerable expense and beyond the budget allocated to this project.

A number of readings were taken of a composite displacement at various voltage levels until the ±75 nm limit was reached. Table 4.01 details the results of the driving voltage and the displacement response. As can be seen, no significant acousto-optic

effect is apparent, indicating that the acousto-optic effect is of no concern at the voltage levels used in this thesis.

Excitation (v)	Displacement (nm/v)
2	1.64
5	1.59
7	1.59
9	1.66
10	1.60
15	1.66
25	1.62
40	1.61

Table 4.01 Displacement at Various Voltage Levels

It is possible to conclude, therefore, that laser interferometer scans through water can be shown to be accurate, once the refractive index of water is taken into account using Equation 4.24, a simple computational procedure.

4.7 Conclusions

In this chapter, laser interferometer scanning has been proposed as an accurate, non-contacting experimental method to measure the surface displacement of an ultrasonic transducer. Even scanning through water, it is possible to compensate for additional problems in a relatively straightforward manner, particularly at the low power levels that are relevant in this thesis.

This chapter has demonstrated the viability of the experimental scanning apparatus for analysing ultrasonic transducers. Combined with the finite element theoretical modelling capabilities outlined in chapter 3, it is evident that a powerful suite of theoretical and experimental tools exist for the analysis of piezocomposite transducers. These preceding chapters form a firm foundation for the chapters which follow, a detailed analysis of 1-3 and 2-2 composites, and a new type of transducer, the 'piezo-platelet' transducer.

Chapter 5

Analysis of Piezocomposites using Surface Displacement Profiles and Finite Element Analysis

5.1 Introduction

Previous chapters have detailed the benefits of piezocomposite transducers, the manufacturing methods used, and the additional modes generated by the periodic nature of such devices. Unidimensional modelling techniques may be used to accurately predict the thickness mode behaviour of composite transducers, but fail to account for inter-pillar modes introduced due to device microstructure. Thus, modelling results may predict transducer behaviour that differs significantly from its real world counterpart. Another method of modelling that considers both thickness and inter-pillar resonances is required, should the full range of ultrasonic transducer microstructure be studied.

Finite element analysis (FEA) offers the ability to model fully, virtually all types of piezocomposite connectivity, considering resonances in all three axes. It is the intention of this chapter to study the two most common connectivities of piezocomposite, the 1-3 and the 2-2, by means of FEA, with experimental verification in the form of electrical impedance and surface displacement profiles, with particular attention paid to the various resonant modes.

The Bragg scattering model detailed in chapter 2 is currently used to predict the frequency of the inter-pillar resonances, and relies on the inter-pillar waves constructively and destructively interfering to form the inter-pillar mode shapes. This method has become accepted as the 'state of the art' in inter-pillar resonance theory due to its accuracy in predicting the frequency of these modes. Despite its success in determining mode frequencies this method, by its very nature, cannot be used to describe the modal behaviour in all composite transducers as it is limited to 1-3

composites with finely spaced structures and low pillar width to height aspect ratios. It stands to reason therefore, that while it may produce the correct numerical results, that Bragg scattering fails to correctly describe the *mechanism* by which the inter-pillar modes are produced. Understanding of the behaviour of piezocomposites would be greatly enhanced by a more consistent theory of inter-pillar mode generation, and it is the intention of this chapter to develop such a theory.

In order to study such behaviour in piezocomposites, finite element modelling, combined with the laser scanning facility described in chapter 4, is used to view the mode shapes of the various resonances in a range of high quality piezocomposite devices, with excellent correlation between modelled and experimental results. Careful examination of these results, and comparison to existing theory, will lead to a new theory of inter-pillar mode resonances based upon *Lamb Wave* generation.

5.2 1-3 Connectivity Piezocomposite Transducers

To verify the finite element model, a range of 1-3 composite transducers were constructed, covering a range of volume fractions (VF) and pillar aspect ratios (AR). All devices utilised PZT-5H as the ceramic and CIBA-GEIGY CY1300/HY1301 hard setting epoxy as the polymer, and measured 15 mm along each side. Table 5.01 lists the relevant details of all the devices used in this chapter and, additionally, includes the Maximum Pillar Aspect Ratio (MPAR) for a device of that volume fraction. MPAR is the highest ceramic pillar width to height ratio in a 1-3 piezocomposite of given VF, under which the device will continue to show unimodal behaviour. Operating with an AR greater than MPAR generally results in inter-pillar resonances impinging upon the thickness mode resonance of the device, with corresponding loss

of piston like displacement at the transducer surface. Work by Bennett [41] gives guidelines as to the MPAR for composites constructed using PZT-5A and hardset epoxy. While this work produced results for PZT-5A/Hardset transducers, the limiting factors in all cases were inter and intra-pillar modes, the frequencies of which are generally determined by the shear velocity of sound in polymer and ceramic which have either not changed, or have changed by less than 5%. These values of MPAR, therefore, are still relevant to PZT-5H/Hardset transducers.

Device	Kerf (mm)	Pitch (mm)	Thickness (mm)	VF (%)	AR	MPAR	Centre Freq. (kHz)
13A	0.30	1.02	3.00	50	0.24	0.39	500
13B	0.30	0.73	2.50	35	0.17	0.27	590
13C	0.30	0.54	1.07	20	0.22	0.17	1300
13D	0.30	0.73	1.40	35	0.31	0.27	1041
13E	0.30	0.73	1.00	35	0.43	0.27	1424

Table 5.01 Constructional Parameters of 1-3 Composite Transducers

It is apparent that the 50% VF device 13A is well within the MPAR limits, that the 20% VF device is outside the limit, and of the three 35% VF devices one falls well within, one just outside, and one well outside the MPAR guidelines.

5.2.1 Experimental Arrangement

The devices were initially analysed in the simplest arrangement possible, with electrodes attached to the front and rear faces while operating in air. Under these conditions, the electrical impedance profile was obtained, and surface displacement profiles (SDP) measured at all the main resonances indicated by the impedance

profile. FEA would then be used to predict the impedance profile and the relevant SDP, to be used as a tool in the understanding of the device resonant behaviour.

Once all measurements had been taken, each transducer was placed in a holder with a hardset epoxy matching layer, a quarter wavelength thick at the thickness mode electrical resonance frequency. The transducer was surrounded by hardset epoxy on the four edges, but was air backed. A co-axial cable 1 m long provided the electrical connection, and the entire device was sealed with hardset epoxy at the cable gland to ensure it was waterproof. A diagram of the holder arrangement is provided as Figure 5.01.

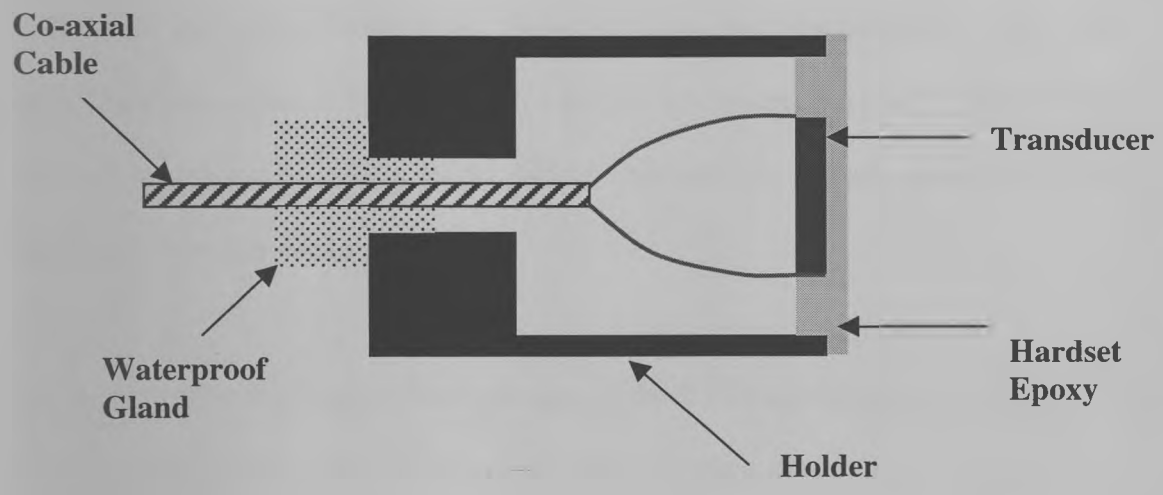

Figure 5.01 Transducer Holder Arrangement

Any impedance measurements taken with the transducer in this holding arrangement used the cable compensation feature of the HP 4194A impedance analyser to ensure compatibility with the finite element calculations.

5.2.2 Finite Element Modelling Techniques

An important element of efficient FEA is the ability of the designer to reduce the model to the minimum required for accurate results. For example, to obtain surface displacement profiles for a transducer in air, one-eighth symmetry is used, taking advantage of the symmetry in each axis. In the case of electrical impedance profiles, however, the important aspects are not the displacements at every point on the surface, but rather the frequencies and magnitude of the thickness and lateral modes. Therefore, for FEA to obtain impedance profiles, a 2.5 D approach was used, as detailed in chapter 3. Impedance is calculated as normal, but charge must be scaled up to the actual surface area to correct for the 2.5 D limitations. All modes are therefore predicted at their correct frequencies and magnitudes, with the exception of the width mode. As all transducers modelled in this chapter are square, the y-axis width mode is identical to the x-axis width mode, and is consequently already accounted for in frequency, although not magnitude.

It is apparent that the limited disadvantages of the 2.5 D approach in this instance are heavily outweighed by the reduction in model size (typically an order of magnitude). It should be noted, however, that in cases where the width mode frequency is close to that of the thickness mode, it is likely that 2.5 D will fail to fully account for the interaction between the modes.

5.2.3 Analysis of Composite 13A in Air

The impedance of composite 13A was experimentally measured, and compared with that predicted by FEA. The results shown in Figure 5.02 detail the magnitude and

phase of the impedance, with the magnitude impedance displayed on a log scale to allow all modes to be clearly seen.

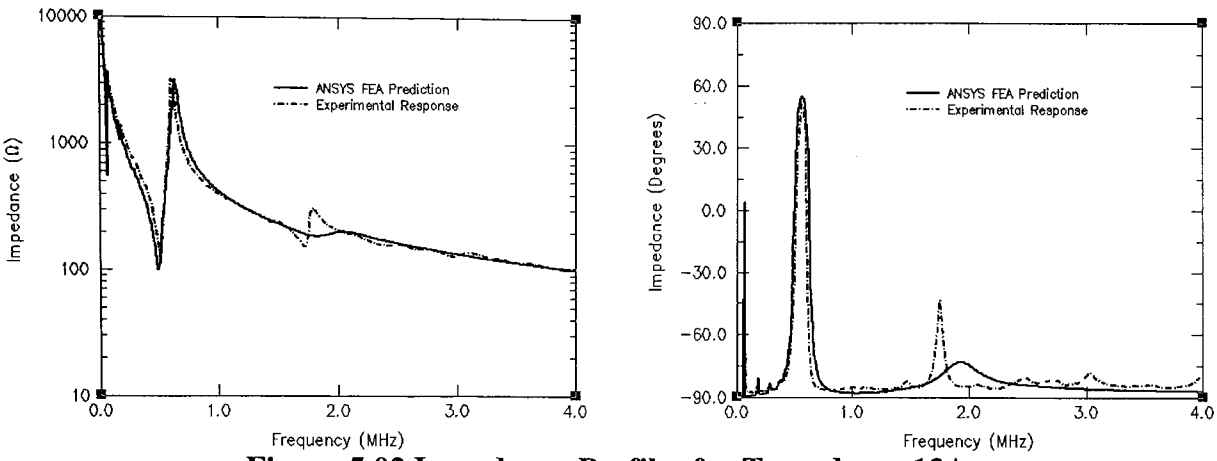

Figure 5.02 Impedance Profiles for Transducer 13A

It is clear that FEA has accurately predicted both the frequency of the thickness mode resonance at 500 kHz, and its impedance magnitude. The thickness mode third harmonic is visible at just below 1700 kHz, but while FEA predicts a mode at this location, its resonance and anti-resonance are separated more than is shown experimentally.

This is due to the limitations of the damping models in ANSYS, as detailed in chapter 3. Additionally, the damping coefficients used in the modelling had been obtained in an empirical manner, by an iterative process of varying the damping to match the electrical impedance of modelled and experimental transducers. The thickness mode frequencies in these transducers ranged from approximately 300 kHz to 2 MHz, thus limiting the most accurate results to these frequencies. Whilst the damping is obviously accurate at the fundamental thickness mode, the third harmonic is sufficiently far removed that damping at this frequency is incorrect. This limitation is

inherent to the ANSYS code and will remain until further refinements are made to the damping models.

A possible solution to this problem would be to dynamically change the elemental damping with frequency, corresponding to either a mathematical relationship or a look-up table. No facility inherently exists at present within ANSYS for this procedure, but could still be possible although in a slightly cumbersome manner. The initial model database would be constructed as normal and saved under a temporary filename just before solution. The solution phase would be implemented as normal, but the entire solution command structure could be set within a 'do loop' ranging between frequencies. Within each loop, the temporary database would be loaded in place of the old database, and the elemental damping properties altered to the appropriate values, and the matrices solved for that frequency. This looping would continue until the solution was complete. While this model would provide great control over the damping within a model, a number of difficulties exist. Firstly, this method would increase solution time due to the constant loading of databases and results files, and result in a larger number of files. Additionally, damping values at all frequencies are required before modelling can begin as too many variables exist for determination of values by iterating towards experimental results. As this data was not available for all materials during the writing of this thesis, this method of damping is left as a suggestion for further work.

It is quite clear from the impedance plot that no strong inter or intra-pillar modes exist in the vicinity of the main thickness mode resonance, with very weak modes at 1000 kHz and 1500 kHz. Using Bragg scattering to determine the frequencies of the first

two inter-pillar resonances (Equation 2.23), results in modes predicted at 1110 kHz and 1565 kHz. Bragg scattering has perhaps predicted the frequency of the laterally resonant modes, but it is difficult to determine due to the weakness of the modes experimentally. As these resonances depend upon waves generated laterally by the pillars, the magnitude of these resonances depends upon the displacement of the pillars in the 1 and 2 axes, which is related to the thickness mode behaviour by Poisson's ratio. As the inter-pillar modes are significantly removed in frequency from the thickness mode, thickness mode displacement at these frequencies is minimal, resulting in minimal inter-pillar activity. Thus only in composites where the inter-pillar resonances are of similar frequencies to the thickness mode (i.e. AR larger than MPAR) will significant displacement be found.

As this is a transducer with an AR well below the MPAR, it is fully expected that this transducer should behave in a unimodal fashion, and should displace in a piston like manner at the thickness mode. To confirm this, SDPs were obtained at the various resonant frequencies, and the response at thickness resonance is displayed in Figure 5.04 in both magnitude and phase. Throughout this thesis, when results are displayed in both magnitude and phase, the left hand image corresponds to magnitude and the right hand image to phase. Figure 5.05 presents the FEA predicted surface displacement.

As depicted in Figure 5.03, Figures 5.06 and 5.07 detail the surface displacement of the transducer from a cross section, with Figure 5.06 taken as a slice through a line of alternating ceramic and polymer. Figure 5.07 represents a line parallel to that in Figure 5.06, but moving through polymer only. This method of presenting the data in

'slices' ensures that the SDP data can be interpreted even following poor quality printing or multiple photocopying.

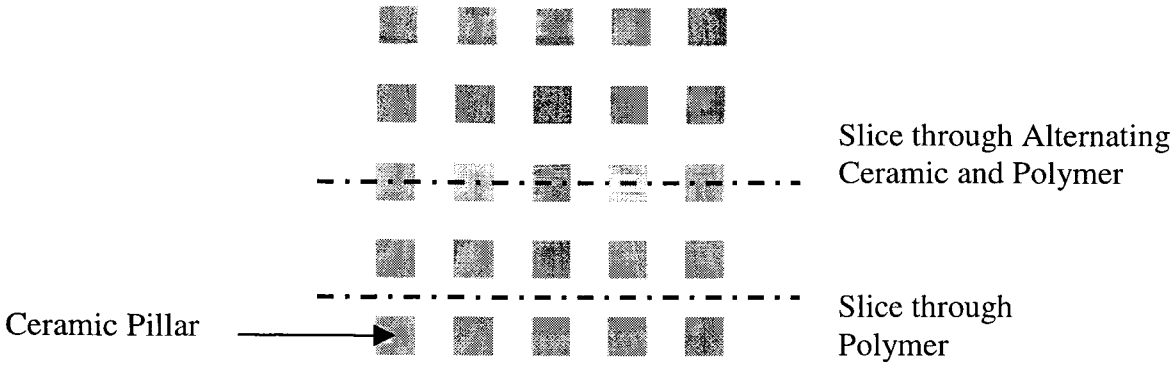

Figure 5.03 Cross-sections through 1-3 Composite

Surface displacement at thickness mode electrical resonance for this transducer shows each ceramic pillar within the composite displacing by a slightly greater quantity than the surrounding polymer, with overall pillar displacement magnitude increasing in the centre of the device due to the lack of support at the transducer edges. Any asymmetry within the response is due to the holding arrangement for the transducer, which consists of a holder gripping at 2 points on both the upper and lower surface. These results correlate well with results previously obtained by Gururaja [12], and are typical of a 1-3 composite displacing at the thickness mode in a unimodal manner. Phase response indicates that all pillars are moving in phase, with any abrupt colour change due to the crossover between $\pm\pi$. The figures show the transducer edges displacing by a slightly greater quantity than its neighbouring material, due to the absence of mass loading on one side.

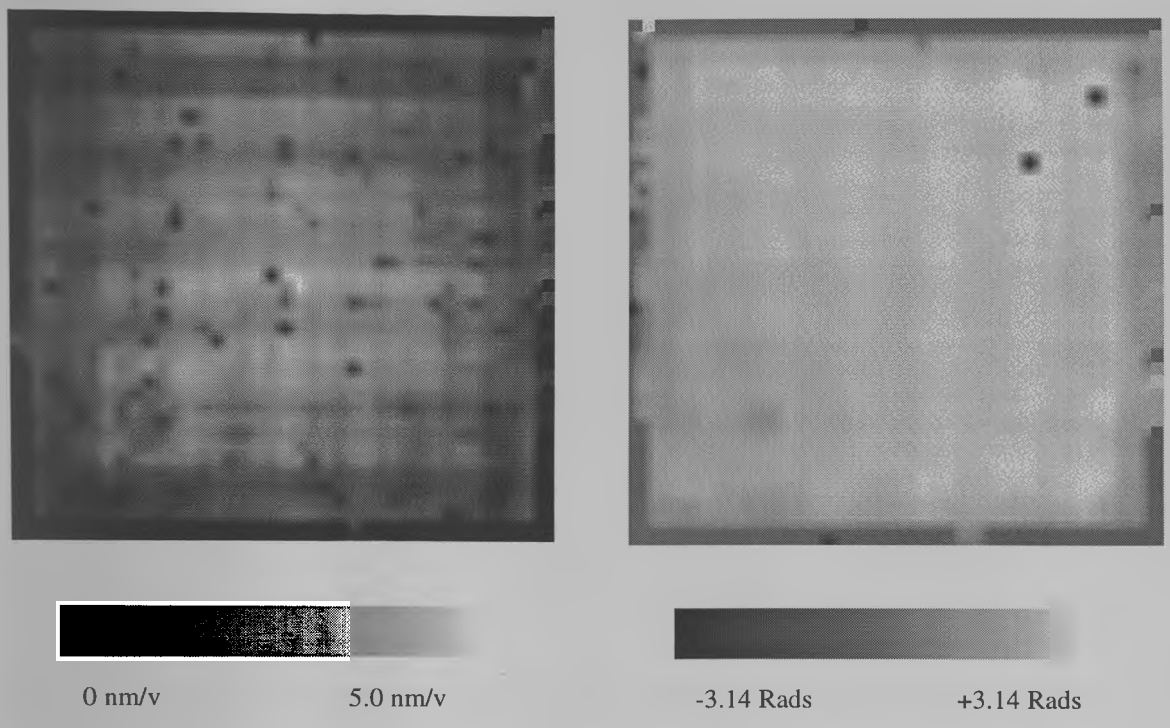

Figure 5.04 Experimental SDP of Composite 13A in Air at 500 kHz

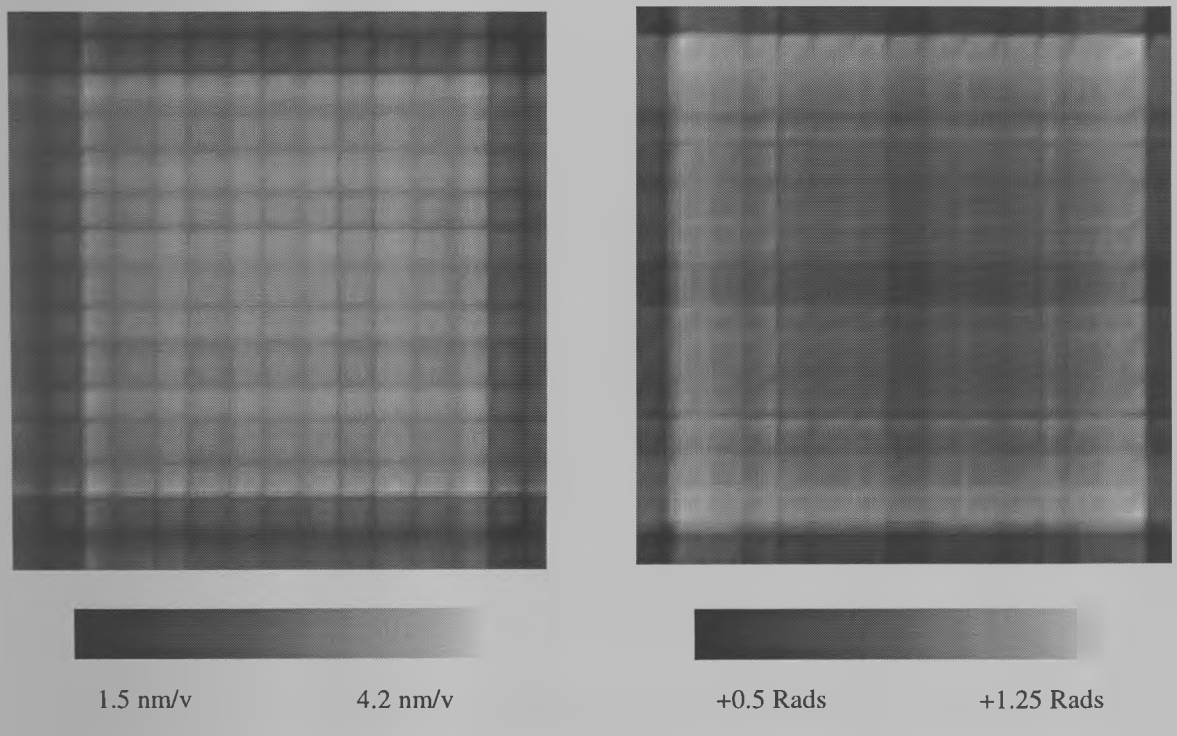

Figure 5.05 FEA SDP of Composite 13A in Air at 500 kHz

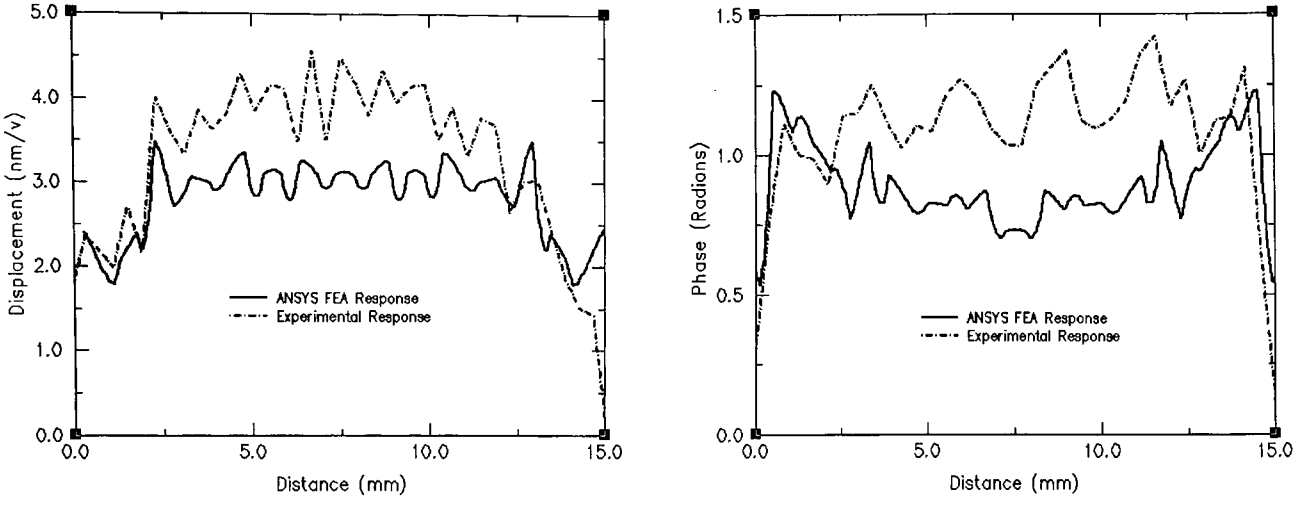

Figure 5.06 Cross-section Through Ceramic Pillars in Composite 13A at 500 kHz

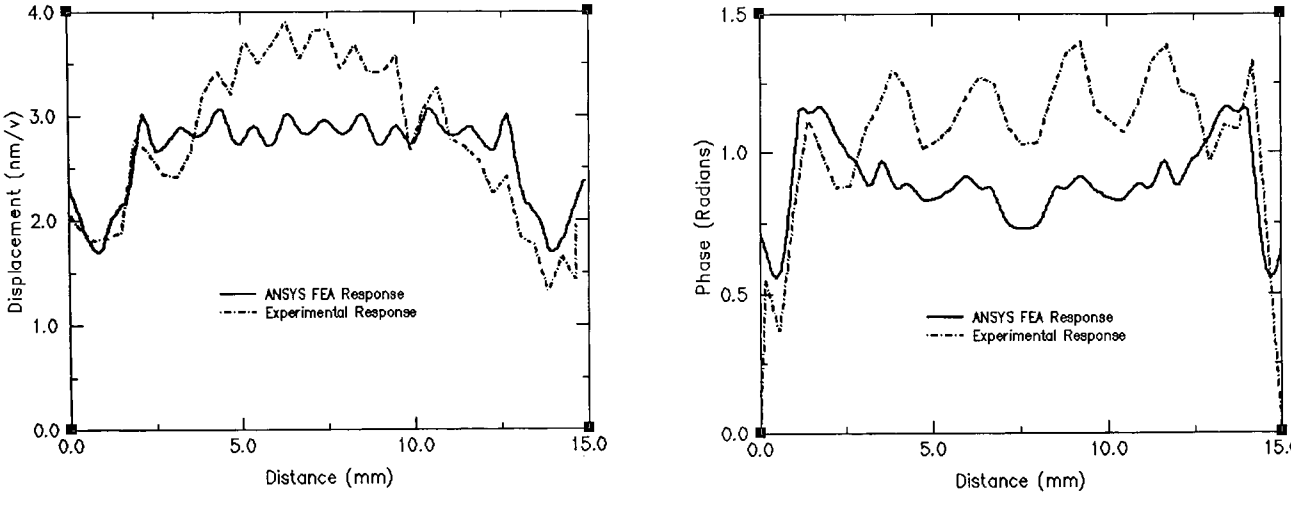

Figure 5.07 Cross-section Through Polymer in Composite 13A at 500 kHz

5.2.4 Analysis of Composite 13B in Air

Following analysis of the 50% volume fraction composite, a 35% VF composite was studied, beginning with 13B which has an AR considerably below the MPAR. As before, initial comparisons were made between experimental impedance profiles and the corresponding FEA results. Figure 5.08 show a very unimodal response, similar to the results from 13A with the fundamental thickness mode at 590 kHz, what appears to be the third harmonic at 1600 kHz, and a weak mode exists at 1.9 MHz.

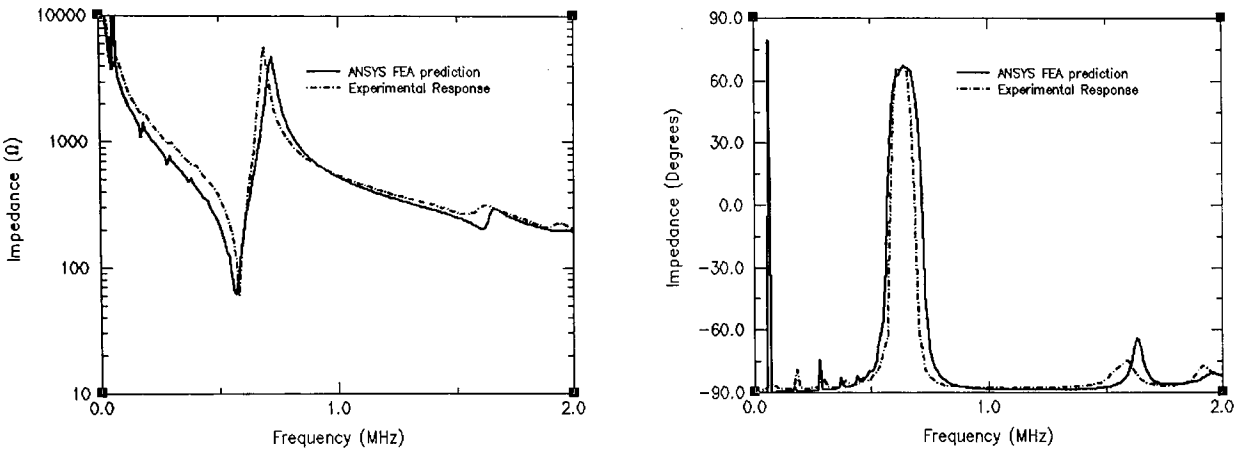

Figure 5.08 Impedance Magnitude and Phase of Composite 13B

For the saw pitch of this transducer, Bragg scattering predicts the first two inter-pillar modes to occur at 1551 kHz and 2186 kHz. The first inter-pillar mode is unlikely to be detectable due to its close proximity to the thickness mode third harmonic. As in composite 13A, the significant frequency separation of thickness and inter-pillar modes ensures that the inter-pillar modes are insignificant. This, due to the low AR, indicates that the SDP of this transducer should show a very unimodal and piston like response.

Whilst the device is extremely unimodal in behaviour, it is apparent that the odd harmonics of the width mode do not disappear until very close to the fundamental thickness mode. This is due to the transducer overall width to height ratio being 6, considerably lower than the generally recommended 10. Consequently, the thickness mode frequency is not as well separated from the width mode as is generally recommended, but should still be sufficiently far apart to prevent interference.

This again shows similarities to the responses of transducers analysed by Gururaja [75]. In his paper, he suggested that for there to be no appreciable difference in displacement between ceramic and epoxy, the transverse wavelength at thickness mode resonance must be more than three times the periodicity. When the transverse wavelength is significantly greater than the periodicity there is little lateral activity within the polymer, and the polymer effectively becomes 'tied' to the ceramic, and displaces in phase with similar magnitude. As the transverse wavelength approaches the value of the periodicity, more activity is found within the polymer until eventually the ceramic and polymer are effectively decoupled and vibrate independently, often in anti-phase to one another. Gururaja estimated the effectiveness of a transducer by the figure of merit Gain Bandwidth Product, G, defined as the product of the maximum voltage sensitivity and the 3 dB bandwidth. For this transducer, the transverse wavelength at 590 kHz is 1.92 mm compared to a periodicity of 0.73 mm, giving a ratio of 2.63 : 1. While less than the recommended value, Gururaja indicates that even with a ratio as low as 2 : 1, the value of G should still be 75% of that at a ratio of 3 : 1. It is therefore expected that this transducer should vibrate uniformly with little difference in displacement magnitude between ceramic and polymer. Experimental

SDP at 590 kHz and the FEA equivalent for composite 13B can be seen in Figures 5.09 and 5.10, with the 'slice' data presented in Figures 5.11 and 5.12.

Whilst the FEA accurately predicts the general magnitudes of displacement and the phases, it can be seen that there is more 'activity' predicted by FEA than exists in experiment. Both the displacement magnitude and phase are modelled to rise and fall across the device, but do not do so in reality. This is due to two reasons. Firstly, the single damping constant ANSYS applies to each material must be a compromise between longitudinal and shear damping. As the SDPs shown in this thesis utilise the same damping coefficients as are used in the impedance calculations, it is apparent that without significant further work in obtaining material properties combined with an alteration in the ANSYS damping model, accurate impedance modelling will not always guarantee accurate displacement data.

Secondly, there appears to be an additional mode travelling across the surface of the transducer. In total 7 bands in both the horizontal and vertical directions are visible, indicating that the 7^{th} harmonic of a width mode has been excited. Given that the fundamental width mode occurs experimentally at 70 kHz, the seventh harmonic should occur at 490 kHz, close to the thickness mode operating frequency of 590 kHz. The combination of this width mode and the compromise damping has resulted in the FEA surface displacements being less uniform than found experimentally.

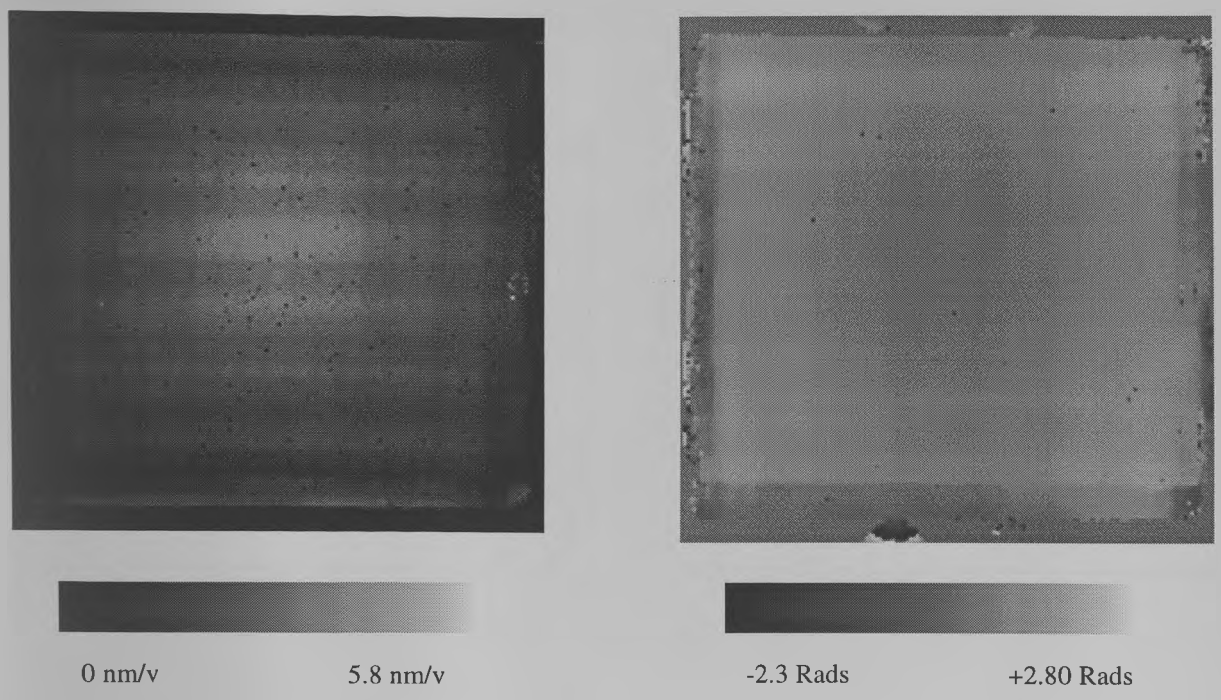

Figure 5.09 Experimental SDP at 590 kHz for Composite 13B

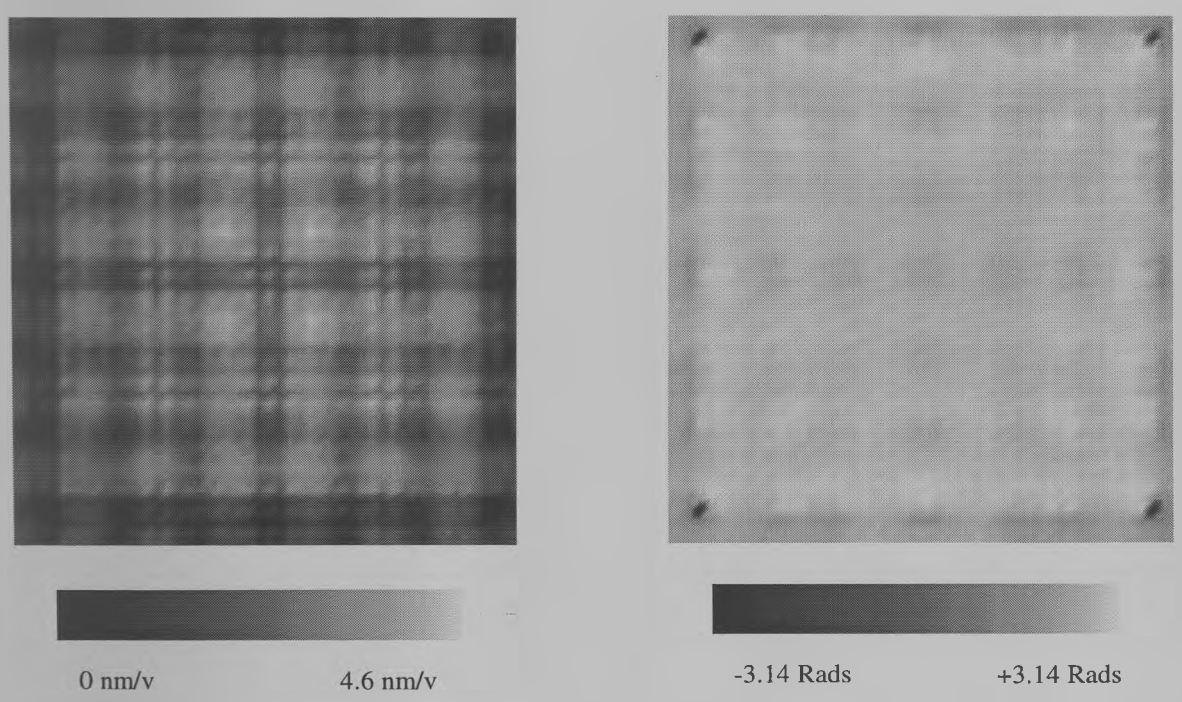

Figure 5.10 FEA SDP at 590 kHz for Composite 13B

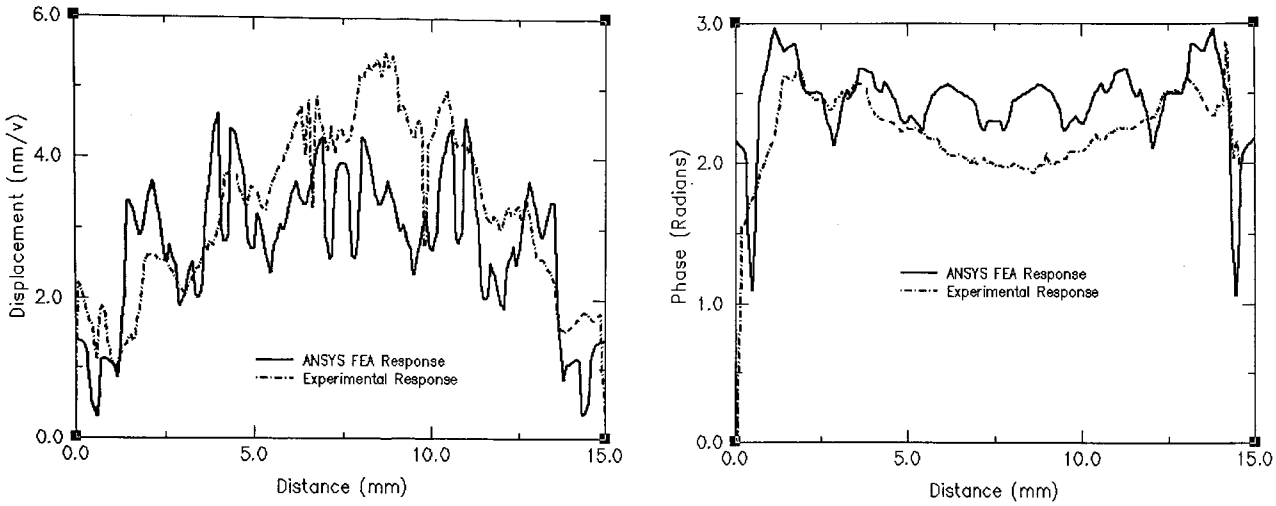

Figure 5.11 Cross-section Through Ceramic Pillars in Composite 13B at 590kHz

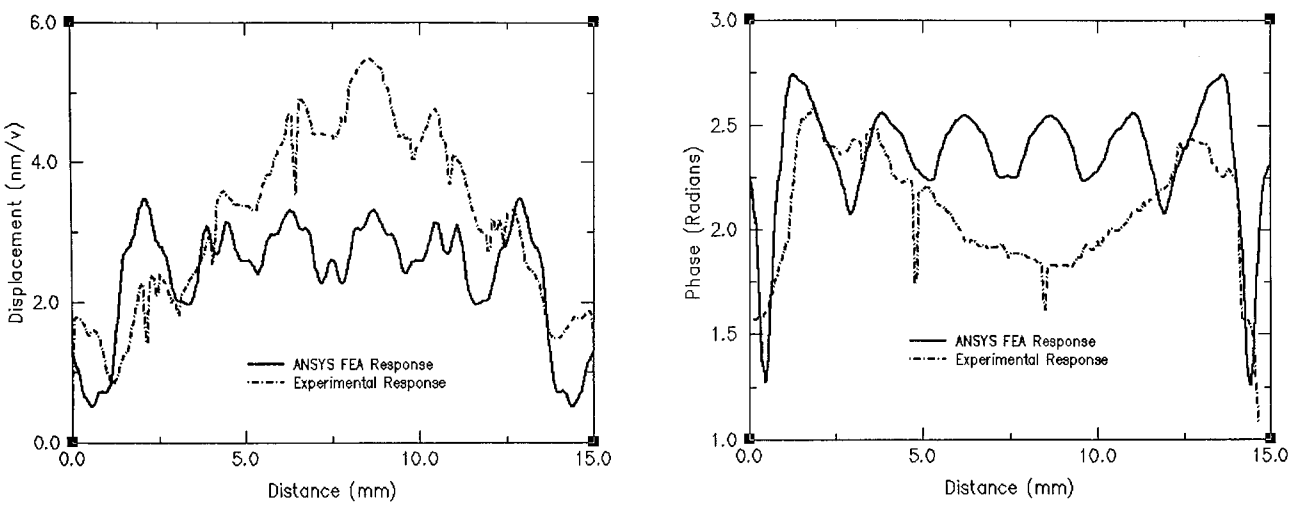

Figure 5.12 Cross-section Through Polymer in Composite 13B at 590 kHz

It is expected that the seventh harmonic of any resonant mode will be weak in comparison to the fundamental mode, indicating that for such a high order mode to have a visible effect upon the fundamental thickness mode, then the fundamental width mode must be very strong in itself. To confirm this, an experimental SDP of the width mode was obtained, and is presented as Figure 5.13.

It is apparent that the width modes in the x and y-axes are different, due to the holding arrangement (clearly visible as the two triangles at the base of each image). The magnitude of displacement, at 2.1 nm/v, is over a third of the displacement at thickness mode resonance (5.8 nm/v), giving weight to the theory that the width mode 7^{th} harmonic could be strong enough to still be evident at 590 kHz. The asymmetry within the response is due to the holding arrangement, which is clearly visible in the figures. This clamping was designed to minimise the effect of observation upon the transducer, and could not be reduced further. The clamping at the edges suppresses the vibration in the width directions, thus altering the displacement. This image therefore gives an indication of magnitude of mode displacement rather than mode shape, and consequently no FEA result is presented for this mode.

As expected, the ceramic and polymer displace by similar quantities, and also displace in phase. The magnitude of displacement increases towards slightly the centre of the device. Indeed, the difference in displacement between ceramic rods and surrounding polymer is less than is present in 13A. This is to be expected as the ratio of transverse wavelength to periodicity in 13A is 2.2 : 1, compared to 2.63 : 1 in 13B.

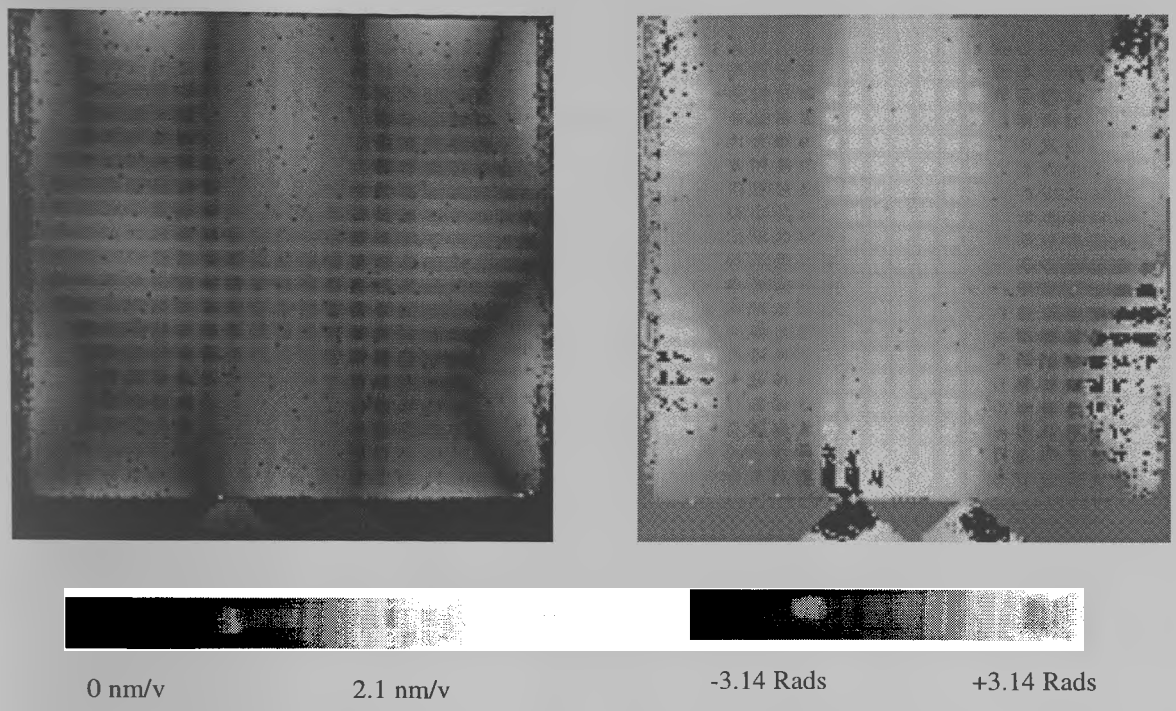

Figure 5.13 Experimental SDP at 70 kHz for Composite 13B

It appears that despite ensuring that AR was significantly below MPAR, that failing to have an overall width to height aspect ratio of 10 or greater has resulted in a harmonic of the width mode being present at thickness mode resonance. While this would likely have no significant negative impact upon the behaviour of the device, it is clear that in certain cases, such as very low frequency transducers, where a strong width mode could disturb the uniformity of transducer displacement, width aspect ratio is an important consideration. It is apparent that these modes require suppression, and this can be achieved in a number of ways. A more highly damped polymer could be used, or a large 'rim' of epoxy left on the transducer during manufacture to reduce the mode frequency, and also increase attenuation to reduce the magnitude of the mode displacement. This possibility is left as a suggestion for further work.

5.2.5 Analysis of Composite 13C in Air

Following the analysis of two below-MPAR transducers, it is of interest to analyse a transducer that has an AR significantly greater than MPAR. Additionally, composite 13C is a 20% VF transducer and is more likely to behave in a manner similar to that predicted by the Bragg scattering model. Impedance characteristics are shown as Figure 5.14 and again show excellent correlation between FEA and experiment.

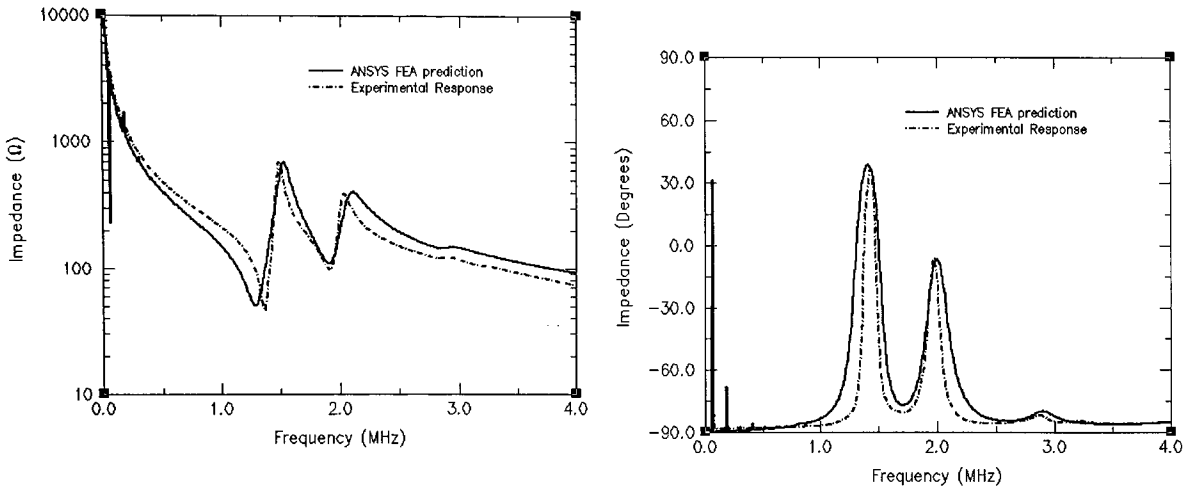

Figure 5.14 Impedance Profiles for Composite 13C

While impedance magnitudes have all been correctly identified, certain of the resonances are not quite as accurately predicted as in 13A or 13B, and is likely due to additional ceramic depoling during manufacture due to the lower volume fraction [21]. Unlike the previous two transducers, the thickness mode at 1300 kHz is extremely close to the first inter-pillar resonance, occurring at 1910 kHz. For this transducer, Bragg scattering predicts modes at 2100 kHz and 2956 kHz. While the prediction of the first mode is approximately 10% out, there does appear to be a very weak mode just below 3 MHz. It appears that for the lower volume fraction composite

that Bragg scattering has more accurately predicted the frequencies at which inter-pillar resonances will occur.

The thickness mode SDP for composite 13C (Figure 5.15) is significantly different from that of 13A or 13B. The SDP consists of a regularly repeating pattern across the entire surface, with all polymer areas displacing by a greater magnitude than the ceramic pillars. The displacement in the ceramic is consistent across the entire surface, while the polymer peaks at the diagonals between the ceramic. This can be difficult to determine from such large scale diagrams, and so enlarged sections are displayed as Figures 5.17 to 5.20. The phase diagram indicates that the entire surface is moving in phase.

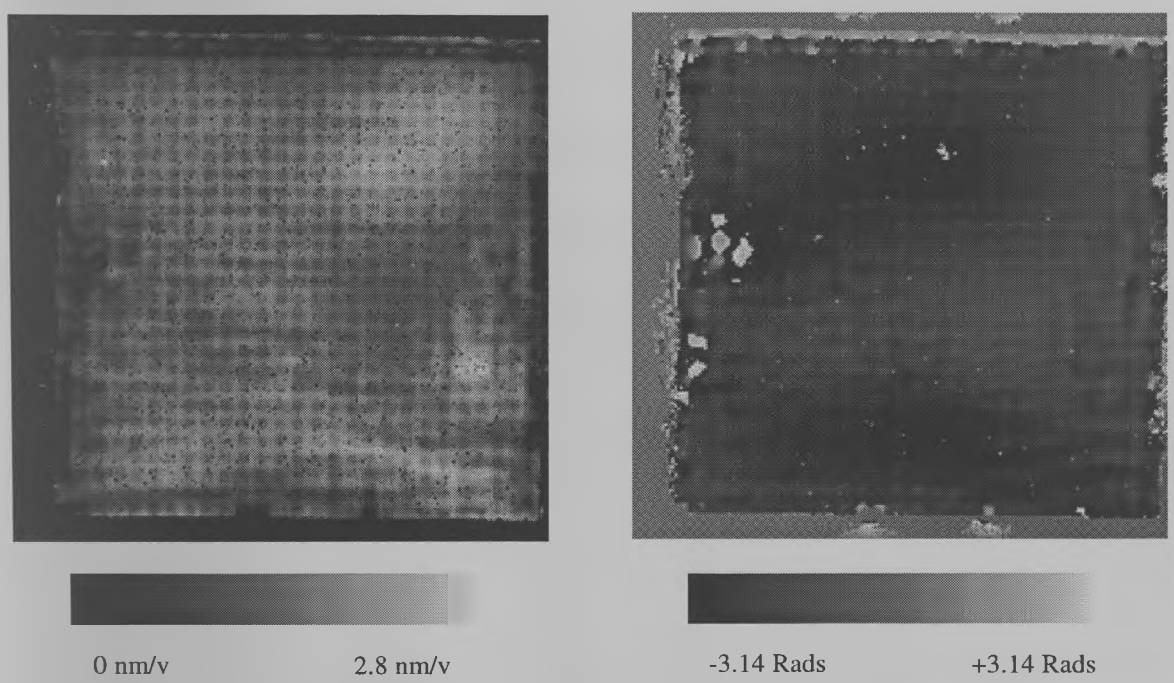

Figure 5.15 Magnitude and Phase SDP at 1300 kHz for Composite 13C

Overall displacement magnitude at the thickness mode electrical resonance (1300 kHz) is approximately one-half that for 13A, typical for a lower VF composite

(Gururaja [76]). Given the transverse velocity in hardset epoxy as 1132 ms^{-1}, the transverse wavelength in 13C is 0.87 mm, compared to a periodicity of 0.54 mm. The proximity of the transverse wavelength and the periodicity of the device has led to an extremely non-uniform surface displacement. It is clear that in this case, the high aspect ratio has resulted in a non-ideal surface displacement, with the polymer displacement greater than that of the ceramic.

While FEA is perfectly capable of producing a SDP for the entire transducer surface at electrical resonance for transducer 13C, it was clear that this was a considerable waste of computing resources. Unlike the thickness mode in 13A or 13B where the displacement increases in magnitude toward the device centre, 13C is like a single cell repeated symmetrically across the entire transducer surface. Under these circumstances, therefore, it was faster and more efficient to model the transducer as an infinite plate, consisting of a unit cell arrangement with symmetrical boundaries on all edges. This technique allowed mode shapes to be quickly and accurately computed, with little loss of time should it become apparent that the entire surface required modelling. The results of these analyses are presented as a 2 by 2 cell arrangement, as described in Figure 5.16, and always measure twice the composite saw pitch along each side.

Utilising this method, the SDP at the thickness mode was determined using FEA. It is apparent from Figures 5.17 to 5.20 that prediction closely resembles experimental response, with polymer displacing considerably more than the ceramic, thus validating the technique. Unless otherwise stated, all future FEA SDPs will be calculated using this method, and at the FEA calculated resonant frequency.

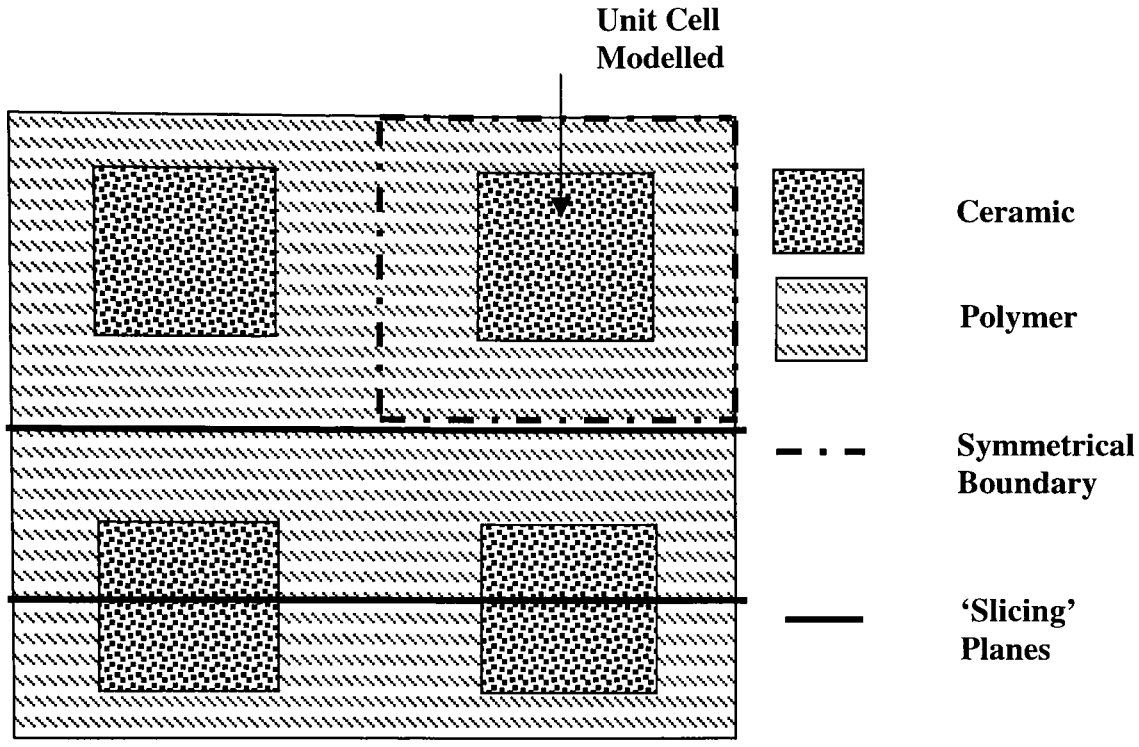

Figure 5.16 Diagram of Modelling Technique for 'Infinite' Transducers

The polymer at the thickness mode for composite 13C is moving independently of the ceramic, as is expected for a composite with an AR higher than MPAR. It is apparent that as well as the thickness mode at 1300 kHz, an additional mode is present at 1910 kHz that impinges closely upon that mode. Given the volume fraction of the composite and the frequency at which it occurs, it is most likely an inter-pillar mode. The Bragg scattering model predicts a mode at 2100 kHz, and while nearly 10% out, current theory would indicate that this is the mode seen at 1910 kHz.

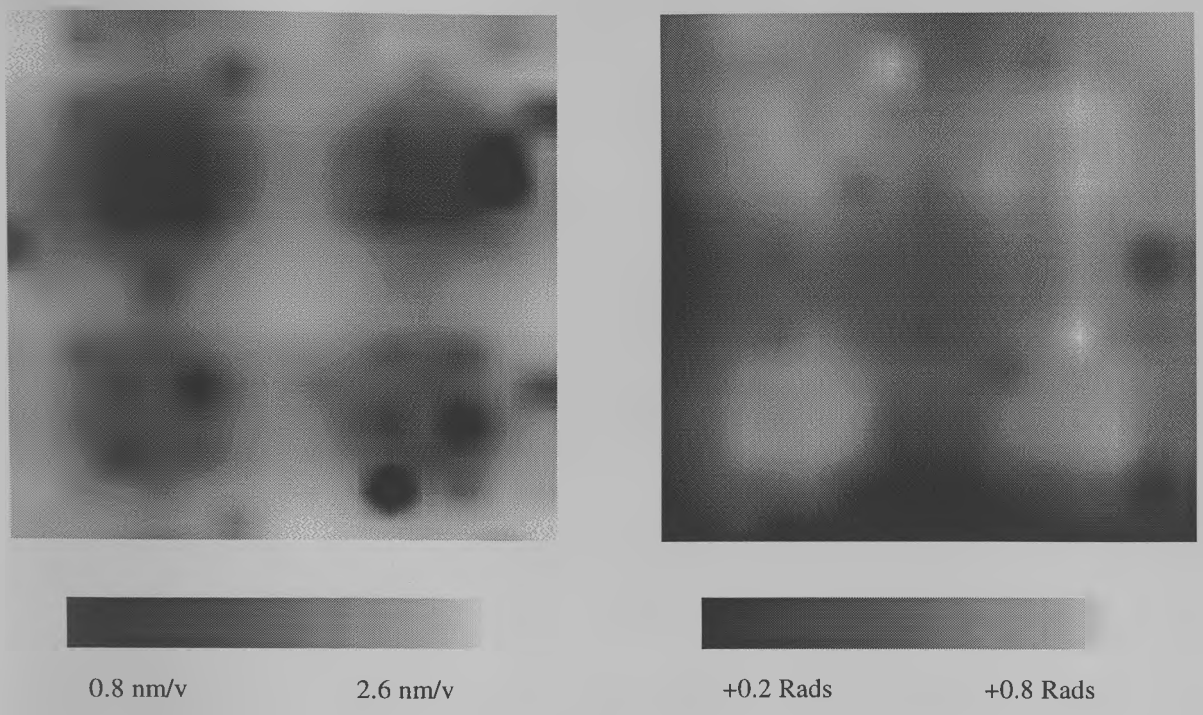

Figure 5.17 Experimental SDP at 1300 kHz for Composite 13C (Zoom)

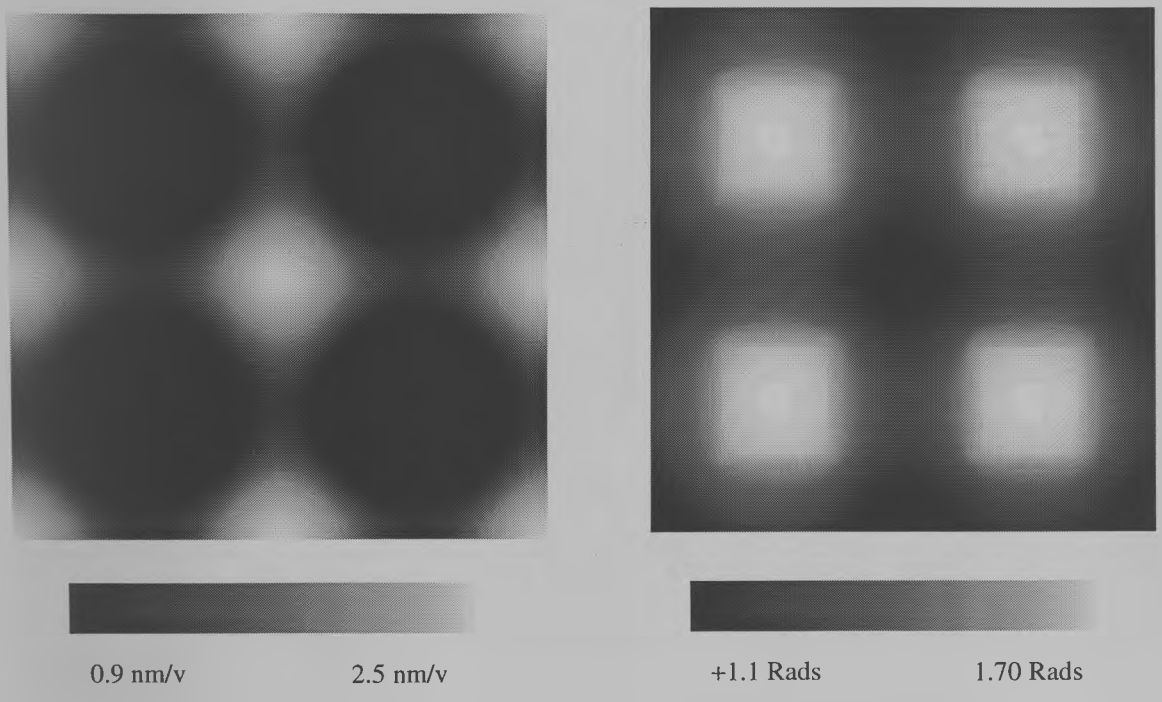

Figure 5.18 FEA SDP at 1261 kHz for Composite 13C (Zoom)

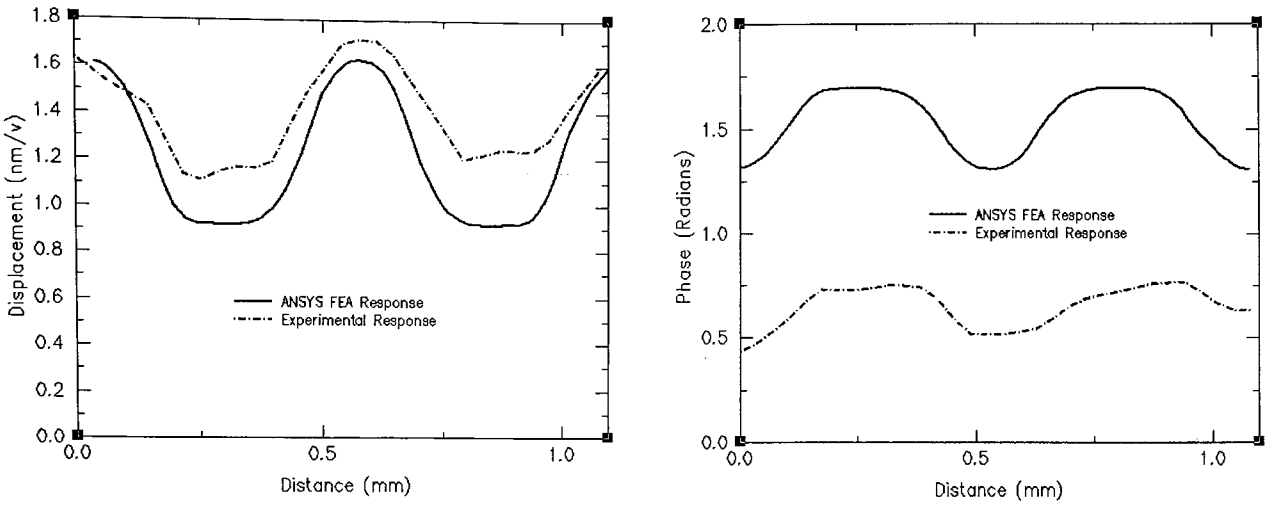

Figure 5.19 Cross-section Through Ceramic Pillars in Composite 13C at 1300 kHz

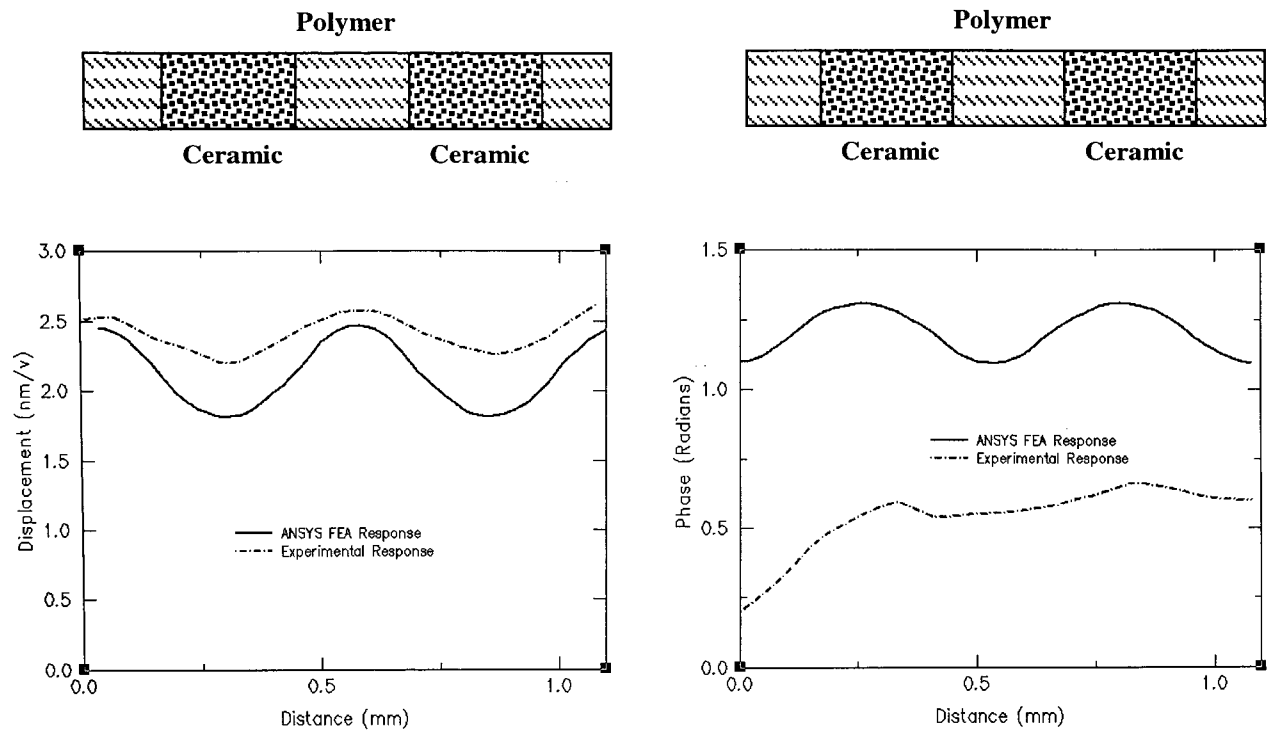

Figure 5.20 Cross-section Through Polymer in Composite 13C at 1300 kHz

Figure 5.21 illustrates the experimental surface displacement profile obtained at 1910 kHz, and clearly shows a non-uniform surface behaviour. Again, for clarity, enlarged sections and slices through these sections are displayed as Figures 5.22 to 5.25, showing excellent correlation between FEA and experiment.

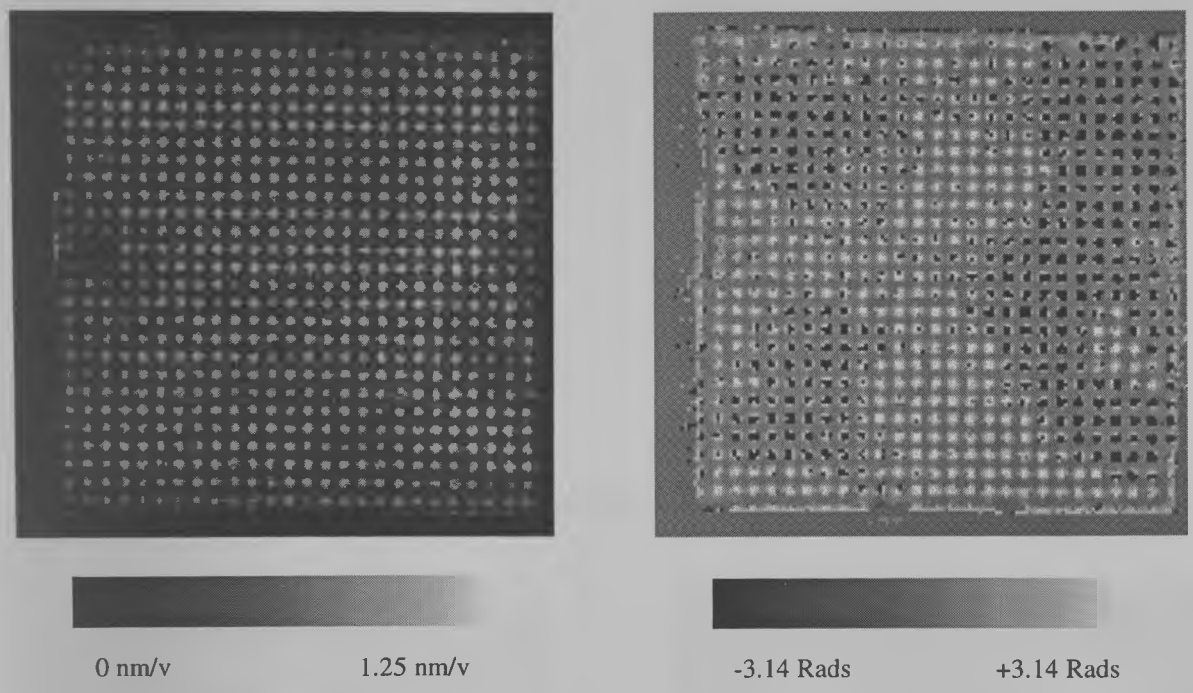

Figure 5.21 Experimental SDP Magnitude and Phase of 13C at 1910 kHz

The phase diagram shows the polymer in grey, displacing in phase regardless of magnitude, and the pillars also in phase in white (or black where they have just crossed the $\pm\pi$ boundary). It is clear from the phase diagram that as the ceramic pillars constrict in the thickness direction, they expand in the lateral axes by a quantity determined by Poisson's ratio. The polymer is compressed in the x and y-axes and therefore expands in the thickness direction, again by a quantity related to Poisson's ratio. The polymer and ceramic therefore move out of phase with one another.

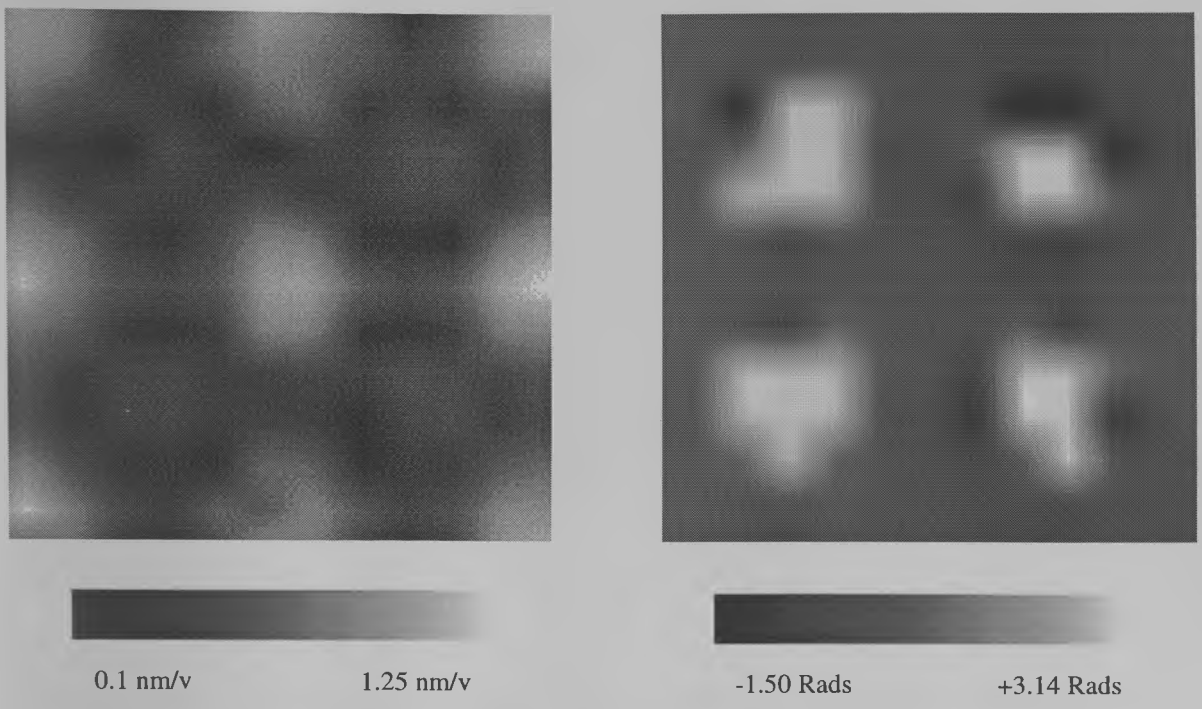

Figure 5.22 Experimental SDP at 1900 kHz for Composite 13C (Zoom)

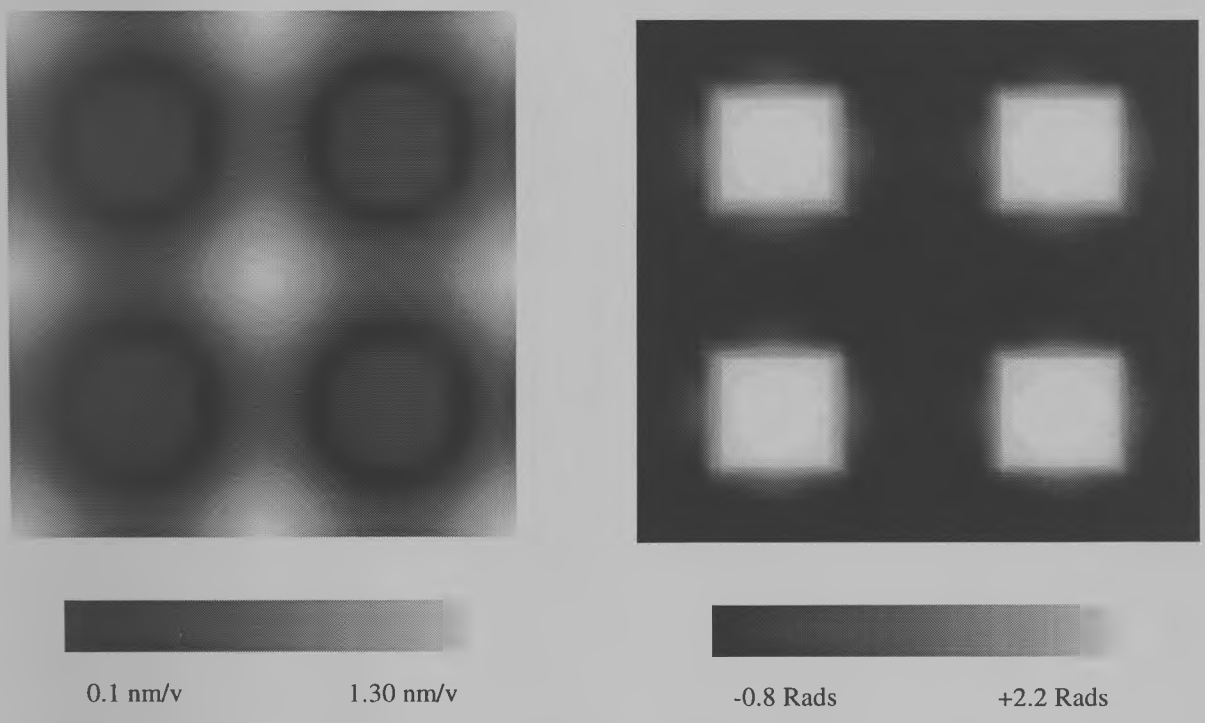

Figure 5.23 FEA SDP at 1900 kHz for Composite 13C (Zoom)

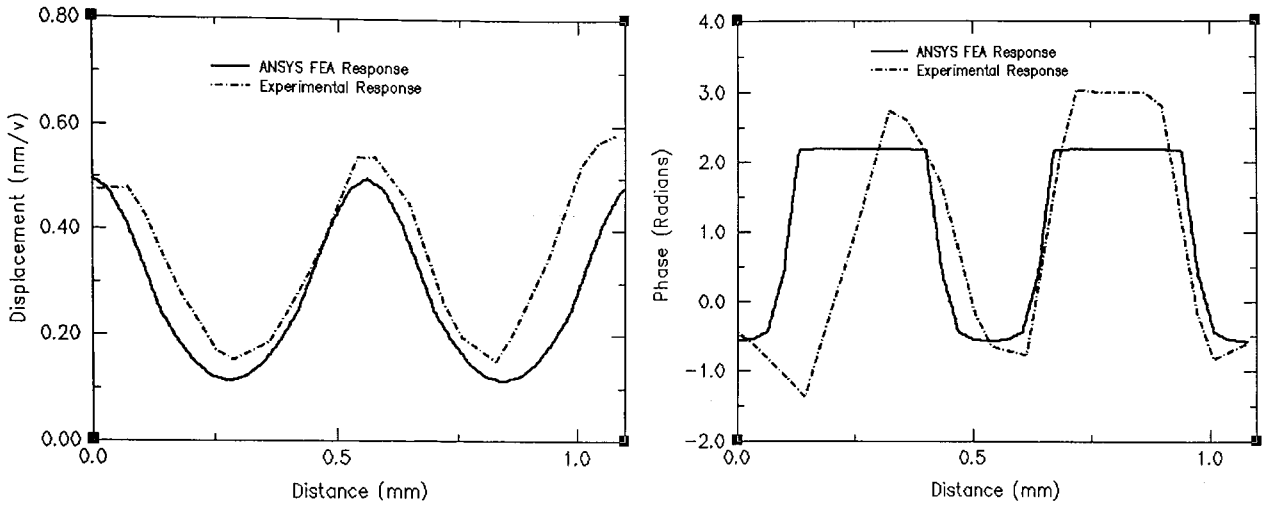

Figure 5.24 Cross-section Through Ceramic Pillars in Composite 13C at 1900 kHz

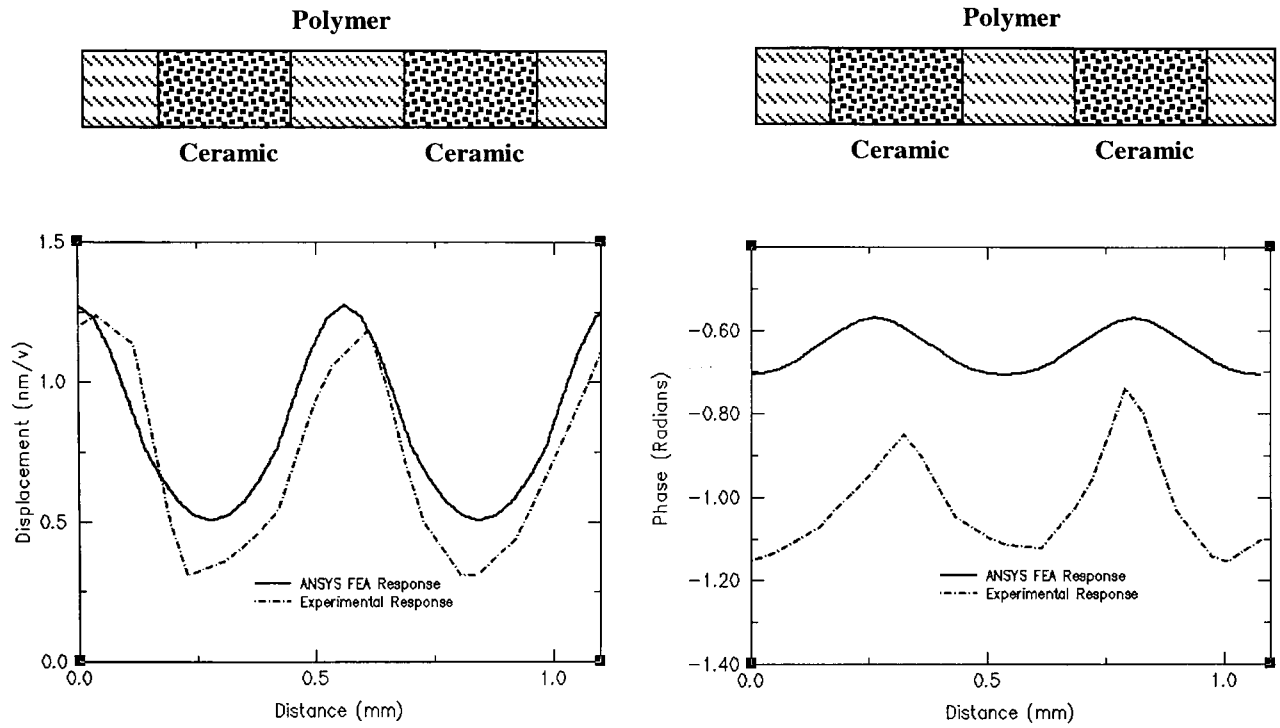

Figure 5.25 Cross-section Through Polymer in Composite 13C at 1900 kHz

These results indicate that in the first inter-pillar resonance, the polymer should displace more than the ceramic, particularly in the diagonals between the ceramic pillars. Bragg theory indicates that this is caused by the transverse waves generated by the displacing ceramic scattering as they strike neighbouring pillars, and constructively interfering. While results appear to indicate that this is a possible explanation, Figures 5.24 and 5.25 in particular seem to show a wave that is travelling through the polymer, as opposed to one scattering against pillars. It may be that a mode is being generated in the polymer by the regularly spaced ceramic pillars, each pillar acting as a source of laterally propagating waves. Given the regular nature of the composite structure it is possible that these modes are in fact the result of Lamb waves being generated in the composite.

5.2.5.1 Lamb Waves

A full description of the mechanisms which generate Lamb waves are detailed by Viktorov [77], and Monkhouse, Cawley, Castaings, Wilcox, and Lowe [78,79], but a brief description of the generation of these modes will be given to assist the reader.

Lamb waves are ultrasonic waves that propagate in plates of a material, and travel along the axes perpendicular to the thickness direction. They can be split into two classes symmetrical (s_x) and antisymmetrical (a_x) depending upon the symmetry of the mode displacement about the plate centre line, as depicted in Figure 5.26. These modes can typically be generated by the use of interdigital transducers (IDT), which attempt to apply force to a plate in lines (fingers) at spacing equivalent to the wavelength of the Lamb wave.

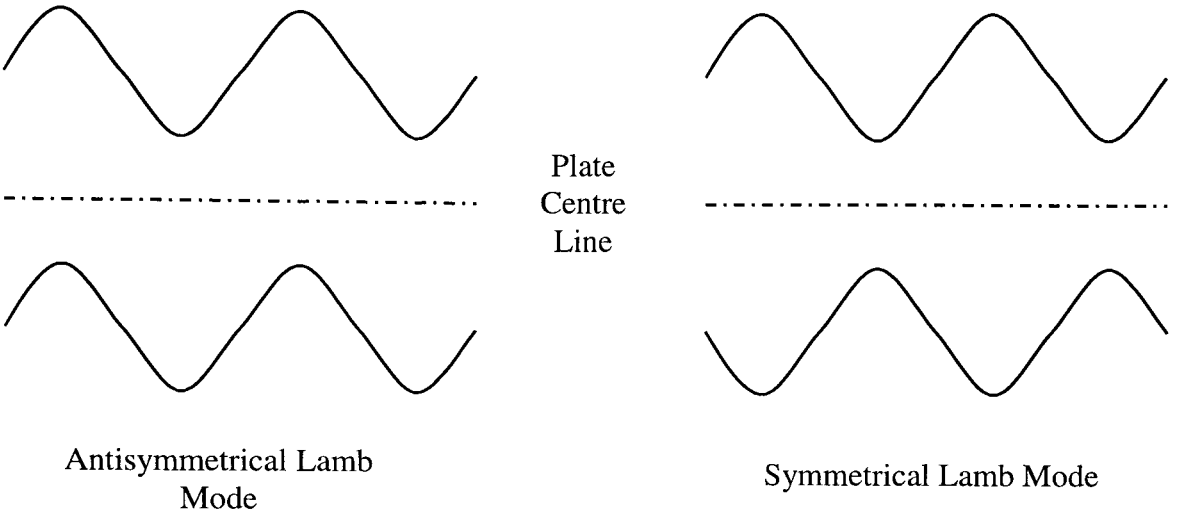

Figure 5.26 Mode Shapes for Lamb Waves

It is possible that inter-pillar resonances in 1-3 composite transducers are generated by the ceramic pillars acting as IDTs, causing a Lamb wave to be propagated into the polymer. If this were the case, the 'IDT fingers' in the composite would be formed as described by Figures 5.27 and 5.28. In both these cases, a single wavelength of the Lamb wave would exist between the fingers. For the first inter-pillar resonance, this requires a wavelength to equal d_0, the saw pitch. For the second inter-pillar resonance, although the distance between a ceramic pillar and its nearest neighbour on a diagonal is $\sqrt{2}d_0$, the distance between each 'finger' is $d_0/\sqrt{2}$, as shown in Figure 5.28. Thus the wavelength of the second inter-pillar resonance is $d_0/\sqrt{2}$. Obviously, additional 'fingers' would exist at right angles to those shown in the diagrams, that is, the structure is doubly periodic. It would be expected, therefore, that for the first inter-pillar resonance of a composite that waves would propagate normal to the transducer edges, while for the second resonance they would propagate in a 'diagonal' manner.

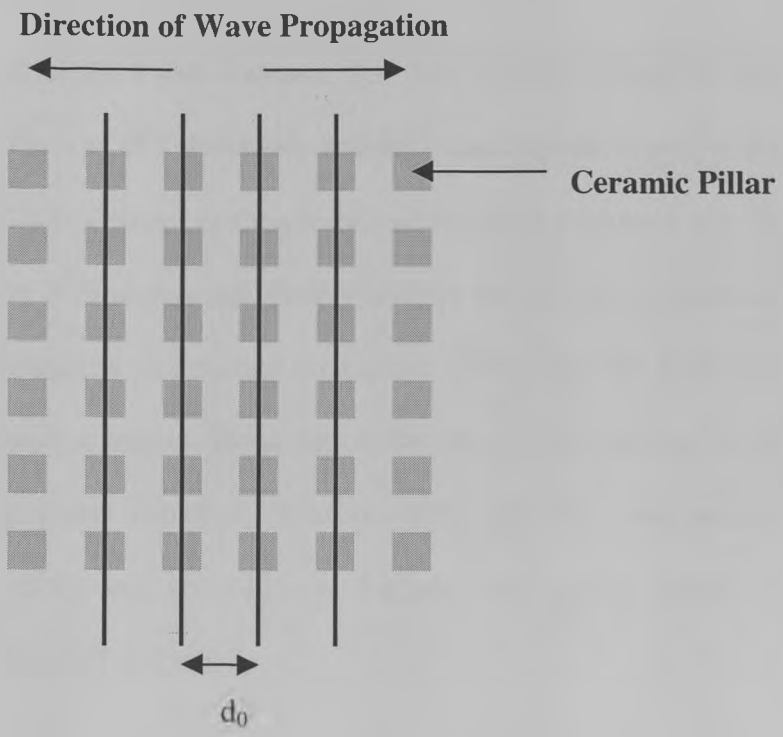

Figure 5.27 Generation of Lamb Waves at First Inter-pillar Resonance

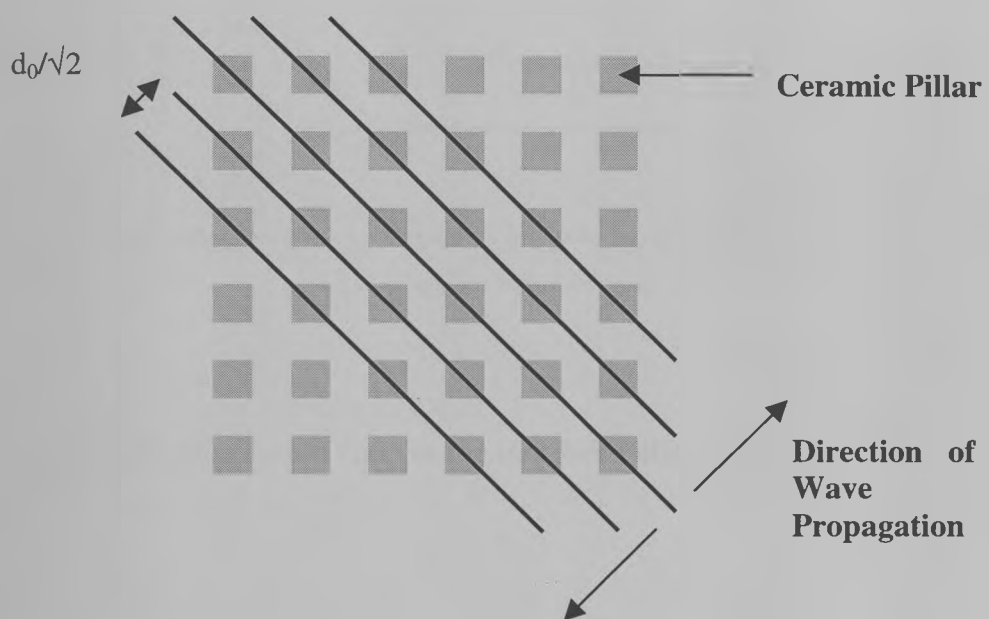

Figure 5.28 Generation of Lamb Waves at Second Inter-pillar Resonance

An additional complication of the Lamb waves is that their velocity (phase velocity v_{phase}), is dependent upon the type of Lamb mode and the frequency-thickness product (FTP) of the plate. The FTP is defined as the product of the plate thickness with the operating frequency. Figure 5.29 shows the phase velocities for the two fundamental antisymmetric (a_0) and symmetric (s_0) modes for hardset epoxy, and for PZT-5H – these are often called *dispersion curves*. These curves are obtained by solving for the real roots of the Rayleigh-Lamb equation, (Viktorov [77] page 72), and assumes isotropic material properties, and so will not include any poling effects or piezoelectric stiffening in the PZT-5H results.

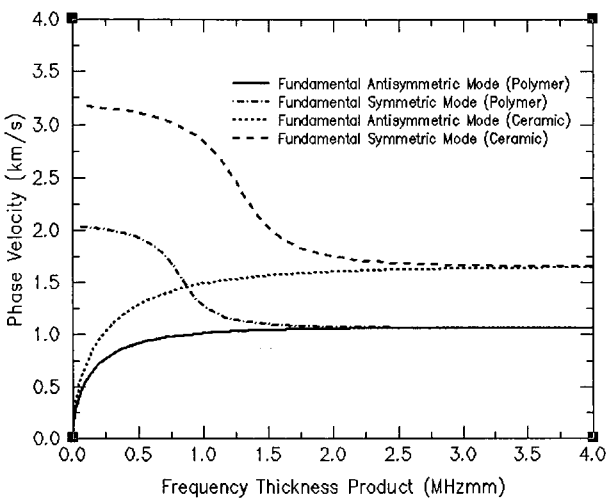

Figure 5.29 Dispersion Curves for Hardset Polymer and PZT-5H

The wavelength of a Lamb wave can therefore be expressed as

$$\lambda = \frac{v_{phase}}{f} \qquad \textbf{Eqn. 5.01}$$

where

λ is the Lamb wave wavelength

v_{phase} is the appropriate phase velocity

f is the operating frequency.

The phase velocity of a material can be determined, for any particular wavelength, by drawing a line of the form of Eqn. 5.02 on the dispersion curve.

$$v_{phase} = \lambda f \qquad \textbf{Eqn. 5.02}$$

The x-coordinate at which the line crosses the curve for each mode type (a_0 or s_0) is the FTP for that mode, while the y-coordinate is the phase velocity. Figure 5.30 demonstrates how this would be done for a 1mm thick hardset polymer plate, with ID finger spacing of 2 mm. This arrangement would result in an a_0 mode of frequency 455 kHz and phase velocity 889 ms^{-1}, and an s_0 mode at 800 kHz with a phase velocity of 1580 ms^{-1}.

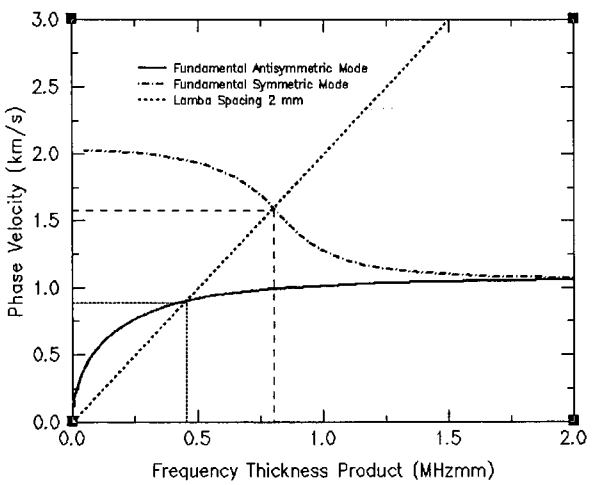

Figure 5.30 Determination of Mode Frequency and Phase Velocity

Since the wavelength is determined by the ID finger spacing (d_0 and $d_0/\sqrt{2}$), it is apparent that the first two mode frequencies generated by the Lamb modes will be

$$f_{L1} = \frac{v_{phase}}{d_0} \qquad f_{L2} = \frac{\sqrt{2}v_{phase}}{d_0} \qquad \textbf{Eqn. 5.03 (a) and (b)}$$

Rather than approaching the shear wave velocity of the medium, the phase velocity of the fundamental Lamb modes approaches the *Rayleigh* velocity at high values of FTP. An effective approximation for the Rayleigh wave velocity (v_R) can be found in Achenbach [80] and is expressed as

$$v_R = \frac{0.862 + 1.14\upsilon}{1+\upsilon} v_{shear} \qquad \textbf{Eqn. 5.04}$$

where υ is Poisson's ratio and v_{shear} is the shear velocity of the material. This gives a Rayleigh wave velocity of 1062 ms^{-1} for hardset epoxy.

If it is assumed that the longitudinal velocity in a 1-3 piezocomposite of extremely low volume fraction approaches the longitudinal velocity of sound in hardset polymer (v_L equals 2565 ms^{-1}), then for a transducer of thickness 1mm (d_T), Eqn. 5.05 gives the lowest possible thickness mode FTP as 1.283 MHzmm.

$$FTP = \frac{v_L}{2d_T} d_T = \frac{v_L}{2} \qquad \textbf{Eqn. 5.05}$$

As the frequency of the mode is proportional to the inverse of the thickness, then the FTP for that particular mode in that transducer will not change. Viewing Figure 5.29, it can be seen that at this FTP the phase velocities are 1120 ms^{-1} for the s_0 and 1023 ms^{-1} for the a_0 mode, within 5% of the Rayleigh velocity of 1062 ms^{-1}. Since all 1-3

composites with an AR of considerably less than 1 will have their inter-pillar resonances at frequencies higher than the thickness mode resonance, it appears that for these transducers an approximate velocity to be used in Lamb wave frequency calculation is the Rayleigh velocity. Only in composites where the pillar periodicity is significantly greater than the transducer thickness will this not be the case.

Since the phase velocities of the a_0 and s_0 Lamb waves at high FTPs are almost identical, it is unlikely that in most transducers they could be separated to be easily identified. To determine which mode type is responsible for the generation of the inter-pillar resonances, two sets of FE analyses were performed, the first simulating a 25% VF PZT-5H/Hardset transducer, thickness 1 mm, centre to centre pillar spacing 4 mm, and the second an identical transducer with the ceramic replaced by hardset polymer (effectively a plate of polymer). No electrical excitation was applied to the model, but rather a sinusoidal force of peak magnitude 1N was applied at the central node of each ceramic pillar (or the equivalent location on polymer). For each of these 'composites', three structural arrangements were used, as described by the model slices shown in Figure 5.31.

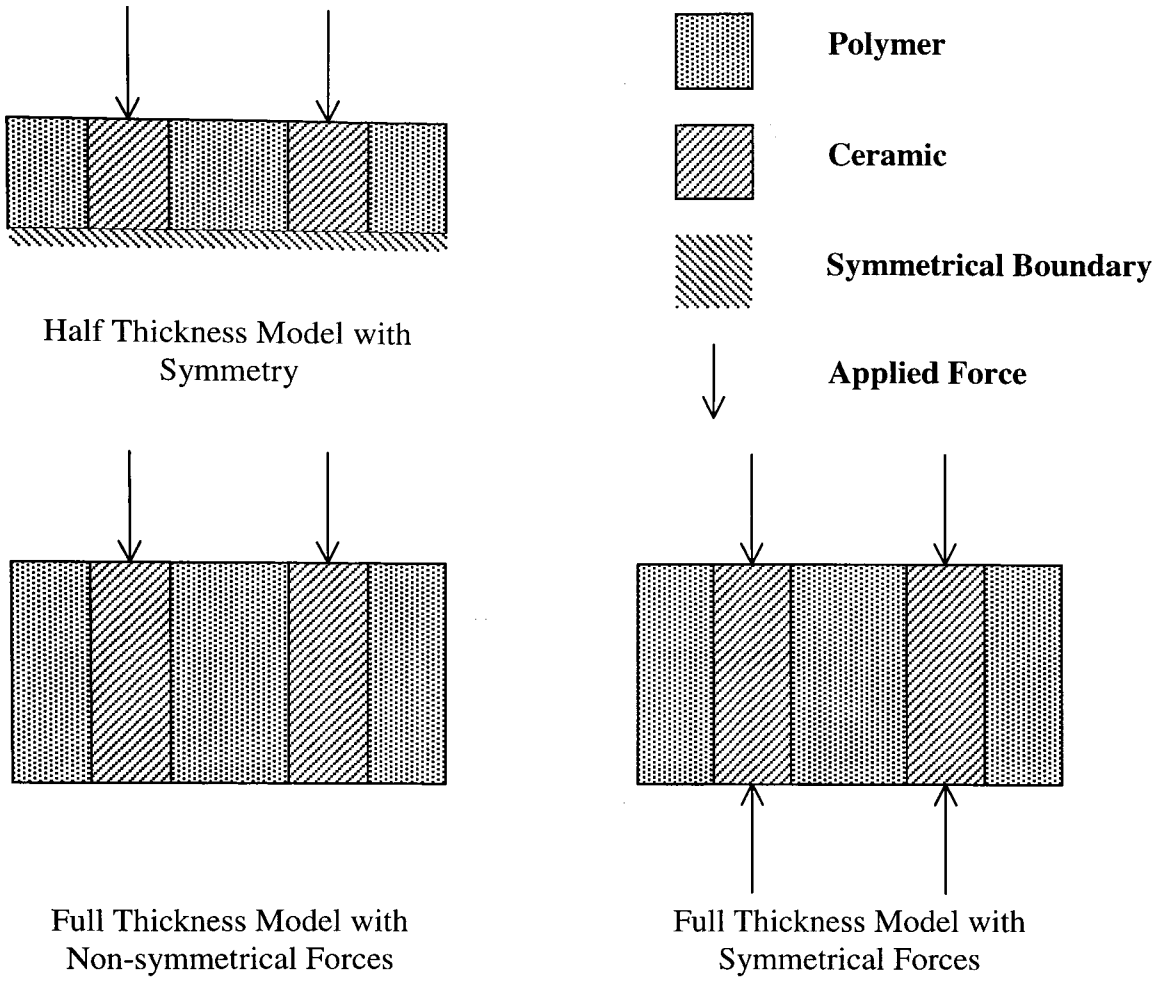

Figure 5.31 Modelling Arrangements for Lamb Wave Simulations

The half thickness model with symmetry was the model type used throughout this thesis to predict the behaviour of composite structures without matching in air. Since it has consistently provided excellent correlation with experimental results, it was believed that this model would provide accurate data for the prediction of Lamb wave frequencies. However, since the antisymmetrical mode cannot be sustained in a model using symmetry, two further FE models incorporating the full thickness of the device were analysed. The first of these new models provided force loading at both the upper and lower surfaces of the composite, with the forces of equal but opposite magnitude

to those on the alternate surface. This was the 'fully expanded' version of the half-thickness model, and was expected to produce identical results to the half thickness model. The final model also simulated the full thickness of the device, but provided loading at only the upper surface. While not a true reflection of any composite behaviour in air, this model would indicate the behaviour of a composite device when one surface is in contact with a load, backing or other solid medium. The 'polymer only' analyses were included to provide an exact match to the dispersion curves used to predict the modal frequencies.

The driving function should generate Lamb waves of wavelength corresponding to saw pitch (4 mm), and the distance between the pillar diagonals (2.84 mm). As can be seen from Figure 5.32, the a_0 and s_0 phase velocities are significantly separated in the frequency range of interest, and should therefore be easily differentiated. Should the a_0 mode be responsible for the inter-pillar activity, then strong modes should be detected at approximately 175 kHz and 280 kHz, while should the s_0 mode be responsible, the modes will be at 480 kHz and 640 kHz. By viewing a graph of average thickness direction displacement magnitude across the transducer surface against frequency, the frequencies of the strong modes can be easily determined. Figure 5.33 shows the results for the polymer only, half thickness with symmetry model in this format.

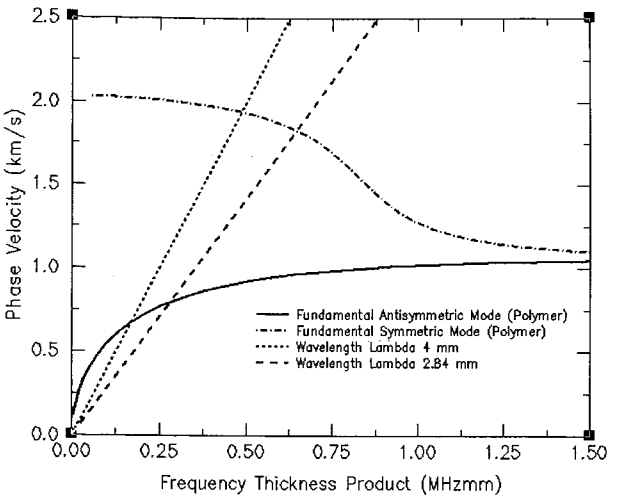

Figure 5.32 Prediction of Lamb Wave Frequencies using Dispersion Curves

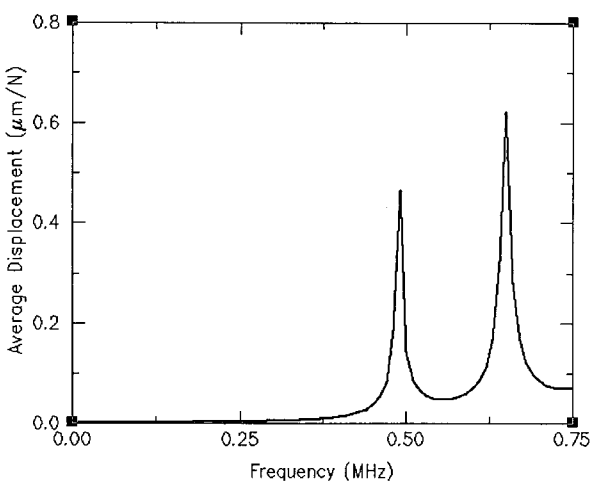

Figure 5.33 Average Surface Displacement in Polymer due to Lamb Waves

	Half Thickness Model with Symmetry	Full Thickness Model with Symmetrical Forces	Full Thickness Model with Non-symmetrical Forces
Polymer Only	490/640 kHz	490/640 kHz	180/290 kHz
Composite	600/790 kHz	600/790 kHz	180/310 kHz

Table 5.02 Mode Frequencies for FE Lamb Wave Simulations

Table 5.02 presents the results from the six FE models. In the both polymer only models with symmetry, strong modes were detected at 490 kHz and 640 kHz, indicating that in fact the symmetrical s_0 mode is responsible for the laterally resonant modes. This is to be expected in a model with no asymmetrical forces or structure. In the equivalent ceramic/polymer models the frequencies were found at 600 kHz and 790 kHz, the higher frequency indicating phase velocity has been increased by the addition of ceramic. In the model with non-symmetrical forcing functions, the modal frequencies were found to be 180 kHz and 290 kHz (composite results 180 kHz and 310 kHz), indicating that only under non-symmetrical conditions will the antisymmetrical Lamb wave be propagated in a composite. While this has implications for composites when attached to backing blocks and other components, the similar velocities of the s_0 and a_0 waves at large values of FTP ensure that the frequencies of the inter-pillar modes will be unchanged for the majority of transducers. The small change in frequencies between the polymer and composite models for the antisymmetrical case is likely due to the small difference between the a_0 phase velocities of ceramic and polymer at very low frequencies.

As final confirmation, another FE model was simulated, again using the 25% VF, 1mm thick, 4mm pitch transducer. In this case, the model included electrodes and was stimulated electrically, thus simulating a real piezocomposite transducer. The impedance profile can be seen in Figure 5.34. As can be seen, modes exist at 585 kHz and 725 kHz which are at similar frequencies to those in the previous composite Lamb wave model. The resonances at 810 kHz and 920 kHz are likely due to a higher order Lamb mode – this will be discussed later. It is evident that no resonances exist below 580 kHz, eliminating the a_0 mode and confirming the s_0 mode as the carrier of the inter-pillar resonance in 1-3 piezocomposites in air.

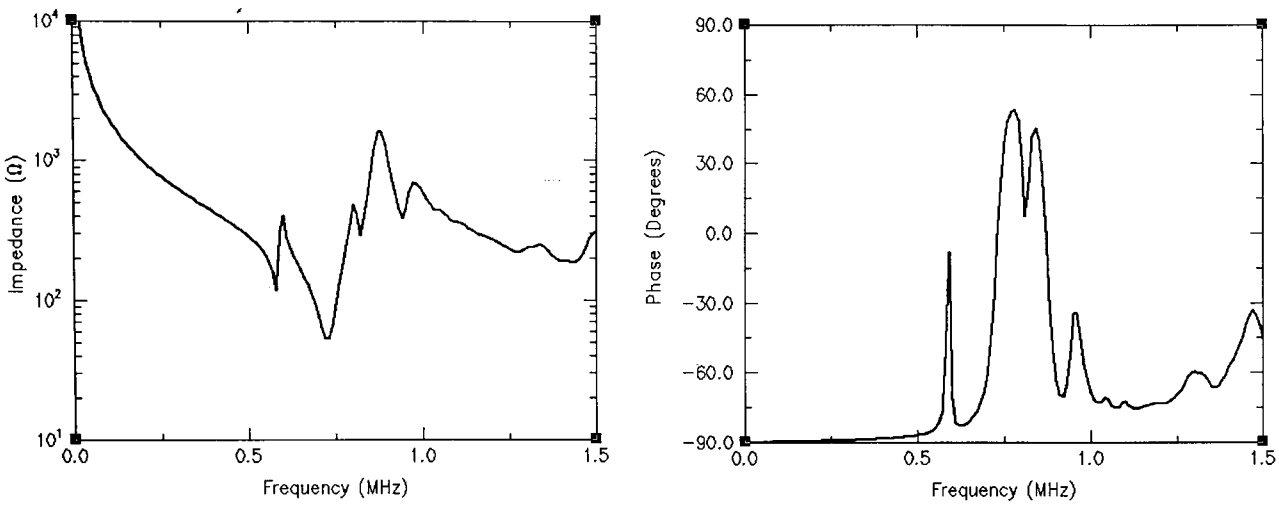

Figure 5.34 Impedance Profile of 25% VF, 1mm Thick, 4mm Saw Pitch PZT-5H/Hardset 1-3 Piezocomposite

5.2.5.2 Generation of Higher Frequency Modes by Lamb Waves

It appears from Figure 5.34 that higher frequency modes exist in a 1-3 composite beyond the first two resonances already discussed. While it is beyond the scope of this thesis to analyse all the resonances in such composites, a brief discussion of the possible form they would take is relevant.

Lamb wave generation relies upon the forcing of a surface at points corresponding to wavelength spacing, and not on the formation of a standing wave within a cavity, as occurs in the thickness mode. It is therefore impossible for harmonics of an inter-pillar mode to exist, as there are no surfaces at which wave reflection or phase inversion can occur. There are two possible explanations for the formation of higher frequency modes.

Firstly, it may be possible for a Lamb wave to consist of 2 (or any whole number of) wavelengths between each ID finger. Figure 5.35 shows how this may be possible.

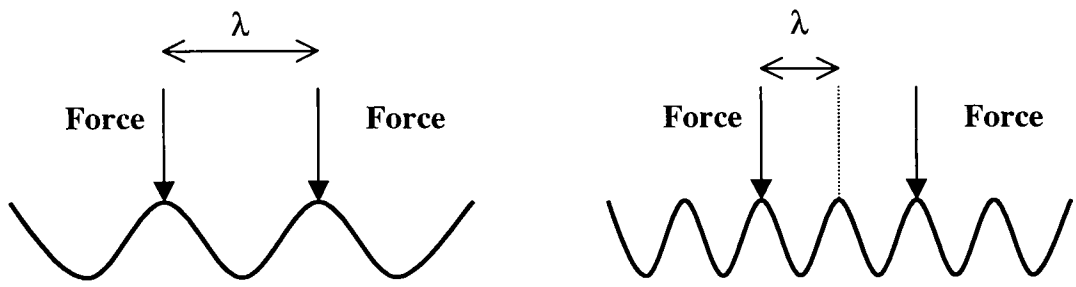

Figure 5.35 Generation of Higher Frequency Modes by Lamb Waves

While at first this may seem reasonable, it is most likely that, as shown in Figure 5.35, there will be insufficient force applied to sustain such a mode, as there is an ID finger 'missing'. As the number of wavelengths between the points of force application increase, the likelihood of a mode existing decreases. An alternative explanation must therefore be found.

Figure 5.36 shows the dispersion curves for a hardsetting polymer, including all higher order symmetrical and antisymmetrical modes up to the fourth and third respectively. As can be seen, for a given wavelength spacing it is possible for a large number of modes to exist. It is likely that these modes would be responsible for any higher frequency inter-pillar modes encountered in a 1-3 composite. This is recommended as a topic for further study.

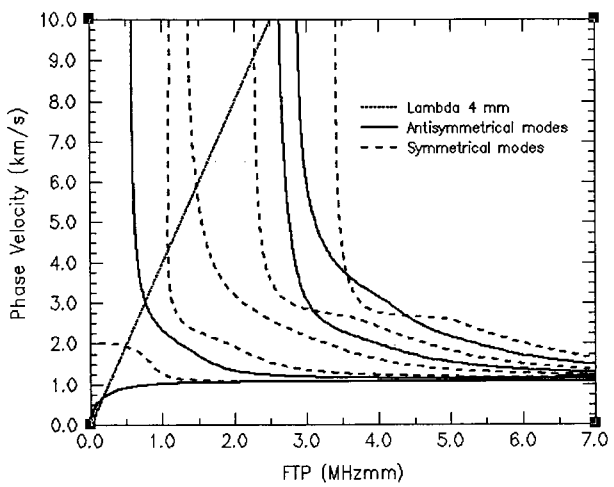

Figure 5.36 High Order Lamb Wave Dispersion Curves

5.2.5.3 Phase Velocity of Piezocomposites

All discussion has so far assumed that the plate through which the Lamb wave propagates is a single material, such as polymer. The very nature of 1-3 composites, however, ensures that there will always be an additional material, ceramic, to a greater or lesser extent. It is therefore likely that the phase velocity of a particular Lamb wave in a composite will alter with volume fraction, rendering the prediction of Lamb wave frequency by Equations 5.03 (a) and (b) inaccurate due to poor phase velocity data. To determine how this velocity varies with VF suggestion, a number of FE simulations were carried out. Using the half thickness with symmetry model shown in Figure 5.31, a 1 mm thick, 0.73 mm saw pitch 1-3 piezocomposite was modelled. A one Newton sinusoidal point force was applied at the centre of each ceramic pillar, and the structure was analysed across a range of frequencies, and the first two Lamb modes obtained. A number of simulations were carried out at various volume fractions to obtain the full range of results. The 0.73 mm saw pitch (d_0) ensured that the modes encountered would have a phase velocity approaching the Rayleigh velocity for the material. Table 5.03 gives the results for the various simulations, with 0% VF indicating pure polymer. Equations 5.03 (a) and (b) then used the two inter-pillar resonance frequencies, f_{L1} and $f_{L2,}$ to calculate the phase velocities, v_{pfl1} and v_{pfl2}, and then an average phase velocity v_{pav} calculated.

It appears that the phase velocity does not increase significantly at the lower volume fractions, but then rapidly increases when the VF passes 50%. As the phase velocities of the Lamb waves will approach the Rayleigh wave velocity for polymer and ceramic at 0% and 100% VF respectively, the phase velocity of a composite may be a function of the square of the VF.

VF (%)	f_{L1} (kHz)	f_{L2} (kHz)	v_{pfl1} (ms^{-1})	v_{pfl2} (ms^{-1})	v_{pav} (ms^{-1})
0	1510	2110	1102	1092	1097
20	1520	2195	1110	1136	1123
35	1720	2310	1256	1196	1226
50	1850	2210	1351	1144	1247
75	1910	2620	1394	1356	1375
90	1782	2832	1301	1466	1384

Table 5.03 Variation of Phase Velocity with Volume Fraction

If this were to be the case, the phase velocity of the composite material would be

$$v_{phase} = v_{RPOLY} + (VF^2)(v_{RCER} - v_{RPOLY}) \qquad \textbf{Eqn. 5.06}$$

where

v_{RPOLY} is the Rayleigh wave velocity in the polymer

v_{RCER} is the Rayleigh wave velocity in the ceramic

VF is the ceramic volume fraction, ranging from 0 to 1.

Given that the Poisson's ratio of PZT-5H is 0.293, and the shear velocity is 1751 ms^{-1}, the Rayleigh wave velocity in PZT-5H using Eqn. 5.04 is 1619 ms^{-1}. Figure 5.37 plots the phase velocity results from Table 5.03, and the results using Equation 5.06 against volume fraction. While not an exact match, there is strong correlation between the two sets of results.

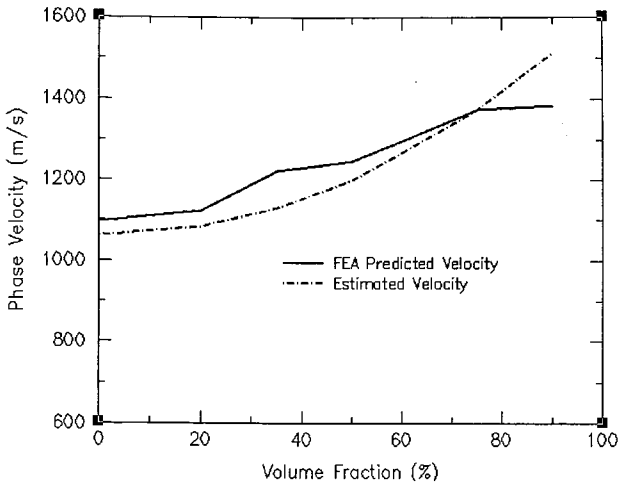

Figure 5.37 Phase Velocities in 1-3 Piezocomposites

Equation 5.06 is intended as a method of estimating the phase velocities in composites with large FTPs, by assuming that the composite behaves as a homogenous medium. It is recommended that further work in this area should develop a range of appropriate dispersion curves for the various volume fractions.

To further test this proposed Lamb wave theory, an additional two 1-3 composite transducers were tested, with particular attention paid to the first two inter-pillar resonances.

5.2.6 Analysis of Composite 13D in Air

The next transducer to be studied was 13D, identical to 13B in all respects except thickness. This transducer was thinner at 1.4 mm (as opposed to 2.5 mm), resulting in an AR of 0.31, slightly greater than the MPAR of 0.27. This configuration was expected to give a transducer with inter-pillar modes impinging upon the thickness mode, resulting in non-uniform behaviour at electrical resonance. The experimental impedance profile and the FEA prediction are shown in Figure 5.38, and again show excellent correlation.

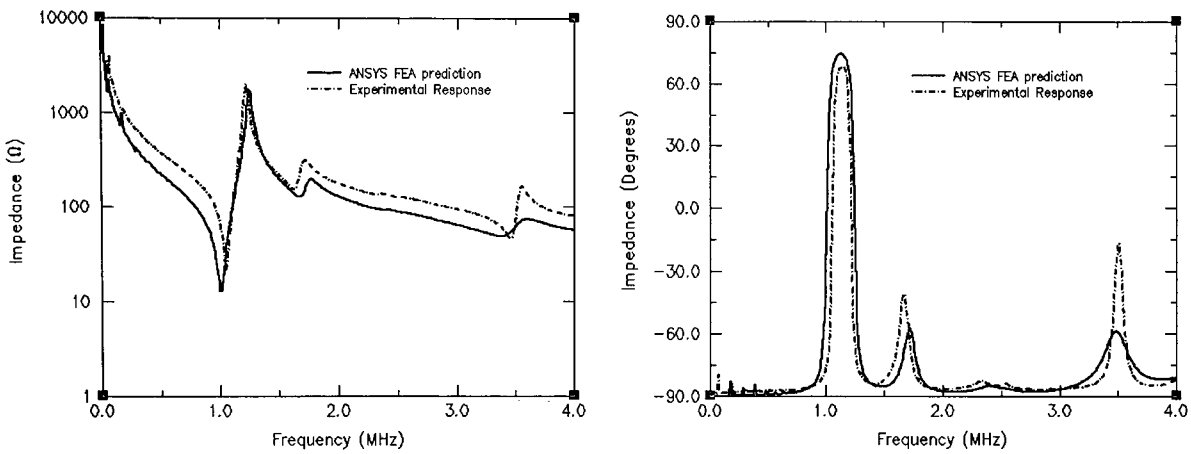

Figure 5.38 Impedance Profile of Composite 13D

While the FE model accurately predicts the resonant mode frequencies, the impedance magnitude is predicted as slightly lower than is found in practice across most of the frequency range, and is again due to the limited damping models available within ANSYS, which are not capable of accurately predicting damping across a frequency range as wide as 4 MHz. The main thickness mode resonance is found to occur at 1041 kHz, with a inter-pillar mode occurring at 1620 kHz, a weak resonance at 2400 kHz, and the thickness mode third harmonic at 3457 kHz. Bragg scattering theory

would place the first and second inter-pillar resonances at 1551 kHz and 2186 kHz, while the Lamb wave model, assuming the ceramic has no effect upon phase velocity, would result in frequencies of 1455 kHz and 2051 kHz. Using Equation 5.06 to estimate the phase velocity in the composite as 1130 ms^{-1} results in frequencies of 1548 kHz and 2183 kHz. It appears that for this transducer, the Lamb wave theory produces almost identical numerical results to Bragg scattering, despite the different mechanisms proposed in each.

An FE simulation of composite 13D under sinusoidal point loading indicates that the modes should appear at 1700 kHz and 2330 kHz, extremely close to those predicted by Equations 5.03 and 5.06.

By their very nature, the wavelength of the inter-pillar modes matches the periodicity of the transducer. At these wavelengths, it is possible that the composite will fail to act as a homogenous medium to the Lamb waves, and consequently this will be a possible source of error in phase velocity estimation.

The experimental SDP of 13D is shown in Figure 5.39, with an expanded experimental result, the FEA prediction, and comparison of theory and experiment as slices, in Figures 5.40 to 5.43

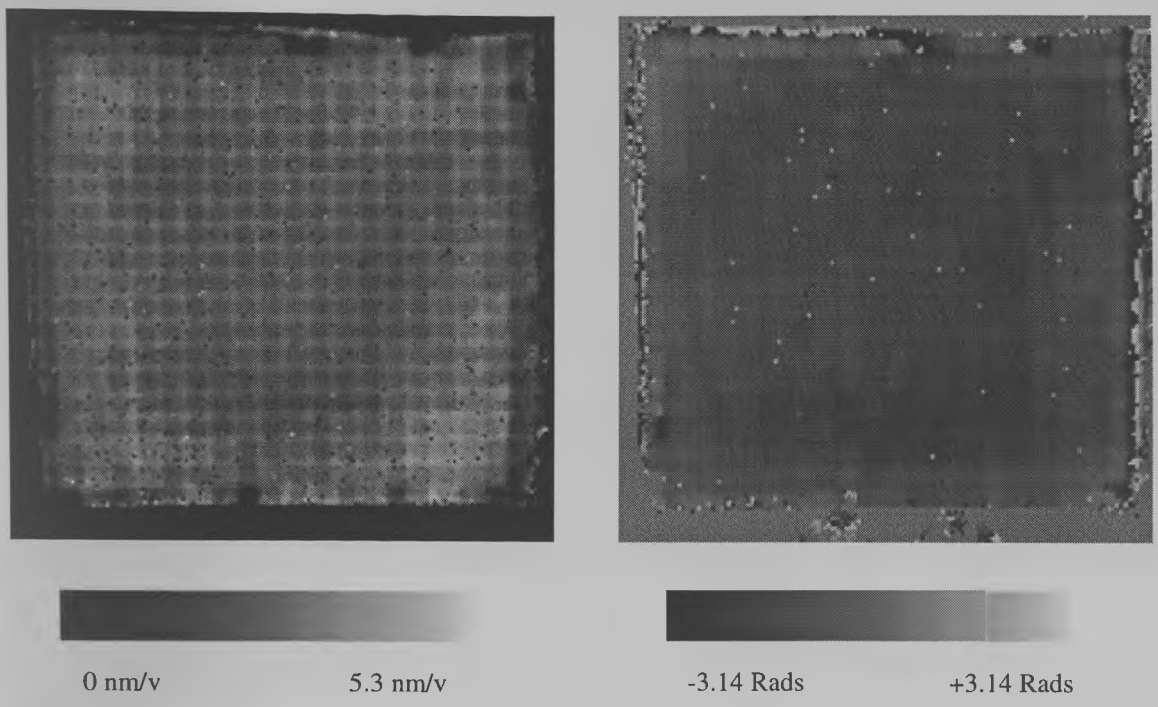

Figure 5.39 Experimental SDP at 1041 kHz of Composite 13D

The SDP is very similar to the thickness mode resonance in transducer 13C with the polymer surrounding the ceramic displacing by a greater quantity, although in this case it is apparent that the polymer is displacing by a greater quantity (5.3 nm/v in 13D as opposed to 2.8 nm/v in 13C), although greater displacement is expected in a transducer of higher VF. It is apparent that as the inter-pillar modes in a composite approach the frequency of the thickness mode, the large thickness mode displacements induce strong inter-pillar modes, and consequently less energy is available for thickness mode operation. This can result in the polymer displacing independently from the ceramic, with greater magnitude of displacement, and therefore extremely non-uniform surface displacements will occur.

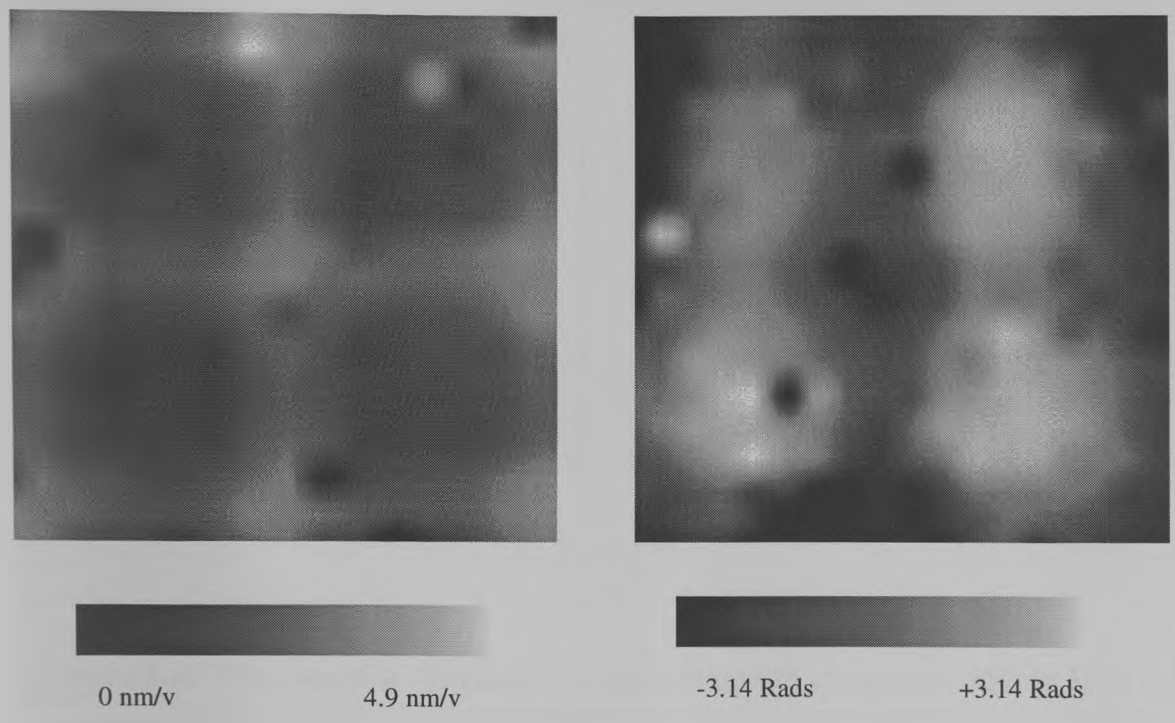

Figure 5.40 Experimental SDP at 1041 kHz for Composite 13D (Zoom)

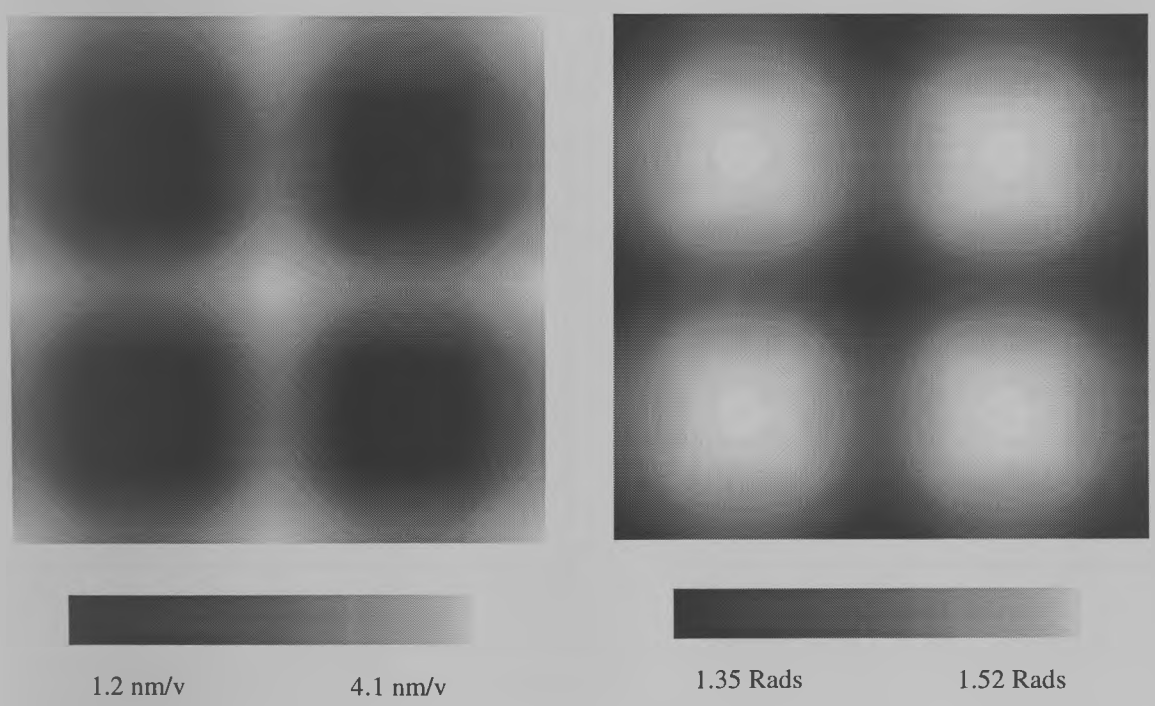

Figure 5.41 FEA SDP at 998 kHz for Composite 13D (Zoom)

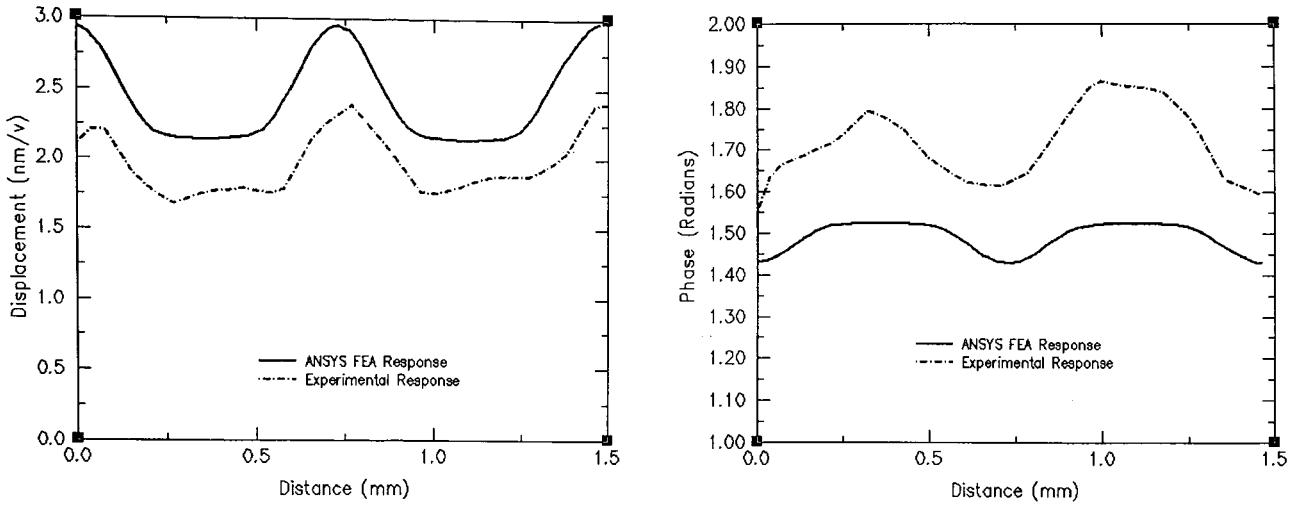

Figure 5.42 Cross-section Through Ceramic Pillars in Composite 13D at 1041 kHz

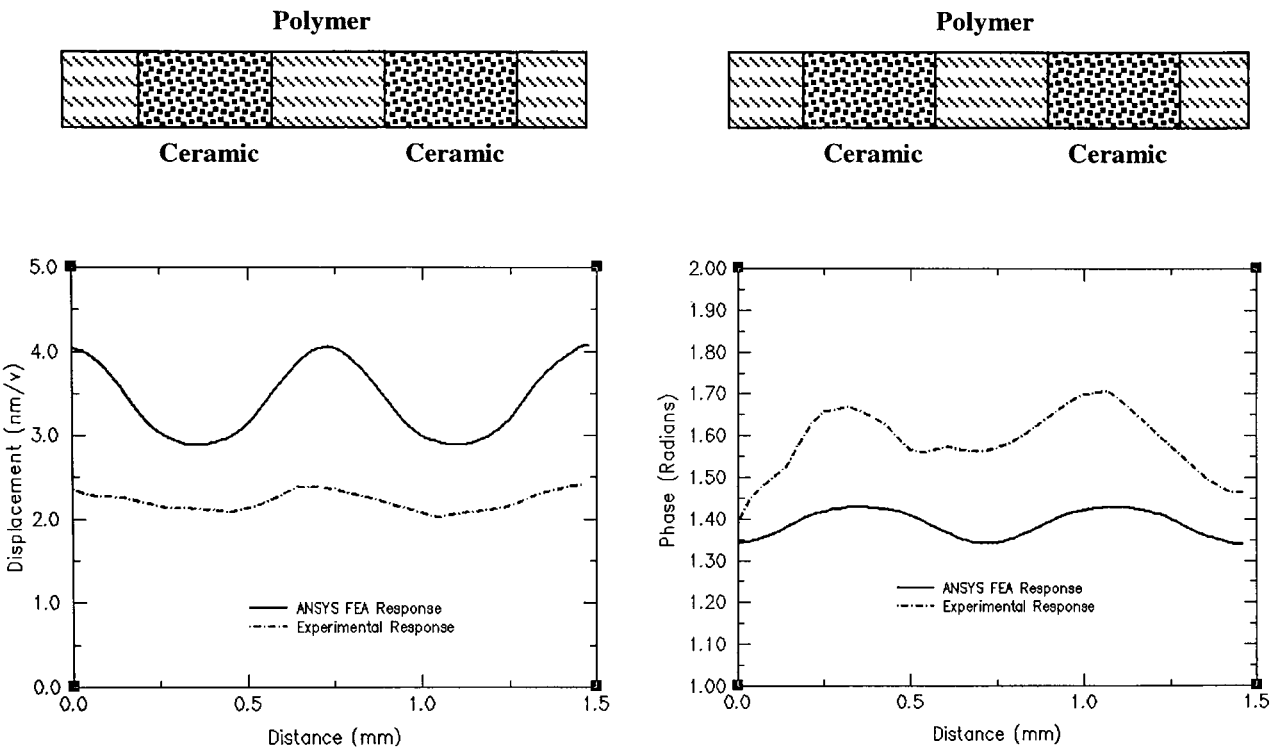

Figure 5.43 Cross-section Through Polymer in Composite 13D at 1041 kHz

Continuing the comparison between 13C and 13D, it would be expected that at 1620 kHz, the first inter-pillar mode would result in a similar SDP to that shown in Figure 5.21. The experimental response at this frequency is shown in Figure 5.44, and the zoomed section, the FEA equivalent, and comparative slices are shown as Figures 5.45 to 5.48.

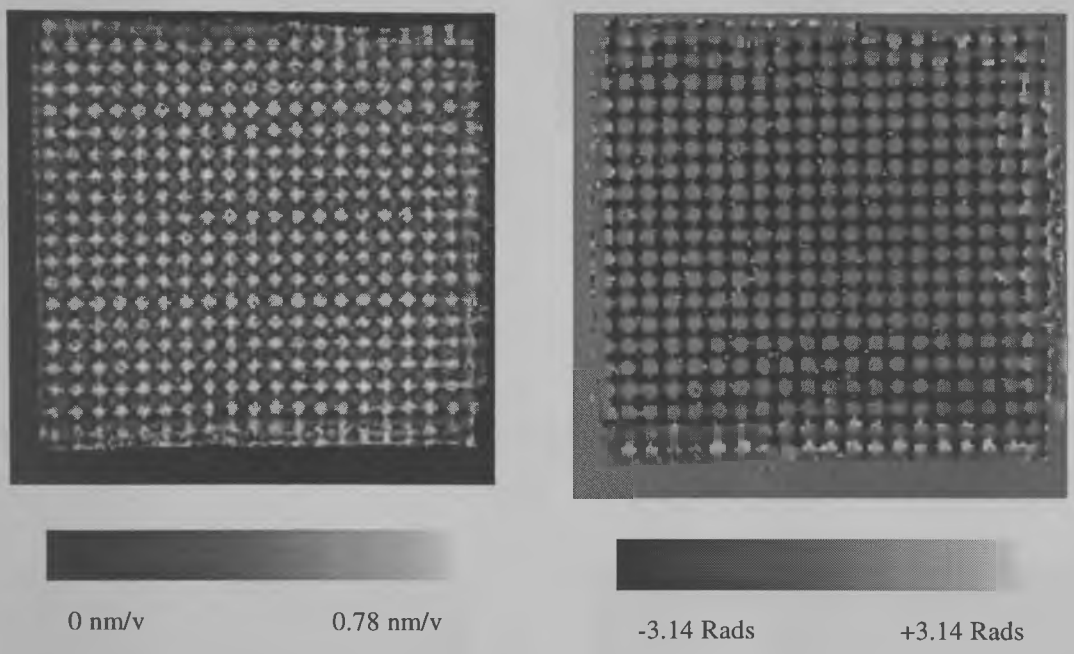

Figure 5.44 Experimental SDP at 1620 kHz for Composite 13D

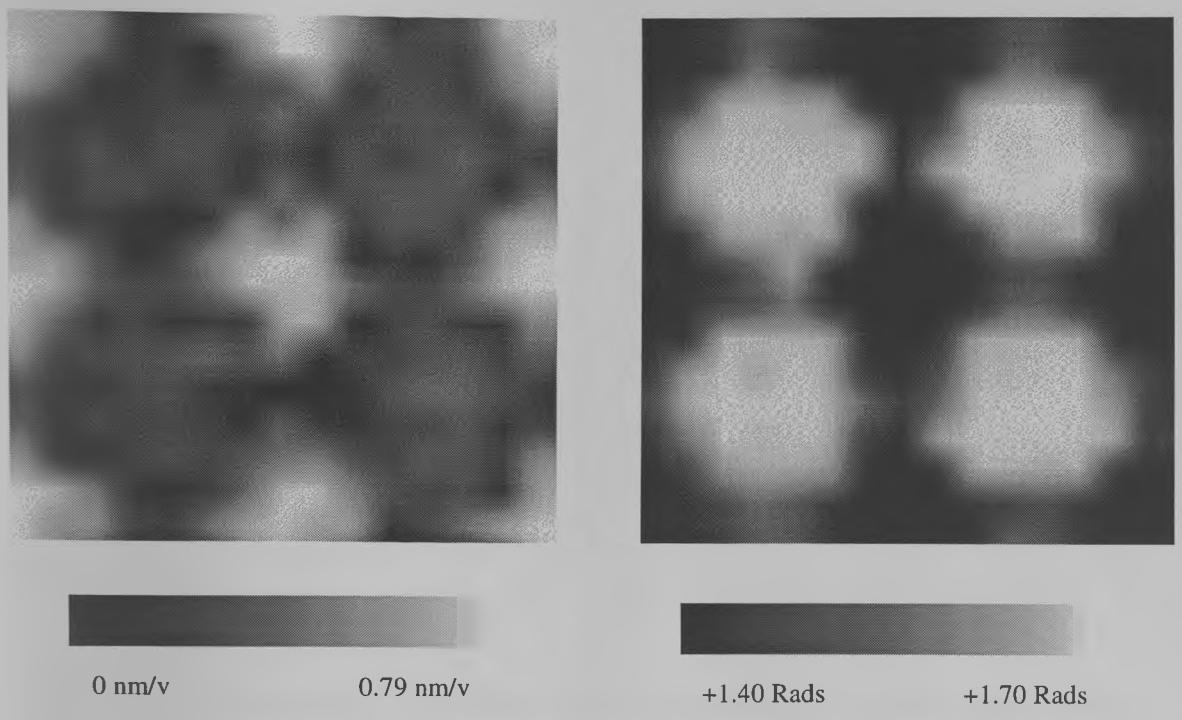

Figure 5.45 Experimental SDP at 1620 kHz for Composite 13D (Zoom)

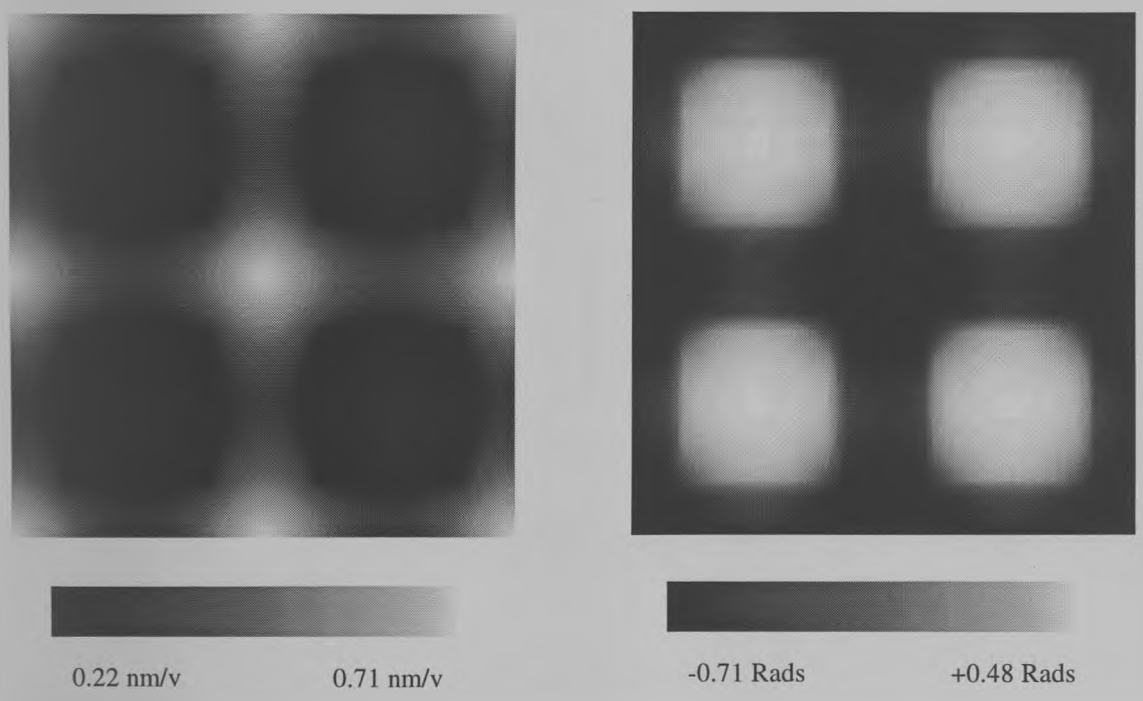

Figure 5.46 FEA SDP at 1671 kHz for Composite 13D (Zoom)

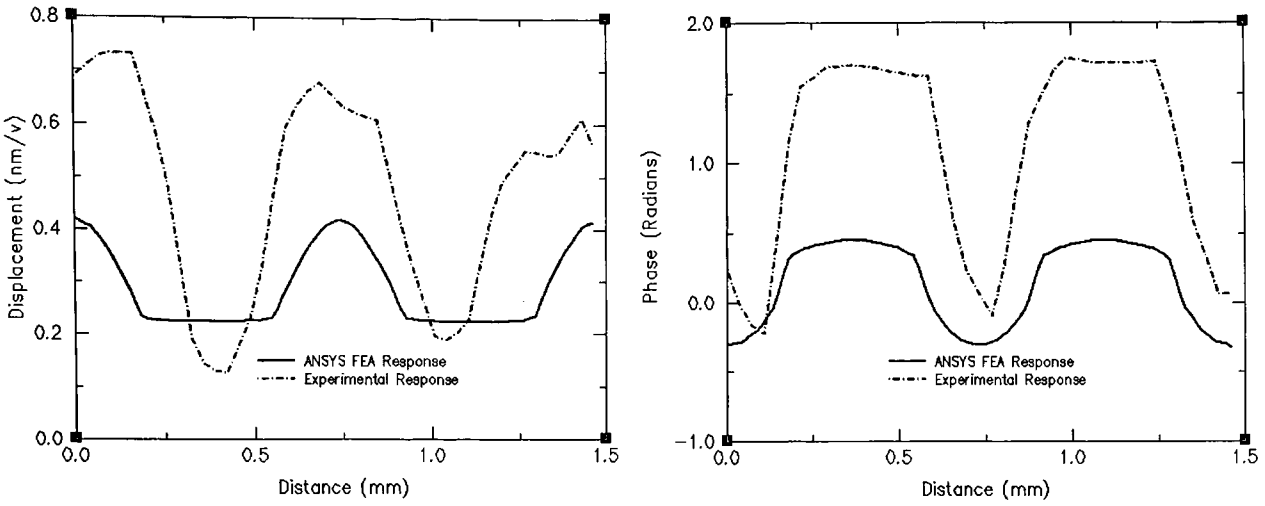

Figure 5.47 Cross-section Through Ceramic Pillars in Composite 13D at 1620 kHz

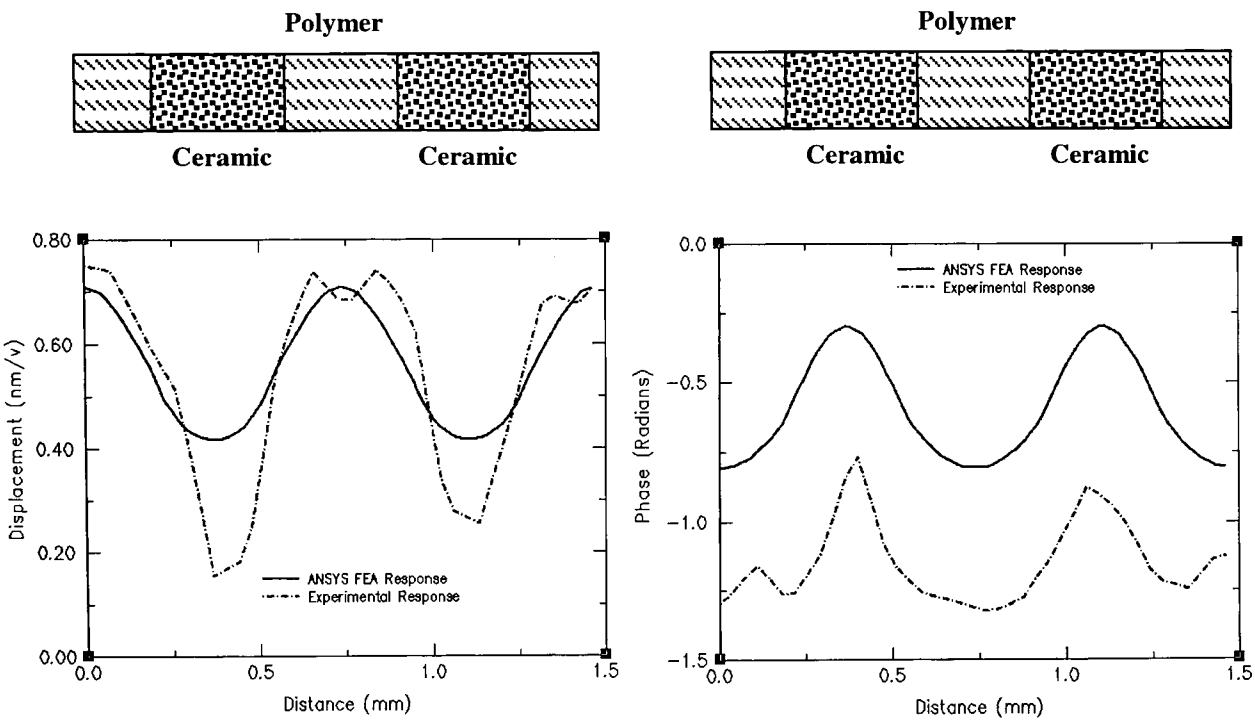

Figure 5.48 Cross-section Through Polymer in Composite 13D at 1620 kHz

The surface displacement at this frequency is similar in nature to that exhibited in transducer 13C, with the maximum displacement magnitude between the ceramic pillar diagonals. The phase diagram details all ceramic pillars in grey, moving in phase, with the polymer (black) moving entirely in phase despite differences in displacement magnitude. While not as accurate as previous modelling, the FEA still shows excellent correlation with experiment, showing all major trends and surface displacement characteristics. Magnitude of displacement is small, at around 0.8 nm/v, but the difference between polymer and ceramic displacement is clear.

5.2.7 Analysis of Composite 13E in Air

Given that the AR of 13E is 0.43, and that the MPAR is 0.27, it is likely that there will be at least one inter-pillar mode impinging upon the thickness mode. Experimental and FEA impedance plots are presented as Figure 5.49, and detail two inter-pillar modes at 1722 kHz and 2301 kHz, close to the fundamental thickness mode at 1424 kHz.

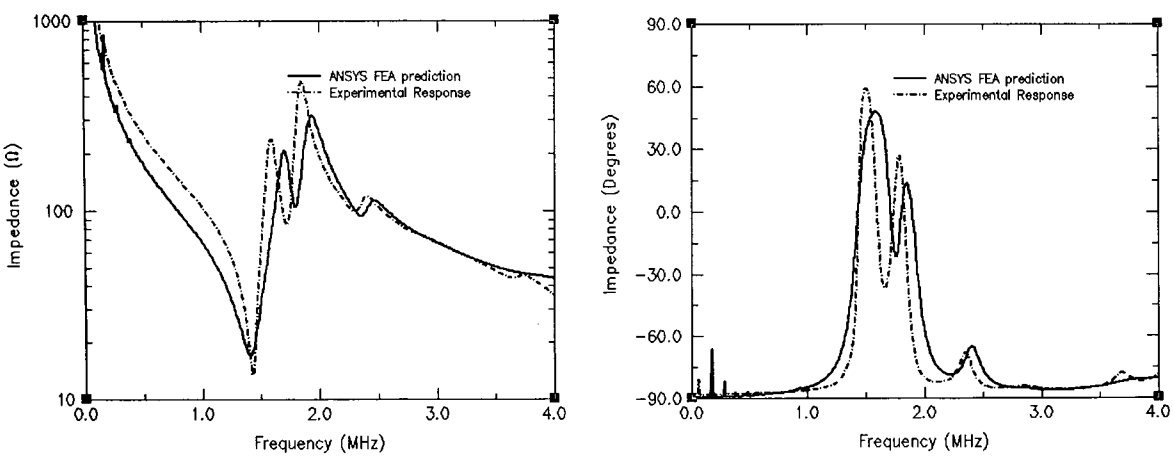

Figure 5.49 Impedance Profiles for Composite 13E

Bragg scattering predicts the first two inter-pillar resonances for this transducer to occur at 1551 kHz and 2186 kHz. The Lamb wave 'polymer only' theory indicates 1455 kHz and 2051 kHz, while inclusion of the VF effect upon phase velocity alters these to 1548 kHz and 2183 kHz. Again the Lamb wave theory produces similar results to Bragg scattering, as does the FE point force Lamb wave model, giving 1720 kHz and 2310 kHz as the first two inter-pillar resonances.

While it is clear that FEA has correctly predicted the frequency of the thickness and second inter-pillar modes, as well as the magnitudes of the three modes, the first inter-pillar mode is nearly 10% removed from the experimental values. While this is clearly the least accurate of the FEA simulations for the 1-3 composites, it should be remembered that the material properties of the ceramic are stated by the manufacturer to be accurate to within 10% and the attempt to obtain accurate damping across such a frequency range will limit modelling effectiveness. Any modelling that matches to within 10% of experiment under such conditions should be considered successful.

The surface displacement profile at thickness mode electrical resonance was obtained experimentally, and is presented as Figure 5.50. Due to the obvious similarities with the thickness mode displacement in composites 13C and 13D, and for space considerations, no expanded or FEA results are presented for this frequency.

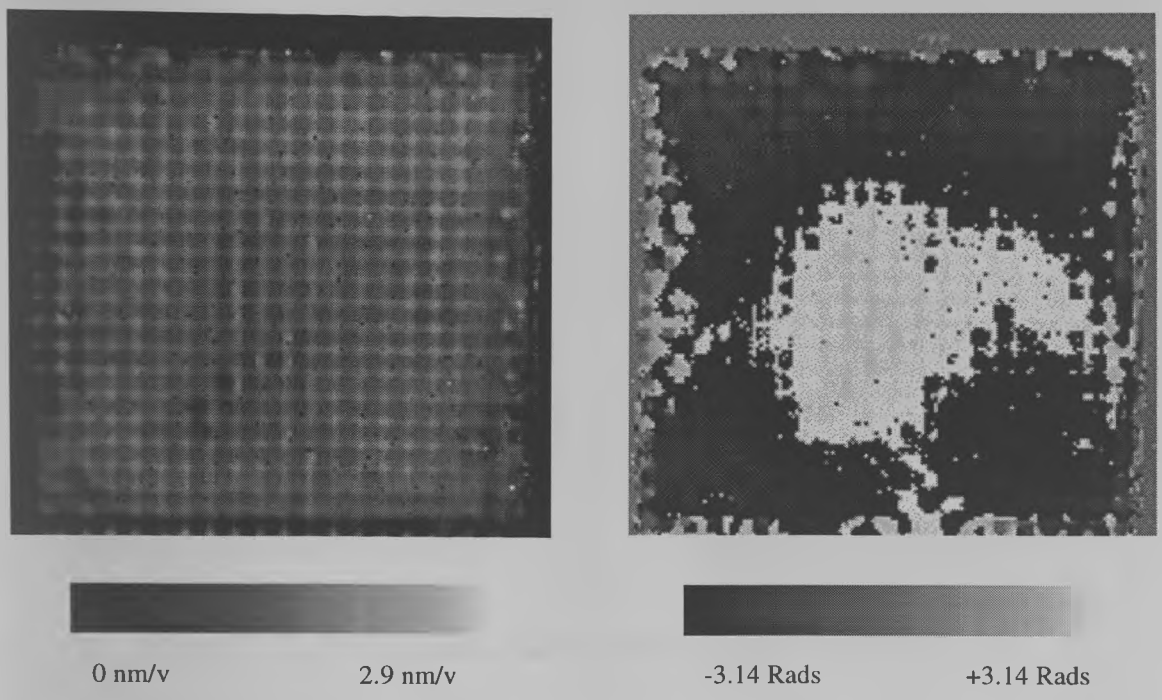

Figure 5.50 Experimental SDP at 1424 kHz for Composite 13E

Like composites 13C and 13D, the SDP at thickness mode electrical resonance is expected to consist of polymer displacing by a greater quantity than ceramic, exactly what is seen experimentally in Figure 5.50. This figure clearly shows the polymer on the diagonal displaces more than the neighbouring polymer.

While the phase appears to shift dramatically at the centre of the device, it must be remembered that this is merely the phase crossing the $\pm\pi$ boundary. The magnitude of displacement is nearly identical to that of 13C at electrical resonance.

It is expected that the first inter-pillar resonance mode shape should be of a similar nature to that found in composites 13C and 13D. This is exactly what is found experimentally, and is shown as Figure 5.51.

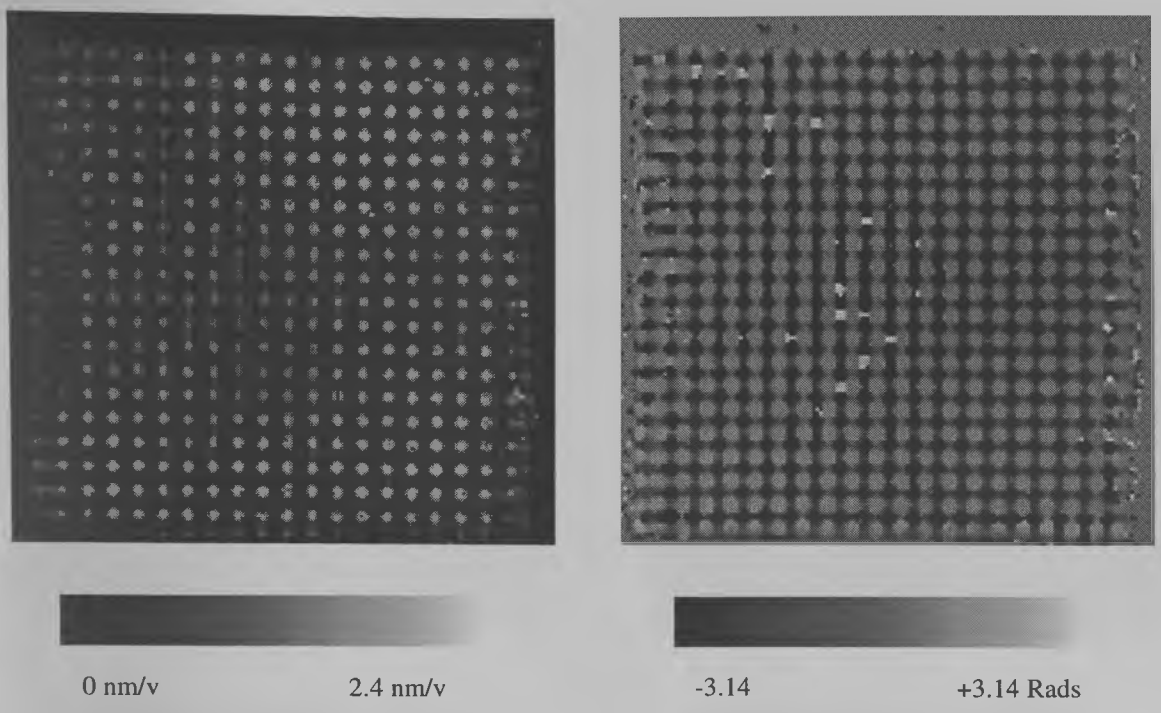

Figure 5.51 Experimental SDP at 1722 kHz for Composite 13E

An enlarged section of the experimental response, and the FEA equivalent response for this frequency are shown as Figures 5.52 and 5.53, and show good correlation. As the mode shape is similar to that seen in previous composites, no slices through the composite are provided for space considerations.

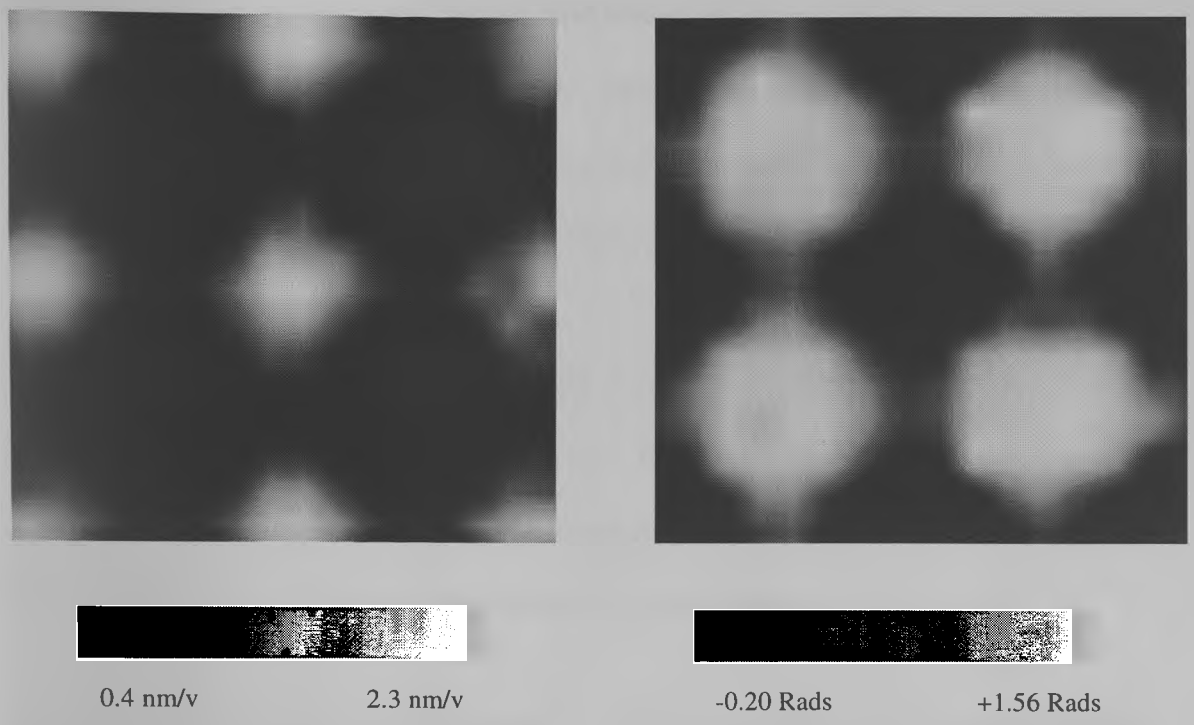

Figure 5.52 Experimental SDP at 1722 kHz for Composite 13E (Zoom)

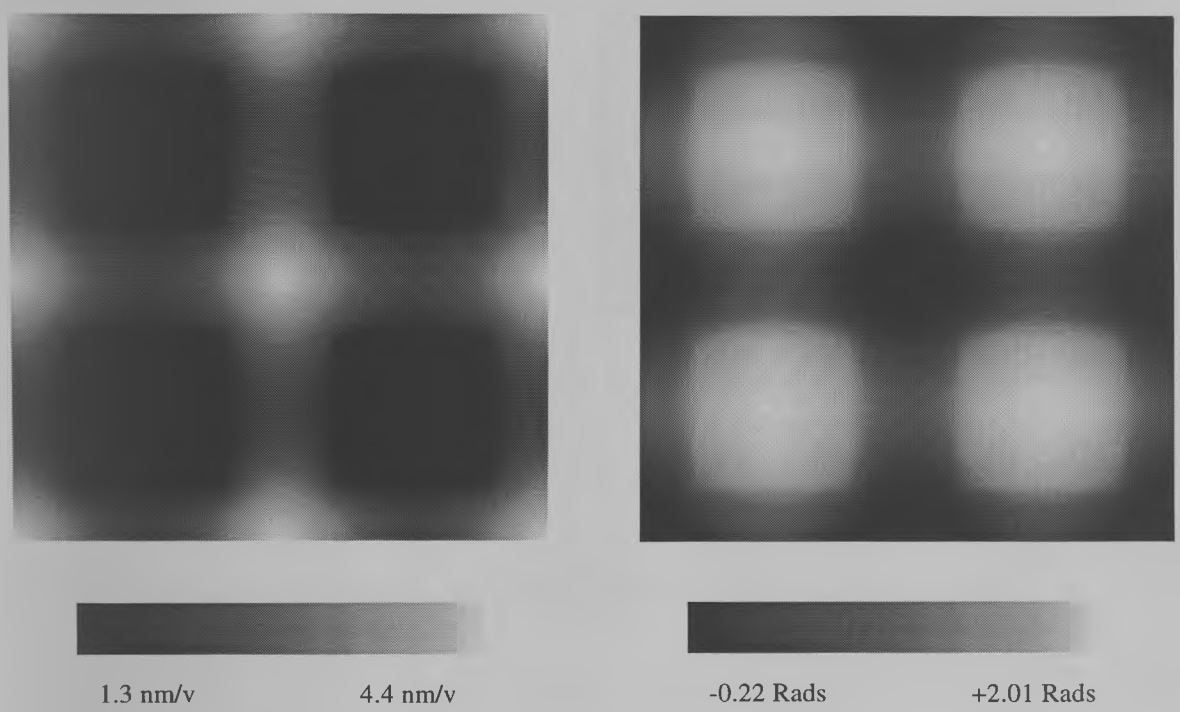

Figure 5.53 FEA SDP at 1790 kHz for Composite 13E (Zoom)

It is clear that the mode shapes for the first inter-pillar resonance of a 1-3 composite transducer can be viewed experimentally, and compared to a FEA response with excellent correlation. Composite 13E offers the opportunity to view a strong second inter-pillar resonance, appearing experimentally at 2301 kHz.

Figure 5.54 shows the surface displacement profile for the entire composite 13E, and is clearly a highly complex pattern with very fine detail. More than in the previous composites, the enlarged sections, FEA response, and comparative slices of Figures 5.55 to 5.58 are needed for understanding of the mode shape.

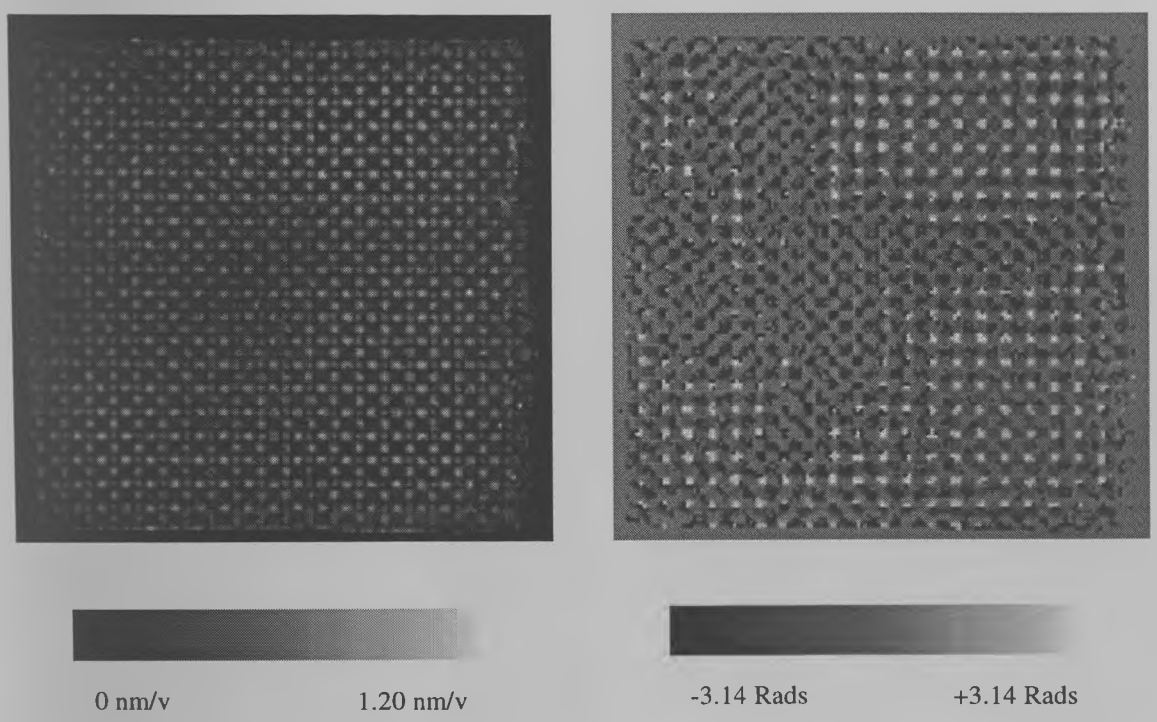

Figure 5.54 Experimental SDP at 2301 kHz for Composite 13E

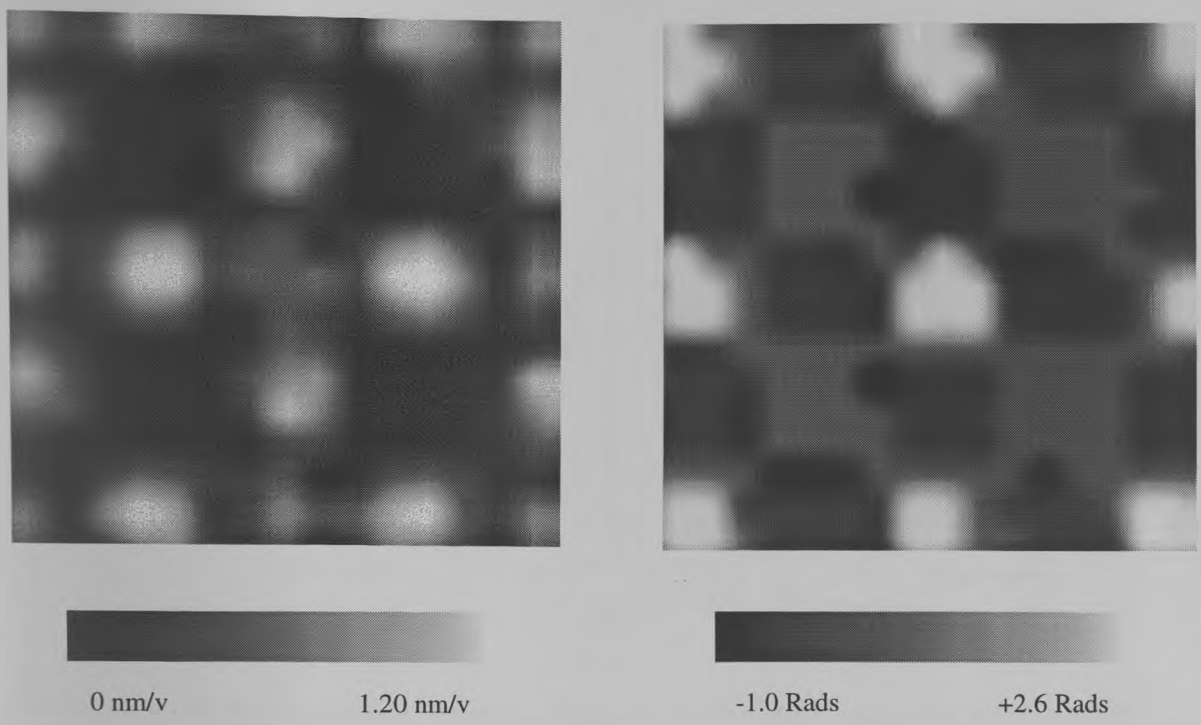

Figure 5.55 Experimental SDP at 2301 kHz for Composite 13E (Zoom)

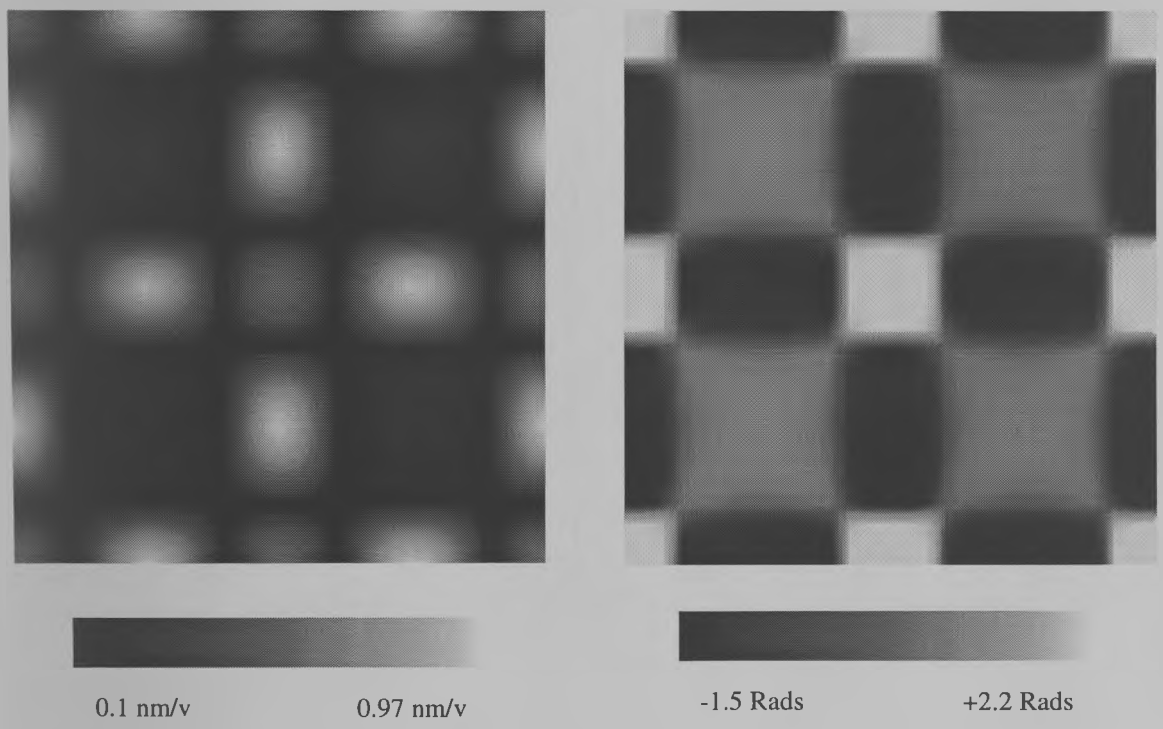

Figure 5.56 FEA SDP at 2341 kHz for Composite 13E (Zoom)

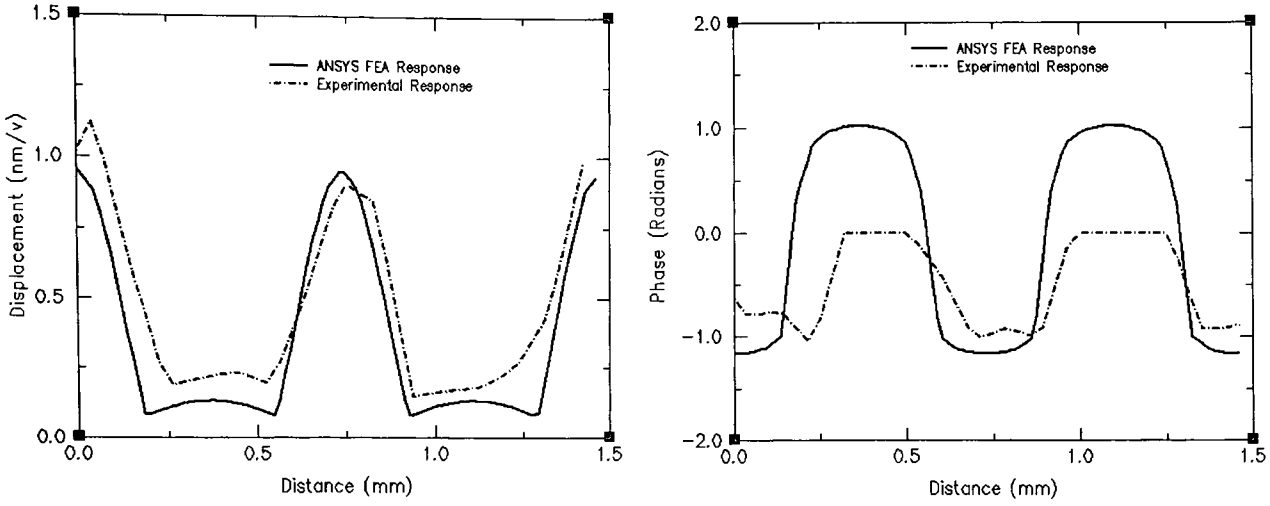

Figure 5.57 Cross-section Through Ceramic Pillars in Composite 13E at 2301 kHz

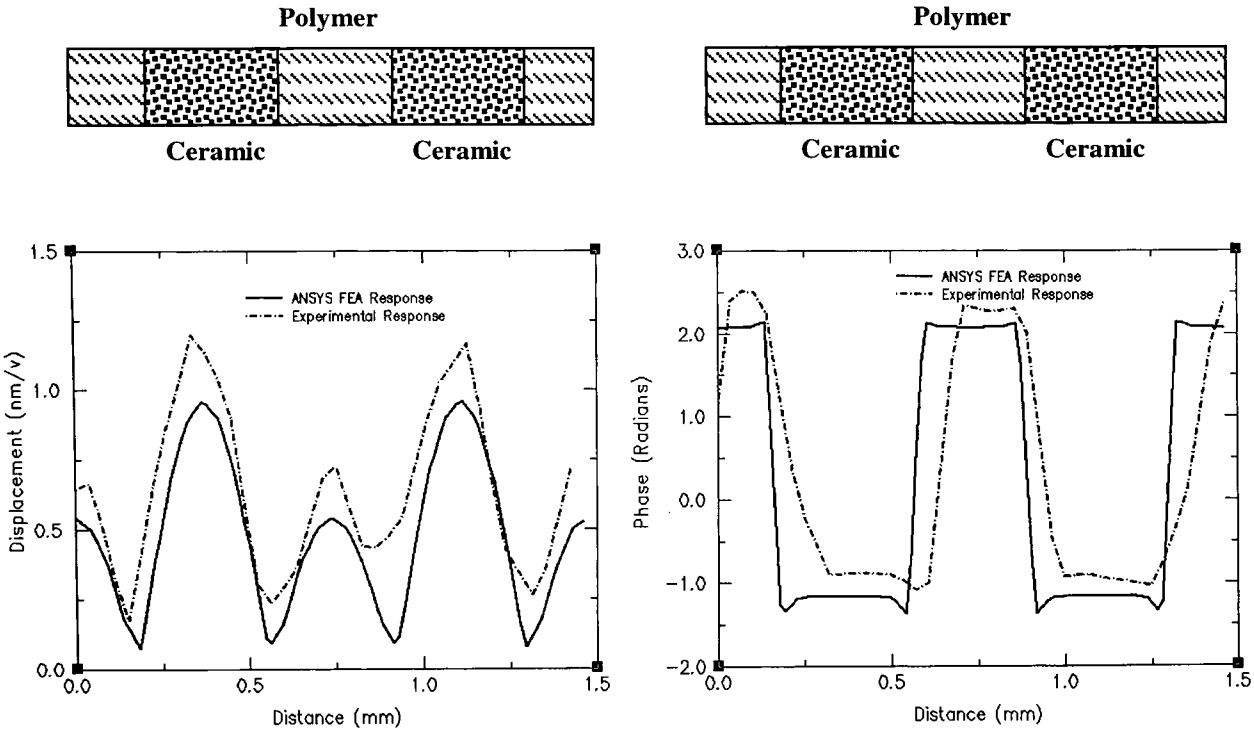

Figure 5.58 Cross-section Through Polymer in Composite 13E at 2301 kHz

Once again excellent correlation between modelling and experiment can be observed. Should the Lamb wave model be correct, it is expected that the displacement should take a mode shape along the diagonals of the composite.

It is evident that there is a resonance along the diagonals of this composite. Along the diagonals (as indicated by Figure 5.28) there is significant displacement all in phase, while on a diagonal at a distance of $d_0/2\sqrt{2}$, which should correspond to a half wavelength of a Lamb mode, the displacement is completely anti-phase to the first diagonal. The displacement on the diagonal including ceramic is less than that along the diagonal that is solely polymer, even on the polymer itself. This is likely due to the stiffer ceramic on the diagonal restricting motion. In addition, the magnitude of displacement in this mode is small in comparison to the other modes in this composite, and consequently would contribute little to the overall response when excited with a broadband impulse.

5.2.8 Generation of Lamb Waves in Piezocomposite Plates

At this stage, it has been demonstrated that the finite element model can accurately predict the frequencies and mode shapes of 1-3 composite resonances, and that these mode shapes have the potential to have been generated by Lamb waves. In order to verify that these modes are indeed produced by Lamb waves, additional finite element models were run to demonstrate the viability of this theory.

In a similar manner to the models used in section 5.2.5.1, the first model to be run was almost identical in structural parameters to composite 13E. The ceramic/polymer

structure of the composite was left as before, and no voltage coupling was applied to the surfaces, but rather the driving force applied was a sinusoidal force of peak amplitude 1 N at the centre of each ceramic pillar, normal to the surface, and applied at a single node. Theory indicates that strong modes should occur at wavelengths corresponding to pillar spacing. Symmetrical boundary conditions ensured that an equal but opposing force was applied on the opposite side of the transducer. A harmonic analysis was performed across a wide frequency range (0 to 4 MHz) and the first two strong modes examined. It is of interest to note that the maximum value of displacement at what would normally be the thickness mode resonance was typically at least two orders of magnitude smaller than in strongly coupled modes. The second model to be run was identical to the first, except that all ceramic material was replaced by polymer – that is, the model consisted entirely of a plate of solid polymer. Results for both cases are presented as Figures 5.59 to 5.70.

Comparing Figures 5.59 and 5.60 to Figures 5.45 and 5.46, and their appropriate slices, it can be seen that the first inter-pillar mode shapes are identical. There is excellent correlation between experiment, FE piezoelectric simulation and FE composite Lamb wave simulation. The 'polymer only' response in Figures 5.63 and 5.64, however, do not match so well to Figures 5.47 and 5.48. This is due to polymer replacing the stiffer ceramic at the point of load, and the corresponding large displacements at the load point altering the results from the composite case.

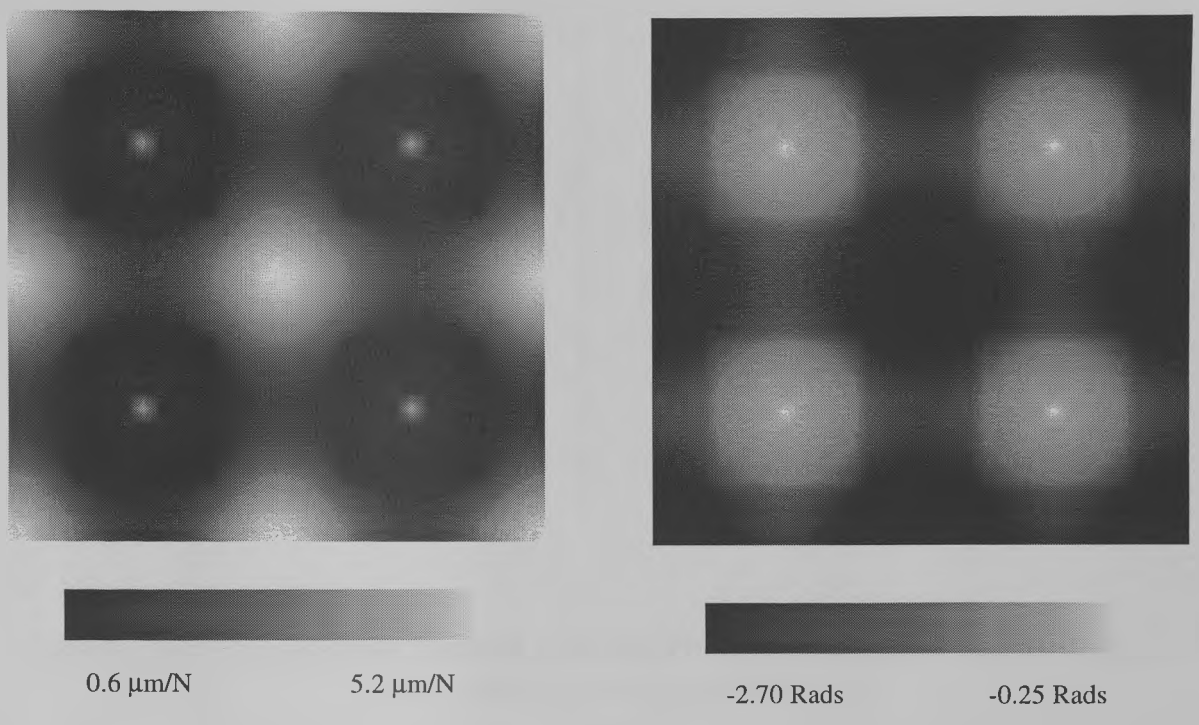

Figure 5.59 FEA SDP at 1700 kHz for Composite 13E - Lamb Wave Generation

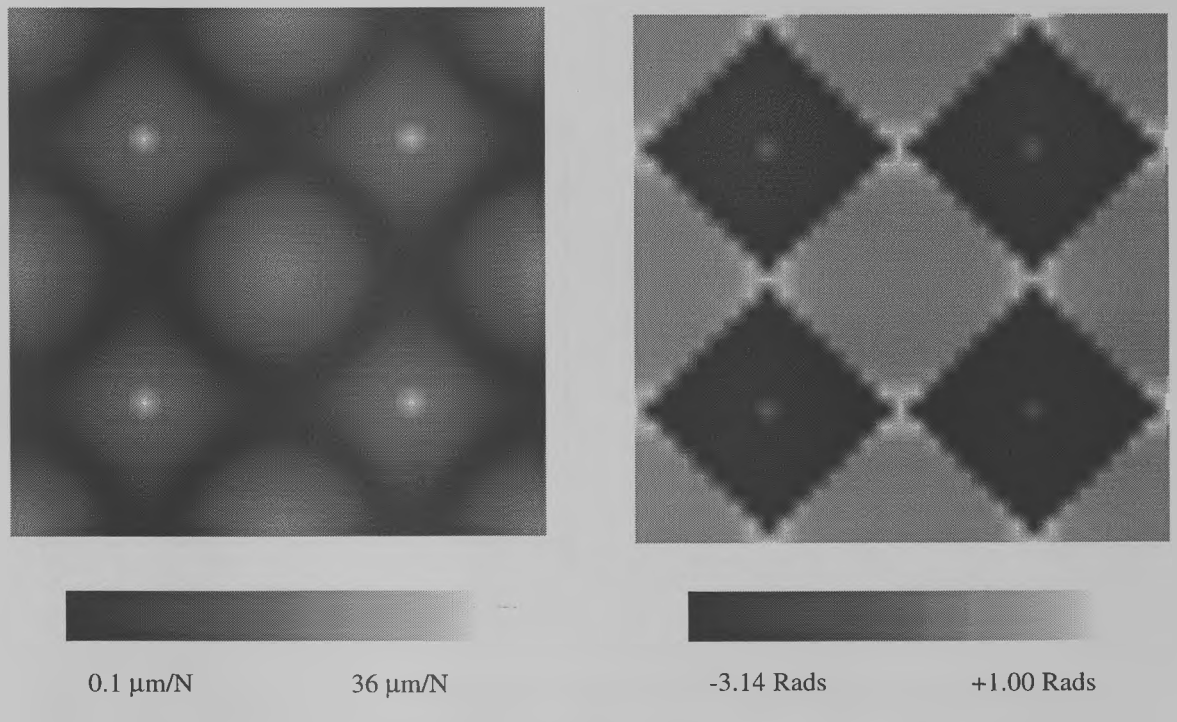

Figure 5.60 FEA SDP at 1510 kHz for Solid Polymer - Lamb Wave Generation

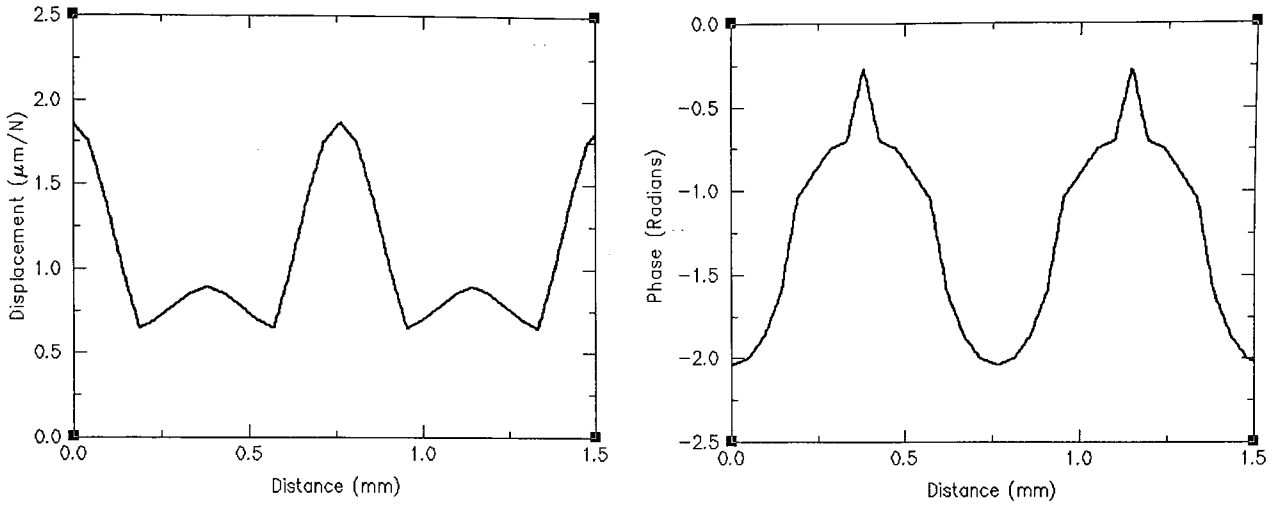

Figure 5.61 Cross-section Through Ceramic Pillars in Composite 13E at 1700 kHz – Lamb Wave Generation

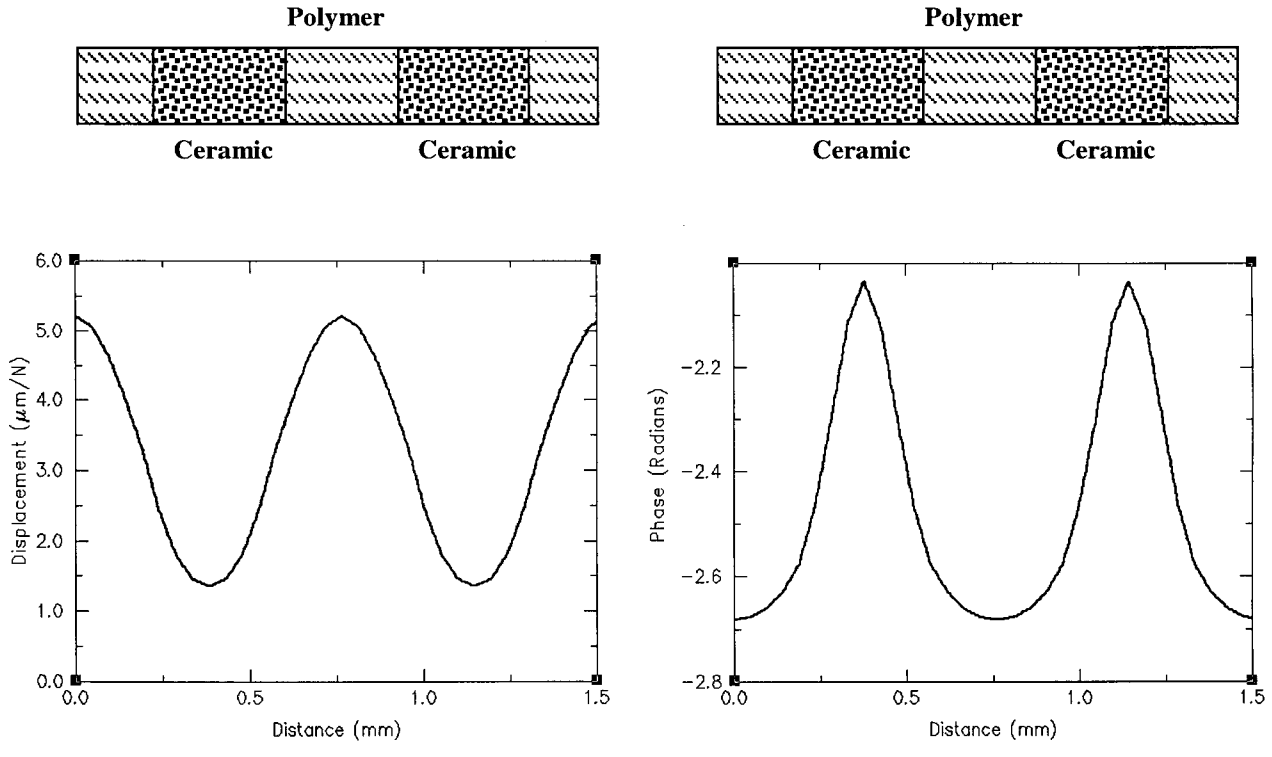

Figure 5.62 Cross-section Through Polymer in Composite 13E at 1700 kHz – Lamb Wave Generation

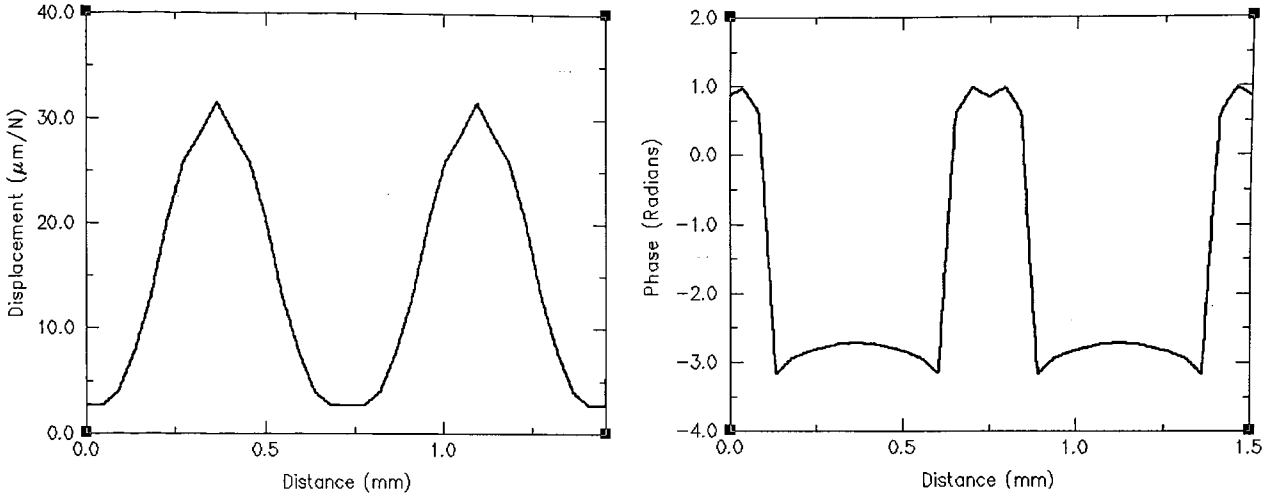

Figure 5.63 Cross-section Through 'Ceramic Pillars' in Solid Polymer at 1510 kHz – Lamb Wave Generation

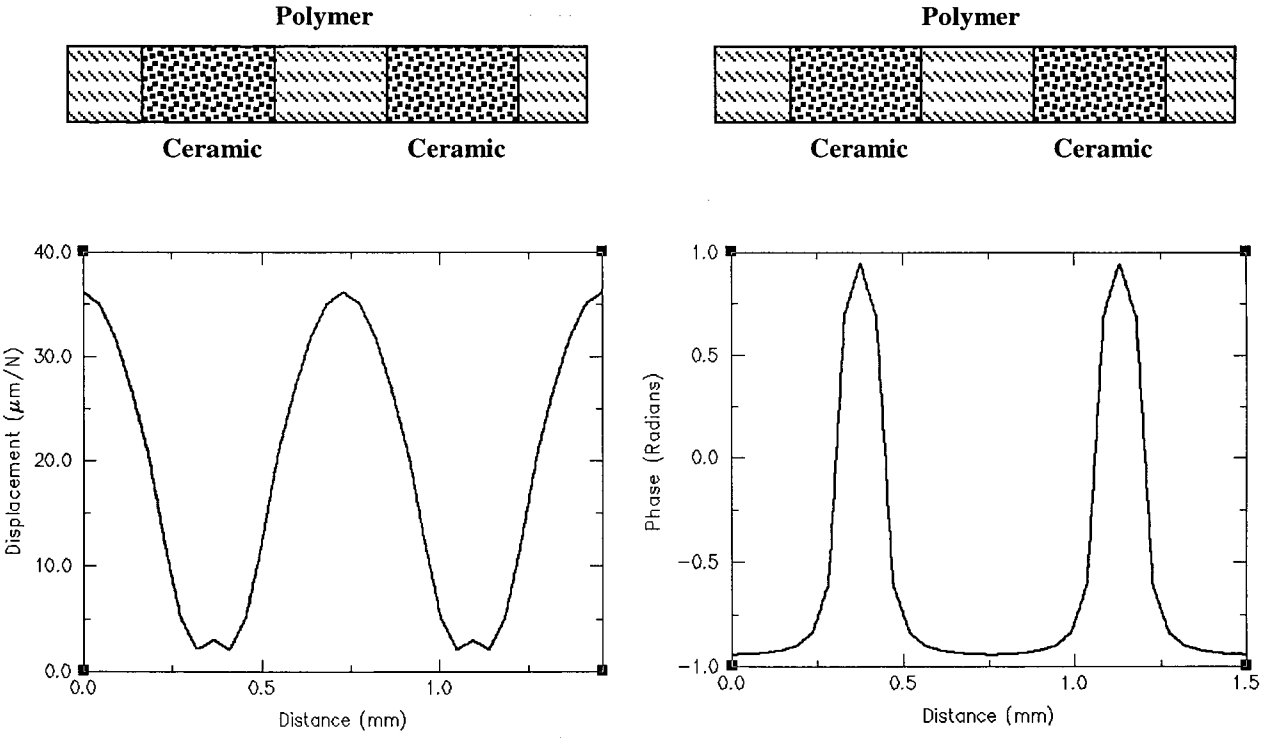

Figure 5.64 Cross-section Through 'Polymer' in Solid Polymer at 1510 kHz – Lamb Wave Generation

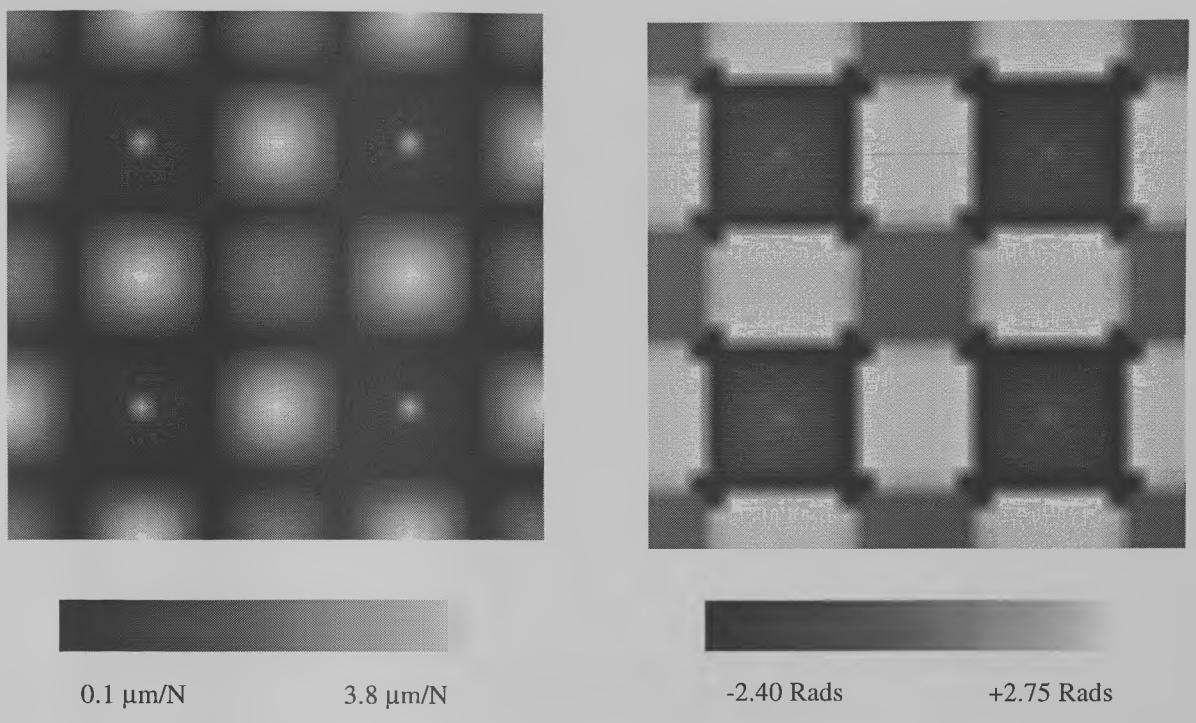

Figure 5.65 FEA SDP at 2310 kHz for Composite 13E - Lamb Wave Generation

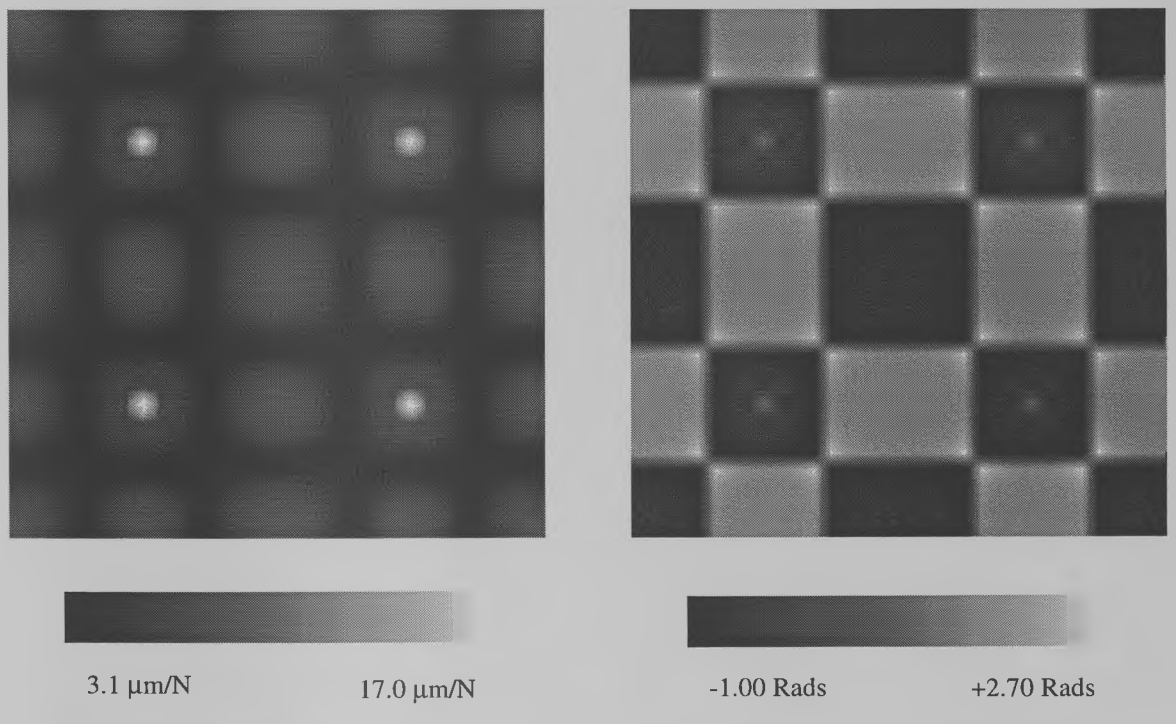

Figure 5.66 FEA SDP at 2160 kHz for Solid Polymer - Lamb Wave Generation

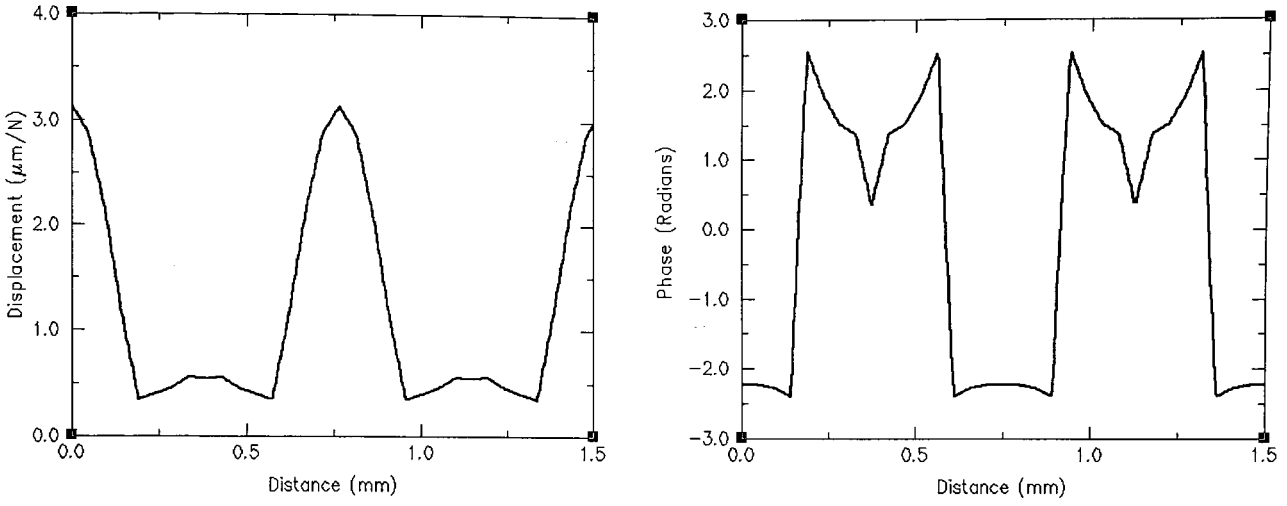

Figure 5.67 Cross-section Through Ceramic Pillars in Composite 13E at 2310kHz – Lamb Wave Generation

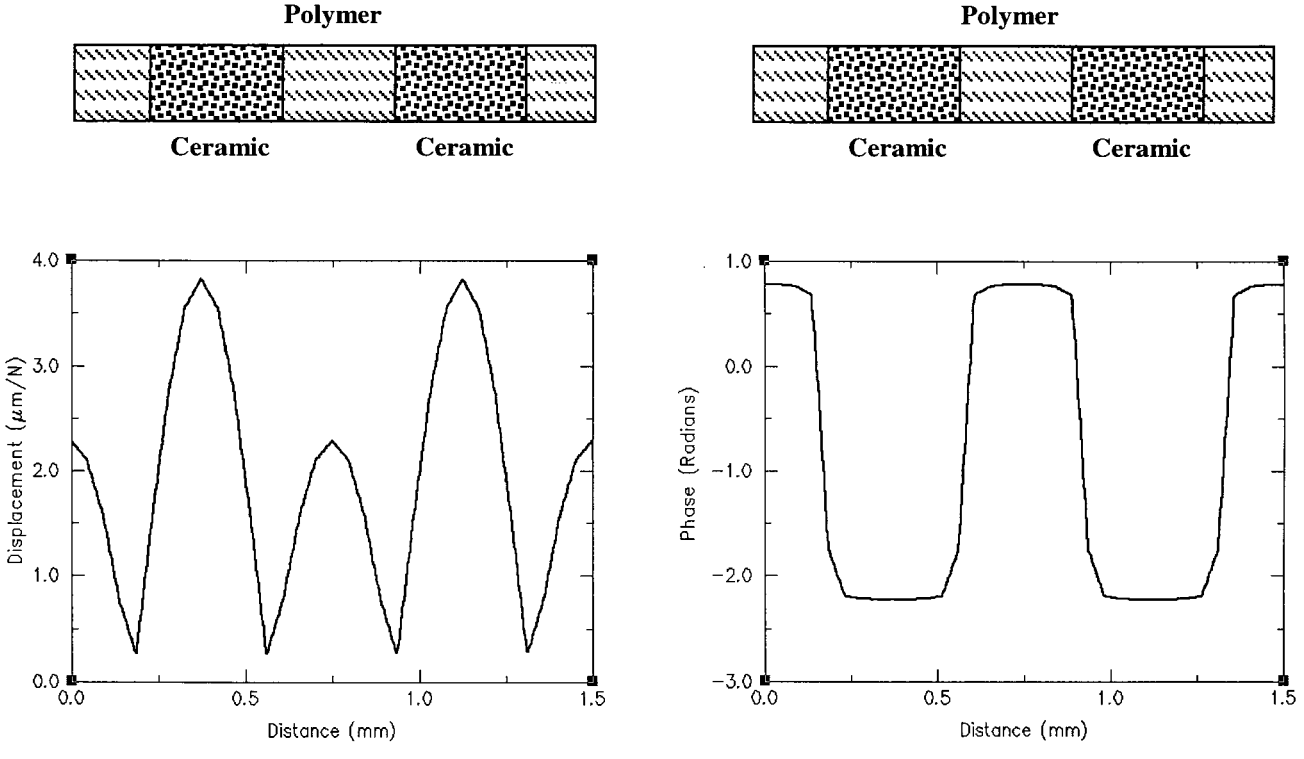

Figure 5.68 Cross-section Through Polymer in Composite 13E at 2310 kHz – Lamb Wave Generation

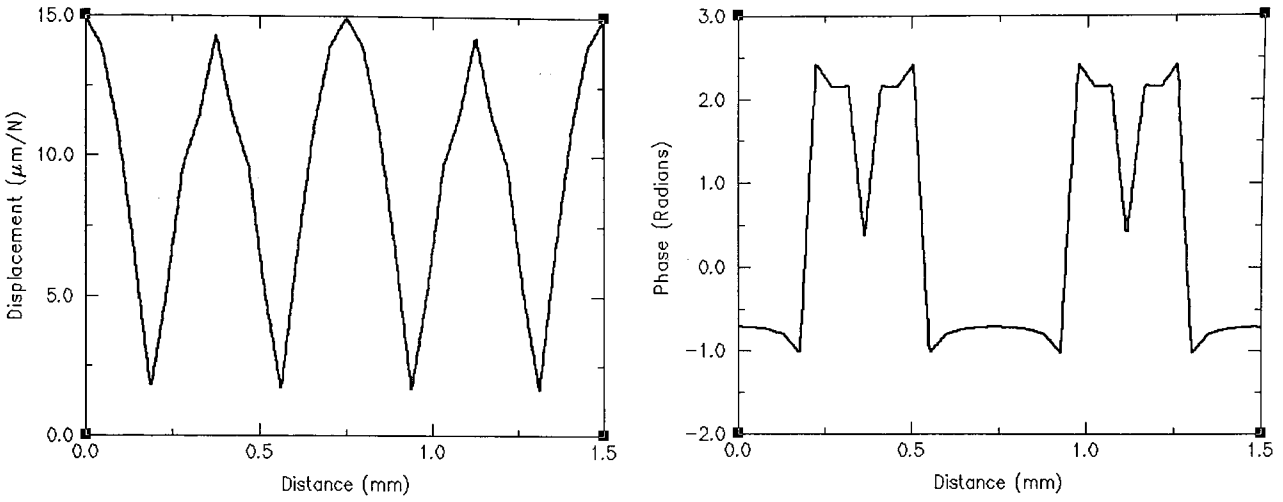

Figure 5.69 Cross-section Through 'Ceramic Pillars' in Solid Polymer at 2160 kHz – Lamb Wave Generation

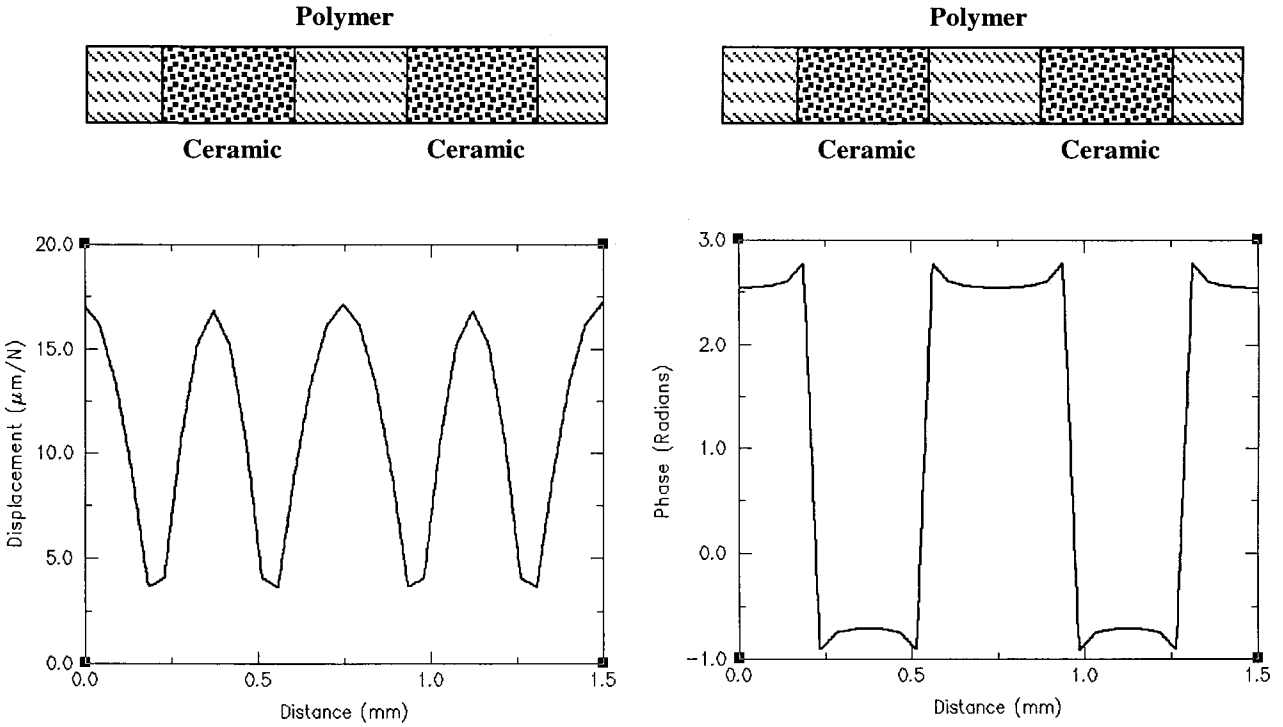

Figure 5.70 Cross-section Through 'Polymer' in Solid Polymer at 2160 kHz – Lamb Wave Generation

Comparison of Figures 5.65 and 5.66, with Figures 5.55 and 5.56, yield equally similar results for the second inter-pillar mode. The Lamb mode is clearly propagating along the diagonals of the transducer with a wavelength of $d_0/\sqrt{2}$. Unlike the models for the first inter-pillar mode, the 'polymer only' FE model shows excellent correlation to be experiment and the composite FE point loading model. While displacement magnitudes cannot be directly compared due to differing driving functions, the mode shapes, particularly in the ceramic models, are almost identical to the experimental models in both magnitude and phase (Figures 5.57 and 5.58, 5.67 and 5.68, and 5.69 and 5.70). Only in the polymer only models, in the areas adjacent to the driving force, is there any aberration from previous results due to the reduced stiffness in these areas causing increased displacement.

The correlation between the Lamb wave models and the experimentally obtained results is exceptionally good, lending considerable weight to the proposition that the first two laterally resonant modes in a 1-3 composite transducer are generated by Lamb waves.

To summarise, it is proposed that inter-pillar resonances in a 1-3 composite transducer in air are due to symmetrical Lamb wave propagation in the material, and will propagate with frequencies determined by Equation 5.03 (a) and (b). Phase velocities in piezocomposites can be estimated by Equation 5.06, and will have mode shapes as described by Figures 5.46 and 5.56.

5.3 Analysis of 1-3 Composites with Matching Layer

While all modelling and analysis has concentrated on free standing transducers in air, it is important to remember that in reality transducers will be in holders with some form of matching or protective layer on the front face. For this section of the thesis, the composites were placed in holders as described in section 5.2.1, with a matching layer on the surface, thickness one quarter wavelength at the 'in air' thickness mode electrical resonance frequency. For composite 13A with hardset epoxy, this resulted in a 1.48 mm layer for matching an in air electrical resonance of 500 kHz. The experimental impedance plot and its FEA counterpart are presented as Figure 5.71.

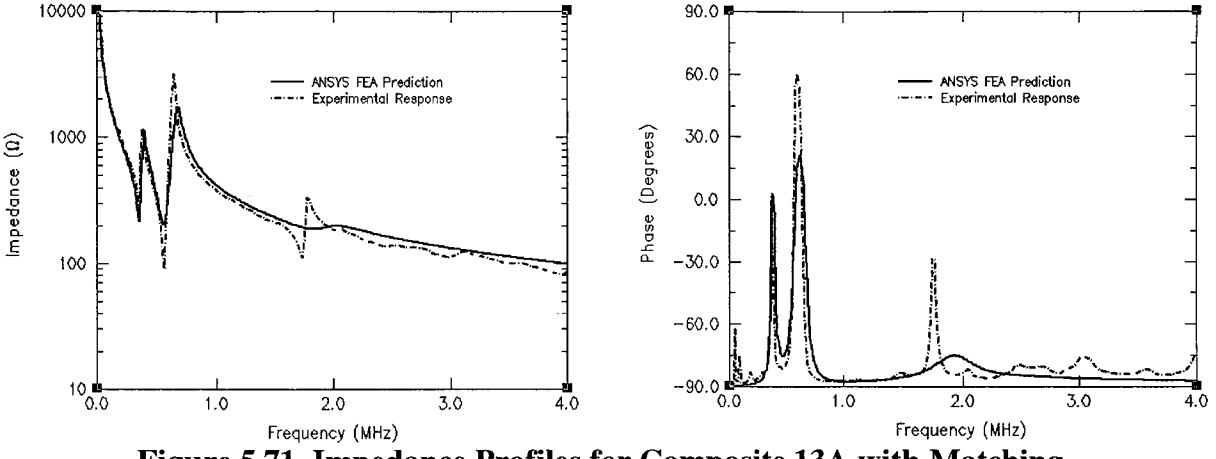

Figure 5.71 Impedance Profiles for Composite 13A with Matching

The impedance plot presents results for composite 13A when matching has been added. Three strong resonant modes exist in this transducer. The first, occurring at 359 kHz, is the result of the addition of the matching layer, creating a larger structure through which sound must propagate, thus lowering the resonant frequency. The mode at 565 kHz is apparently the electrical resonance of the composite, but appears to have increased from the in air value of 500 kHz. The final mode is the third harmonic of the composite resonance, at 1725 kHz. FEA has accurately predicted the

location of the all resonances, although the second and third modes are slightly heavily damped.

Experimental SDPs were obtained at the these three modes, and the first matching layer mode is presented as Figure 5.72, along with its full transducer FEA counterpart in Figure 5.73.

The magnitude response of the device at 359 kHz shows the displacement building rapidly towards a peak across the centre of the transducer, using the same mechanism as is seen in the thickness mode of the bare transducer. Phase is almost entirely uniform across the surface, indicating the transducer is acting in a very piston like manner. The displacement magnitude of 8.9 nm/v is extremely high, and would normally indicate efficient conversion of electrical to mechanical energy at this frequency. Given the impedance mismatch between the polymer and the air, it is likely that the vast majority of the energy is trapped within the structure and it is this which causes the large surface displacements. No transducer structure can be observed at this frequency, although this is to be expected as this mode is generated by the entire composite/matching layer combination. Displacement at a slice through the composite is presented as Figure 5.74, and in this case only a single slice is presented due to their being no apparent difference between ceramic and polymer slice displacements.

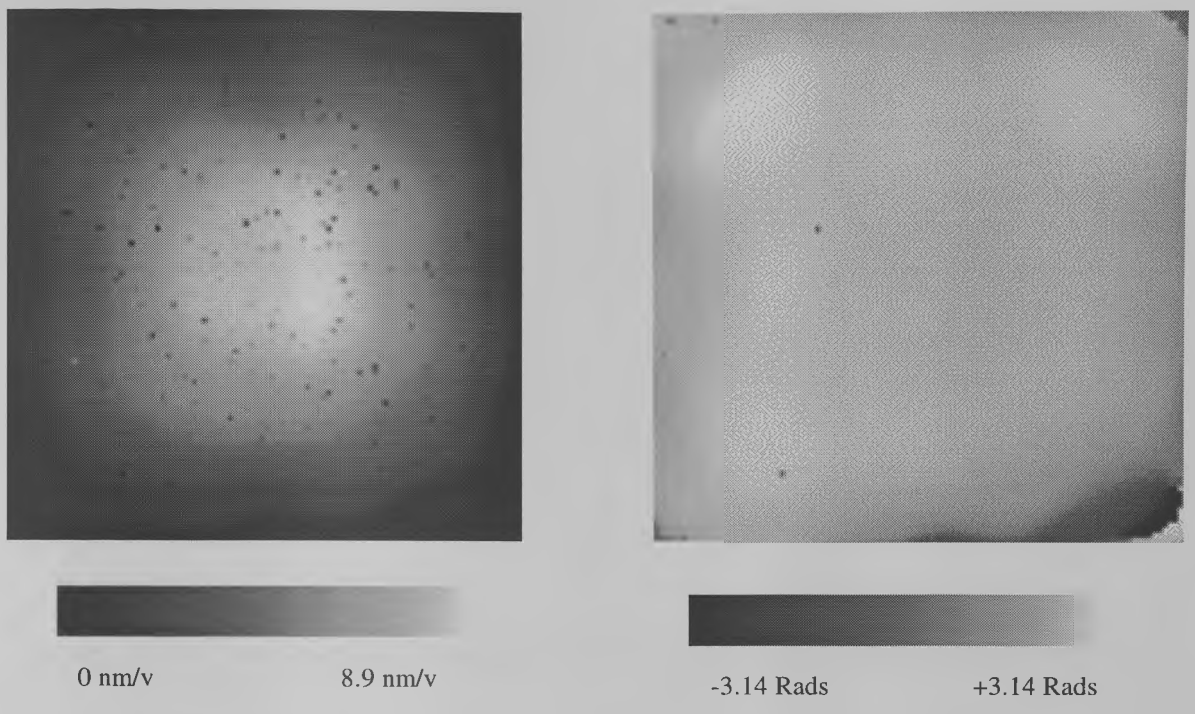

Figure 5.72 Experimental SDP at 359 kHz of Composite 13A with Matching

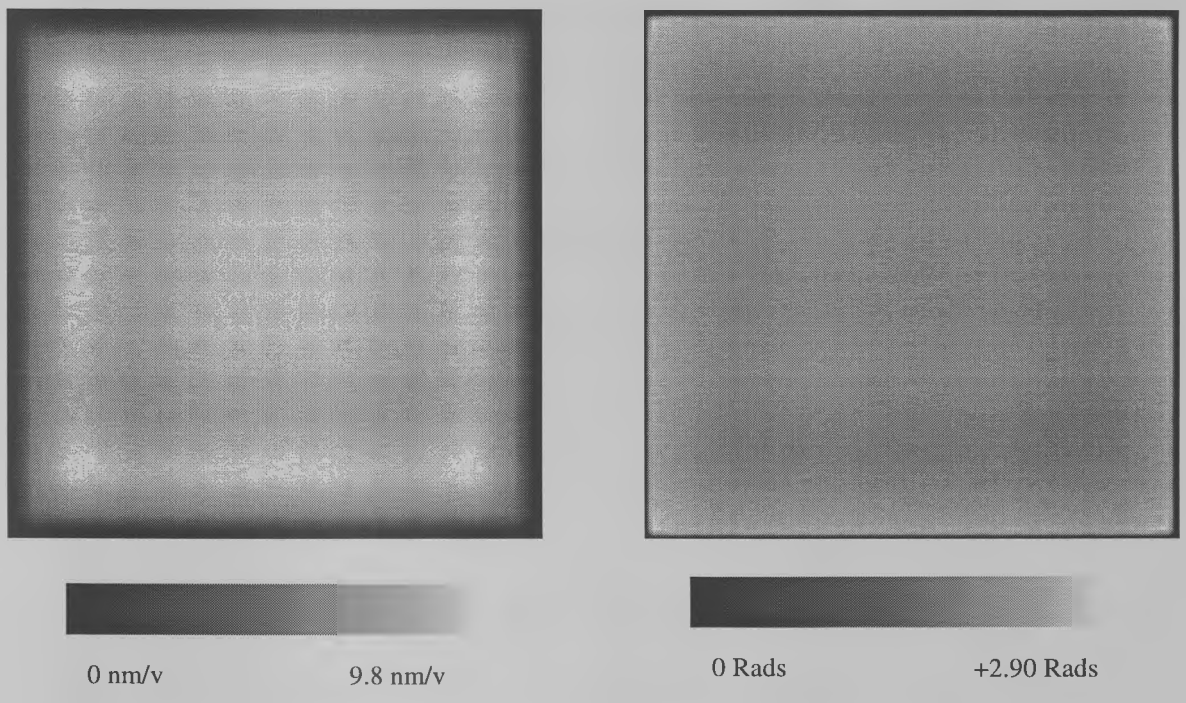

Figure 5.73 FEA SDP at 359 kHz of Composite 13A with Matching

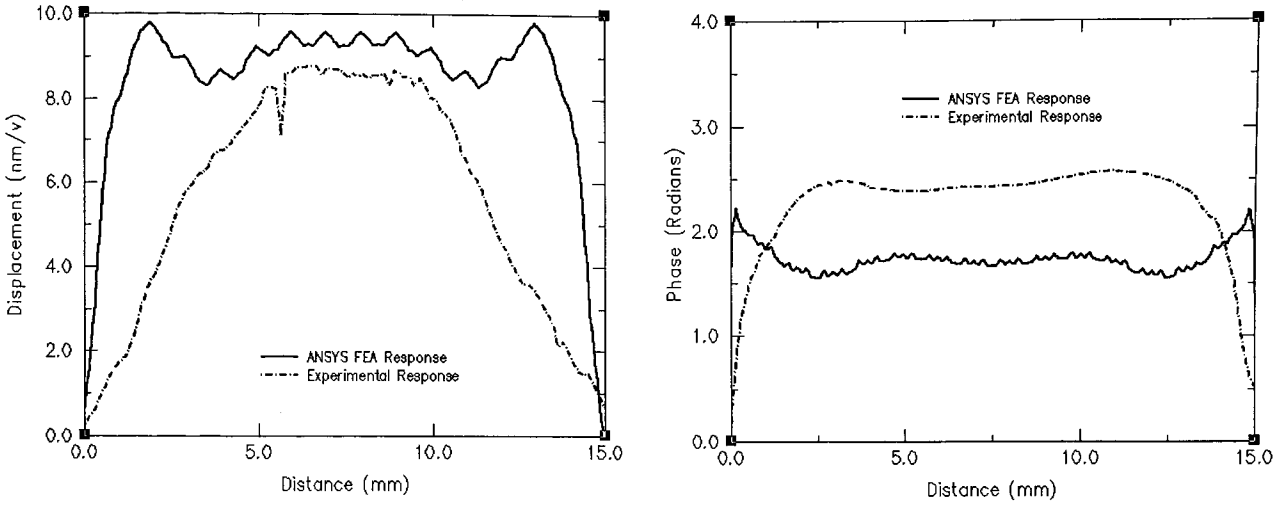

Figure 5.74 Cross-section Through Composite 13A with Matching at 359 kHz

Whilst all the general trends of transducer behaviour are predicted, along with accurate general values for magnitude and phase, FEA prediction is not as accurate as has been seen in previous structures, and is likely due to two reasons. Firstly, the single compromise value of damping that is required in ANSYS may not adequately represent both shear and longitudinal damping. Secondly, the FE model did not fully simulate the entire transducer casing, but rather approximated it by addition of a polymer boundary four times the saw pitch in length, with clamped, rigid boundaries at the edges. While not ideal, this compromise was required to reduce the simulation time to days, rather than the weeks an entirely accurate model would have required.

It is of interest to note that, in the case of the water loaded response that will be discussed later, the polymer boundary was 50% longer than in the 'in air' case, and results more consistent with experiment were obtained, but with a greatly increased computational load.

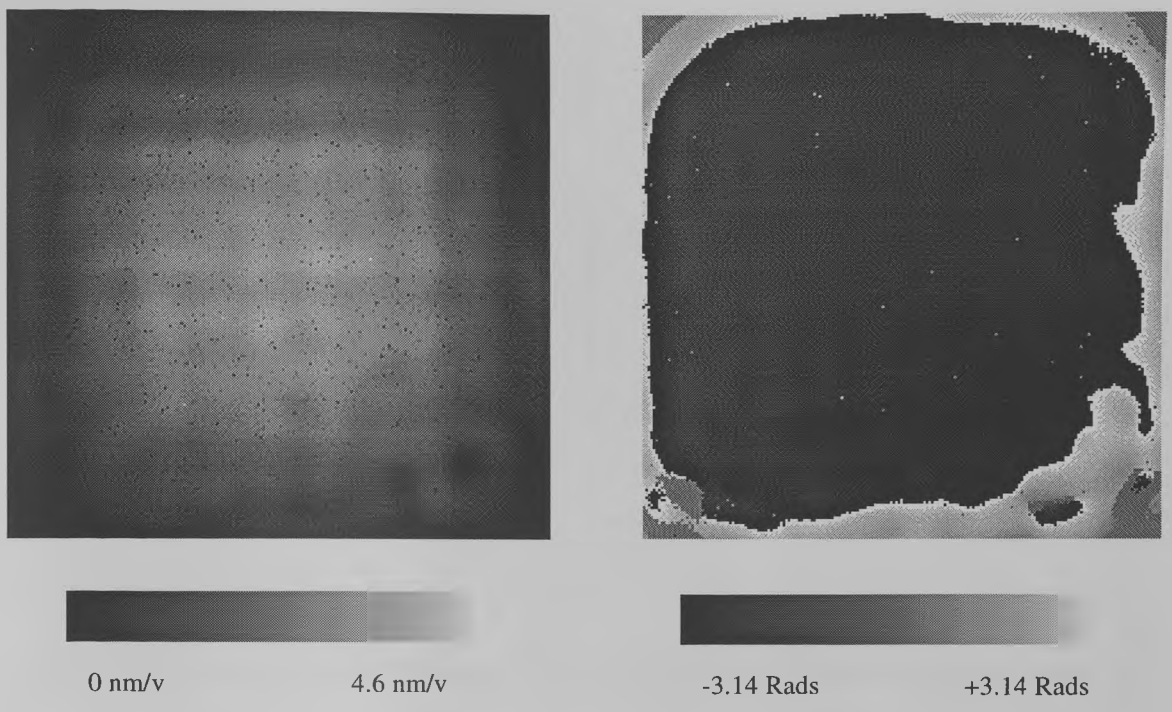

Figure 5.75 Experimental SDP at 565 kHz of Composite 13A with Matching

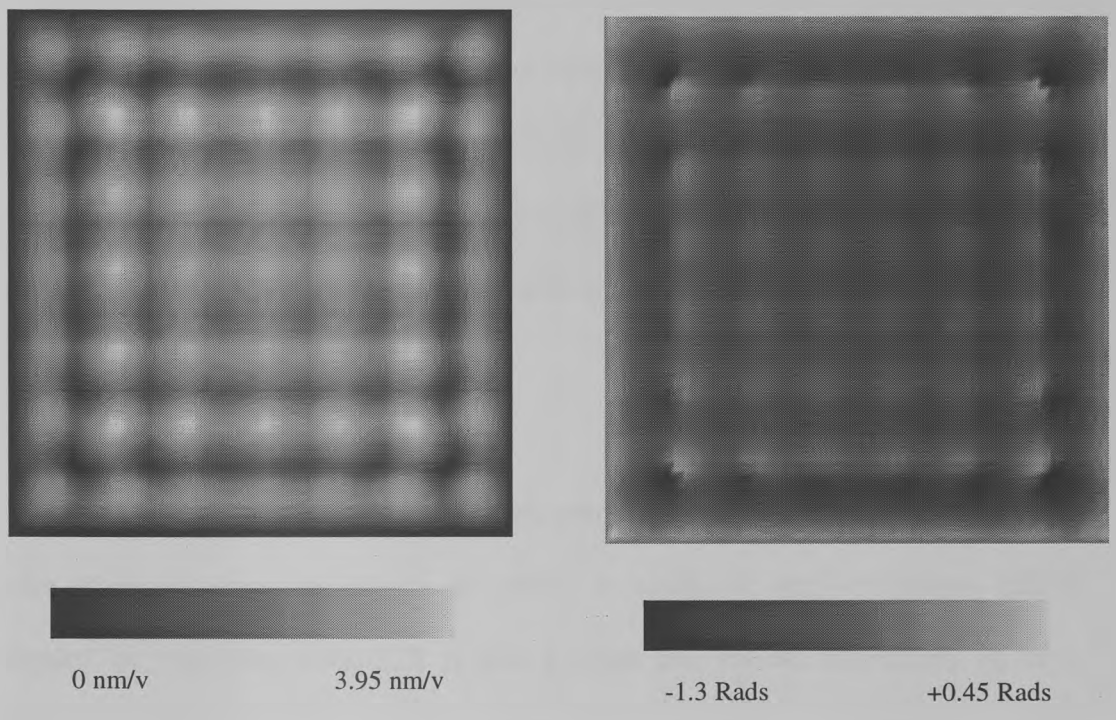

Figure 5.76 FEA SDP at 565 kHz of Composite 13A with Matching

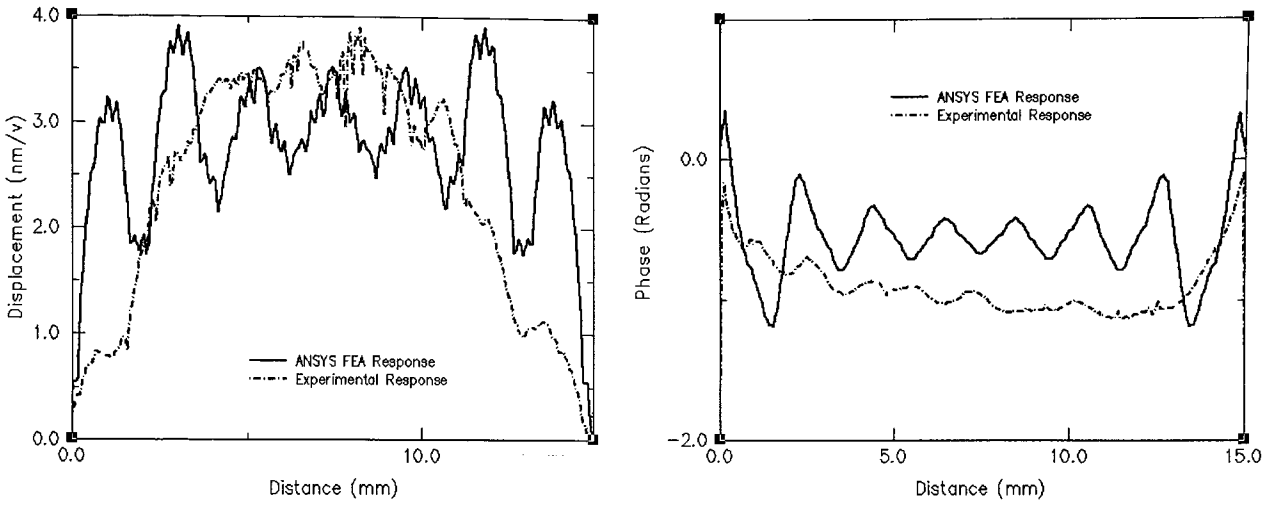

Figure 5.77 Cross-section Through Composite 13A with Matching at 565 kHz

The behaviour at the 565 kHz resonance can be seen in Figure 5.75, with the FEA predicted behaviour in Figure 5.76. Figure 5.77 shows the displacement at a slice through the structure. FEA predicts the behaviour well, but again not as accurately as in previous models, for similar reasons to those mentioned earlier. While FEA has predicted the behaviour of the matched composite with reasonable accuracy, it is clear that a composite designed to operate at 500 kHz should not operate at 565 kHz when a matching layer has been added.

A continually repeated point made during chapter 2 was that a mode would exist and resonate strongly when the cavity in which it resonated was of length half a wavelength or multiples thereof. It is also evident that should this cavity be of a quarter wavelength in size (or three quarters, five quarters etc), then *destructive* interference would occur and no mode would exist at that frequency.

By addition of a quarter wavelength matching layer at thickness mode electrical resonance, the cavity is effectively three quarters of a wavelength long at electrical resonance, as the thickness of the bare transducer in air operating at the thickness mode is half a wavelength. Thus by addition of a matching layer of a quarter wavelength thickness, conditions have been set up whereby destructive interference will occur at the desired frequency of operation.

The thickness mode frequency of the matched transducer will therefore change to the frequency at which the thickness of the transducer plus matching layer is an entire wavelength. Given that the velocities of sound in the materials will not change, then this will result in a higher thickness mode resonance, as is seen in Figure 5.71.

Thus, for a transducer to have a thickness mode resonant frequency that is identical in both the matched and unmatched case for operation into air, then the matching layer must be of thickness half a wavelength at thickness mode electrical resonance, or multiples thereof. The finite element model for composite 13A with matching was run again, this time with a half wavelength matching layer (2.96 mm). The impedance response can be seen in Figure 5.78.

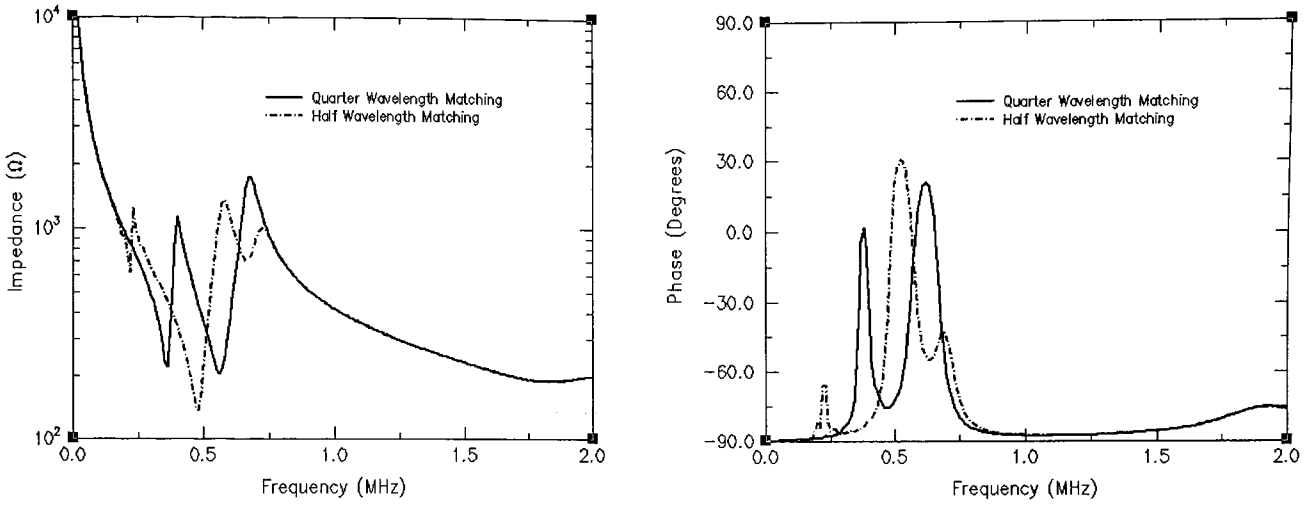

Figure 5.78 Electrical Impedance Profiles for Composite 13A with Quarter and Half Wavelength Matching Layers

Due to the increased thickness of the matching layer, the entire structure/matching layer resonance frequency has been lowered to 220 kHz, but in this case the thickness mode resonance frequency appears just below 500 kHz, the desired frequency. An additional mode appears at 690 kHz, corresponding to a one and a half wavelength total cavity size.

Average surface displacement across the entire matching layer surface for both cases was calculated, and is presented against frequency in Figure 5.79. This diagram clearly shows that the greatest average displacement occurs at the entire composite/matching layer structural resonance, with a second peak occurring at the thickness mode of about 40% the displacement at the lower frequency.

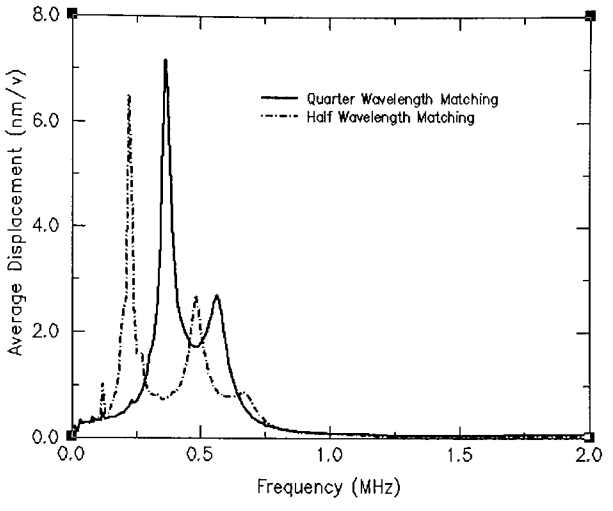

Figure 5.79 Average Displacement across Entire Transducer Surface of Composite 13A with Quarter and Half Wavelength Matching Layers

Given the transducer response of 13A, it may be that a composite displacing polymer more than ceramic at thickness mode would be better suited to matching layer operation in air. As polymer would be the main source of coupling of ultrasonic energy to the matching layer, it is possible that more energy will be coupled to the load at both the thickness mode resonance and the first inter-pillar resonance.

To test this theory, the remaining composites were housed in identical containers to 13A, with quarter wavelength matching layers appropriate to their own in air thickness mode electrical resonance frequency. Laser scans were obtained for all devices at frequencies corresponding to the full composite/matching layer resonance, composite only thickness mode resonance, and the first inter-pillar mode. Table 5.04 lists the maximum displacements for each of those modes, at in both the matched and unmatched cases. Obviously, there is no matching layer displacement for the unmatched devices, and the first inter-pillar resonance, is, in the case of 13A and 13B, the third harmonic of the thickness mode.

Device	Mode	Unmatched Displacement (nm)	Matched Displacement (nm)
13A	Thickness	5.0	4.6
	Harmonic	0.56	0.53
	Matching	N/A	8.9
13B	Thickness	5.8	4.9
	Harmonic	0.3	0.3
	Matching	N/A	8.4
13C	Thickness	2.8	2.8
	Lateral	1.25	1.0
	Matching	N/A	6.0
13D	Thickness	5.3	2.0
	Lateral	0.78	1.3
	Matching	N/A	4.1
13E	Thickness	2.9	1.5
	Lateral	2.4	2.3
	Matching	N/A	6.2

Table 5.04 Maximum Displacements in Composite Transducers

In all cases, it is interesting to note that the unmatched transducer has maximum displacement greater than or equal to its matched counterpart. This is due to the additional mass loading of the matching layer itself. In the case of the two transducers where the thickness mode harmonic was examined (13A and 13B), there is no improvement in maximum displacement, but this is expected as the coupling mechanism for the harmonic is identical to that of the fundamental mode.

In the remaining three transducers, one has improved displacement, one has reduced displacement, and the third is approximately equal to the unmatched case. It appears that there is no significant benefit to be gained from attempting to drive the transducers at their first inter-pillar resonance, as there is no improved coupling due to the composite polymer displacement.

Of great interest, however, is that the displacement at the matching layer resonance is, in all cases, at least 70 % greater than the displacement at the matched thickness resonance (and ranging as high as 300%), while displacing more than the unmatched thickness resonance in all cases but one. As indicated earlier, this is likely due to the resonance of the matching layer/composite trapping the vast majority of the energy within its structure.

To summarise, in terms of increasing overall displacement for the in-air case, there is no advantage in the addition of a matching layer when driven at either the thickness mode or the first inter-pillar mode. However, for in-air operation, a composite with matching layer driven at the matching layer/composite resonance will produce significantly greater displacements than at thickness mode in either the matched or unmatched case.

In addition, for operation into air, a composite transducer matching layer should be of half wavelength thickness at the thickness mode frequency to ensure that the transducer operates at the original, desired, thickness mode frequency.

5.4 Analysis of Composite 13A in Water

The addition of a matching layer is to improve the transmission of energy from the composite into the load media, in particular when the load is water. When a well matched composite/matching layer combination is placed in water, the additional resonance due to the matching layer should disappear to leave the transducer operating in a unimodal fashion. Transducer 13A (with $\lambda/4$ matching layer as used in section 5.3) was placed in water to obtain the impedance profile, which is detailed in Figure 5.80.

As can be seen, the experimental matching layer resonance has gone due to the improved coupling of energy into the water, to leave an almost unimodal response with the resonance at 525 kHz, a lower frequency due to the water loading. Whilst considerably reduced, there is still some evidence of the composite/matching layer resonance, most likely due to the non-ideal impedance of the matching layer. The FEA matching layer resonance, whilst reduced, has not been removed entirely, and is likely due to a mixture of non-ideal matching and an insufficiently fine mesh in the water. Whilst further computations could be performed, the computation time for the results in Figure 5.80 was over 3 weeks, and consequently no further such solutions could be justified given the limited computer resources.

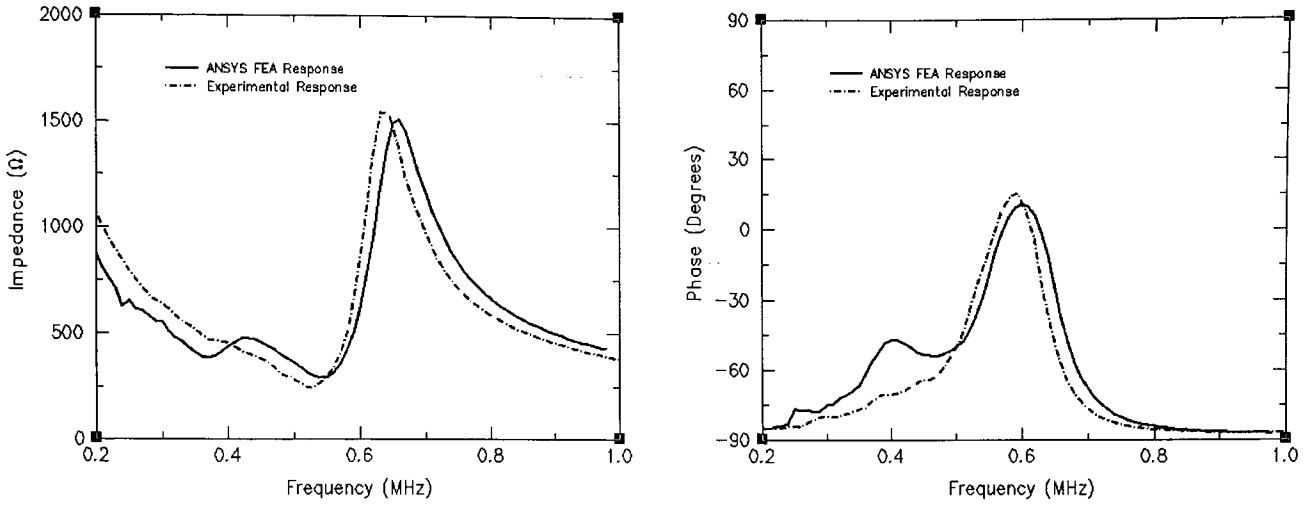

Figure 5.80 Impedance Profiles for Composite 13A in Water

As the solution time for these simulations was long, only a limited frequency range was analysed. An experimental SDP in water at electrical resonance was obtained, and is presented in Figure 5.81 with the appropriate corrections as recommended in chapter 4. The finite element response is shown in Figure 5.82, with a displacement slice provided for comparison in Figure 5.83. In keeping with previous thickness mode results for this transducer, the magnitude of the response peaks across the centre of the device, with the phase constant across the surface. Maximum displacement is smaller than in air displacement at 1.2 nm/v due to the water loading. Considerably more energy, however, will be coupled into the media as the acoustic impedance of water is much closer to that of the polymer than is air.

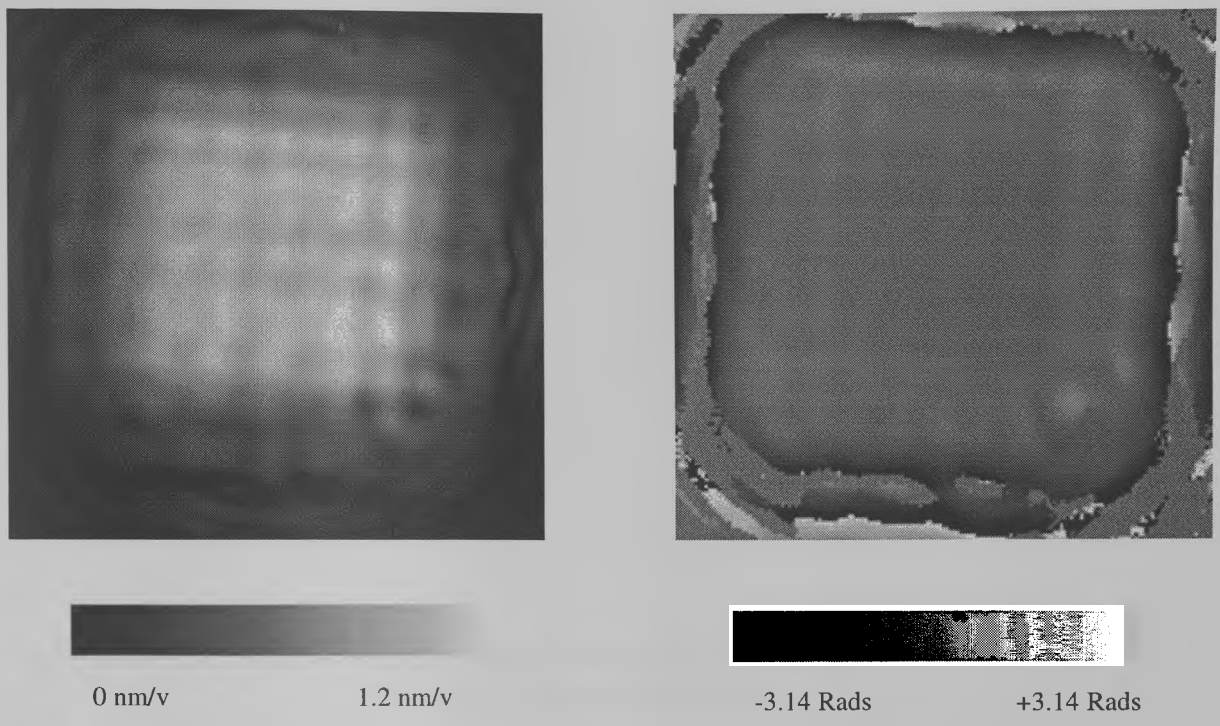

Figure 5.81 Experimental SDP at 525 kHz for Composite 13A in Water

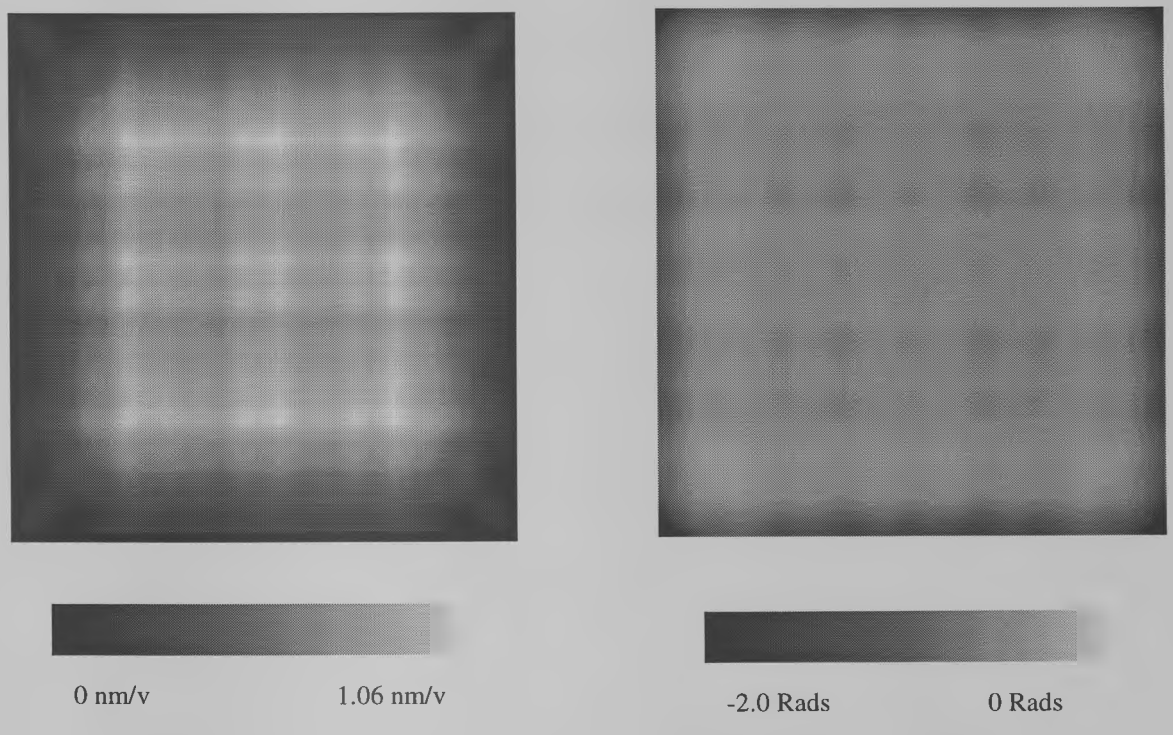

Figure 5.82 FEA SDP at 525 kHz for Composite 13A in Water

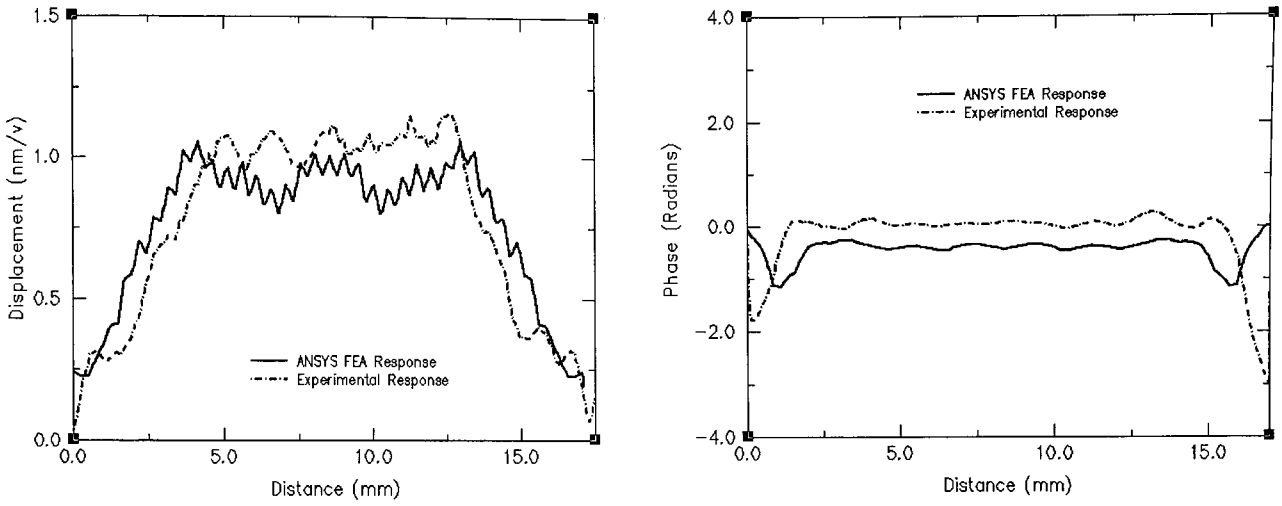

Figure 5.83 Cross-section Through Composite 13A with Quarter Wavelength Matching in Water at 525 kHz

Interestingly, the predicted surface displacement behaviour for the in water case is considerably more accurate than for the matched in air case, due to the additional damping caused by the water, and the increased quantity of polymer at the composite edges. It is still clear, however, that despite the improved correlation that the damping models of ANSYS could be drastically improved by the introduction of separate shear and longitudinal damping factors.

5.5 Analysis of 2-2 Composites

While 1-3 composite transducers have been extensively modelled and examined, less work has been published on the behaviour of 2-2 composites, despite their extensive use in the biomedical industry. Work has been published on 2-2 composites by Shui and Xue [81], Geng and Zhang [82], Shui, Geng, and Zhang [83] and Qi and Cao [84] on the modelling of resonant modes within 2-2 composites. Oakley [23, 85] has done extensive work on the stopband structures, and Richard [86] has proposed novel modelling techniques for 2-2 composites. Should the Lamb wave theory of inter-pillar resonances within composite structures be correct, it should also hold for 2-2 composites, although for the first mode only. Two 2-2 composites have therefore been constructed and are to be analysed in a similar manner to the 1-3 composites listed previously. Both composites were PZT-5H ceramic with hardset epoxy, and measured 15 mm along each side, and all analyses were conducted in air. Table 5.05 lists the properties of the composites.

Device	Kerf (mm)	Pitch (mm)	Thickness (mm)	VF (%)	AR	Centre Freq. (kHz)
22A	0.40	0.60	2.50	33	0.08	622
22B	0.40	0.60	1.50	33	0.13	1000

Table 5.05 2-2 Composite Details

As for the 1-3 composites, all results were modelled using a 2.5 D approach. In certain cases, an enlarged section of the 2-2 composite is used to display surface displacement profiles, as before, along with the displacements along slices through the composite. In such cases, the slices will be across the transducer as a whole or across a limited section such as that described by Figure 5.84. This Figure also identifies the

location of these slicing planes such as across alternating bars of ceramic and epoxy, or along the entire length of a ceramic bar. As in Figure 5.84, all results presented in this section will be shown with the ceramic bars running from the top to the bottom of the page.

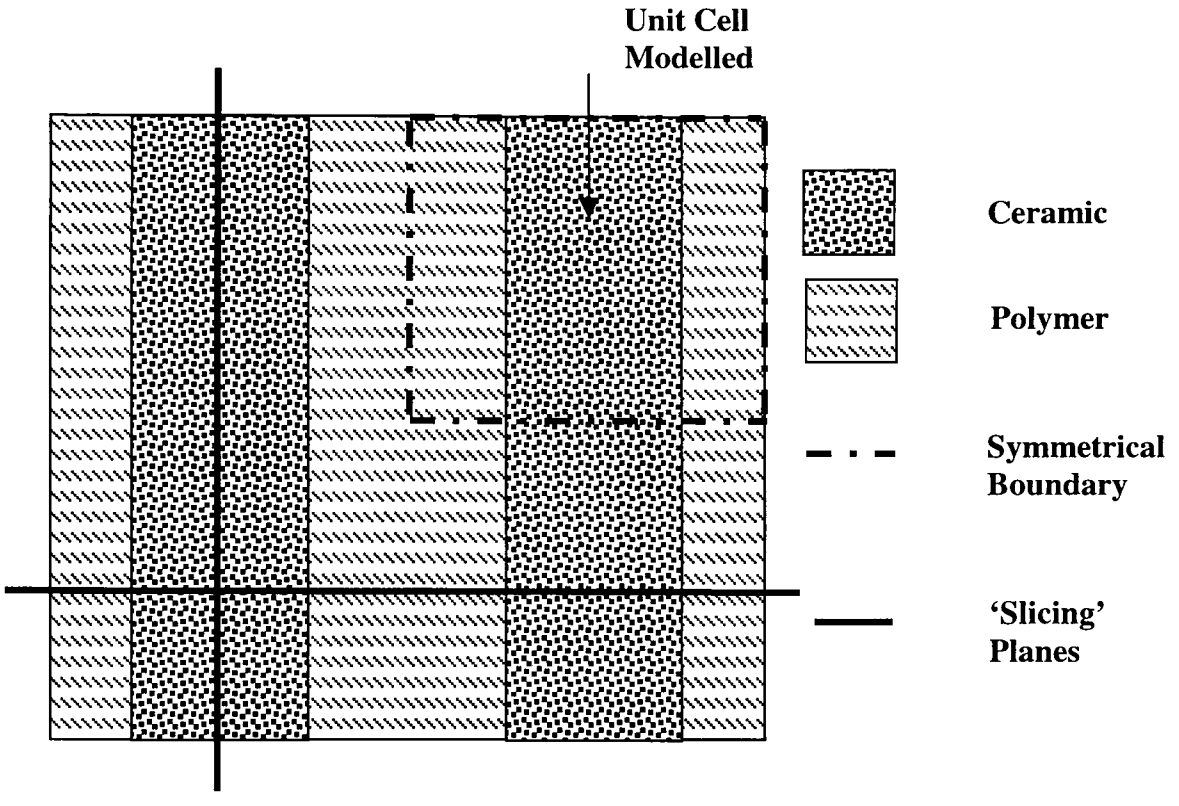

Figure 5.84 Slicing Planes through a 2-2 Composite

An additional function of the 2-2 composites is that by study of their resonant behaviour, it should be possible to rule out Bragg scattering as the method of inter-pillar resonance generation. Unlike the 1-3 composites, 2-2 composites consist of bars of ceramic alternating with bars of polymer – consequently no regular grid of scattering points exists. Thus in 2-2 composites, Bragg scattering *cannot* be responsible for the generation of lateral resonances. A Lamb wave theory, however, still allows for the generation of modes based upon the interdigital structure similar to

that shown in Figure 5.27 – obviously no diagonal type structure can exist in a 2-2 composite like that shown in Figure 5.28, limiting the number of mode types that can be generated. This first inter-plate mode in a 2-2 composite will therefore have a frequency determined by Eqn. 5.03 (a), which is reproduced below for convenience.

$$f_{LI} = \frac{v_{phase}}{d_0}$$

In this equation, the wavelength of the Lamb wave is equal to the inter-plate spacing, d_0.

5.5.1 Analysis of 2-2 Composite 22A

The first 2-2 composite to be analysed is 22A, and the method used was identical to that for the 1-3 composites. The experimental electrical impedance was obtained, to be compared with FEA results. Figure 5.85 shows the experimental impedance response compared FEA. As can be seen, the 2.5 D modelling predicts the low frequency bar length modes and corresponding harmonics which continue strongly until they interfere with the thickness mode resonance, which occurs at 622 kHz. It is likely that these modes are due to bar length modes in the ceramic and polymer bars, which run continuously in one transducer axis, and that any thickness mode resonance SDP will consist of multiple mode shapes superimposed upon one another. A third harmonic of the thickness mode resonance can be seen at 1600 kHz, and another weak resonance at 1800 kHz.

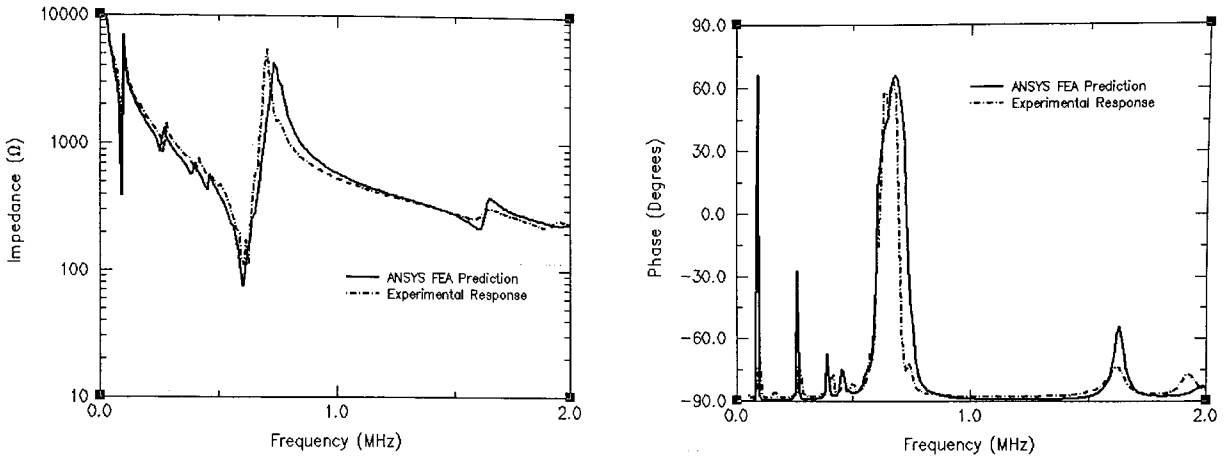

Figure 5.85 Impedance Profile for Composite 22A

Lamb wave theory (Equations 5.03 (a) and 5.06) indicates that for a 33% composite with this saw pitch, the phase velocity will be 1123 ms^{-1}, and the Lamb wave should cause a resonance to appear at 1871 kHz, very close to the frequency of the weak resonance just above the thickness mode third harmonic.

Laser scans were obtained for 22A at the fundamental length and thickness modes, at 91 kHz and 622 kHz. The results for the experimental and FEA response at 622 kHz are shown as Figure 5.86 and 5.87. At first, these results appear confusing, and show little correlation. However, when a slice along the length of a ceramic bar is used to compare the results (Figure 5.88), it can be seen that the two results compare well. It is evident that there is a large variation in the surface displacement characteristics along the length of the ceramic bars, resulting in large ripples across the surface of the transducer perpendicular to the length of the bars.

Given that the Rayleigh wave velocity in the ceramic is 1619 ms^{-1}, and that 5 wavelengths can be counted in the bar length of 15 mm (wavelength 3 mm) the

frequency of this wave can be shown to be 540 kHz – extremely close to the thickness mode resonance of 622 kHz. Thus it is apparent that the mode that prevents the transducers from operating in a piston like manner is a symmetric Lamb wave propagating along the ceramic bar length. This mode is much stronger than the 'width' modes seen in 1-3 composites due to the continuous nature of the ceramic bar, offering an unbroken path for wave propagation. It appears that in this case the length of the ceramic bar is insufficient to ensure that any Lamb waves modes are adequately damped at the thickness mode frequency.

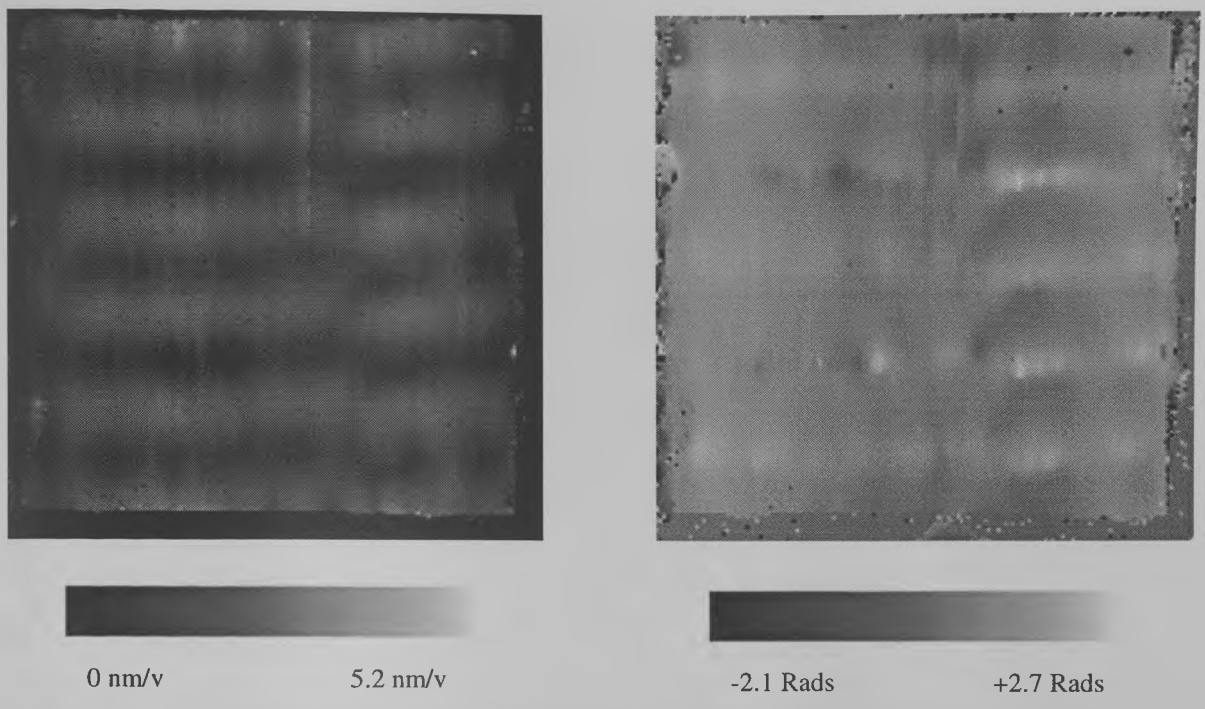

Figure 5.86 Experimental SDP at 622 kHz for Composite 22A

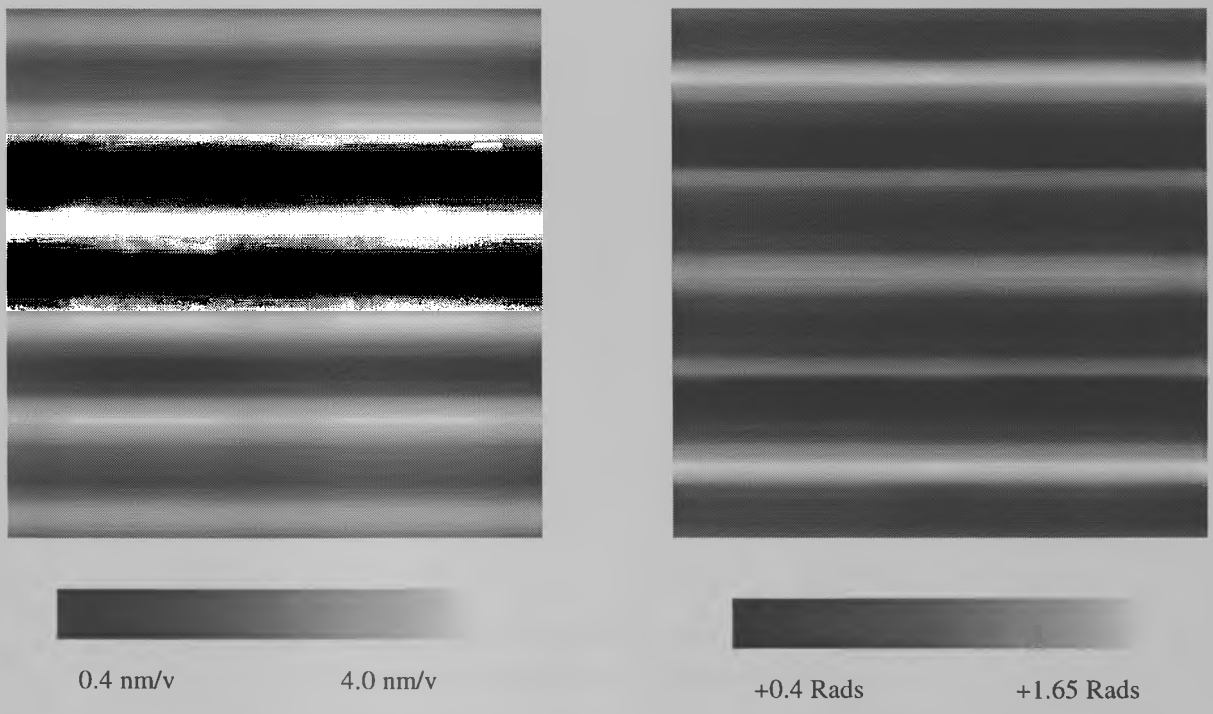

Figure 5.87 FEA SDP at 622 kHz for Composite 22A

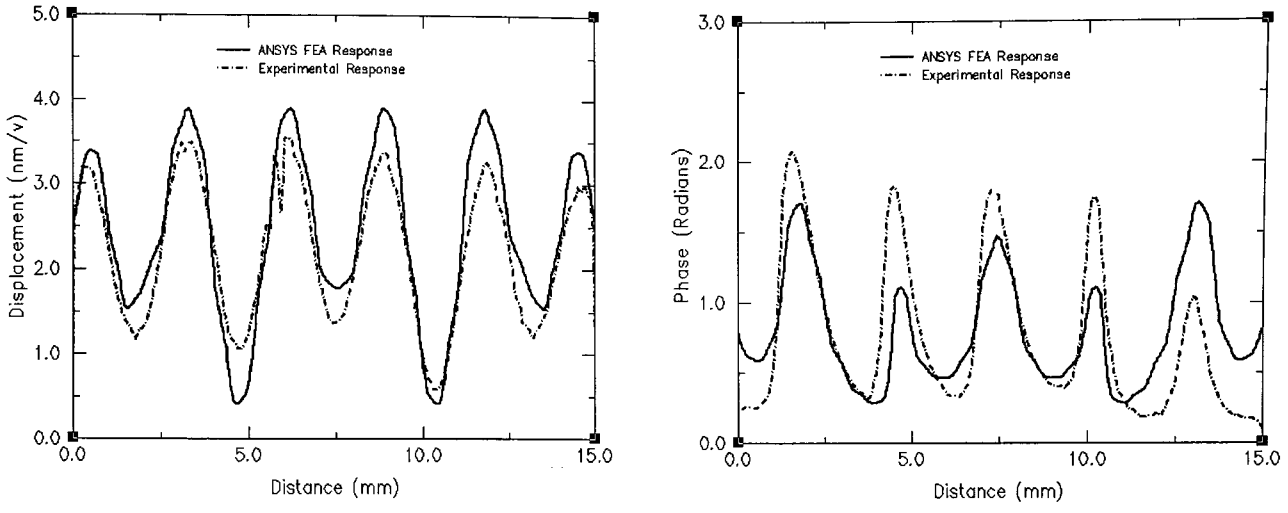

Figure 5.88 Cross-section Displacement along Ceramic Bar Length at 622 kHz for Composite 22A

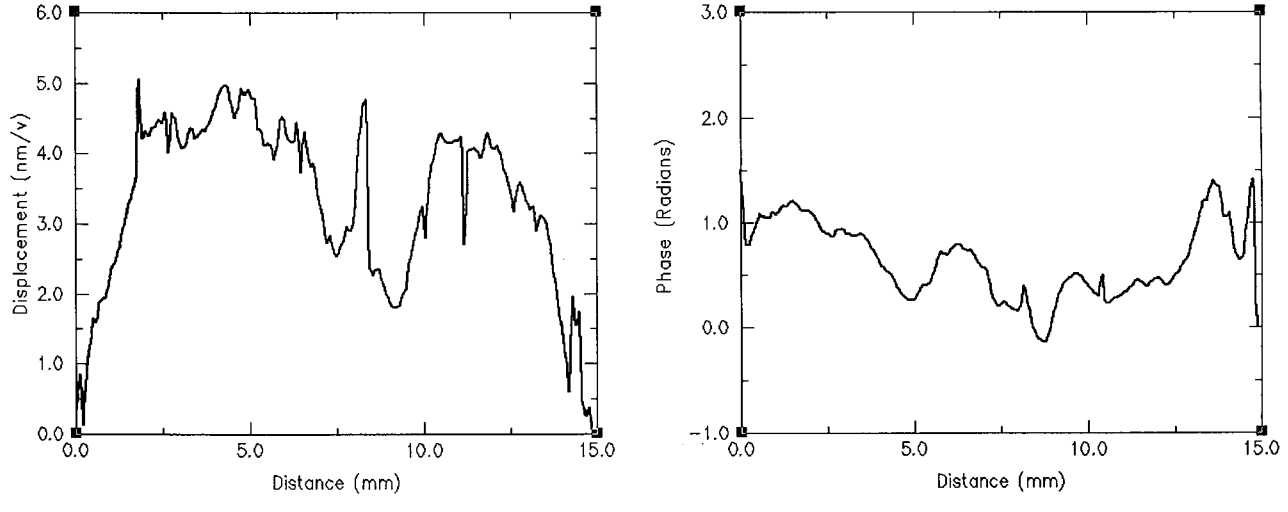

Figure 5.89 Cross-section Displacement Across Alternating Ceramic and Polymer at 622 kHz for Composite 22A

In addition, there appears to be a slight disbond between a ceramic and polymer bar in the top centre of the transducer in Figure 5.86, that while not visible to the eye on the transducer, nor apparent in the impedance profile, has had an effect on the transducer performance. The surface displacement across the entire transducer in Figure 5.89 (alternating ceramic and polymer), shows the location where the disbond causes a rapid fluctuation in surface displacement magnitude approximately 7 mm from the transducer left hand edge. This indicates that flaws within transducers may go undetected by testing procedures as limited as impedance profiles, and these flaws may have significant impact on transducer output. It is likely that laser scanning of composite devices could be a valuable tool in the quality assurance of any transducer manufacturing facility.

The SDP at 91 kHz is displayed in Figure 5.90, with the FEA equivalent as Figure 5.91 and a surface displacement slice along a ceramic bar length as Figure 5.92. Both results indicate that at the ends of the ceramic and polymer bars there is almost zero displacement, which builds toward a peak at the centre of the device. While the FEA again shows good correlation with experiment, the finite element response shows little difference between ceramic and polymer displacement, and as in the 1-3 composites, is due to the inadequate damping models within ANSYS. It appears that the incorrect damping has ensured that the polymer moves entirely in phase with the ceramic, with almost the same magnitude of displacement. These figures illustrate that not only is there a mode formed within the ceramic bars, but that the displacement at 91 kHz is over 50% of that at the thickness mode.

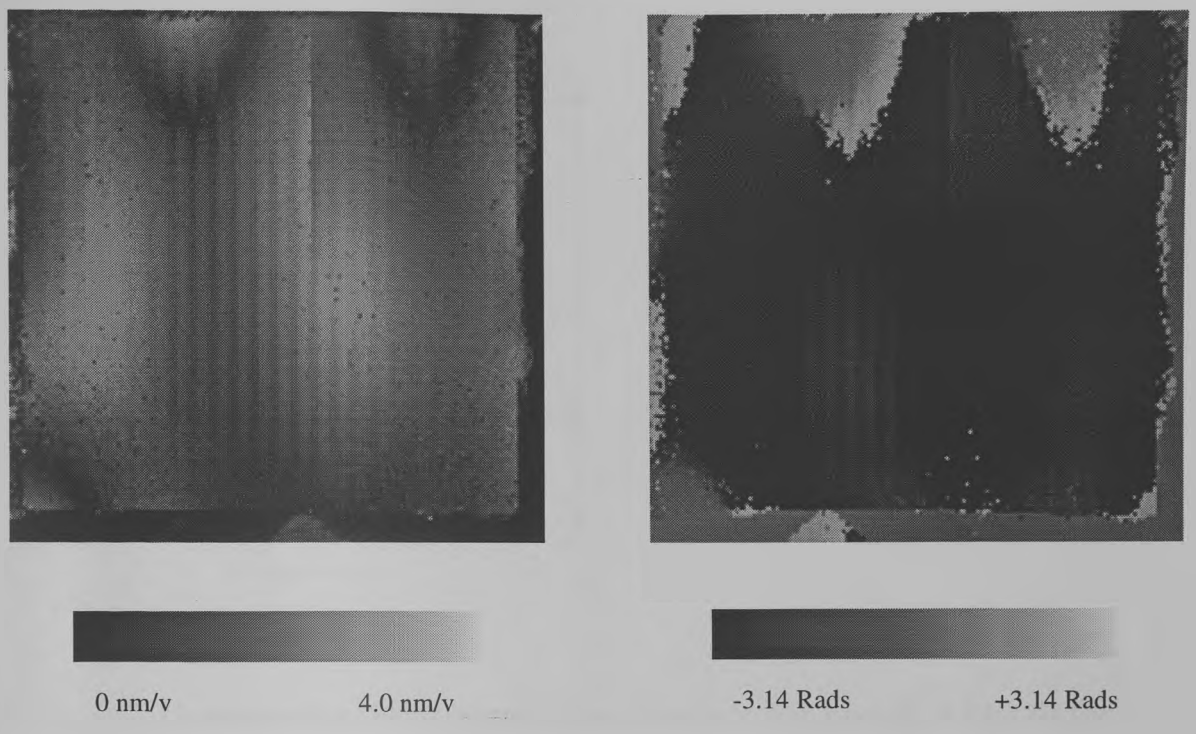

Figure 5.90 Experimental SDP at 91 kHz for Composite 22A

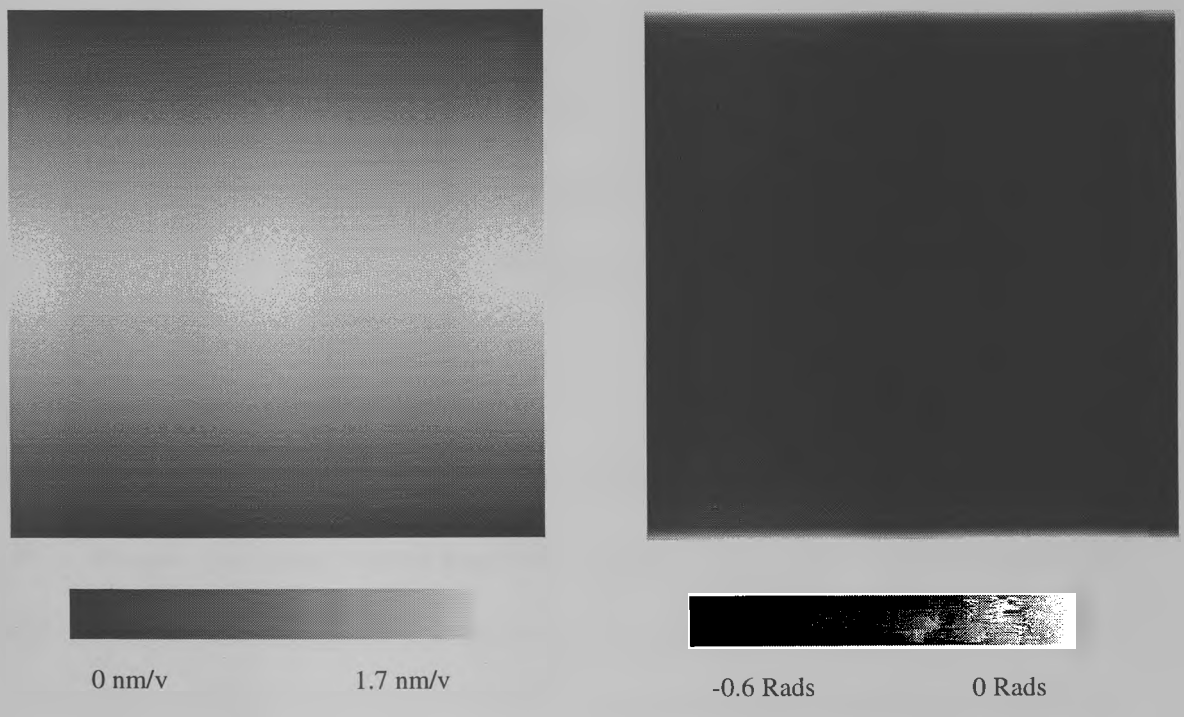

Figure 5.91 FEA SDP at 91 kHz for Composite 22A

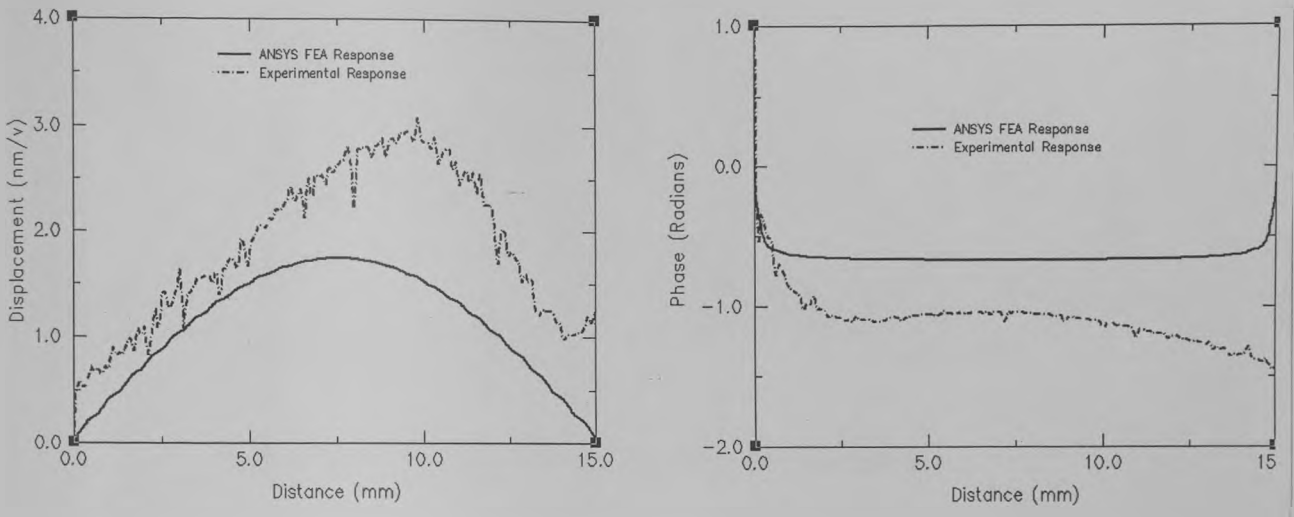

Figure 5.92 Cross-section Displacement along Ceramic Bar Length at 91 kHz for Composite 22A

Transducer 22A has an overall side length to thickness ratio of 6, similar to that of 13B, yet the width mode harmonics do not attenuate with frequency as quickly as in the 1-3 composite due to the more continuous structure. It is clear that, given the continuous bars of material within 2-2 composites, an overall side length to thickness ratio greater than 10 is required for 2-2 composites.

5.5.2 Analysis of Composite 22B

The impedance profile for composite 22B is shown in Figure 5.93, and compares well to FEA. Despite the larger overall length to thickness ratio of 10, the harmonics of a bar length mode still are apparent at the thickness mode. It is likely, therefore, that the overall length to height aspect ratio for 2-2 composites should be increased to at least 15. The main thickness mode of this device occurs at 1000 kHz, with an inter-plate resonance occurring experimentally at 1622 kHz. As with composite 22A, Lamb wave theory predicts the inter-plate resonance to occur at 1871 kHz.

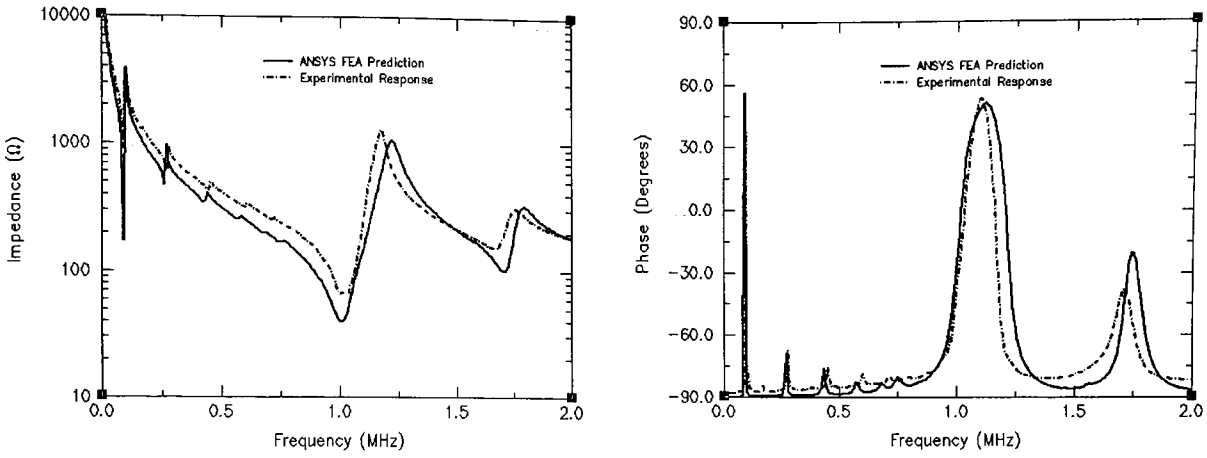

Figure 5.93 Impedance Profile for Composite 22B

Figure 5.94 details the SDP at 1000 kHz, the thickness mode fundamental resonance for this transducer. The proximity of the inter-plate resonance to the thickness mode indicates that the polymer and the ceramic in this transducer will vibrate independently, as in a 1-3 composite transducer with AR greater than MPAR. To facilitate the readers understanding of the SDP, a cross-sectional slice of the response is presented in Figure 5.95, along with the FEA results for comparison. FEA again shows excellent correlation. The polymer bars can be seen to be displacing significantly more than the ceramic, with an even magnitude across their entire length. The entire structure displaces with a very constant phase.

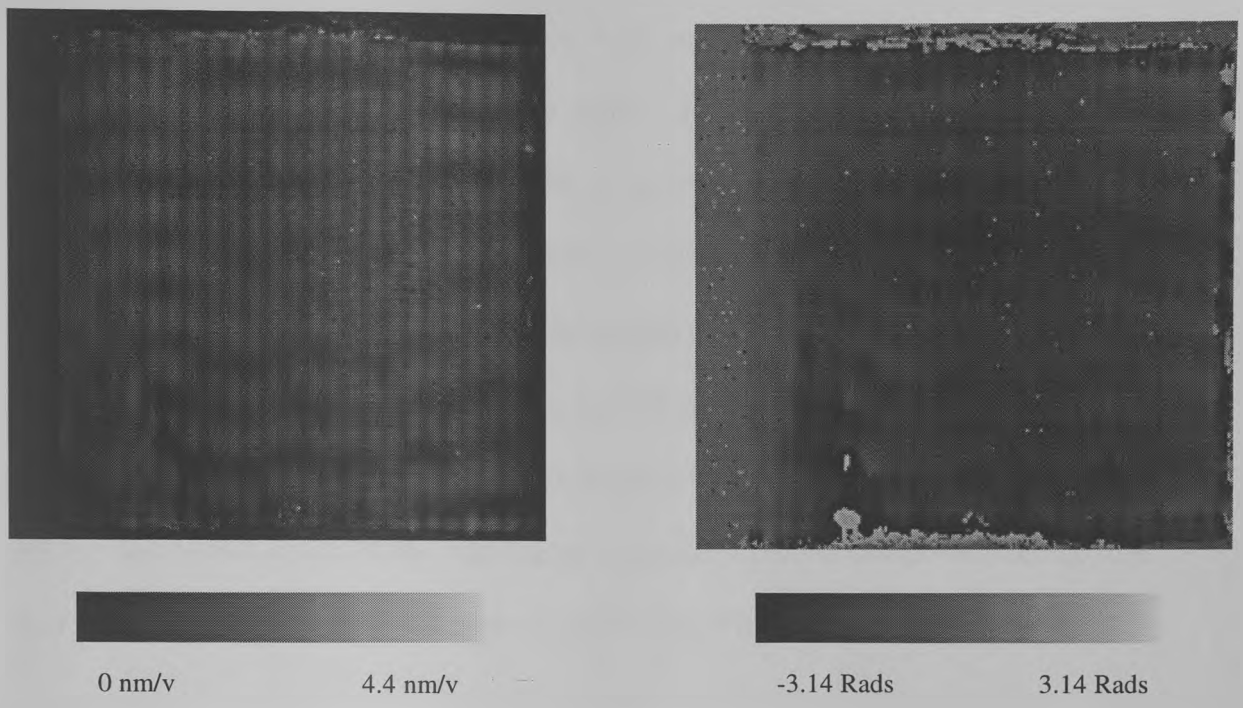

Figure 5.94 Experimental SDP at 1000 kHz for Composite 22B

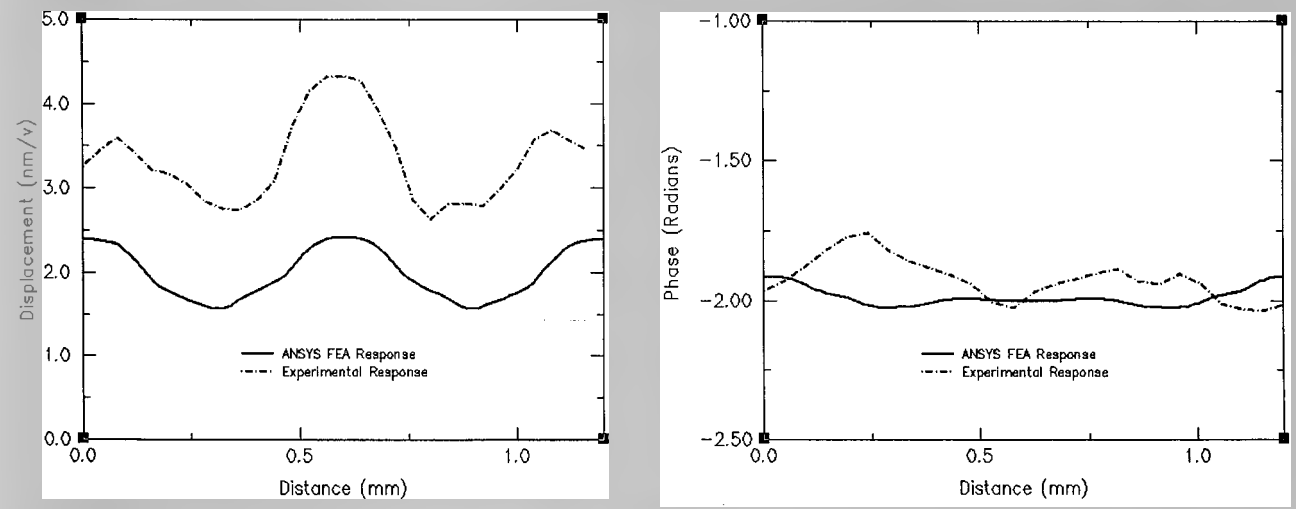

Figure 5.95 Cross-sectional Displacement at 1000 kHz for Composite 22B (Zoom)

The inter-plate resonance SDP at 1622 kHz is shown in Figure 5.96, and details the polymer displacing more than the ceramic, with polymer and ceramic moving out of phase with one another. To assist the reader, an enlarged, cross sectional SDP comparison between FEA and experiment is provided in Figure 5.97, and enlarged section of the experimental and FEA SDPs are presented as Figures 5.98 and 5.99. Once again FEA accurately predicts experimental displacement behaviour. It can be clearly seen that the polymer is displacing significantly more than the ceramic, with a phase difference of almost 180 degrees between the two materials. This is similar to the surface displacement of the first lateral resonance of a 1-3 composite, and in this case the ceramic displacement is approximately that of the polymer.

To confirm this behaviour as a Lamb mode, two non-electrically driven finite element models were written. The first maintained the same physical structure and properties as in the composite, but no electrodes were applied. The driving force was a sinusoidal force peak amplitude 1 N along the centre of each ceramic bar, running along the length. The second model was identical to the first, except the ceramic was replaced with polymer, to leave a solid plate of polymer. Figures 5.100 and 5.101 show the results as a cross sectional slice, and again show excellent correlation. The only significant difference between these and experiment is in the polymer only model, where the region around the driving function again displaces more than is seen in a composite due to the lower stiffness of the polymer. The frequency of the mode shape in 5.101 at 1580 kHz is lower than in 5.100 (1780 kHz), indicating that the additional ceramic has increased the phase velocity.

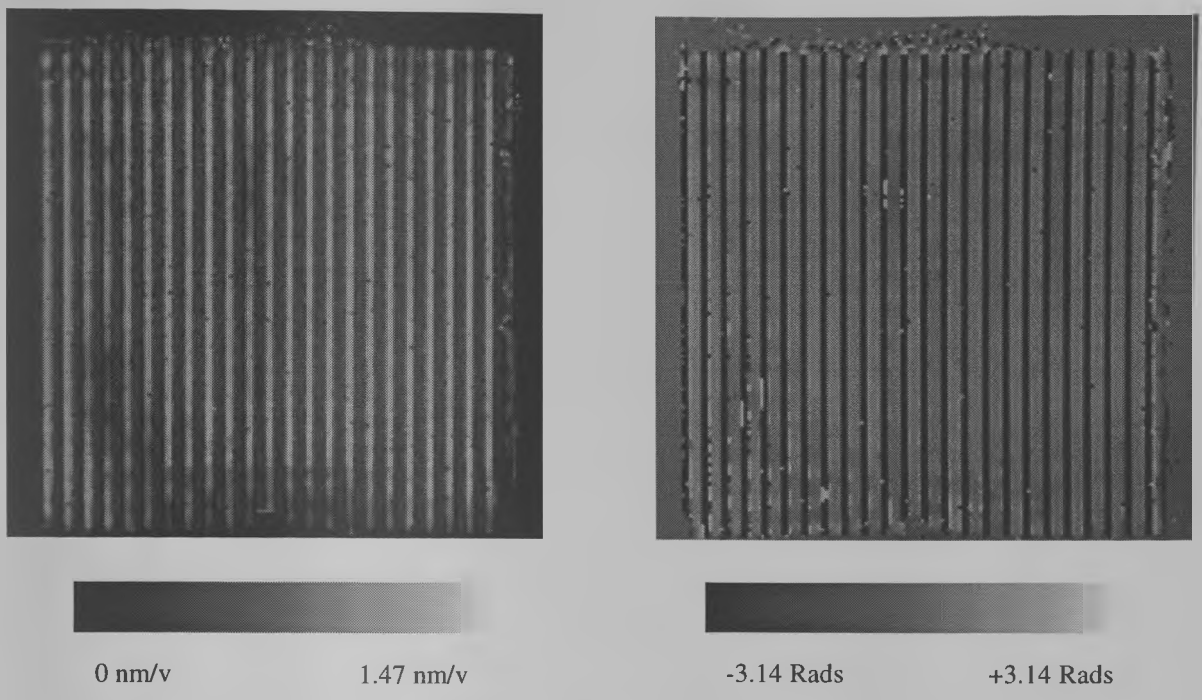

Figure 5.96 Experimental SDP at 1622 kHz for Composite 22B

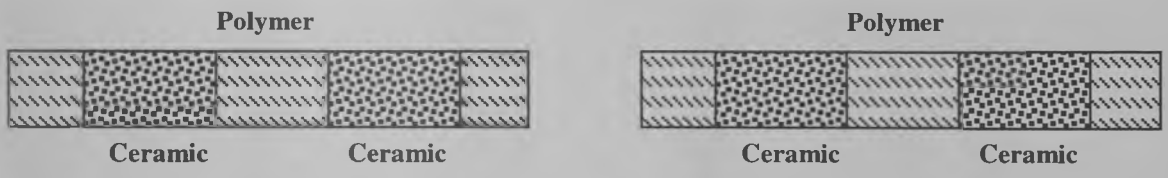

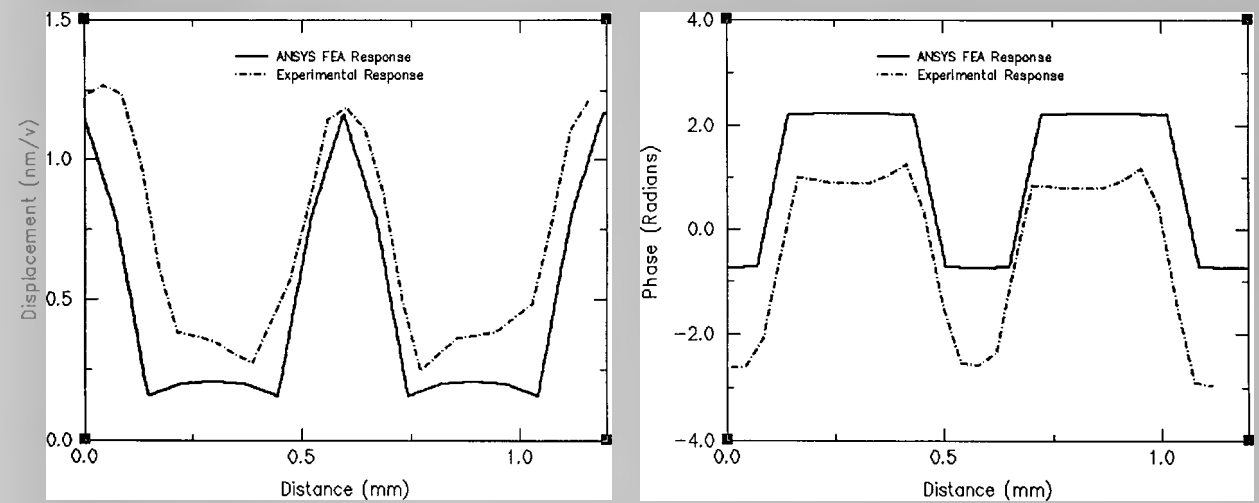

Figure 5.97 Cross-sectional Displacement at 1622 kHz for Composite 22B (Zoom)

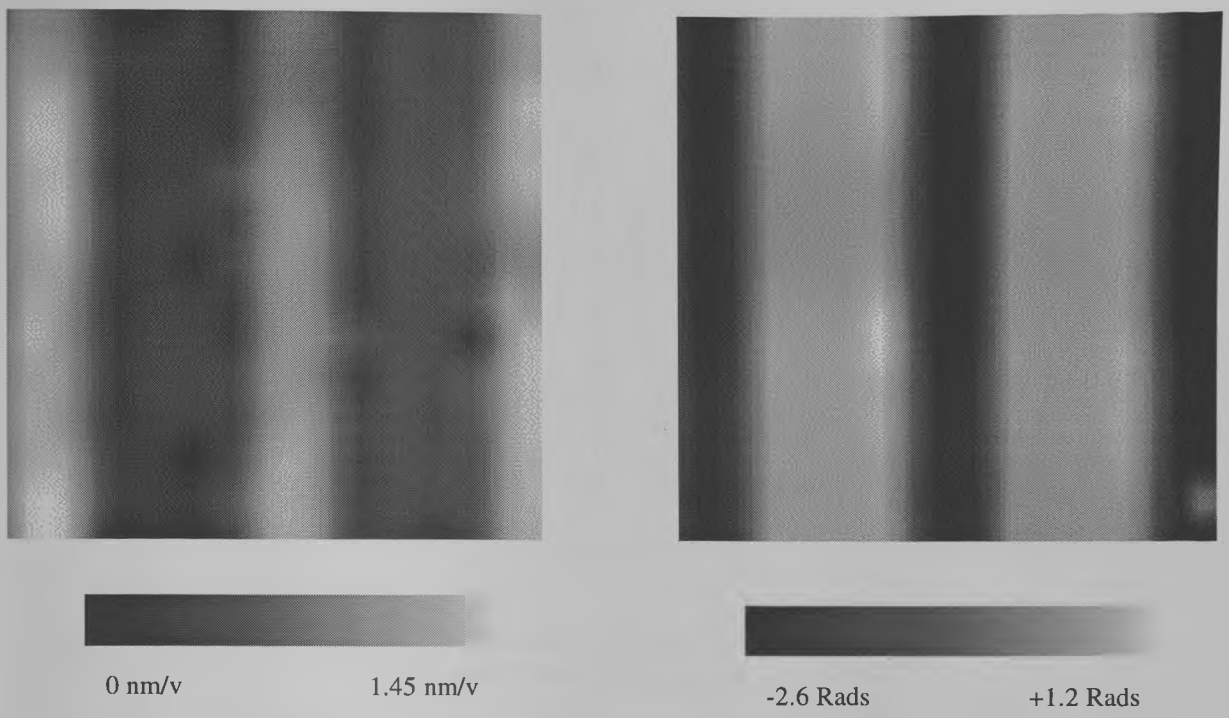

Figure 5.98 Experimental SDP of Composite 22B at 1622 kHz (Zoom)

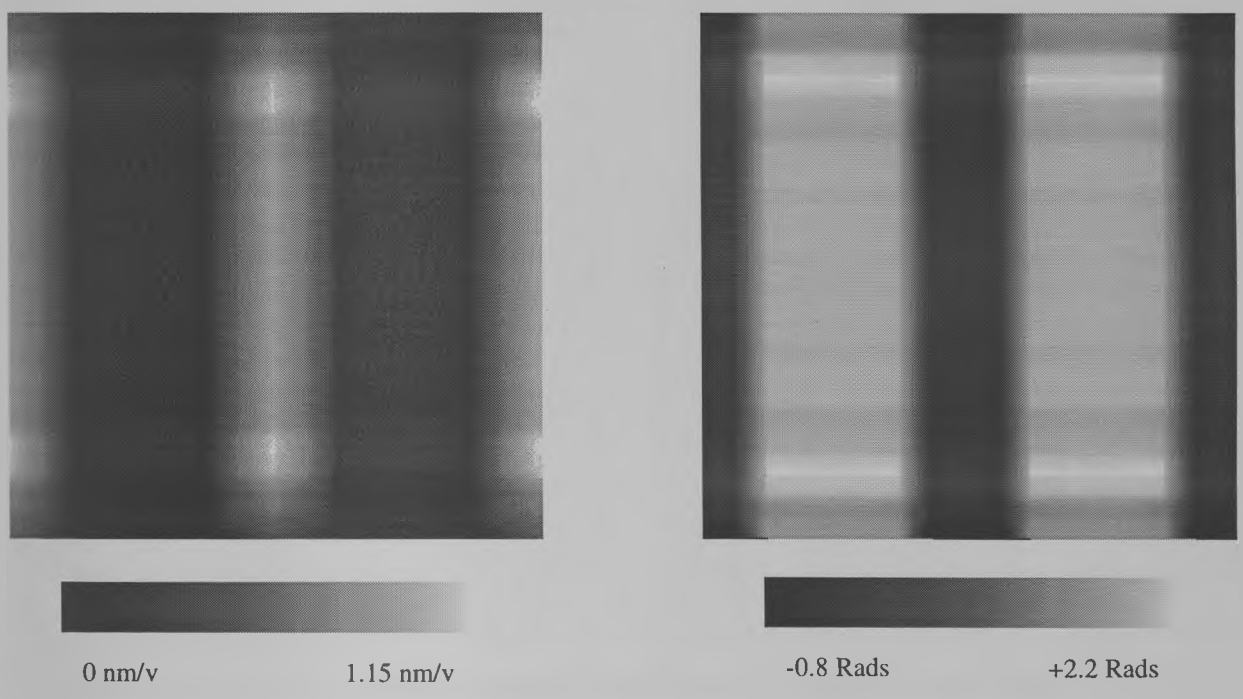

Figure 5.99 FEA SDP of Composite 22B at 1703 kHz (Zoom)

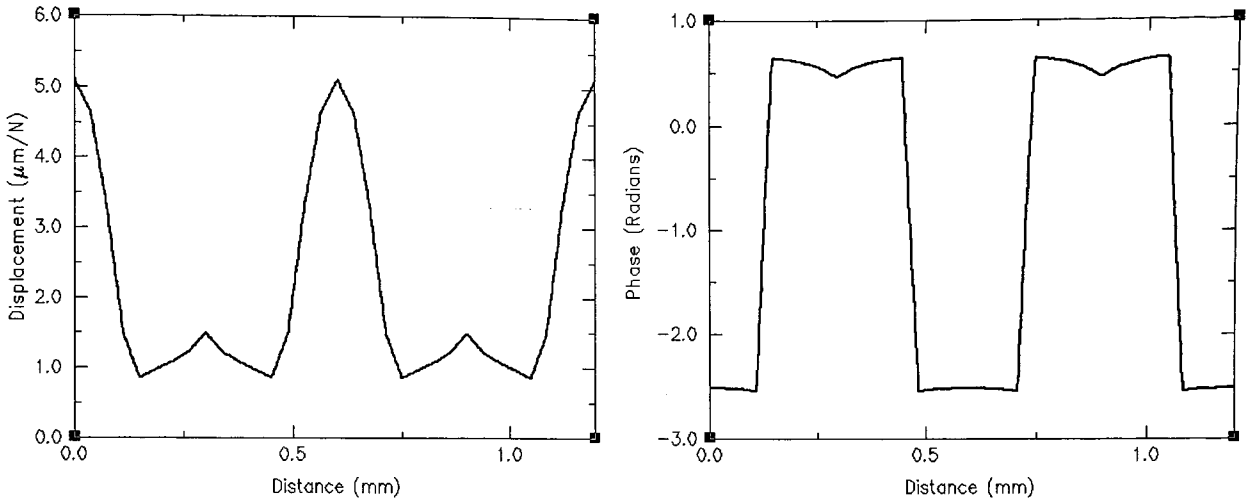

Figure 5.100 Cross-section Displacement across Composite 22B at 1780 kHz – Lamb Wave Generation

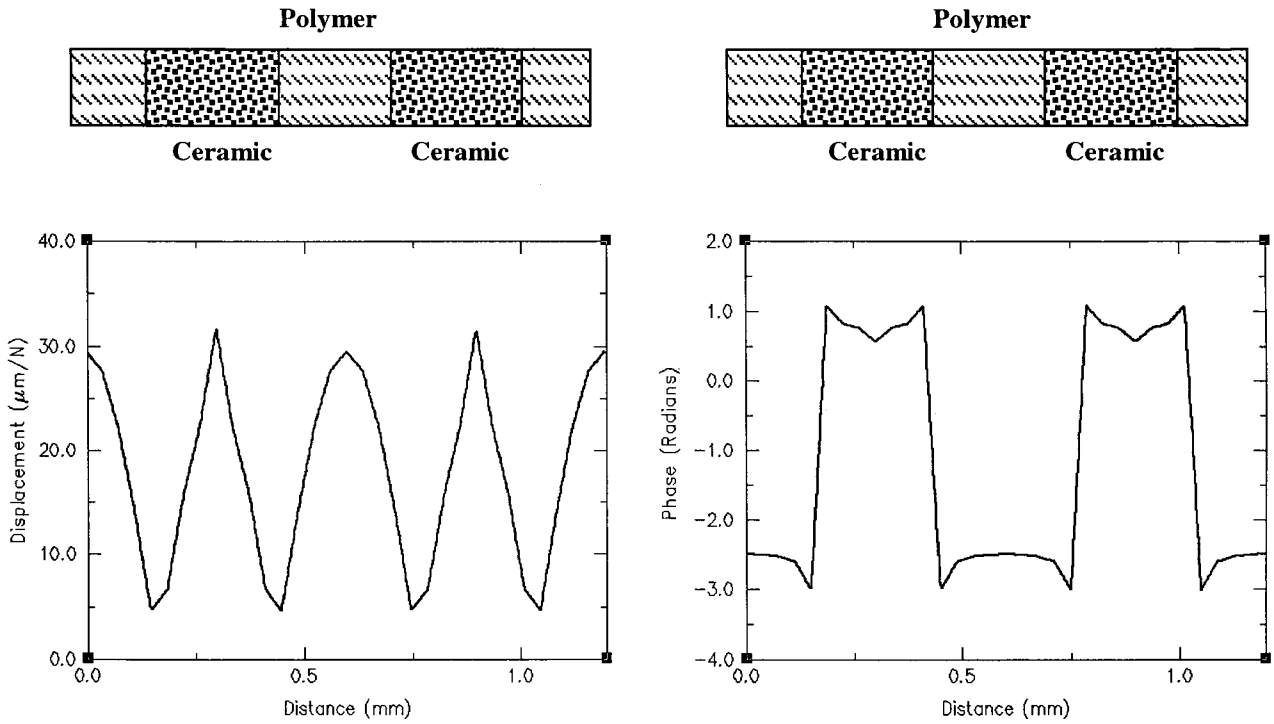

Figure 5.101 Cross-section Displacement across Polymer at 1580 kHz – Lamb Wave Generation

The analysis of both these 2-2 composites has made it abundantly clear that they obey the same basic rules for resonant behaviour, and that a set of design guidelines for their behaviour, similar to those of MPAR for 1-3 composites would be desirable.

5.6 Determination of MPAR limits for 2-2 Composite Transducers

Verification of the finite element model by experimental results leads to the possibility that a range of MPAR values for 2-2 composites can be generated with confidence. These limits would allow a designer to quickly check whether the design of a 2-2 composite was viable, in the same way that can currently be done for 1-3 composites.

Harmonic analysis was used to analyse the impedance profiles and surface behaviour of 2-2 composites in the VF range 10 – 90% in 10% steps. The transducers modelled had a 1.0 mm saw pitch, with ceramic pillar width varied to alter VF, and thickness varied to alter AR. Criteria used to select MPAR were identical to those of Bennett, i.e.

- Surface Dilation Quality greater than 90% at electrical resonance.
- First lateral mode greater than twice the thickness electrical resonance frequency.

As Q_{DIL} is now calculated as Q_{AMP} and Q_{PHI}, this criterion is slightly altered to state that both dilation qualities must be greater than 90% at electrical resonance. The use of harmonic analysis allowed damping to be used, and this was set at a value typical for the frequency range under consideration. As damping was present, certain modes,

although present, may be damped so greatly that their presence is difficult to detect. Should this be the case, the modes were not accounted for as they would fail to influence a transducer in a real world situation.

VF	MPAR	Q_{AMP}	Q_{PHI}	k_t
10	0.035	0.904	0.993	0.51
20	0.060	0.902	0.994	0.50
30	0.090	0.923	0.995	0.55
40	0.135	0.920	0.994	0.55
50	0.235	0.900	0.988	0.57
60	0.36	0.900	0.984	0.57
70	0.46	0.984	0.989	0.58
80	0.42	0.963	0.997	0.59
90	0.44	0.963	0.999	0.58

Table 5.06 MPAR Limits of PZT-5H/Hardset 2-2 Composites

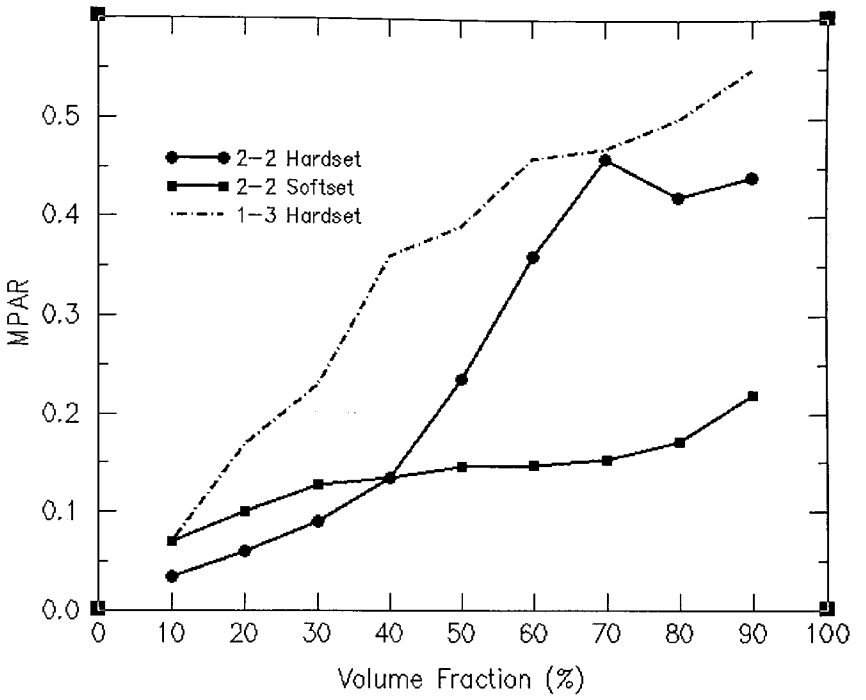

Figure 5.102 Graph of MPAR against Frequency

These results (Table 5.06) indicate that the MPAR for low VF 2-2 hardset composites is extremely small, due to the large periodicity resulting in a very low frequency first inter-plate mode. The 10% MPAR value is much lower than in a 1-3 hardset composite (0.07), but this is expected as any 1-3 composite with the same kerf : pillar ratio would be a 1% VF composite. As VF increases, the MPAR value rapidly increases until a peak MPAR is reached at 70%, due to the increasing frequency of the first inter-pillar mode. Indeed, it is not until a 50% volume fraction is reached that the limitation on MPAR comes from Q_{DIL} rather than the inter-plate mode frequency. Beyond 70%, however, the MPAR decreases slightly, as the limiting factor becomes the intra-plate mode frequency, rather than the inter-plate mode frequency. Figure 5.102 shows how MPAR varies with VF, and is shown against the results for a 1-3 composite. It is clear that as VF increases, the 2-2 MPAR approaches the value for 1-3 composites, which also show a peak at 70% for identical reasons. As 2-2 VF

Using material properties determined for softset epoxy, a table of MPAR for PZT-5H/softset transducers was calculated in the same manner, and is presented as Table 5.07.

The MPAR for 10 and 20% VF softset 2-2 composites is nearly twice that for the equivalent hardset composites. As softset polymer is a more heavily damped polymer, any modes travelling through the large quantity of polymer that makes up 80-90% of the composite will be heavily damped, increasing the frequency at which the first Lamb mode is met. In the volume fraction range 30 – 50%, the MPAR fails to increase at any great rate as the inter-pillar modes, now less significantly damped, impinge on thickness mode operation more readily than in hardset due to the lower Rayleigh velocity. At 60% VF and above, the limiting factor to MPAR is now dilation quality, as the ceramic begins to displace independently of the pliant softset polymer.

Coupling coefficients in softset 2-2 transducers are higher than in their hardset counterparts up to a VF of 50%. As the softset polymer is more pliant than hardset, the ceramic plates are less clamped laterally and consequently more closely approach the value of k_{33}. At higher VF, the limited quantity of polymer cannot allow the ceramic such lateral motion, and coupling begins to reduce toward that of pure ceramic.

It appears from these results that for low volume fraction 2-2 composites (up to 40%), that softset epoxy is the preferred filler, while hardset epoxy is better suited to the higher volume fractions.

5.7 Conclusions

A number of conclusions can be reached following the in air analysis of the five 1-3 composite transducers. Firstly, the MPAR recommendations of Bennett appear to hold for PZT-5H composites. Failing to meet those criteria results in inter-pillar modes impinging upon thickness mode operation. It has been shown that should a transducer not meet these criteria, thickness mode displacement will consist of the polymer displacing by a large quantity, with limited ceramic motion.

Through laser vibrometry, FEA SDPs, and impedance profiles, it has been demonstrated that the Bragg scattering model for inter-pillar mode prediction, while producing acceptable numerical predictions, fails to accurately describe the mechanism by which these modes are generated. Rather, Lamb waves (more specifically the fundamental symmetrical mode, s_0) are formed by the periodicity of the ceramic pillars acting as interdigital transducers of lambda spacing. Should loading conditions of the composite alter, such as with the addition of a matching layer, it was hypothesised that it may be the antisymmetrical a_0 mode that will become the carrier of the inter-pillar resonance. This change of resonance mode will obviously occur under particular conditions, and is recommended as a topic for further study.

The Bragg scattering model has succeeded in producing acceptable numerical results to date due to the identical spacing of the scattering planes and ID fingers, and the similarity of shear velocity and Rayleigh velocity in polymer (which differ by less than 10% for the majority of polymers) for most composites at inter-pillar resonance frequencies. The Lamb wave theory predicts that the first two strongly coupled inter-pillar modes in composites meeting the above criteria are

$$f_{L1} = \frac{v_{phase}}{2d_0} \qquad f_{L2} = \frac{\sqrt{2}v_{phase}}{d_0}$$

where

f_{L1} and f_{L2} are the frequencies of the first two inter-pillar modes

v_{phase} is the phase velocity of the Lamb wave the polymer

d_0 is the pillar separation.

Additionally, it was suggested that an approximation for the phase velocity of an inter-pillar mode could take the form

$$v_{phase} = v_{RPOLY} + (VF^2)(v_{RCER} - v_{RPOLY})$$

where v_{RPOLY} is the Rayleigh velocity of the polymer, v_{RCER} is the Rayleigh wave velocity of the ceramic, and VF is the ceramic volume fraction.

Table 5.08 summarises the results for the composites in this thesis, and again compares the Lamb wave theory predictions with the results from Bragg scattering. In these cases, neither theory clearly stands out as superior, although it should be noted that the Bragg scattering theory is inapplicable to 2-2 composites. Frequency values are in kilohertz

Device	Experiment		FEA		Lamb wave		Bragg	
	f_{L1}	f_{L2}	f_{L1}	f_{L2}	f_{L1}	f_{L2}	f_{L1}	f_{L2}
22A	1800	NA	1901	NA	1871	NA	NA	NA
22B	1622	NA	1703	NA	1871	NA	NA	NA
13A	1000	1500	NA	NA	1177	1660	1127	1590
13B	NA	1900	NA	1957	1548	2183	1551	2186
13C	1910	2800	1910	2815	2007	2830	2100	2956
13D	1620	2400	1671	2352	1548	2183	1551	2186
13E	1722	2301	1790	2341	1548	2183	1551	2186

Table 5.08 Summary of Inter-pillar Resonances for Composites used in this Thesis

It is of interest to note that the FE predicted frequencies are, in most cases, closer to the Lamb wave predictions than the experimental results. This is likely due to small manufacturing imperfections in the composites altering the resonant frequencies, and the difficulty in obtaining a true resonance frequency from an electrical impedance profile.

Due to the reduced pillar displacement at frequencies other than the thickness mode, inter-pillar resonances that are significantly separated in frequency from the thickness mode will not couple strongly, as seen in composites 13A and 13B.

It was also demonstrated that should a composite not meet the criteria of overall width to thickness ratio of at least 10 : 1, that a width mode harmonic may couple into the thickness mode behaviour. While this was shown to be of minimal effect for typical 1-3 composite transducers, extremely low frequency composites or multi-layer stacks

may find significant departure from homogenous surface displacement due to the width mode. Additionally, it was suggested that the overall width to thickness aspect ratio for 2-2 composites be at least 15 : 1 to prevent harmonics of ceramic bar length modes impinging upon the thickness mode.

The addition of a quarter wavelength matching layer was, as expected, shown to introduce an additional mode to composite in-air behaviour. While producing a strong resonance due to the entire composite/matching layer structure as expected, the thickness mode frequency of the device was actually increased. This was shown to be due to the quarter wavelength matching layer causing destructive interference at the desired thickness mode resonance, and it was demonstrated that a half wavelength matching layer (at the thickness mode frequency) would result in the matched composite resonating at the desired frequency.

Laser vibrometry indicated that this composite/matching layer structure displaced by a large quantity in a uniform manner. This identifies a possibility for the improvement of the performance of 1-3 piezocomposites operating into air. By examination of the SDP of a composite with an AR above MPAR, where the polymer displaces more than the ceramic at both thickness mode resonance and the first inter-pillar mode, it appears that ultrasonic energy is coupled no more efficiently to the air than in cases of uniform displacement. This, however, is an area that requires further study and is suggested as an area for further work.

2-2 Composites have also been accurately modelled and scanned, with similar findings to those in 1-3 composites. The MPAR values for PZT-5H/hardset and PZT-

5H/softset 2-2 composites have been calculated for a range of volume fractions, indicating that softset epoxies are more appropriate at low VF, and hardset epoxies at high VF.

FEA has been shown to provide excellent correlation when compared with experiment, in predicting impedance profiles and SDPs, but only when the composites are manufactured to a high standard. Techniques to minimise CPU time for accurate analysis, and criteria for determining type of SDP to perform were also developed. While FE techniques are excellent guides as to structural behaviour, it is important to note that computation times for many of the models presented in this chapter run to days and sometimes weeks with current computing power, indicating that great care must be taken when applying such techniques.

Chapter 6

Design and Construction of an Improved Flexible Array for Non-Destructive Testing

6.1 Introduction

Previous chapters have demonstrated the viability of FEA to model piezocomposite transducers. While the accuracy of the method is clear, the question remains as to whether FEA is a useful tool in improving the design of ultrasonic transducers. Consequently, this chapter will focus on the design of a piezocomposite device, using FEA whenever possible to analyse parameters such as material selection, with the aim of producing a finalised design with the minimum of prototype device construction. The construction and testing of this improved design will then be described to demonstrate the usefulness of FEA.

Ultrasound has found uses in many fields such as biomedicine and non-destructive testing (NDT), given its ability to interrogate targets at remote locations without interfering in the operation of most structures. Extensive work in ultrasonic arrays for NDT was carried out by Powell and Hayward [59,60], culminating in the design of a new type of composite device that could be both flexible and used for array imaging purposes. While proven an acceptable method of obtaining images of flaws within test samples, these devices were far from ideal and so are a suitable candidate to fulfil the aims of this chapter.

6.2 Piezo-platelet Transducers

Previous chapters have stressed the importance of pillar aspect ratio in the construction of any composite transducer, with guidelines indicating that its value be kept significantly below 1, in the region of 0.1 – 0.3 for most transducer types. While this is a reasonable AR to achieve in low frequency (< 1 MHz) transducers, as frequency increases, device thickness decreases and greater demands are made upon

the manufacturing process. Ultimately, there is a finite limit to how thin a saw blade used in the 'Dice and Fill' technique can be; this sometimes results in transducers being manufactured with non-ideal aspect ratios.

6.2.1 Mechanical Description

It should be apparent, however, that it is not a low aspect ratio that is required, but a sufficient difference between pillar width and height to ensure that inter or intra-pillar modes do not interfere with thickness mode operation. Thus, it is evident that an AR of significantly greater than 1 would be as effective in separating resonances as an AR of less than 1 – i.e. the pillar width is greater than the pillar height. This would be particularly useful in high frequency transducers where the pillar height is already small. A composite device manufactured in this manner would consist of ceramic sections more like tile or plates than pillars, as is illustrated in Figure 6.01. To differentiate this type from standard composites, it was decided to name it a *piezo-platelet* device.

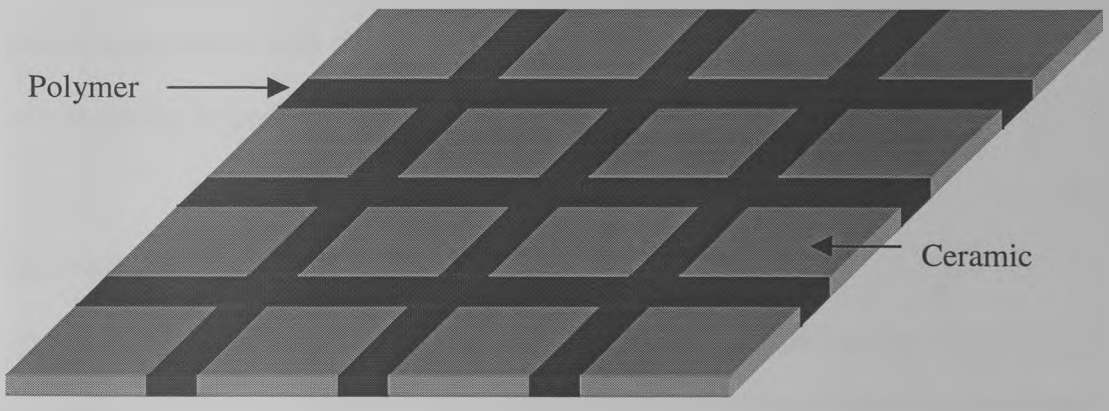

Figure 6.01 Piezo-platelet Transducer Structure

6.2.2 Advantages and Disadvantages of Piezo-platelet Devices

The most obvious benefit of piezo-platelet devices is the higher operating frequency than could typically be achieved by 1-3 composites without encountering intra-pillar resonances. Additionally, by using a soft-setting polymer as the passive filler, these devices could be made flexible, with flexibility limited only by width of each platelet and platelet separation. The combination of flexibility and high-frequency operation make such devices ideal for ultrasonic imaging of test subjects with non-planar surfaces.

Unfortunately, this type of construction also ensures that some of the benefits of 1-3 composites are lost. Due to the width of each ceramic plate, thickness coupling coefficients fail to approach k_{33} and consequently are almost identical to that of the constituent ceramic, typically 0.5. The high volume fraction required by these devices also limits the options for tailoring the acoustic impedance of the transducer to more closely match that of the target media. While this is of little importance for NDT applications where the impedance of the test subjects is typically very high, any biomedical applications will require piezo-platelet devices to be constructed with at least one matching layer to ensure efficient energy transfer.

6.2.3 Alternatives to Flexible Arrays

Current methods of using ultrasonic transducers in the non-destructive testing of curved surfaces encounter many problems. Conventional ultrasonic transducers have a flat profile, preventing more than a limited area of contact between probe and specimen without additional alterations. A transducer could be manufactured in a curved shape, but this would result in a transducer suitable only for one surface

geometry. Alternatively, an 'ultrasonic shoe' could be constructed, with one flat and one curved side, to fit between the flat transducer and the curved surface. While this solves the problem of conformability, it introduces additional boundaries through which the ultrasound must travel, increasing energy loss. A final option is to machine a 'flat' into the surface of the object tested [57]– this, however, has the dual problems of altering the tested object and of limiting the location at which testing can be done.

A flexible ultrasonic transducer overcomes the need for specially shaped transducers, additional equipment or altered test subjects. It is not limited to sections which can be tested, and may fit into areas where conventional transducers would not, due to its low profile. Indeed, a truly flexible array could conform to small irregularities on a test surface, which neither a pre-formed transducer nor an ultrasonic shoe could easily accomplish.

6.2.4 Previous Generation Flexible Transducers

The flexible transducers used by Powell [59] were highly effective in obtaining images from test samples, but were limited in a number of respects. Firstly, in order to make the devices more wideband, a tungsten loaded epoxy backing was added, reducing the sensitivity of the devices, and also increasing their thickness to approximately 10 mm. Secondly, the devices were pitch-catch in nature – that is, they had a large aperture piezo-platelet transmitter and a PVDF receiver. PVDF is a flexible piezo-polymer that is highly conformable but has a low dielectric constant making it difficult to match to drive electronics, a low electromechanical coupling coefficient making it a poor transmitter of ultrasound, and a low acoustic impedance, which can result in large energy losses at boundaries with metals. Finally, these

devices operated at a maximum frequency of 4 MHz. While they proved that the concept of a piezo-platelet transducer was viable, further work was required to move the concept closer to a practical device.

6.3 Design of New Transducers

In designing the next generation of the flexible transducers, the aim was to produce an unbacked, pulse-echo device that could operate in the frequency region 6 – 8 MHz, with less than 1 mm overall thickness. In doing so, great care was required in material selection, platelet construction and manufacturing process – much of which could be assisted by the finite element modelling techniques already developed as described in this thesis.

6.3.1 Material Selection

Requirements for the ceramic material remained similar to those of Powell's [59], who conducted a thorough analysis of material properties. Most importantly, the ceramic used had to have low *cross-coupling* – that is, that the activity of any element should not affect the response of any adjacent element. Low cross-coupling also ensures that any lateral resonances have a limited effect upon the thickness mode resonance within a ceramic plate. Additionally, as these new devices were to be unbacked, the inherent damping within the ceramic had to be high in order to ensure that the transducer response was sufficiently wideband for imaging applications.

As mentioned in earlier chapters, the PZT materials offer excellent coupling coefficients, dielectric constants and sensitivity, making them ideal for many transducers. They are not, however, materials that can be said to have low cross

coupling, and a piezo-platelet device made of this material would have significant cross-talk between elements and many resonances impinging upon the thickness mode resonance. Two alternatives stood out as possible candidates – Modified Lead Titanate (MPT) and Lead Metaniobate (PMN). MPT has good cross-coupling properties, with its lateral piezoelectric strain component ($\mathbf{d_{13}}$) being approximately one-quarter of its thickness component (as compared to approximately a half for PZT-5 materials). However, the dielectric constant of MPT is considerably lower than that of PZT materials, and it is also likely to result in more narrowband devices due to its higher mechanical Q. PMN has a thickness piezoelectric strain component nearly nine times its width component, dielectric constants similar to MPT, but a mechanical quality factor that is very low, implying high damping resulting in shorter ring-down times and therefore more wideband devices. The exact values for these material properties are summarised below in Table 6.01.

	PZT-5A	PZT-5H	MPT	PMN
$\mathbf{d_{13}}$ ($\mathbf{CN^{-1}}$)	-171	-274	-21	-10
$\mathbf{d_{33}}$ ($\mathbf{CN^{-1}}$)	374	593	91	85
$\varepsilon_{33}/\varepsilon_0$	833	1470	200	265
$\mathbf{Q_m}$	75	65	922	15

Table 6.01 Material Properties of Various Ceramics

Ideally, the platelet devices should have an aspect ratio of as close to 10 as possible, but for a thickness mode frequency of greater than 5 MHz, a device 0.3 mm thick is

required, and would result in 3 mm wide plates and a corresponding loss of flexibility. Thinner devices could be constructed, but 0.3 mm was a thickness easily reproducible during manufacture, and so a compromise AR of 5 was chosen. Finite element analysis was used to predict the electrical impedance of platelet devices made from PZT-5H, 5A, MPT and PMN; data are given in Figure 6.03. Additionally, the surface displacement of a single cell of each simulation at electrical resonance is shown in Figures 6.04 (a) to (i). The device modelled had a saw pitch of 1.75 mm, a kerf of 0.25 mm resulting in a 74% volume fraction, a thickness of 0.3 mm, and a CIBA-GEIGY CY208/HY956 soft setting polymer as the passive filler.

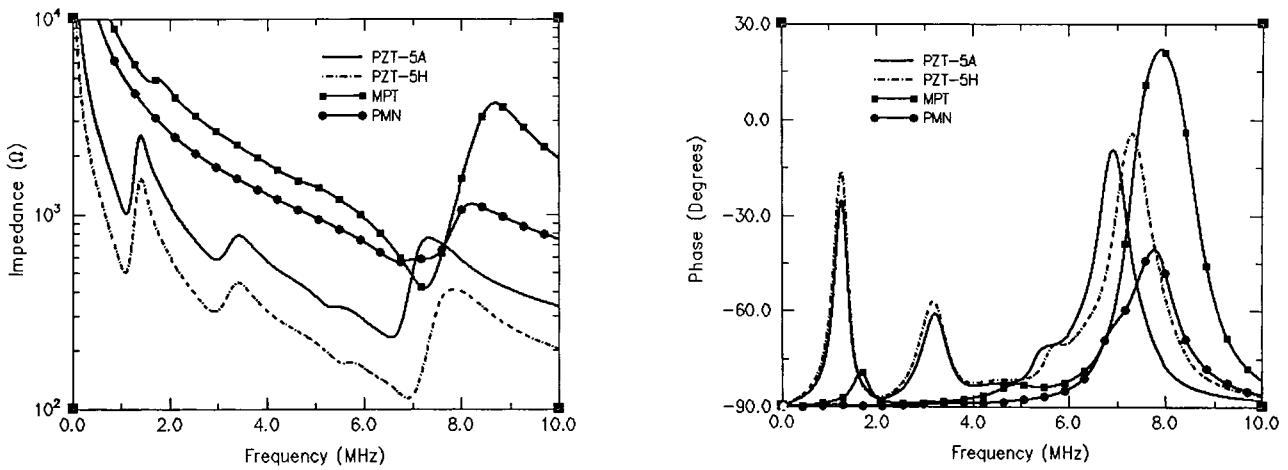

Figure 6.03 Piezo-platelet Impedance Plots for Various Materials

The impedance plots of devices made from PZT materials both exhibit a strong resonance at 1 MHz and its third harmonic at 3 MHz, and a weak fifth harmonic resonance at 5 MHz, just below the thickness resonance at 7 MHz. Both MPT and PMN show much more unimodal responses, with MPT showing a very weak resonance at 1.5 MHz and PMN showing a similarly weak mode at 6.7 MHz. For both

these materials a slightly higher thickness mode electrical resonance frequency is observed than in PZT materials, at approximately 7.2 MHz.

It is important to note that harmonic ANSYS FEA utilises continuous wave narrowband excitation, and any surface displacement profiles produced in this fashion will be for that single frequency only. All the devices modelled showed very 'clean' thickness mode resonances, with little lateral activity, and consequently it was expected that all the SDPs shown in Figure 6.04 would be very uniform in behaviour.

This was not the case, however, as it is clear that the amplitude of displacement varies considerably across the platelet surface in all cases. Table 6.02 list the dilation qualities and maximum displacements for each ceramic piece for comparison. As expected, the MPT and PMN had a Q_{AMP} approximately 50% higher than that of the PZT materials. The PZT materials had the lowest Q_{PHI}, while the MPT and PMN having extremely high qualities at 0.89 and 0.95 respectively. PZT-5A was predicted to have the highest maximum displacement, although the PZT-5H displacement was lower than expected for a PZT material, and was comparable in magnitude to that of the MPT and PMN.

	Max. Displacement	**Q_{AMP}**	**Q_{PHI}**
PZT-5A	0.81 nm/v	0.31	0.81
PZT-5H	0.33 nm/v	0.37	0.65
MPT	0.43 nm/v	0.51	0.89
PMN	0.29 nm/v	0.51	0.95

Table 6.02 Summary of FEA Results for Different Ceramic Materials

It is clear that under broadband excitation the PZT devices would exhibit significant interference from the lateral modes upon thickness mode operation, greatly reducing their efficiency. Additionally, a 'real world' device will have front face loading during operation which may significantly reduce the lateral waves generated. Both these factors lead to concern that PZT materials may not be as poor in practice as modelling suggests. While the results for PZT materials indicate strong lateral modes, it may still be possible to utilise such ceramics if the AR were sufficiently high.

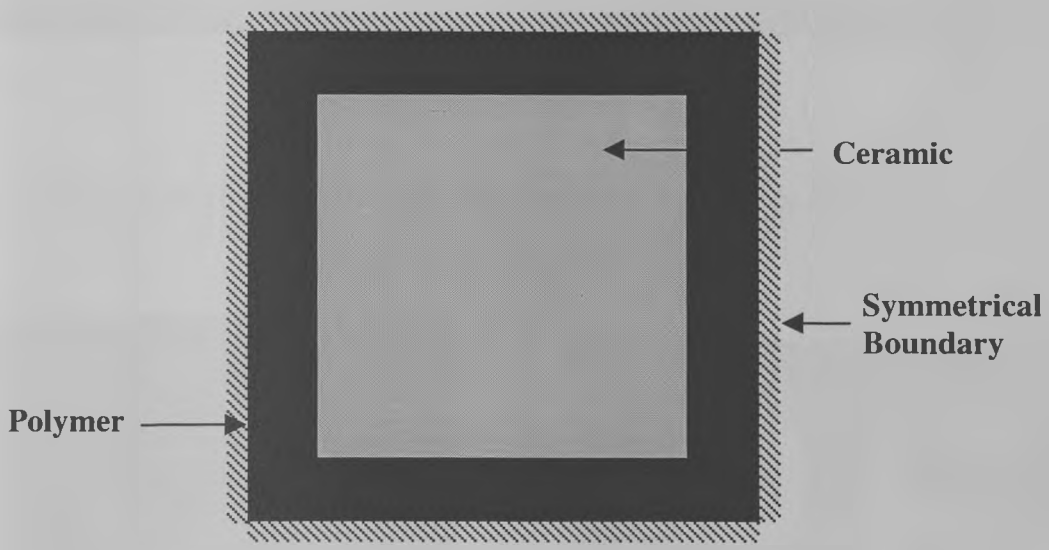

Figure 6.04 (a) Diagram of Unit Cell Model

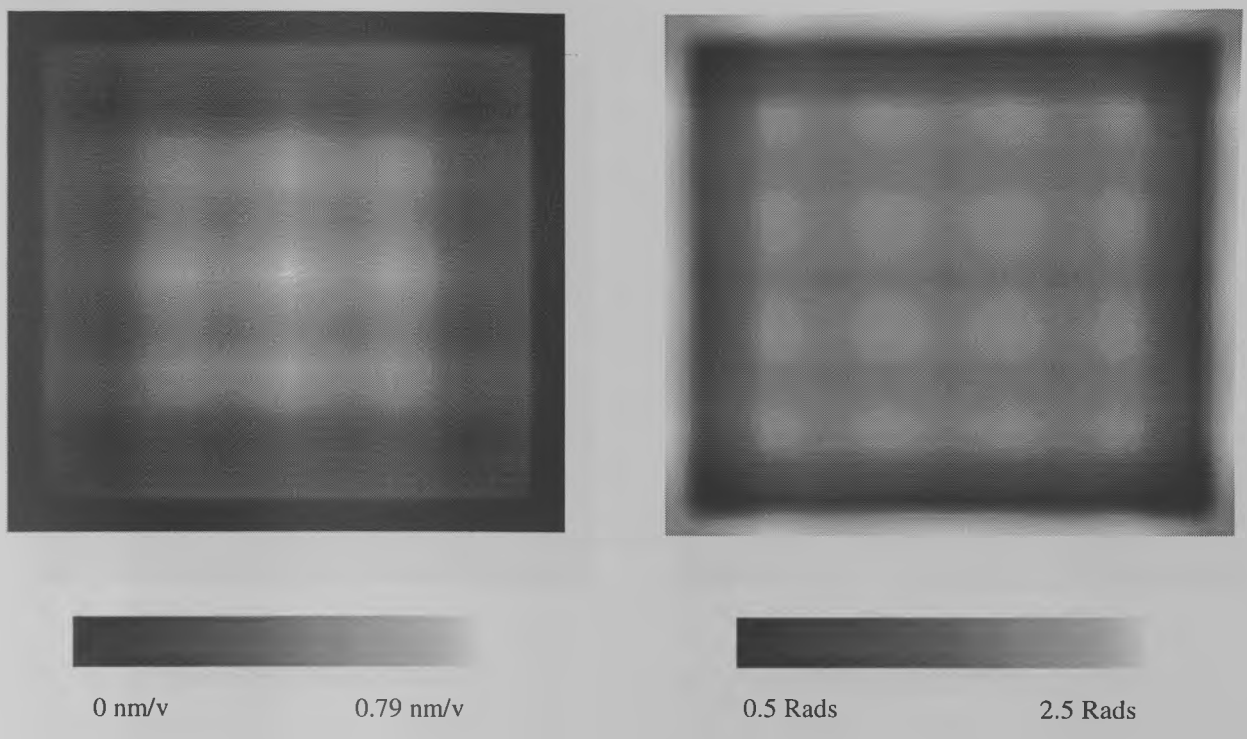

Figures 6.04 (b) & (c) PZT-5A Displacement Amplitude and Phase

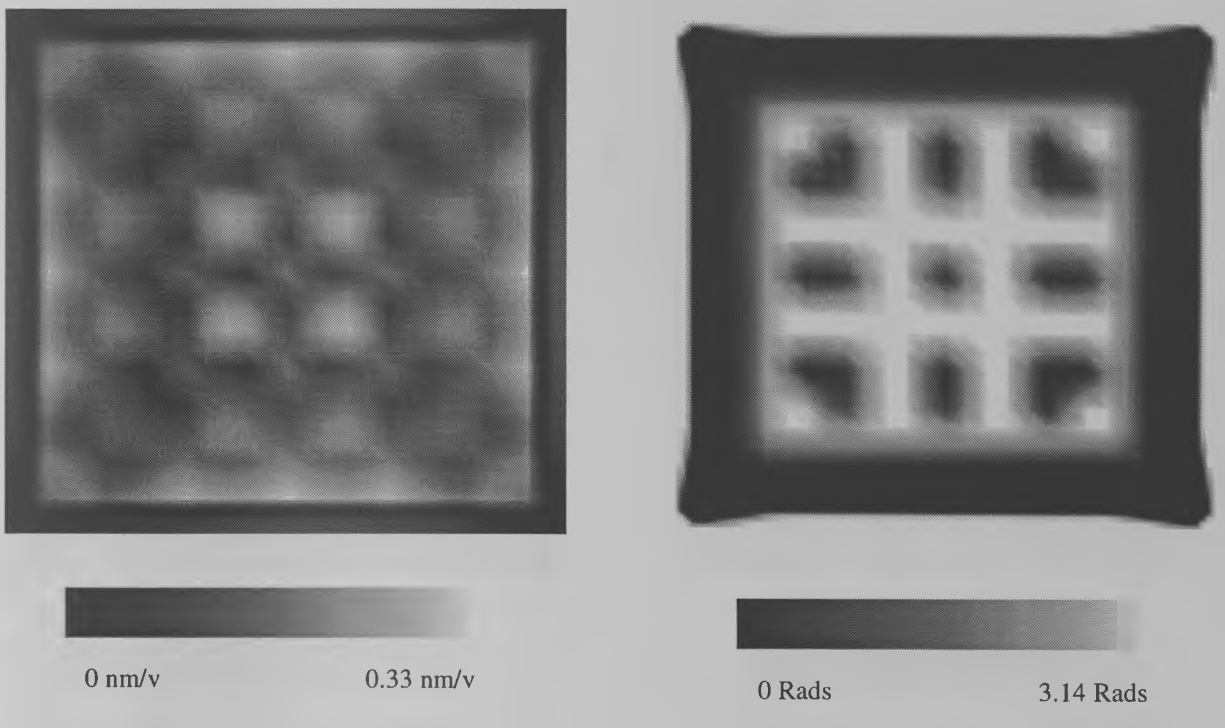

Figures 6.04 (d) & (e) PZT-5H Displacement Amplitude and Phase

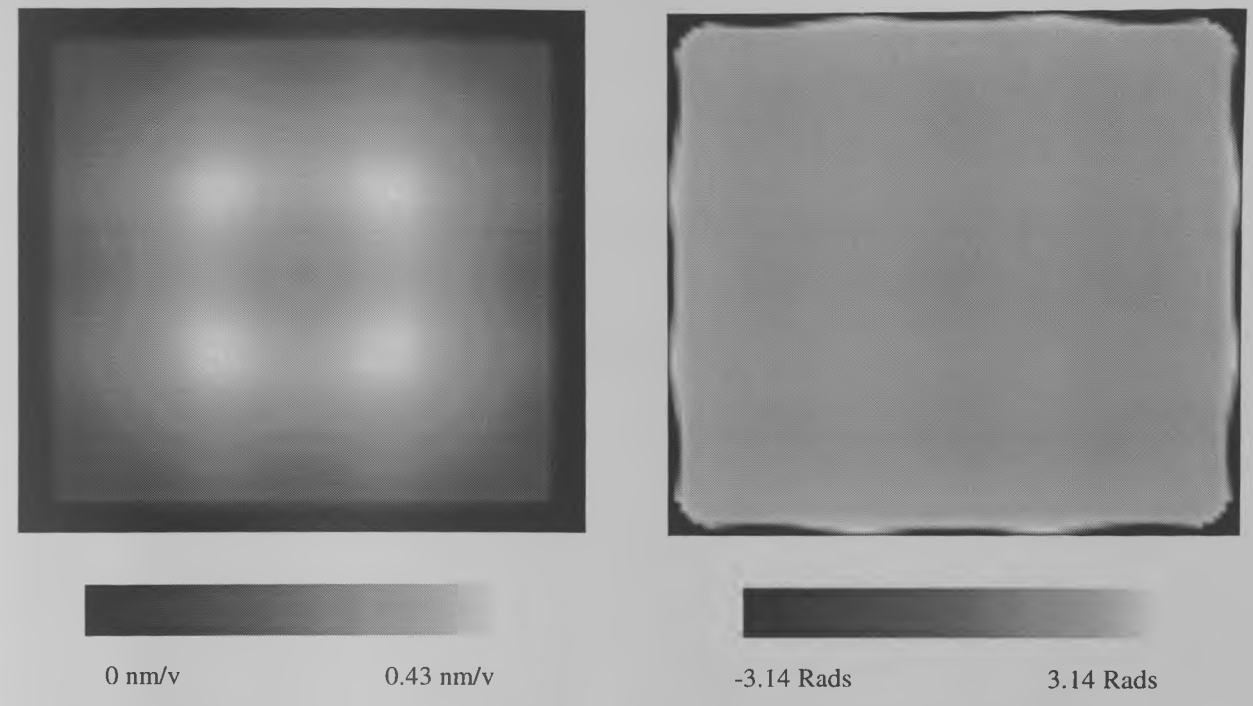

Figures 6.04 (f) & (g) MPT Displacement Amplitude and Phase

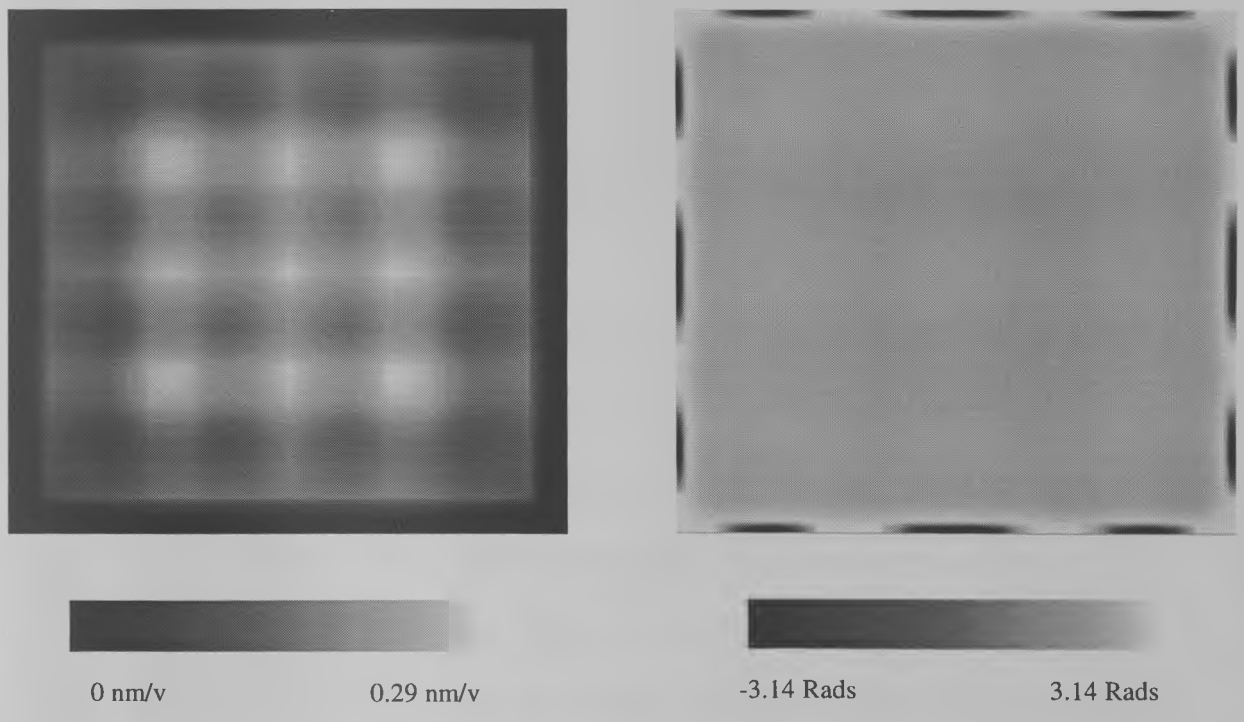

Figures 6.04 (h) & (i) PMN Displacement Amplitude and Phase

Figure 6.05 shows the simulated electrical impedance characteristics of a PZT 5H transducer, saw pitch 3.5 mm, saw blade 0.5 mm, and 0.3mm thick. This results in a transducer of identical volume fraction to those previously manufactured, and of identical thickness mode frequency, but an AR of 10 resulting in width modes being significantly removed from the thickness mode. It appears, that should thinner, higher frequency devices be manufactured, the benefits of PZT-5H (greater dielectric constant and greater piezoelectric strain constant) could be utilised without excessive interference from lateral modes.

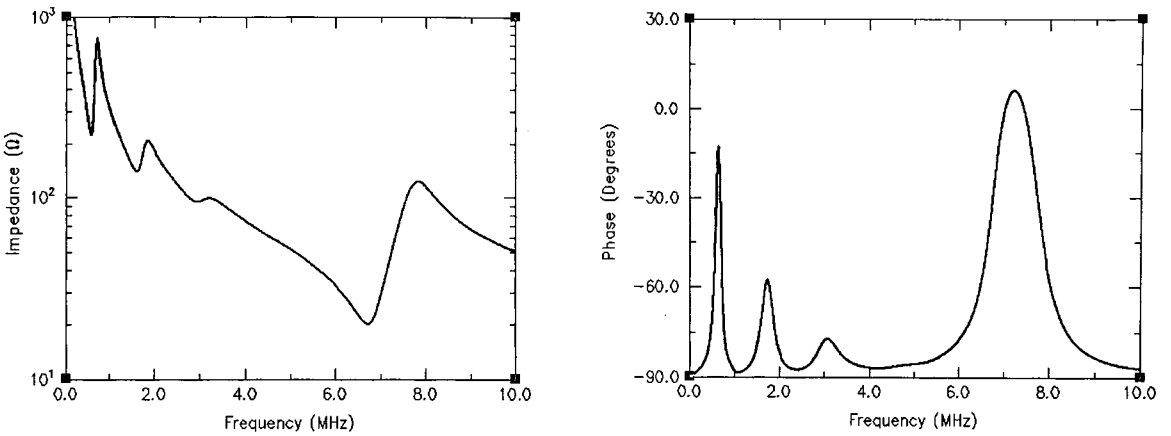

Figure 6.05 Impedance plots for PZT-5H Platelet with AR 10

This modelling, however, assumes that both electrodes are continuous across the entire surface area of the transducer, whereas in reality they will consist of a series of parallel strips as shown in Figure 6.06. In addition to modelling lateral modes, a finite element model can simulate separate electrodes on a transducer surface, and can therefore predict the effect of inter-element cross coupling. A series of FE simulations was carried out, modelling a plate of ceramic, with three parallel electrodes on the upper surface, each 0.3 mm across and separated by 0.3 mm, with a continuous lower electrode acting as the ground plane. The plate modelled had a width of 3 mm and a

height of 0.3 mm for an AR of 10 to ensure that all other resonances were sufficiently removed from the thickness mode, and only the central electrode was driven. Figure 6.07 shows the electrical impedance characteristics for PZT-5H, MPT and PMN. It can be seen that the PZT-5H shows extensive cross coupling with an additional modes interfering with thickness mode operation, whilst MPT and PMN show minimal cross-coupling. Both PZT-5H and PMN show width modes as would be expected in a plate, while MPT shows limited width mode activity. The extent of this cross-coupling is further illustrated in Figure 6.08, which details the displacement across the ceramic plate at the electrical resonant frequency, where all displacements are normalised to their own peak displacement. As can clearly be seen, PZT-5H shows considerable displacement at the adjacent electrodes, particularly when driven at 6.25 MHz. At 5.35 MHz the cross-coupling is reduced, but still more significant than in either PMN or MPT. It is of interest to note that this mode at 5.35 MHz may be due to the Lamb mode predicted by Equation 5.03 (a) which is reproduced below for convenience

$$f_L = \frac{v_{phase}}{\lambda}$$

where λ is the electrode spacing (0.3 mm) and v_{phase} is the s_0 phase velocity at the appropriate ceramic Frequency Thickness Product (1619 ms^{-1}). This results in a predicted frequency of 5.39 MHz, very close to the 5.35 MHz seen.

PMN and MPT show minimal cross-coupling activity, although not sufficient to interfere with thickness mode operation. MPT shows the least displacement in the ceramic adjacent to the driven electrode.

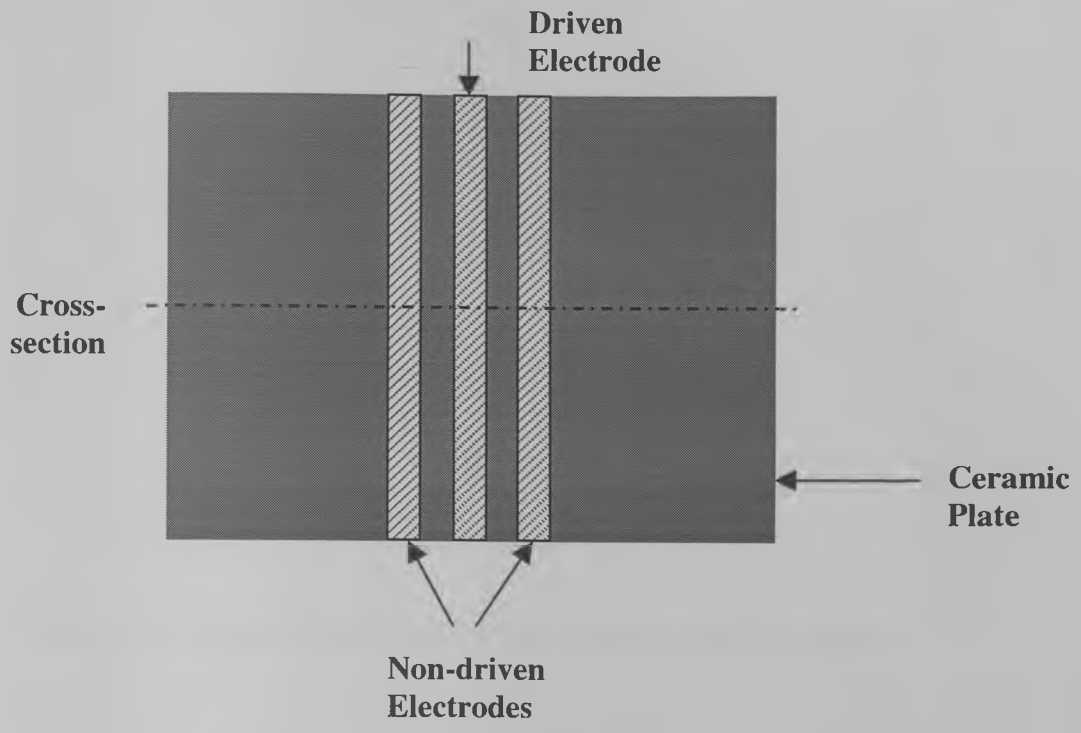

Figure 6.06 Diagram of FEA Cross-coupling Model

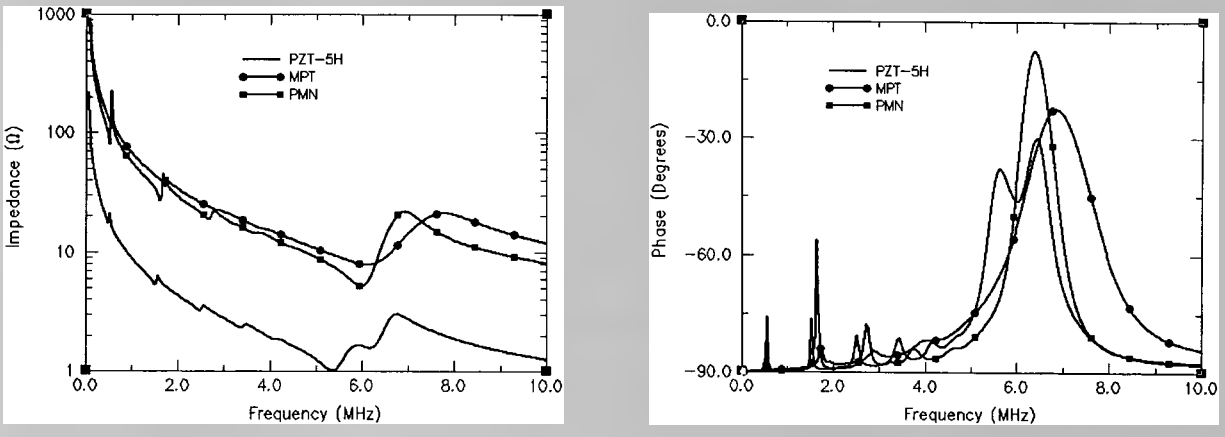

Figure 6.07 Impedance Plots for Element Cross-talk in Various Materials

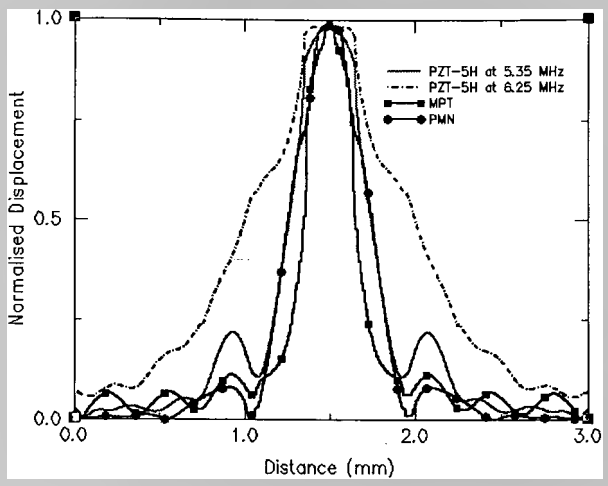

Figure 6.08 Surface Displacement across Electroded Materials.

No evidence of Lamb waves exists in the PMN or MPT, due to the low d_{13} values.

It is evident that this poor inter-element behaviour renders PZT materials unsuitable for array applications. Should Lamb waves be responsible for the additional mode, it would be the inter-element spacing that would determine the dominant laterally resonant activity in PZT, rather than the AR.

Figure 6.09 further demonstrates the capability of FEA to predict the real world response of a transducer. A 0.45 mm thick MPT platelet transducer with copper front face and an upper electrode pattern of a single finger, 1 mm by 30 mm was constructed. This figure shows the electrical impedance of the experimental transducer compared to FEA, with excellent correlation.

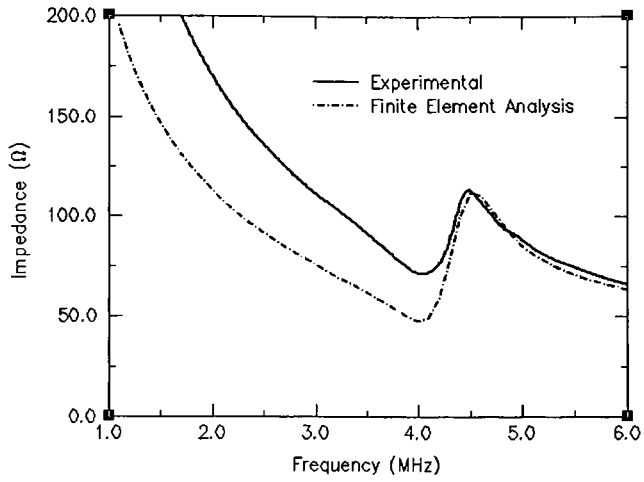

Figure 6.09 Electrical Impedance Profile of MPT Platelet Transducer

6.3.2 Comparison of Experimental and FEA Surface Displacements

In order to compare the experimental and theoretical surface displacements, a flexible transducer, with one continuous electrode on the upper and lower surfaces, was constructed using a PMN platelet device with saw pitch 1.75 mm, kerf 0.25 mm, 74% VF, and 0.45 mm thickness. As bondline thicknesses between the Printed Circuit Board (PCB) support detailed in Figure 6.10 were likely to be on the order of μm, and cannot be accurately measured within the completed device, they were estimated at 4μm. The finite element model was run for the frequency range 3 to 6 MHz, and the output used to construct graphs of predicted Dilation Qualities and Average Surface Displacements. Laser vibrometer results at various frequencies were obtained and are plotted on these graphs (Figure 6.11), with reasonable accuracy. While they do not exactly match the predicted plots, they are very close in magnitude, and closely follow the same trends. The inaccuracies are likely due to the estimates of bond sizes.

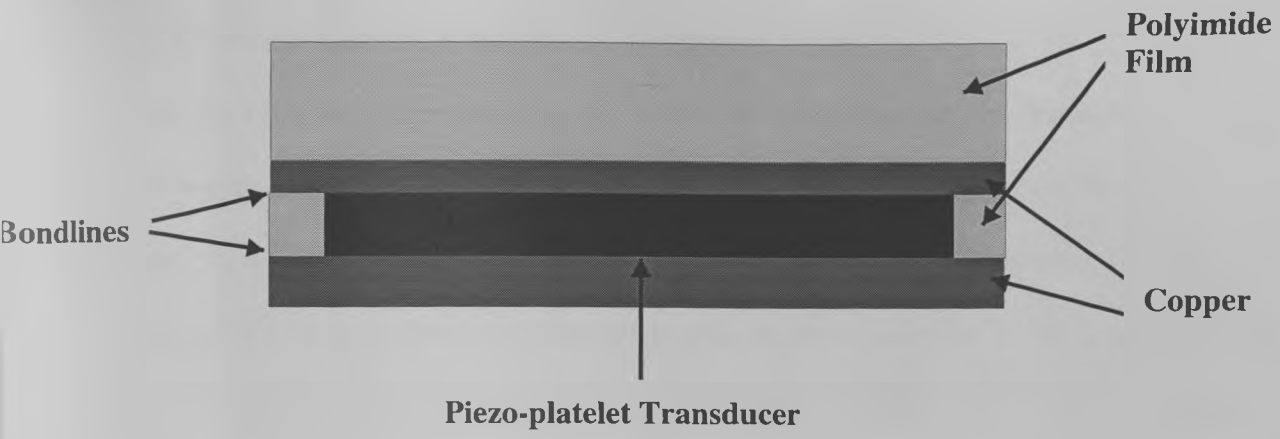

Figure 6.10 Diagram of Flexible array Construction

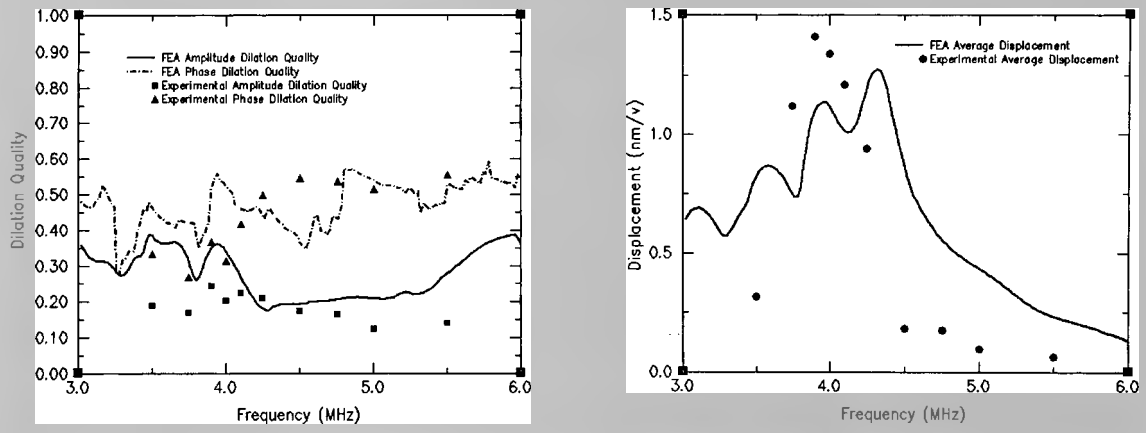

Figure 6.11 Dilation Qualities and Average Displacements of Platelet Devices

It is clear from both a qualitative and quantitative analysis that MPT and PMN are superior choices to PZT for their cross-coupling and damping properties respectively. Both MPT and PMN had similar dilation qualities, but overall MPT appeared to be the best choice of the two given its minimal cross-coupling, minimal lateral resonances, and greater maximum displacement, and consequently it was the preferred material. However, a consistent and reliable source of MPT proved impossible to find and all imaging results were therefore carried out using a PMN device.

6.3.3 Finite Element Prediction of Ultrasonic Waves

All the FEA results presented so far model the transducers in the frequency domain. However, as ANSYS is also capable of transient analyses, it is possible to simulate and view the propagation of an ultrasonic wave through a medium. Therefore, a model of a curved aluminium test piece with an inner radius of 70 mm, and an outer radius of 80 mm was generated. A 0.8 mm thick, 1.4 mm wide PMN element was placed at the centre of this model, and was excited with a single cycle 2 MHz sinusoidal pulse of magnitude 100 V. The propagation of the ultrasonic wave through the aluminium can be observed, and is presented as a series of images in Figures 6.12 (a) to (f). It is therefore possible to use FEA to predict ring-down times, bandwidth, and effect of matching layers on wave propagation.

The images presented clearly show the presence of the main longitudinal wave, as well as shear waves and surface waves. The shear waves have no normal component, and are travelling at a different velocity to the longitudinal wave. While originally it was intended to use this method to further enhance the analysis of the piezo-platelet transducers for NDT, two problems prevented full exploitation of this possibility. An error in the ANSYS 5.4 code, specifically on the Solaris 2.5.1 platform, prevented the transient simulation from running for an extended period of time. A solution was eventually obtained from ANSYS, Inc., however this was received at such a date that limited the time available for such simulations. Additionally, to fully model the transducer and test sample with sufficient accuracy to test all relevant options, would require an extremely large model with correspondingly large solution times. Consequently, the model presented here is of a significantly lower frequency

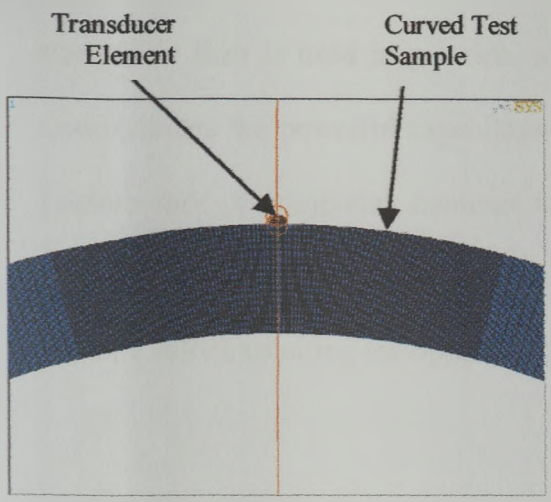

Figure 6.12 (a) Element Meshing

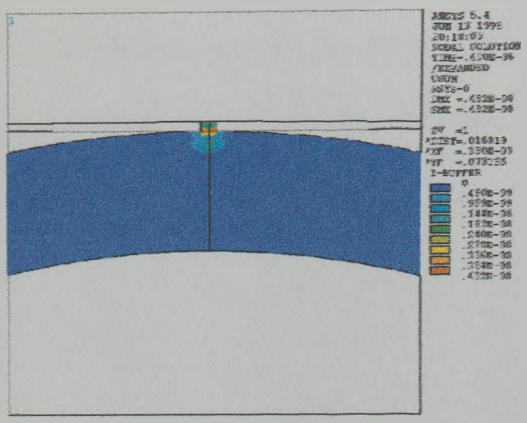

Figure 6.12 (b) Pulse at 4 μs

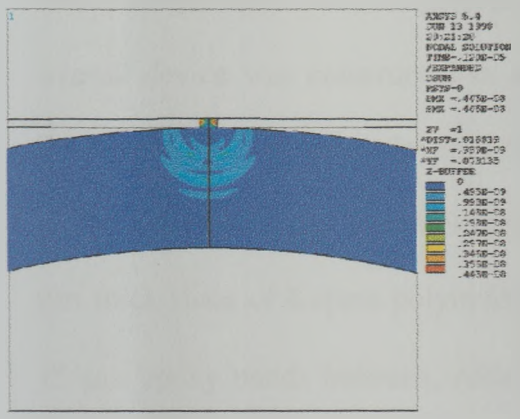

Figure 6.12 (c) Pulse at 12 μs

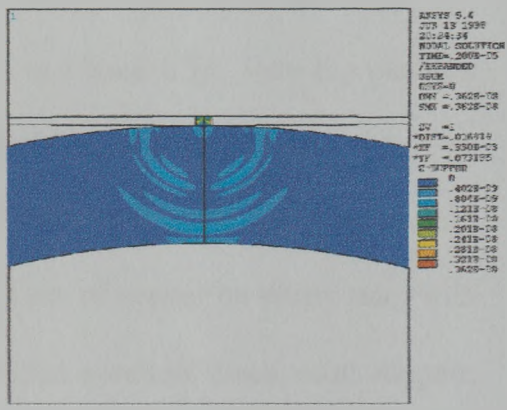

Figure 6.12 (d) Pulse at 20 μs

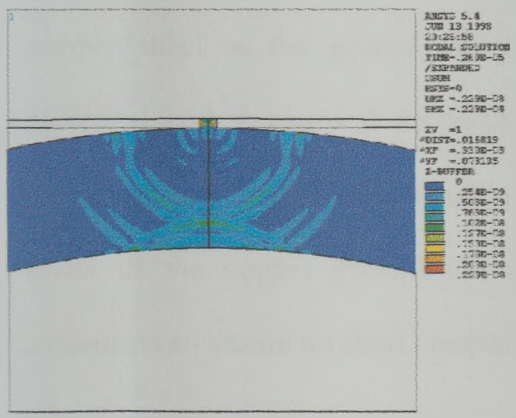

Figure 6.12 (e) Pulse at 26 μs

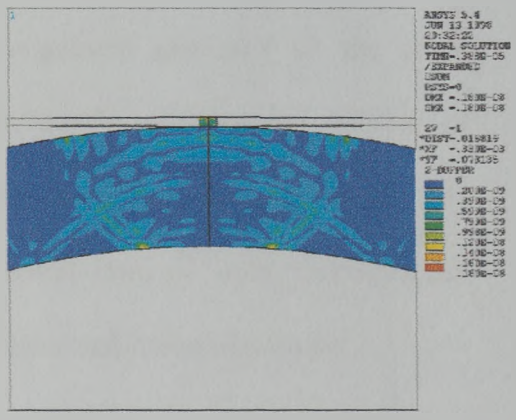

Figure 6.12 (f) Pulse at 39 μs

transducer than is used in practice, with a much thinner test sample. This example demonstrates the powerful capabilities of FEA as a design aid. Should the price and performance of computers continue to improve in a manner similar to the last two decades, it is envisaged that within 5 years desktop computers using FEA will be capable fully exploiting the options presented here.

6.4 Construction of Piezo-platelet Array

While the piezo-platelet device itself is the core of the flexible array, the supporting structure and electrode arrangement are critical to the performance of the array. The overall device was constructed in manner shown in Figure 6.13, with the platelets sandwiched between two layers of flexible Printed Circuit Board (PCB), acting as both mechanical support and electrodes. The PCB used by Powell consisted of a 50 μm thick sheet of Kapton polyimide film, with 25 μm of copper on either side, with 15 μm epoxy bonds between. Although this provided excellent mechanical support, the number of layers, and acoustic mismatch between each layer resulted in poor performance. Consequently, devices constructed for the present work use the same polyimide sheet with 15 μm of copper sputtered on as the upper electrode, and a plain copper sheet as the ground electrode. This arrangement provided all the same electrical and mechanical properties, whilst significantly reducing the number of layers in each device. Additionally, a piece of polyimide film was placed over the areas of the copper ground electrode not in direct contact with piezo-platelet transducer to ensure no short circuits between the upper and lower electrodes.

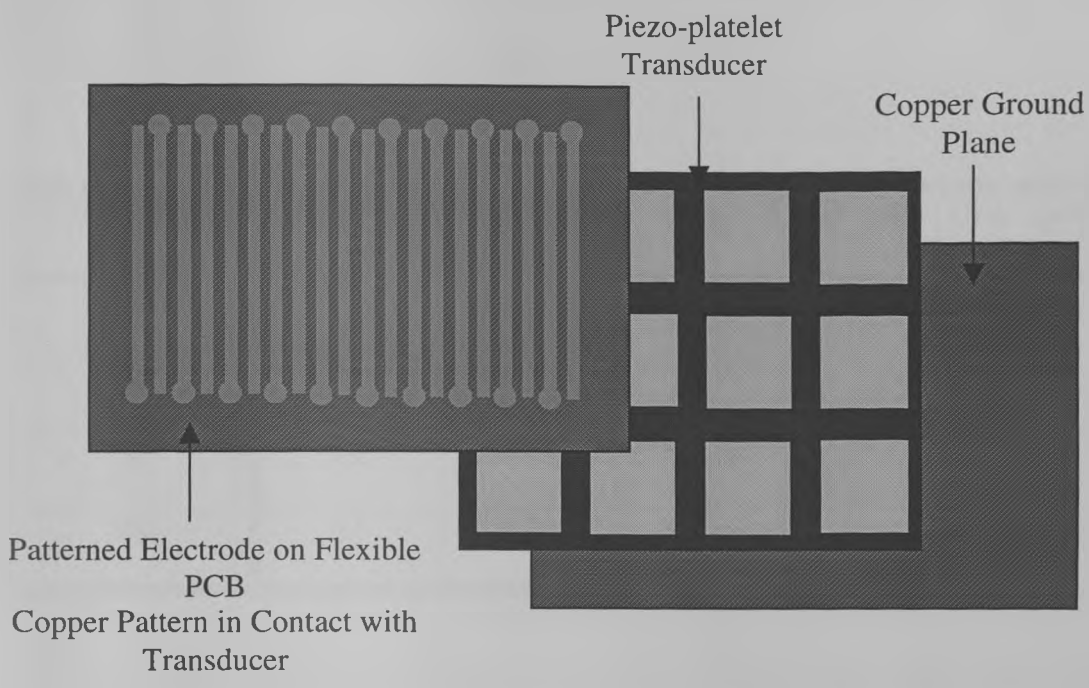

Figure 6.13 Overall Transducer Constructional Arrangement

6.4.1 Thickness of Copper Electrode

As the copper sheet was effectively the 'front face' of the transducer, the effect of its thickness must be considered. Although it would be possible to use the electrode as a half wavelength matching layer, this would result in a thickness of 400 μm for a frequency of 6 MHz, which would limit the flexibility of the transducer too severely. The matching layer is required to be half wavelength rather than quarter wavelength as the matching layer has a higher acoustic impedance than the transducer. Using an FE model, a number of simulations were carried out, each using a different thickness of copper between 12.5 and 100 μm, and at thickness mode electrical resonance. The Dilation Qualities, Average Displacements and Resonance Frequencies are shown in

Table 6.04. From this data a thickness of 25 μm was chosen as a compromise between flexibility, Q_{DIL} and average displacement.

Thickness (μm)	f_e(MHz)	Q_{AMP}	Q_{PHI}	Av. Disp. (pm/v)
12.5	7.0	0.40	0.74	30
25	7.0	0.40	0.50	37
50	7.0	0.35	0.33	50
100	6.8	0.32	0.33	32

Table 6.04 Transducer Properties with Various Copper Electrode Thicknesses

6.4.2 Advantages of Pulse-echo Design Strategy

As noted earlier, Powell's flexible arrays were pitch-catch devices. They consisted of a sparse platelet transmitter and a finely spaced PVDF reception array, while the new devices consist of a finely spaced pulse-echo array based on a piezo-platelet transducer.

In addition to the obvious benefits of simpler design and fewer layers, the new transducer structure allows each element to be excited individually. This extensive array control opens the way to advanced signal generation techniques by varying the signals to each element in both time and amplitude. Appropriate signals can be used to beam steer and focus the array output - thus the new arrays are considerably more 'flexible' than the original.

6.4.2.1 Considerations for Electrode Configuration

The flexible ultrasonic imaging array calls for a multi-element electrode pattern to allow images to be constructed of test subjects. Practical problems exist which limit the range of possibilities available – most notably the existence of *grating lobes.*

Flaws are indicated by the location of points of constructive interference, However, should the path length from a reflector (S1) to an array element differ from the path length to an adjacent element by a multiple of λ/2, then grating lobes (S2) can occur, as is illustrated in Figure 6.14. If the path length differs by exactly λ/2, then, when 2-way travel has been accounted for, total distance travelled will be λ, and constructive interference will occur.

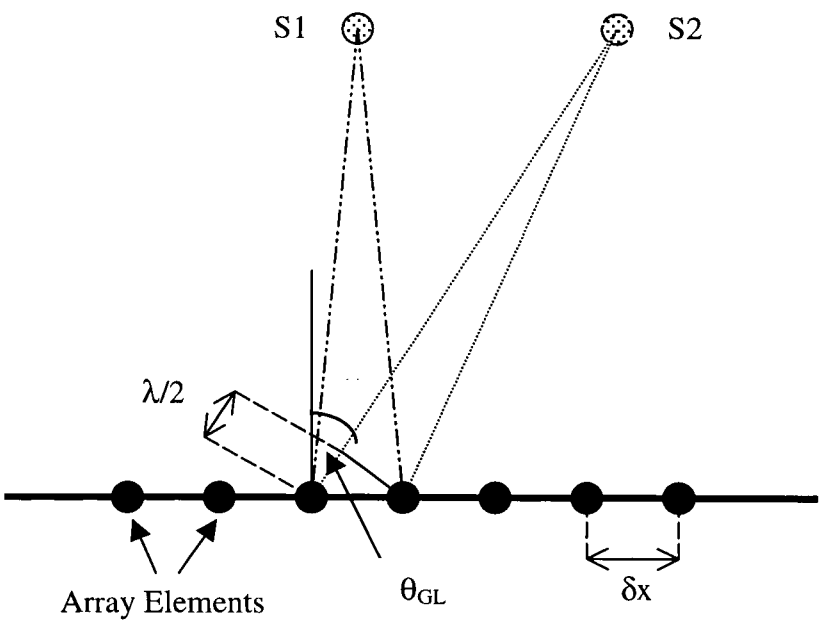

Figure 6.14 Formation of Grating Lobes

It is apparent that there will be additional points that could also experience constructive interference, which will occur at an angle θ. The value of these angles can be determined by

$$\theta_{GL} \cong \sin^{-1}\left(\frac{\lambda}{2(\partial x)}\right) \qquad \textbf{Equation 6.01}$$

where

θ_{GL} is the grating lobe angle

λ is the wavelength of the ultrasonic signal

δx is the separation of the transducers.

It is clear from Equation 6.01 that should the transducer separation become less than half the acoustic wavelength, then the grating lobe angle will become greater than 90° and will not be located in real space. Thus the maximum separation of transducers used for imaging purposes should be no greater than half the minimum wavelength of interest to ensure that no grating lobes will exist in the final image.

In addition to the problem of grating lobes, there is the problem of *ambiguity*. Figure 6.15 (a) shows how artefacts can be created when two transducers attempt to image two flaws, as there are more than two areas of constructive interference created – i.e. the results are ambiguous. If, however, a third transducer is added as shown in Figure 6.15 (b), ambiguity is avoided and both flaws can be located. This analogy can be extended to conclude that there must be at least one more imaging transducer than there are imaging targets to ensure that results are unambiguous.

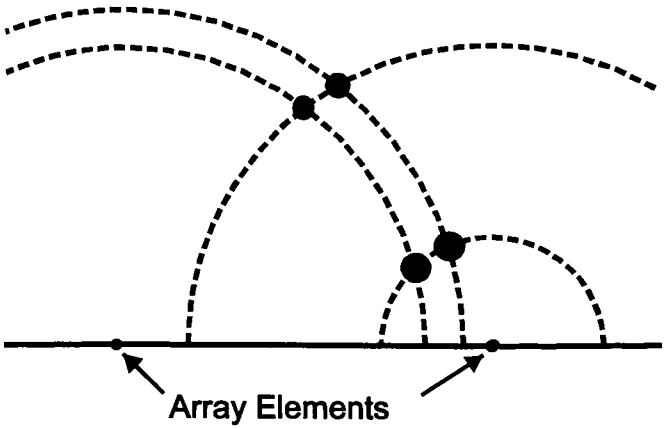

Figure 6.15 (a) Ambiguity in Flaw Location

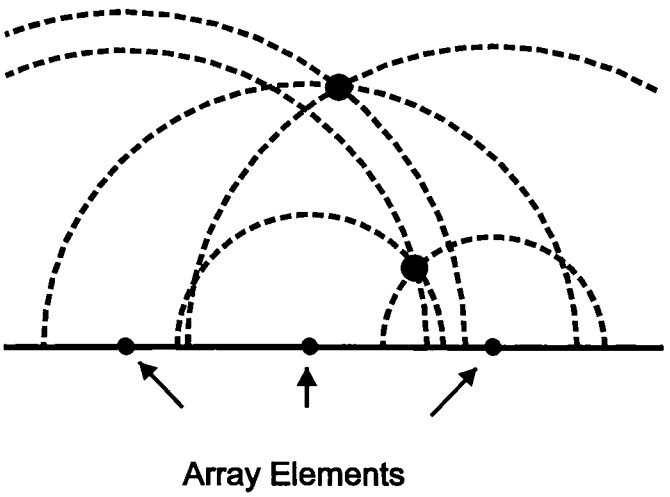

Figure 6.15 (b) Removal of Flaw Ambiguity

The ability of an array to differentiate between two adjacent targets in a plane parallel to it is critical to imaging performance, and is known as *lateral resolution*. It has been shown by Thomson [73], that the lateral resolution of any array is equal to half the individual element width. Thus element width must be minimised in order to increase lateral resolution.

To summarise, an array should have its elements separated by no more than half the wavelength at the highest frequency of interest, with as many elements as possible to reduce ambiguity, each as narrow as possible to maximise lateral resolution.

The frequency of operation of the platelet devices used here varied from 4 to 8 MHz, with 6 MHz the frequency of the transducer used to obtain the results presented in this chapter. Aluminium and steel were the two materials used for test subjects in this thesis, and as aluminium has the higher longitudinal velocity of sound (6420 ms^{-1}) resulting in a smaller wavelength, this was the value used to determine element spacing. At this velocity, a frequency of 6 MHz gives a wavelength of 1.07 mm, indicating element spacing should be 0.54 mm. Practical considerations of design simplicity, meant that a value of 0.5 mm was chosen for the actual element spacing, giving 120 elements in a 60 mm aperture. Figure 6.16 shows the electrode pattern used, with the image of a 30 mm by 60 mm platelet device superimposed.

To ensure that each electrode drives an equal quantity of ceramic, the transducers were cut at 45° relative to the length of each electrode, resulting in platelets that are 'diamond' shaped, as shown in Figure 6.17.

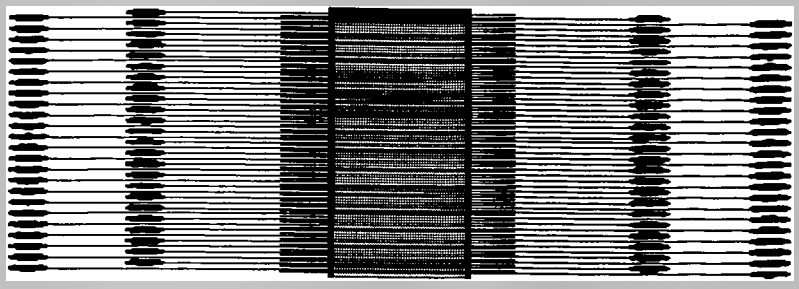

Figure 6.16 Electrode Array Pattern

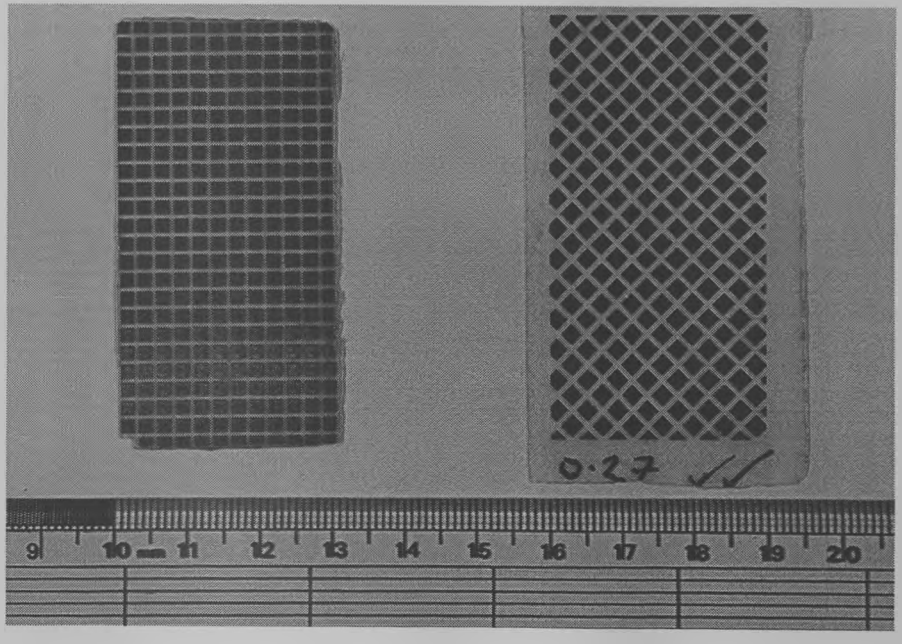

Figure 6.17 Piezo-platelet Transducers cut at 0° and 45°

6.4.2.2 Construction of Array Electrode

Initially, a mask such as that shown in Figure 6.16 was designed on a PC drawing package. The image was then printed in inverted format – that is, areas of copper to be removed are black – and at a scale of 2:1 on a 600 dpi printer, thus giving the final

mask a resolution of 1200 dpi. This image was then transferred to a transparent celluloid sheet to act as the overall mask.

The flexible PCB was coated with photo-resist using a hot film laminating process, and then exposed to ultraviolet (UV) light for 45 seconds whilst covered by the mask to expose certain copper areas. The resist was developed, and placed within a chemical bath containing etching solution to remove unwanted copper. Remaining photoresist was removed using acetone, an abrasive cleaner was used to remove copper oxide deposits from the PCB, which was then cleaned with a solvent such as isopropanol. A multimeter was used to measure the resistance between adjacent electrode elements, and the cleaning process was repeated until at least a 40 MΩ resistance existed between the tracks.

6.4.3 Construction Techniques for Piezo-platelet Arrays

Each of the individual components that goes into making up the piezo-platelet devices must be placed together in a very specific order for the device to function properly. Figure 6.10 shows the order in which all layers must be placed before the final pressing process can take place.

Initially, the construction technique developed by Powell was used in the assembly of the platelet arrays. This involved placing the various array components in their correct orientation, between two rubber pads. These rubber pads were, in turn, placed between two steel plates in a press arrangement, as shown in Figure 6.18. The steel plates ensured an even distribution of force applied by the screw, while the rubber pads ensured that all areas of the transducer had force applied, despite any thickness

differences that might exist. The screw was tightened and the press was placed in an oven at 40°C for 5 hours. Once it had been allowed to sit for 24 hours to ensure that the epoxy had cured, the device was removed from the press.

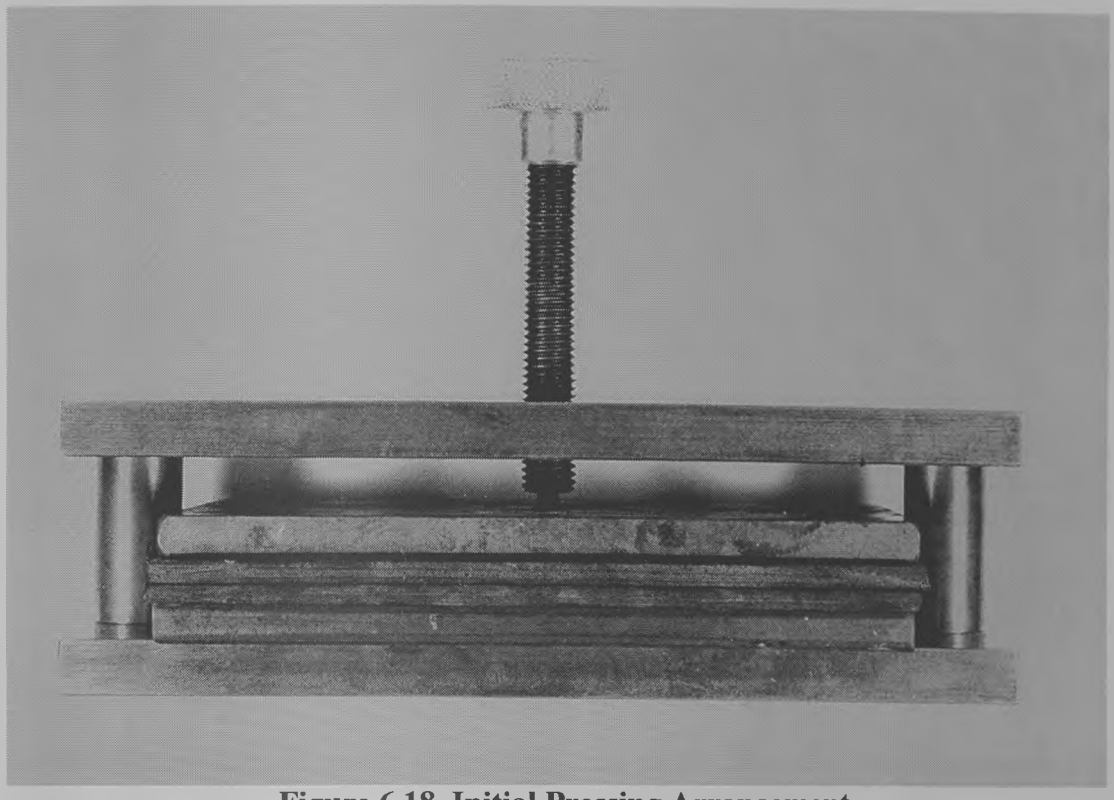

Figure 6.18 Initial Pressing Arrangement

While this technique was sufficient for most applications, certain problems were found to exist. Firstly, as the screw was tightened, applying force in the vertical direction, a small rotational force was also generated, sometimes resulting in small rotational displacements causing misalignment of the electrode pattern, or more importantly of the insulating polyimide layer allowing an electrical short circuit. In order to overcome this problem, the 'screw' press was replaced with a hydraulic press (Figure 6.19). In this, the device is placed between an upper restraining pin, and a lower block whose displacement is controlled by a hand pump. Not only is force

restricted to the vertical direction, but the actual pressure applied can be easily measured by the pressure gauge on the pump (typically 60 bar).

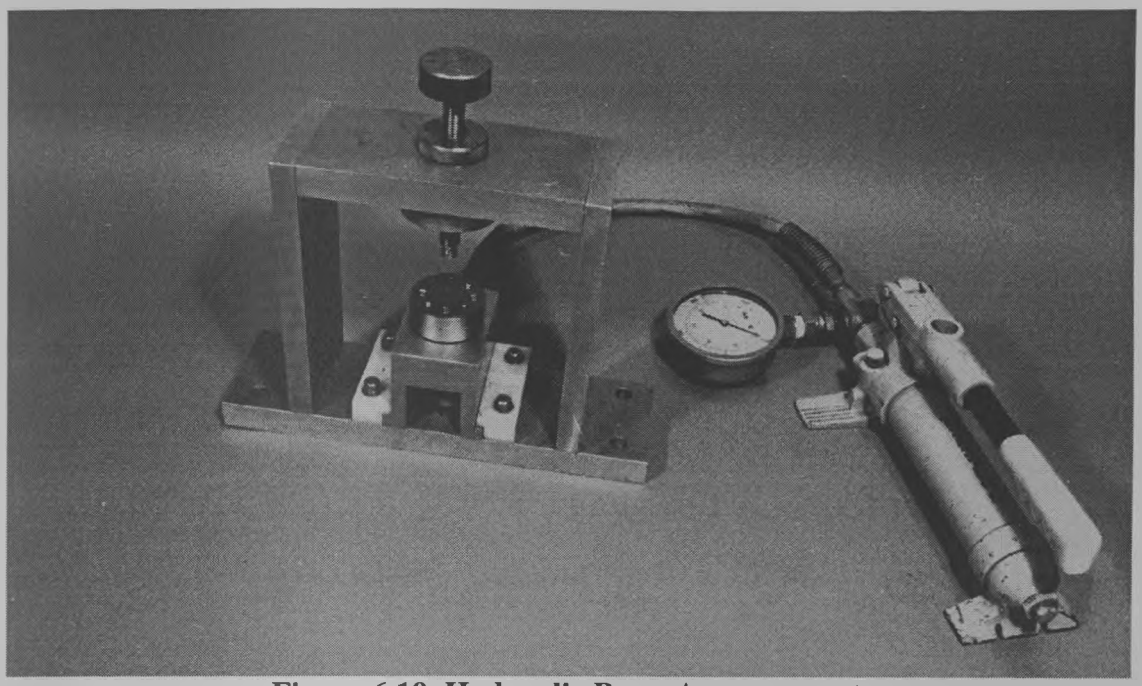

Figure 6.19 Hydraulic Press Arrangement

There also existed a second problem with the rubber pads used to distribute force amongst uneven points on the device. As these sheets were flat, force was applied to all points on the device at the same time, sometimes resulting in areas of 'trapped' excess bonding epoxy, producing poor electrical connections and uneven surfaces, and, in turn, causing difficulties in flexing. A solution was found through the use of an upper rubber press section of half-cylinder shape as opposed to flat, as shown in Figure 6.20.

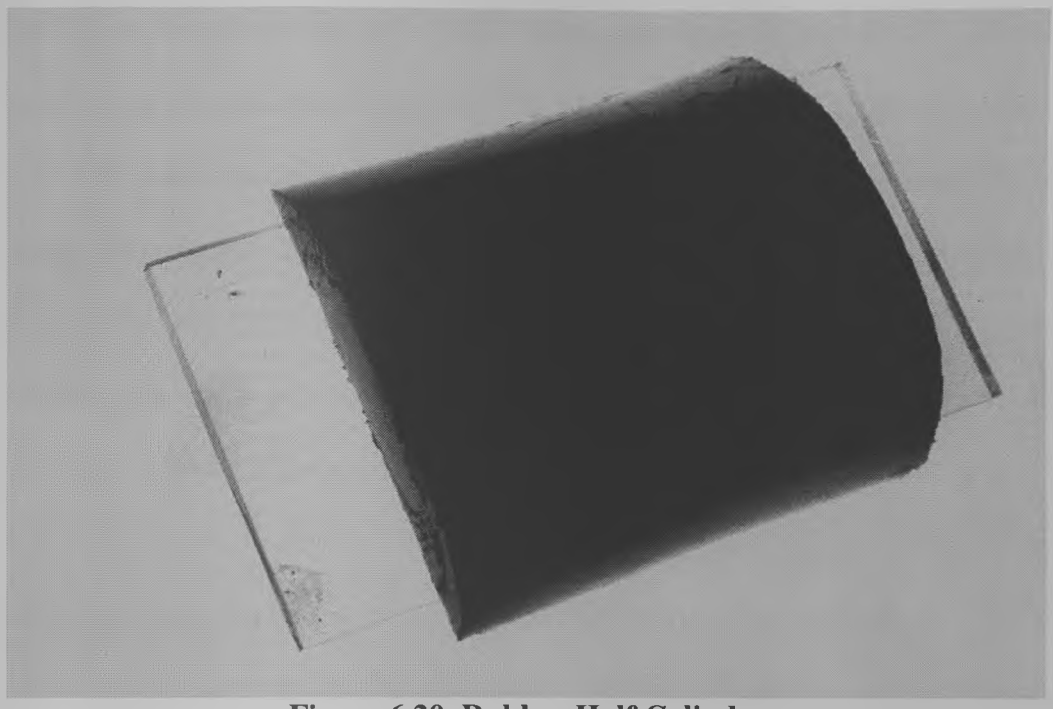

Figure 6.20 Rubber Half Cylinder

This rubber was a specially modified epoxy (standard CIBA-GEIGY CY208/HY956 mixed in the weight ratio of 8 parts resin to 1 part hardener, with additional polysulphide rubber DY041 added in the ratio 60 parts DY041 to 100 parts resin), designed to be easily deformed. In a manufacturing setup using this half-cylinder, pressure is initially applied at a line running along the centre of the device, but as more pressure is applied, the half-cylinder flattens more and therefore applying pressure further across the device until the entire surface is under pressure. In this manner, excess bonding epoxy is pushed from the centre to the outer edges where it can later be removed.

6.5 Image Formation Techniques

Once the A-scan data from the entire array are available on computer, the process of forming an image of the test subject can begin. A collection of A-scans from a test, is referred to as a B-scan. The synthetic aperture focusing technique (SAFT) was used to

construct the images shown here. SAFT relies upon spatially averaging (effectively superimposing) B-scan data to improve signal-to-noise ratio. This technique processes all the individual array element responses as it were originating from a single, large aperture transducer. As all responses from reflecting targets should add constructively, any SAFT image produced will represent a reflector (such as a flaw or specimen back wall) as a large signal, and all other areas as no signal. A fuller explanation of SAFT is detailed by Doctor [74].

Analysis of image processing techniques lies outside the scope of this thesis; here they are used simply as a tool to demonstrate the NDT capabilities of piezo-platelet array transducers. To this end, imaging software programs written by D.Powell and A.Cochran were utilised in all image formation processes [59,60,72].

The B-scan data were time-gated and scaled to remove the majority of the back-wall echo, and to improve the signal strength of any reflected response relative to the strong back wall echo, respectively. A software 'bandpass filter' could also be implemented to remove noise from the response before imaging. Finally, the processed data was imaged using a focussing program that takes into account the radius of curvature of the test piece to produce a focussed image.

6.6 Experimental Work

The experimental arrangement used to acquire pulse-echo test data consists of a Panametrics pulser receiver, Model PR5052, operating in Transmit/Receive mode for array excitation, with data acquired and recorded on a LeCroy Digital Oscilloscope Type LS140.

The LeCroy oscilloscope has the ability to save the digitised element response to a floppy disk, from which it can then be transferred to a computer network. Transferred data consists of a single file per element, each file with two columns – the first column representing time and the second representing voltage magnitude. A single voltage/time response of an array element is called an A-scan.

6.6.1 First Test Piece - Notch and Fatigue Crack

A test piece was required which would demonstrate the practical performance of flexible array transducers on targets typical of NDT, such as those containing large specular reflectors (back wall), and diffuse scatterers (fatigue crack tip). To provide a consistent and reproducible 'flaw', a notch and a slot were cut into a section of 75 mm radius of curvature (ROC) pipe by a 0.3mm diamond wire saw (Figures 6.21 & 6.22).

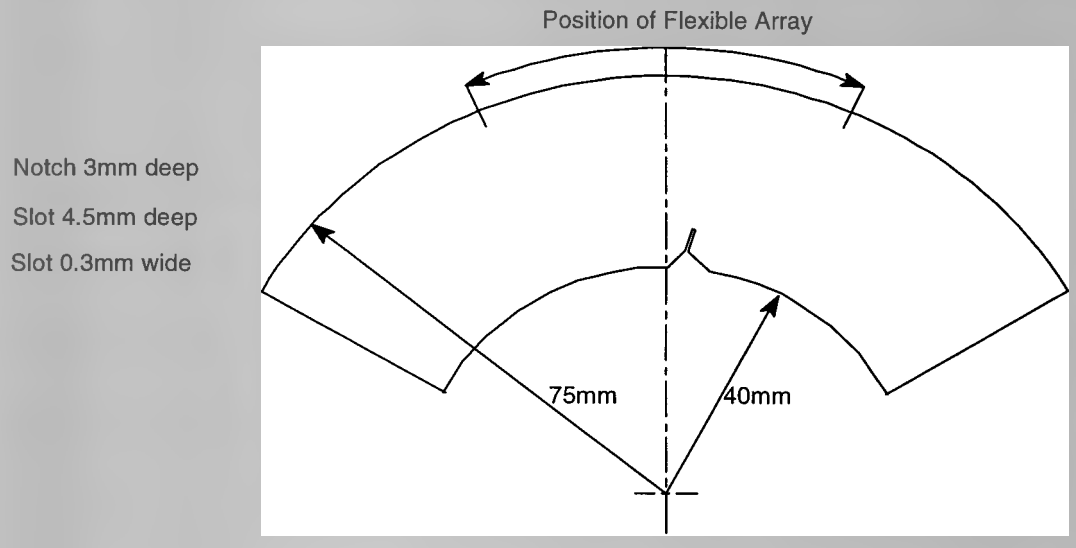

Figure 6.21 Notch and Slot

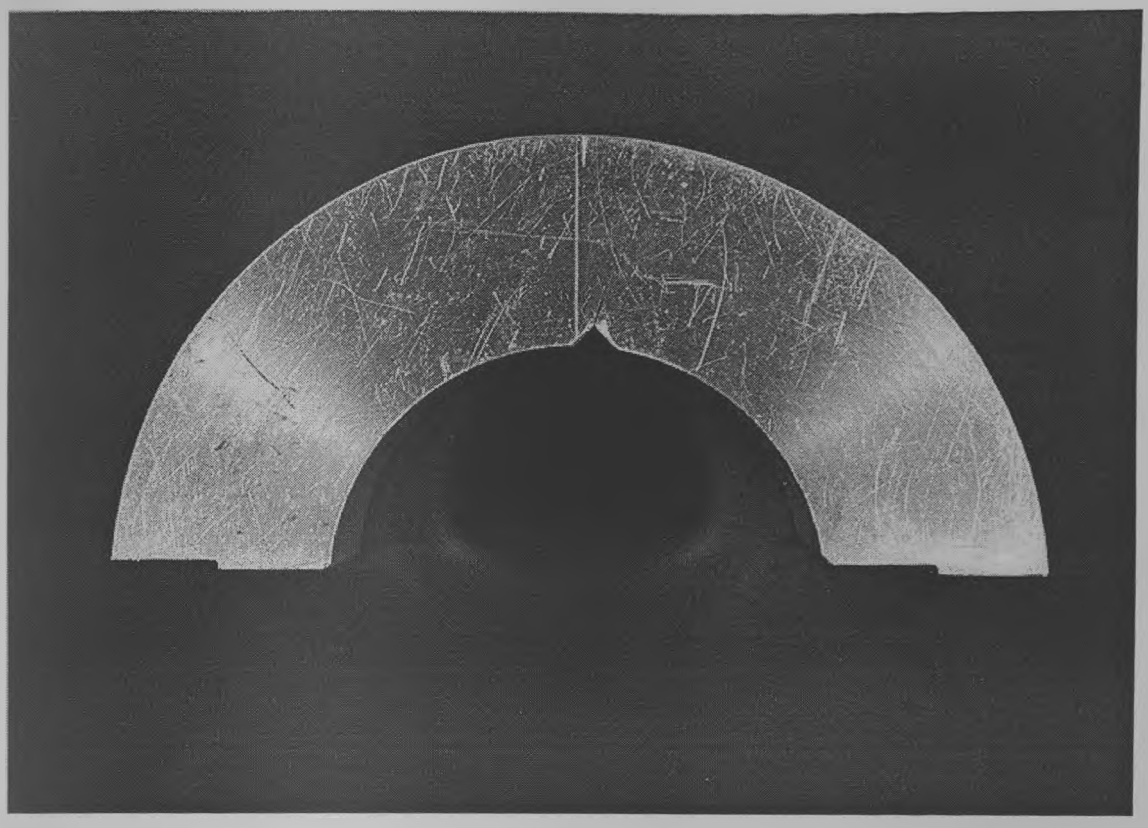

Figure 6.22 Picture of Notch and Slot Test Piece

The multi-element array was employed to obtain experimental data from this test subject and used to create an experimental image of the flawed area by focusing of the B-scan. The B-scan for the notch and slot is presented in Figure 6.23, and the reflection data from the slot tip is clearly visible as a curve starting at 9.3 μs, with the notch appearing at 10.5 μs, and the back wall echo at 11.5 μs. It should be noted that as only 30 element results can be plotted on the graph, only the central 30 elements of the array are shown. Once focussed and presented as an image (Figure 6.24), the slot tip, notch edge, and back wall can be more clearly detected.

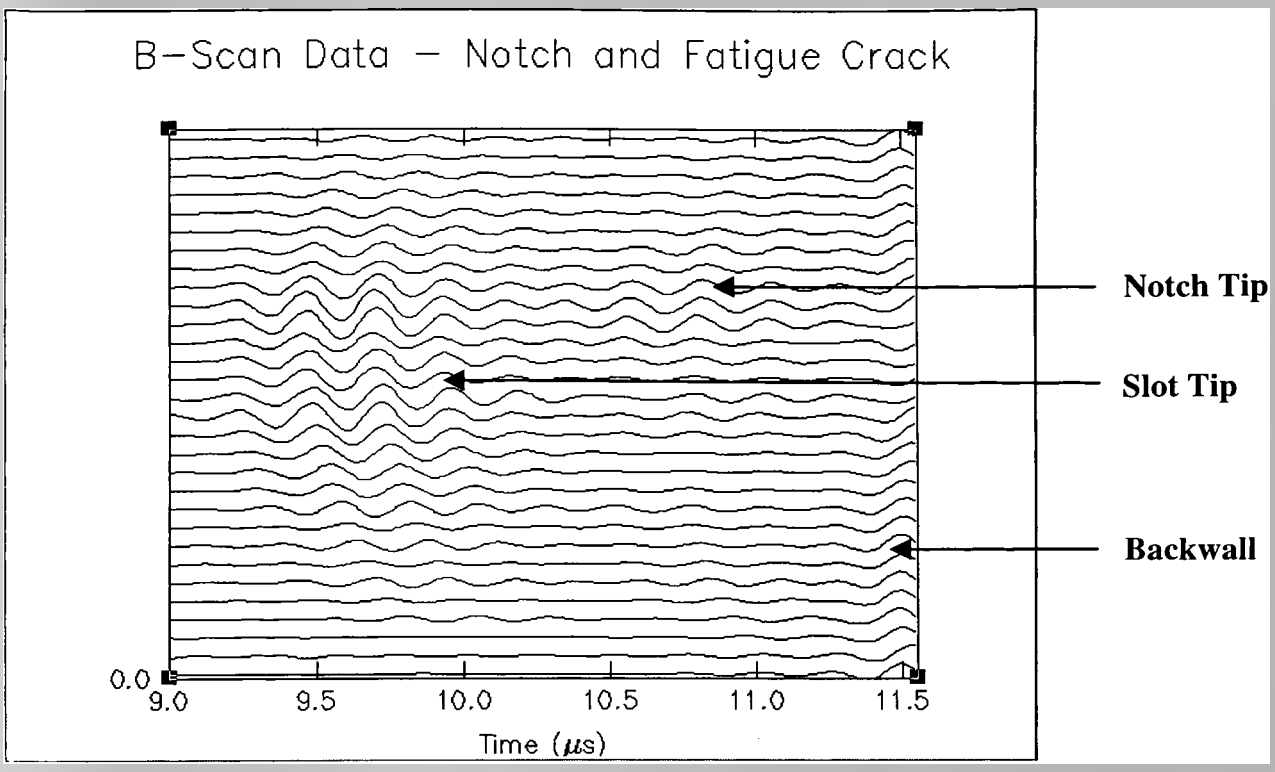

Figure 6.23 B-Scan Data from Notch and Fatigue Crack Specimen

Figure 6.24 Focussed Image for Notch and Fatigue Crack Specimen

Despite being designed for 6 MHz operating frequency, it is likely that the flexible transducer would operate at a lower frequency when attached to a test specimen, due to

the mechanical loading. Using single A-scan obtained experimentally, a Fourier Transform can be used to determine the frequency content of the returned signal, and hence the dominant operating frequencies of the transducer. Figure 6.25 displays the frequency response of a single element used in the formation of Figure 6.24.

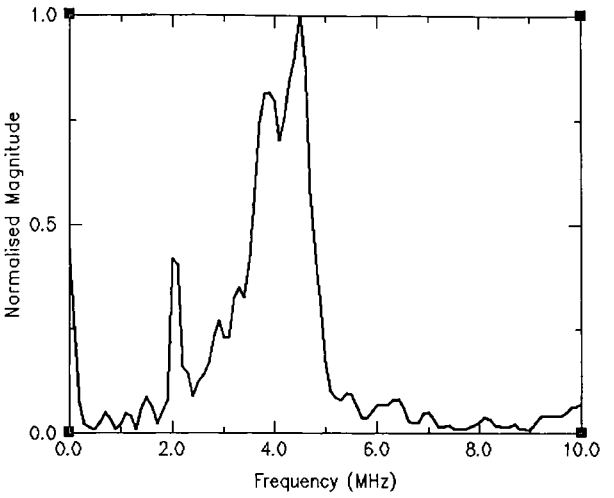

Figure 6.25 Frequency Response of Single Transducer Element

It can be seen that the transducer operates most effectively between 3.55 and 4.75 MHz, lower than the unloaded resonance at 6 MHz. The –6 dB bandwidth was found to be 1.2 MHz with a centre frequency of 4.15 MHz, giving a 29% pulse-echo bandwidth.

6.6.2 Second Test Piece - Three Slot Flaws

Once it had been established that the flexible array was capable of imaging a typical NDE slot, the next step was to image multiple flaws of varying sizes. For this task, another curved aluminium test piece (Figure 6.26 & 6.27) with three slots of 8mm, 4mm, and 2mm depth, separated by 10mm laterally, was examined. This test piece was of a larger radius of curvature (100mm as opposed to 75mm) and was also thinner (29mm as opposed to 35mm), to show the flexibility of the device.

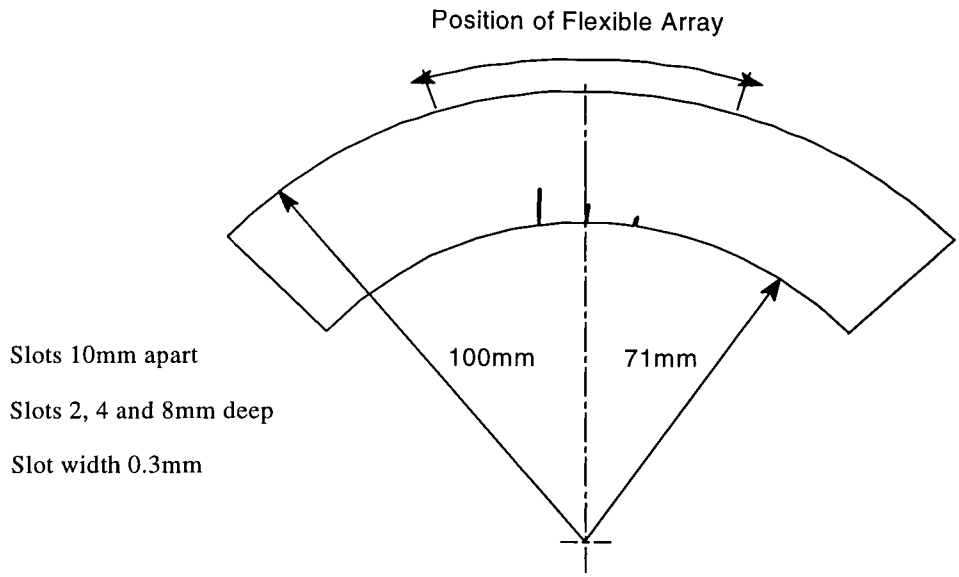

Figure 6.26 Multiple Slot Test Piece

Figure 6.28 is the B-scan data from the multiple slot test sample. Signals from each of the slots can be clearly seen at 7.0, 8.2, and 8.7 μs, with the backwall echo at 9.3 μs. Once focussed and imaged (Figure 6.29) the three slots and backwall are clearly visible.

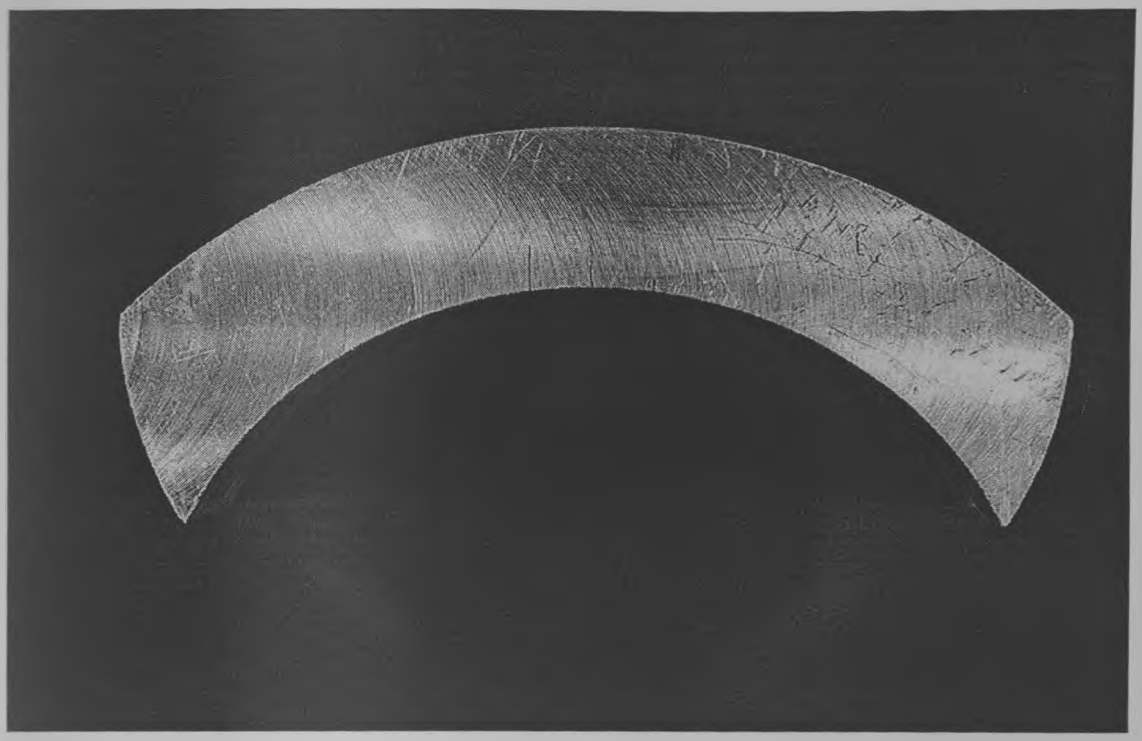

Figure 6.27 Picture of Three Slot Test Piece

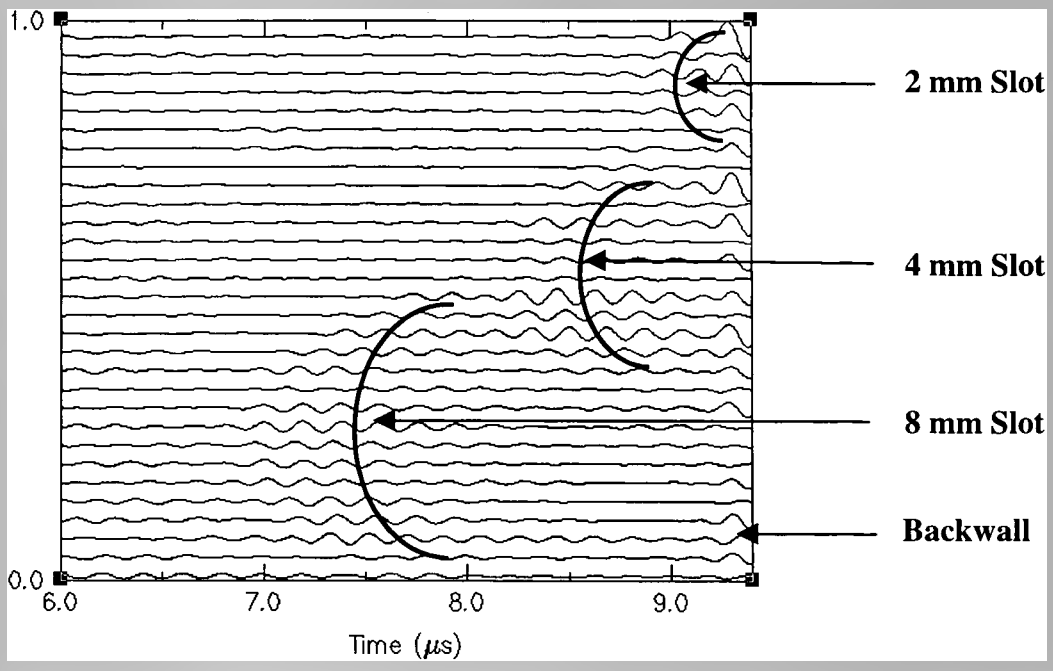

Figure 6.28 B-scan Data for 3 Slot Test Piece

Figure 6.29 Focussed Image of Three Slots in Test Piece

6.7 Conclusions

This chapter has presented a case study in improving the design of ultrasonic transducers through the use of FEA. Modelling was used to predict the preferred material choices, by clear demonstration of cross-coupling effects and of lateral resonance modes. Excellent correlation was obtained between experimental and FEA results, with electrical impedance profiles, surface displacement shapes, and magnitudes being accurately predicted. An experimental device was constructed using the FEA model as a guide, which resulted in a flexible ultrasonic transducer array capable of imaging a range of flaws in curved surfaces. This device was superior to its

predecessor in its significantly reduced thickness, increased frequency, simplified design, as well as introducing the possible benefits of a phased array.

Whilst FEA has been used extensively to improve the design of the flexible transducer, it is important to realise that despite the power of today's computers, they are still not fast enough to use ANSYS to test every aspect of an ultrasonic transducer. At present only strategic points can be extensively modelled without resorting to overly large models and extended solution times. The designer of an ultrasonic transducer must still, therefore, bring knowledge of transducer behaviour to any FEA procedure, in order to carefully select which areas require modelling – the computer is still no substitute for the experienced human.

Chapter 7

Conclusions and Recommendations for Further Work

7.1 Conclusions

In today's world, great expectations are placed upon the state-of-the-art technology to deliver ever improving performance, under more difficult operating conditions, and at a reduced cost. No longer can a technology be expected to last 20 or 30 years unchanged, and any ultrasonic transducer manufacturer must remain at the leading edge of technology to remain competitive. Continual prototyping is an expensive and time consuming method of transducer design analysis, thus restricting the range of devices that can be examined within a project budget and time scale.

Finite element analysis offers the opportunity to model almost any transducer configuration with all ancillary components included, in both the time and frequency domain. Such modelling takes into account all effects of the device microstructure and is consequently a significant improvement over unidimensional modelling techniques. In general, past work has paid little attention to the mechanism of inter-pillar resonance generation and their effect upon the thickness mode, other than to suggest design criteria to ensure the separation of the various modes. By examination of the modes of resonance and the equivalent modelled responses, significant insights into composite transducer behaviour have been obtained. Additionally, knowledge and techniques developed in the early chapters of the thesis are applied in Chapter 6, to assist in the design of an improved flexible ultrasonic transducer for non-destructive testing. The major contributions of this thesis are listed below.

7.1.1 Main Findings of this Thesis

- Bragg scattering has been shown to be an inadequate theory of inter-pillar resonance generation. While the frequencies predicted by this method are generally accurate, the mechanism is incorrect. An alternative theory of inter-pillar resonance generation by Lamb waves is presented, with resonant frequencies and mode shapes accurately predicted. Excellent correlation between theory, experiment, and finite element models demonstrates the superiority of this theory to Bragg scattering.
- A scanning system capable of resolving sub-nanometer displacements with micron resolution in the lateral axes has been developed, by use of a heterodyne laser vibrometer and a micropositioning rig.
- The acousto-optic effect has been shown to have minimal consequences for laser scanning of ultrasonic transducers through water, provided the acoustic pressure in the water is sufficiently low.
- A range of finite element models has been developed, capable of analysing a range of connectivity types, a range of materials, with additional components such as matching layers, in both the time and frequency domain.
- Techniques for minimising the computing time required for a finite element model, with no reduction in quantity or accuracy of data obtained, have been developed. Suggestions for the appropriate use

of 2.5, or 3D modelling have been made, along with recommendations for appropriate mesh sizes and time steps.

- The finite element models have been shown to accurately predict the impedance and surface displacement profiles of piezocomposite transducers.
- FEA has been used to assist in the design of an improved flexible ultrasonic transducer array, demonstrating its uses in material selection and prediction of cross-coupling, and choice of component sizes. Techniques for improvement in manufacture have been suggested.
- It was recommended that the overall width to thickness ratio for 2-2 composites be at least 15 : 1 to prevent the harmonics of width modes impinging upon the thickness mode.
- A range of MPAR values for homogenous displacement has been presented, for PZT-5H hardset and softset transducers. It was recommended that low volume fraction 2-2 composites be manufactured with soft setting epoxies, with higher volume fraction devices filled with hard setting epoxies.
- Finally, while FEA has been shown to be a powerful and accurate tool in the analysis of piezocomposite devices, care must still be taken in its use and analysis methods applied. Computing power is not yet at a stage where every aspect of a transducer can be modelled economically, and there is still, therefore, a requirement for an experienced ultrasonic design engineer to ensure the most effective application of this highly advanced tool.

7.2 Suggestions for Further Work

It is impossible to completely examine all aspects and areas of interest arising during the writing of a thesis. There are therefore a number of topics which require further study, and these are detailed below.

7.2.1 Material Characterisation

It is apparent that the results from any finite element model can only be as accurate as the input information. Exact material characteristics are therefore essential, but are not always available. Ceramic manufacturers state a maximum 10% variation from their published material properties, with properties varying from batch to batch. Polymer properties vary depending upon the curing time and temperature, and upon the accuracy of the mixing and evacuation processes. It is recommended that a comprehensive series of material characteristics be developed for all materials likely to be used in any ultrasonic analysis. The stiffness, dielectric, and piezoelectric parameters for ceramic should be identified, and the actual variance from typical values noted. This will allow the reliability of ceramic manufacturers to be determined, and appropriate steps can then be taken to ensure that modelling is accurate. Polymers should be manufactured under a strict set of guidelines to ensure consistency across batches.

Most importantly, it is suggested that exact values of shear and longitudinal damping at a range of frequencies be obtained. With these values, the analysis method suggested in chapter 5 could be used to ensure that modelling of transducers with modes across a large frequency range is accurate at all points.

7.2.2 Validation of the Acousto-optic Effect at High Power Levels

While it has been theoretically shown that the acousto-optic effect will have no significant effect until high power levels, there is limited experimental evidence to support this. It is recommended that the laser vibrometer be adapted such that it no longer is limited by the range resolution that prevents displacements larger than 75 nm being measured. If this is implemented, measurements of displacements at high power levels can be obtained, up to a driving voltage of several hundred volts. At this power level the acousto-optic effect should become significant, and should be relatively easy to demonstrate. In addition, it is recommended that the linearity of displacement against driving voltage for various ceramics, as well as any hysteresis effects, be quantified. As any non-linearities at higher voltages may contribute to the alteration in predicted displacement readings, this would be a necessary step in ensuring the acousto-optic effect is the only effect being measured.

7.2.3 Transient Analysis of Piezocomposite Transducers

Although this thesis has demonstrated the capability of FEA to model piezoelectric devices in the time domain to study wave propagation, all experimental results have been measured in the frequency domain. The software controlling the laser vibrometer system could be altered such that a displacement against time response is stored for each point on the transducer surface. This data could then be used to form an animation of the behaviour of the transducer surface with time, and could be compared with the finite element simulation. A system such as this could be used to examine any mode-coupling effects that may exist, such as that described by Gachagan [71], who demonstrated that a piezocomposite with inter-pillar and thickness modes at similar frequencies produced increased bandwidths. It was

proposed that the inter-pillar mode acted in a parasitic fashion, removing energy from the thickness mode, and reducing the ring-down time (and therefore increasing bandwidth). By examination of transducer behaviour in the time domain, any mode interaction could be easily observed, and bandwidth calculated from a Fourier Transform of the transient output. It may be feasible to construct a set of guidelines for each volume fraction, the aspect ratio at which maximum bandwidth is achieved due to mode coupling in piezocomposite devices.

7.2.4 Lamb Wave Propagation in Piezocomposites.

While it has been demonstrated that the fundamental symmetric Lamb wave is responsible for the first two inter-pillar resonances, experimental and finite element results indicated that the composite structure has altered the Lamb wave phase velocity from that of the pure polymer. For accurate prediction of inter-pillar resonance frequency, the effect of ceramic on the phase velocity should be quantified. Ideally, a relationship between the phase velocity and volume fraction should be obtained.

Although the first two inter-pillar resonances are the most commonly encountered lateral modes, it is possible that higher frequency modes are generated by higher order Lamb waves (s_1, s_2, etc). Finally, while it has been suggested that the phase velocity of the Lamb waves is somewhere between that of polymer and ceramic for piezocomposites, it is possible that the antisymmetrical mode, displacing primarily out of plane, is supported more by the polymer only, and will consequently maintain a phase velocity close to that of the pure polymer. These, and circumstances under

which the antisymmetrical mode becomes responsible for inter-pillar resonance propagation require investigation.

7.2.5 Development of a Transducer for Through Air Transmission.

A significant limitation of piezocomposite transducers is the acoustic mismatch between the constituent components and air, causing a large energy loss at such boundaries. Solutions to this problem include the use of specially designed matching layers to minimise overall energy loss and the use of electrostatic transducers. With a finite element modelling system, it would be possible to analyse an entirely new design of composite transducer with minimal prototype construction. By utilisation of the inter-pillar resonances, perhaps at identical frequencies to the thickness mode, it would be possible to cause the polymer in a composite to displace significantly more than the ceramic. It may be possible to use the displacing polymer as the main driving material behind acoustic pressure generation, thus reducing the mismatch of acoustic impedances. Possible approaches include the design of high Poisson's ratio polymers, or polymers with low acoustic impedances developed by addition of air filled microspheres. The ceramic itself in a 2-2 design could be rotated 90 degrees and poled on the sides, thus ensuring that the greatest ceramic displacement was in the lateral axes, therefore increasing the thickness displacement of the polymer.

By use of FEA, even the wildest 'blue sky' transducer design can be economically analysed to determine its viability before extensive investment in time and money is committed to a project.

7.2.6 Development of the Flexible Ultrasonic Array

Although it has been demonstrated that the improved design of the flexible array is practical, significant work must be done before this could be said to be a completed system. Ideally, matching electronics would be designed for this device, along with an automated means of signal application and capture. Such an improvement would not only improve the amplitude and noise characteristics of any signals, but would allow the advantages of phased arrays (focussing, beam steering and apodisation) to be brought into play.

A flexible array such as this, designed for highly variable surface geometries, is ideally suited to adapting to the diversity present in human bodies. The flexible array is suitable as a bio-medical scanner in that there will be very few places in the human body to which it cannot conform. Unfortunately, the copper front face arrangement of the existing optimises energy transfer to high acoustic impedance media such as metals, rather than human tissue. By sputtering or evaporation of an electrode onto the platelet front face, and replacement of the copper front face with an appropriate flexible matching layer such as soft setting epoxy, energy transfer to body tissue could be maximised, making the flexible ultrasonic transducer array an excellent choice for ultrasonic imaging of low acoustic media.

References

[1] Pauer, L.A, 'Flexible Piezoelectric Material', *IEEE Intl. Conv. Rec.*,1973

[2] Newnham, R.E, Skinner D.P., Cross L.E.,, 'Connectivity and Piezoelectric-pyroelectric Composites', *Materials Research Bulletin,* Vol 13, 1978, pp 525-536

[3] Savakus, H.P., Klicker K.A., Newnham R.E., 'PZT-Epoxy Piezoelectric Transducers: A Simplified Fabrication Procedure', *Materials Research Bulletin,* Vol 16, 1981, pp 677-680.

[4] Smith, W.A, Shaulov A.A., Singer B.M. 'Properties of Composite Piezoelectric Materials for Ultrasonic Transducers', *1984 IEEE Ultrasonics Symposium Proceedings,* 1984, pp 539-544.

[5] Shaulov, A.A., Smith W.A., Singer B.M., 'Performance of Ultrasonic Transducers made from Composite Piezoelectric Materials', *1984 IEEE Ultrasonics Symposium Proceedings,* 1984, pp 545-548.

[6] Smith, W.A., and Auld B.A., 'Modelling 1-3 Composite Piezoelectric Thickness Mode Oscillations', *IEEE Transactions on Ultrasonics, Ferroelectrics and Frequency Control,* Vol 38, No. 1, 1991, pp 40-47.

[7] Auld, B.A., Kunkel H.A., Shui Y.A., and Wang Y., 'Dynamic Behaviour of Periodic Piezoelectric Composites', *1983 IEEE Ultrasonics Symposium Proceedings,* 1983, pp 554-558

[8] Auld, B.A., Shui Y.A., and Wang Y., 'Elastic Wave Propagation in Three-Dimensional Periodic Composite Lattices', *Journal de Physique*, Vol 45, 1984, pp 159-163.

[9] Auld, B.A., and Wang Y., 'Acoustic Wave Vibrations in Periodic Composite Plates', *1984 IEEE Ultrasonics Symposium Proceedings,* 1984, pp 528-532.

[10] Wang, Y., and Auld B.A., 'Acoustic Wave Propagation in One-Dimensional Periodic Composites', *1985 IEEE Ultrasonics Symposium Proceedings*, 1985, pp 637-641.

[11] Wang, Y., Schmidt E., and Auld B.A., 'Acoustic Wave Transmission through One-Dimensional PZT-Epoxy Composites', *1986 IEEE Ultrasonics Symposium Proceedings,* 1986, pp 685-689.

[12] Gururaja, T.R., Schulze W.A., Cross L.E., Newnham R.E, Auld B.A., and Wang Y., 'Piezoelectric Composite Materials for Ultrasonic Transducer Materials Part 1: Resonant Modes of Vibration in PZT Rod-Polymer Composites', *IEEE Transactions Sonics and Ultrasonics,* Vol. 32, 1985, pp 481-498.

[13] Gururaja, T.R., Schulze W.A., Cross L.E., Newnham R.E, 'Piezoelectric Composite Materials for Ultrasonic Transducer Materials Part 2: Evaluation of Ultrasonic Medical Applications', , *IEEE Transactions Sonics and Ultrasonics,* Vol. 32, 1985, pp 499-513.

[14] Hayward, G., Macleod C.J., and Durrani T.S., 'A Systems Model of the Thickness Mode Piezoelectric Transducer', *Journal of the Acoustic Society of America,* Vol 76, 1984, pp369-375.

[15] Hayward, G. and Jackson, M.N., 'A Lattice Model of the Thickness Mode Piezoelectric Transducer', *IEEE Transactions on Ultrasonics, Ferroelectrics and Frequency Control,* Vol 33, 1986, pp41-50.

[16] Hayward, G., 'Using a Linear Systems Model to Assess the Influence of Some design, Constructional and Measurement Parameters on the Performance of NDT Probe Assemblies', *NDT International,* Vol 19, 1986, pp67-75.

[17] Hayward, G., and Gillies D., 'Block Diagram Modelling of Tall Thin Parallelepiped, Piezoelectric Structures', *Journal of the Acoustic Society of America,* Vol 86, 1989, pp 1643-1653.

[18] Hayward, G., 'Using a Block Diagram Approach for the Evaluation of Electrical Loading Effects on Piezoelectric Reception', Ultrasonics, Vol. 24, May 1986, pp 156–163.

[19] Hayward, G., and Gillies D., 'Five Port Lattice Model for Simulation of Piezoelectric Structures Possessing Twin, Compressional Modes of Vibration', *Ultrasonics,* Vol 28, 1990, pp363-369.

[20] Hossack, J.A., and Hayward G., 'Finite-Element Analysis of 1-3 Composite Transducers', *IEEE Transactions on Ultrasonics, Ferroelectrics and Frequency Control,* Vol 38, No. 6, 1991, pp 618-629.

[21] Hayward, G., and Hossak J.A., 'Uni-dimensional Modelling of 1-3 Composite Transducers', *Journal of the Acoustic Society of America,* Vol 88, 1990, pp599-608.

[22] Hossack, J.A., ' Modelling Techniques for 1-3 Composite Transducers', *PhD Thesis,* University of Strathclyde, Glasgow, Scotland, 1990.

[23] Oakley, C.G., 'Analysis and Development of Piezoelectric Composites for Medical Ultrasound Applications', *PhD Thesis,* Pennsylvania State University, U.S.A, 1991.

[24] Oakley, C.G., 'Geometric Effects on the Stop-band Structures of 2-2 Piezoelectric Composite Plates', *1991 Ultrasonics Symposium Proceedings,* 1991, pp 657-660.

[25] Certon, D., Pata F., Levassort F., Feuillard G., Karlsson B., 'Lateral Resonances in 1-3 Piezoelectric Periodic Composite: Modeling and Experimental Results', *Journal of the Acoustic Society of America,* Vol 101, 1997, pp 2043-2051.m

[26] Smith, W.A., 'New Opportunities in Ultrasonic Transducers Emerging from Innovations in Piezoelectric Materials', *1992 SPIE International Symposium,* July 1992.

[27] Mason, W.P., 'Electromechanical Transducers and Wave Filters', Van Nostrand-Rheinhold, Princeton, 1948.

[28] Krimholtz, R., Leedom D., and Matthei G., 'Equivalent Circuits for Transducers having Arbitrary Even-or-Odd Symmetry Piezoelectric Excitation', *IEEE Transactions on Sonics and Ultrasonics,* Vol 18, 1971, pp 128-141.

[29] Hayward, G., 'Transient Performance of a Piezoelectric Transducer', *PhD Thesis,* University of Strathclyde, Glasgow, Scotland, 1981.

[30] Allik H., and Hughes T.J.R., 'Finite Element Method for Piezoelectric Vibration', *International Journal for Numerical Methods in Engineering,* Vol 2, 1970, pp151-157

[31] Kagawa, Y., and Yamabuchi T., 'Finite Element Approach for a Piezoelectric Circular Rod', *IEEE Transactions on Sonics and Ultrasonics*, Vol 23, No 6, 1976, pp 379-385

[32] Kagawa, Y., and Yamabuchi T., 'Finite Element Simulation of a Composite Piezoelectric Ultrasonic Transducer', *IEEE Transactions on Sonics and Ultrasonics,* Vol 26, No. 2, 1979, pp 81-88

[33] Ostergaard, D.F., Pawlak T.P., 'Three-Dimensional Finite elements for Analyzing Piezoelectric Structures', *1986 IEEE Ultrasonics Symposium,* 1986, pp639-644.

[34] Lerch, R., 'Simulations of Piezoelectric Devices by Two- and Three-Dimensional Finite Elements', *IEEE Transactions on Ultrasonics, Ferroelectrics and Frequency Control,* Vol 37, No 2, 1990 pp 233-247.

[35] Rajakumar, C., Ali A., Yunus S.M., 'A New Acoustic Interface Element for Fluid-Structure Interaction Problems', *International Journal for Numerical Methods in Engineering,* Vol 33, 1992, pp369-386.

[36] Friedrich, W., Kaarmann H., Lerch R., 'Finite element Modeling of Acoustic Radiation from Piezoelectric Phased Array Antennas', *1990 IEEE Ultrasonics Symposium Proceedings,* 1990, pp 763-767.

[37] Wojcik, G.L., Vaughan D.K., Abboud N., Mould J. Jr., 'Electromechanical Modeling using Explicit Time-Domain Finite Elements', *1993 IEEE Ultrasonics Symposium Proceedings,* 1993, pp 1107-1112.

[38] Wojcik, G.L., Vaughan D.K., Murray V., and Mould J. Jr., 'Time-Domain Modeling of Composite Arrays for Underwater Imaging', *1994 IEEE Ultrasonics Symposium Proceedings,* 1994, pp 1027-1032.

[39] Lerch, R., Landes H., and Kaarmann H.T., 'Finite-element modeling of the Pulse-echo Behaviour of Ultrasound Transducers', *1994 IEEE Ultrasonics Symposium Proceedings,* 1994, pp 1021-1025.

[40] Hladky-Hennion, A.C., Decarpigny J., 'Finite Element Modeling of Active Periodic Structures: Application to 1-3 Piezocomposites', *Journal of the Acoustic Society of America,* Vol 94, 1993, pp 621-635.

[41] Bennett, J.T., 'Finite Element Modelling of 1-3 Piezocomposite Transducers', *PhD Thesis,* University of Strathclyde, Glasgow, Scotland, 1995.

[42] Hayward, G., Bennet, J. and Hamilton, R., 'A Theoretical Study on the Influence of Some Constituent Material Properties on the Behaviour of 1-3 Connectivity Composite Transducers', *Journal. Acoustic. Society of America,* Vol. 98, No. 4, Oct 1995, pp 2187-2196

[43] Pa Park, S., and Shrout, T.R., 'Characteristics of Relaxor Based Piezoelectric Single Crystals', *IEEE Transactions on UFFC,* 1997, v.44, No.5, September 1997.

[44] Bowen, L.J., 'Fabrication of Piezoelectric Ceramic Polymer Composites by Injection Moulding', *Proceedings of the IEEE Symposium on the Applications of Ferroelectrics,* 1992, CH 155, pp 160-163.

[45] Kino, G.S., 'Acoustic Waves: Devices, Imaging and Analog Signal Processing', Prentice-Hall Inc., New Jersey, 1987, ISBN 0-13-003-47-3 025.

[46] Jackson, M., 'Simulation and Control of Thickness-Mode Piezoelectric Transducers', *PhD Thesis,* University of Strathclyde, Glasgow, Scotland, 1984.

[47] Kossoff, G., 'The Effects of Backing and Matching on the Performance of Piezoelectric Ceramic Transducers', *IEEE Transactions on Sonics and Ultrasonics,* Vol 13, No. 1, 1966, pp 20-31.

[48] DeSilets, C.S., Fraser J.D., and Kino G.S., 'The Design of Efficient Broad-Band Piezoelectric Transducers', *IEEE Transactions on Sonics and Ultrasonics,* Vol 25, No. 3, 1978, pp 115-125.

[49] Smith, W.A., Shaulov A., and Auld B.A., 'Tailoring the Properties of Composite Piezoelectric Materials for Medical Ultrasonic Transducers', *1988 IEEE Ultrasonics Symposium Proceedings,* 1988, pp617-622.

[50] Wang, Y., and Auld, B.A., 'Numerical Analysis of Bloch Wave Theory for Acoustic Wave Propagation in One-Dimensional Periodic Composites', *Proceedings of the 1986 IEEE International Symposium on the Applications of Ferroelectrics,* 1981, pp261-264.

[51] Hossack, J.A., Auld, B.A., and Batha, H.D, 'Techniques for Suppressing Spurious Resonant Modes in 1-3 Composite Transducers', *Proceedings of the 1991 IEEE International Symposium on UFFC,* 1991, pp 651-655

[52] Chandrupatla, T.R. and Belegundu, A.D., 'Introduction to Finite Elements in Engineering', Prentice-Hall, New Jersey, U.S.A., 1991, ISBN 0-13-483082-2

[53] Silvester, P.P., Ferrari R.L., 'Finite Elements for Electrical Engineers 3rd Edition', Cambridge University Press, Cambridge, U.K., 1996, ISBN 0-521-44505-1

[54] ANSYS, Inc, 'Ansys Users Manual for Revision 5.3', 1996

[55] Golub, G.H, Van Loan C.F., 'Matrix Computations' John Hopkins University Press, Baltimore, Maryland, 1983, ISBN 0-8018-3010-9

[56] N.A.F.E.M.S, 'A Finite Element Primer', Dept. Trade and Industry, National Engineering Laboratories, Glasgow, 1991, ISBN 0903640-171

[57] Kirk,, K.J., Cornwell, I., McNab, A., Cochran, A., and Hayward, G., 'An Array-based System for Monitoring Cracks in Industrial Plant at High Temperatures', *Insight,* Vol. 38, No. 10, Oct 1996, pp 722-727

[58] Ostergaard ,D.F., Pawlak T.P., 'Three Dimensional Finite Elements for Analysing Piezoelectric Structures', *Proceedings of the 1996 IEEE International Symposium on UFFC,* 1996

[59] Powell, D.J., Hayward, G., 'Flexible Ultrasonic Transducer Arrays for Non-Destructive Evaluation Applications – Part 1: The Theoretical Modelling Approach', *IEEE Transactions on UFFC,* May 1996, pp385-392

[60] Powell, D.J., Hayward, G., 'Flexible Ultrasonic Transducer Arrays for Non-Destructive Evaluation Applications – Part 1: Peformance Assensment of Different Array Configurations', *IEEE Transactions on UFFC,* May 1996, pp393-402

[61] Zienkiewicz, O, 'The Finite Element Method' McGraw Hill, London, U.K., 1971, CSN 070941386

[62] Frey, A.R., Kinsler, L.E., 'Fundamentals of Acoustics', John Wiley and Sons, New York, U.S.A, 1982, ISBN 0-471-09410-2

[63] Monchalin, J.P., 'Optical Detection of Ultrasound', IEEE Transactions on UFFC, Vol. 33, No. 5 September 1986, pp 485-499

[64] Polytec, 'Vibrometer Operator's Manual for Polytec Ultrasonic Vibrometer Series'

[65] Kaye, G.W.C, Laby T.H., 'Tables of Physical and Chemical Constants', Longman, 1995 16th Edition, London, ISBN 0-582-22629-5

[66] Sliwinski, A. 'Acousto-optics and its Perspectives in Research and Applications', *Ultrasonics,* Vol. 28, July 1990, pp 195-213

[67] Bacon, D.R., 'Primary Calibration of Ultrasonic Hydrophones Using Optical Interferometry', *IEEE Transactions on UFFC,* Vol. 35, No. 2, March 1998, pp152-161

[68] Royer, D., Dunois N., Benoist P., 'Optical Probing of Acoustic Fields – Application to the Ultrasonic Testing of Steam Generator Tubes', *1992 IEEE Ultrasonics Symposium Proceedings,* 1992, pp 805-888

[69] Bacon, D.R., Chivers, R.C. Som J.N., 'The Acousto-optic Interferometric Measurement of Ultrasonic Transducer Surface Motion', *Ultrasonics,* Vol. 31, No. 5, 1993, pp321-325

[70] Dixon, R.W., 'Photoelastic Properties of Selected Materials and Their Relevance for Applications to Acoustic Light Modulators and Scanners', *Journal of Applied Physics,* Vol. 38, No. 13, Dec 1967, pp 5149-5153

[71] Gachagan, A., 'An Evaluation of 1-3 Connectivity Composite Transducers for Air-coupled Ultrasonic Applications', Ph.D. Thesis, University of Strathclyde, Glasgow, Scotland, 1996

[72] Cochran, A., 'Ultrasonic Arrays Used to Monitor the Condition of Solid Test Subjects', Ph.D. Thesis, University of Strathclyde, Glasgow, Scotland, 1990

[73] Thomson, R.N., 'Transverse and Longitudinal Resolution of the Synthetic Aperture Focusing Technique', *Ultrasonics*, January 1984, pp 9 - 15

[74] Doctor, S.R., Hall, T.E., and Reid, L,D., 'SAFT – The Evolution of a Signal Processing Technology for Ultrasonic Testing', *NDT International*, Vol. 19, No. 3, June 1986, pp 163 – 167

[75] Gururaja, T.R., Schulze, W.A., Cross, L.E., and Newnham, R.E., 'Ultrasonic Properties of Piezoelectric PZT Rod-polymer Composites', *Proc. Of the 1984 Ultrasonics Symposium*, 1984, pp 533-538

[76] Gururaja, T.R., Schulze, W.A., Cross, L.E., Newnham, R.E., Auld, B.A., and Wang, J., 'Resonant Modes in Piezoelectric PZT Rod-polymer Composite Materials', *Proc. Of the 1984 Ultrasonics Symposium*, 1984, pp.523-527.

[77] Viktorov, I.A., 'Ultrasonic Technology A Series of Monographs. Rayleigh and Lamb Waves – Physical Theory and Applications', Plenum Press, New York, 1967, Library of Congress No. 67-10537.

[78] Monkhouse, R.S.C., Wilcox, P.D., and Cawley, P., 'Flexible Interdigital PVDF Lamb Wave Transducers for the Development of Smart Structures', Review of Progress in Quantitative Nondestructive Evaluation, Vol. 16, Plenum Press, New York, 1997, pp 877-884.

[79] Wilcox, P., Castaings, M., Monkhouse, R., Cawley, P., and Lowe, M., 'An Example of the Use of Interdigital PVDF Transducers to Generate and Receive a High Order Lamb Wave Mode in a Pipe.', Review of Progress in Quantitative Nondestructive Evaluation, Vol. 16, Plenum Press, New York, 1997, pp 919-884926.

[80] Achenbach, J.D., 'Wave Propagation in Elastic Solids', North-Holland Publishing Company, Amsterdam, Netherlands, 1973. ISBN 0-7204-2367-8

[81] Shui, Y., Geng, X., and Zhang, Q.M., 'Theoretical Modeling of Resonant Modes of Composite Ultrasonic Transducers', *IEEE Transactions on Ultrasonics, Ferroelectrics and Frequency Control*, Vol. 42, No. 4, July 1995, pp 766-773

[82] Geng, X., and Zhang, Q.M., 'Evaluation of Piezocomposites for Ultrasonic Transducer Applications —Influence of the Unit Cell Dimensions and the Properties of Constituents on the Performance of 2-2 Piezocomposites', *IEEE Transactions on Ultrasonics, Ferroelectrics and Frequency Control*, Vol. 44, No. 4, July 1997, pp857 – 872.

[83] Shui, Y., and Xue, Q., 'Dynamic Characteristics of 2-2 Piezoelectric Composite Transducers', *IEEE Transactions on Ultrasonics, Ferroelectrics and Frequency Control,* Vol. 44, No. 5, September 1997, pp 1110 – 1119.

[84] Qi, W., and Cao, W, 'Finite Element Analysis of Periodic and Random 2-2 Piezocomposite Transducers with Finite Dimensions', *IEEE Transactions on Ultrasonics, Ferroelectrics and Frequency Control*, Vol. 44, No. 5, September 1997, 1168 – 1171

[85] Oakley, C.G., 'Geometric Effects on the Stopband Structure of 2-2 Piezoelectric Composite Plates', *Proc. Of the 1991 Ultrasonics Symposium*, 1991, pp.657- 660

[86] Richard, C., Guyomar, D., and Eyraud, L., 'Influence of the Stress-transfer on the Dynamic Properties of the 2.2 PZT-polymer Composites', *Ultrasonics,* Vol. 34, 1996, pp 163 – 167.

[87] Mason, P. M., 'Physical Acoustics : Principles and Methods – Methods and Devices',Academic Press, London, U.K., 1964, Vol. 1. Part A, p190, Library of Congress No. 63-22327

Appendix

Material Properties

Ceramic

Ceramic	PZT-5A	PZT-5H	MPT	PMN
Stiffness (10^{10} Pa)				
c_{11}^E	12.03	12.72	14.92	8.40
c_{12}^E	7.52	8.02	3.68	3.83
c_{13}^E	7.51	8.47	3.24	4.94
c_{33}^E	11.09	11.74	12.76	10.94
c_{44}^E	2.11	2.30	5.52	2.8
c_{66}^E	2.26	2.35	5.65	2.5
Piezoelectric Stress (Cm^{-1})				
e_{13}	-5.4	-6.5	-0.953	3.04
e_{33}	15.8	23.3	10.24	8.36
e_{15}	12.3	17.0	5.25	2.53
Relative Permittivity				
ε_{11}^S	916	1700	263	265
ε_{33}^S	830	1470	210	265
Density (kgm^{-1})	7750	7500	6900	5900

Superscript S denotes constant strain, superscript E denotes constant electric field.

Polymer

Material	Hardset	Softset
Mix	CY1301/HY1300	CY208/HY956
Youngs Modulus (10^9 Pa)	4.03	2.0
Poisson's ratio	0.3791	0.393
Density (kgm^{-1})	1140	1150
Relative Permittivity	4	3
Longitudinal Velocity (ms^{-1})	2565	1880
Shear Velocity (ms^{-1})	1132	790